EMPIRICAL MEASUREMENTS OF MASSIVE GALAXY AND ACTIVE

GALAXY EVOLUTION

by

Richard Jacob Cool

A Dissertation Submitted to the Faculty of the

DEPARTMENT OF ASTRONOMY

In Partial Fulfillment of the Requirements
For the Degree of

DOCTOR OF PHILOSOPHY

In the Graduate College

THE UNIVERSITY OF ARIZONA

2 0 0 8

THE UNIVERSITY OF ARIZONA
GRADUATE COLLEGE

As members of the Dissertation Committee, we certify that we have read the dissertation prepared by Richard Jacob Cool entitled "Empirical Measurements of Massive Galaxy and Active Galaxy Evolution" and recommend that it be accepted as fulfilling the dissertation requirement for the Degree of Doctor of Philosophy.

_____ Date: 12 May 2008
Daniel Eisenstein

_____ Date: 12 May 2008
Buell Jannuzi

_____ Date: 12 May 2008
Dennis Zaritsky

_____ Date: 12 May 2008
Romeel Dave

_____ Date: 12 May 2008
Edward Olszewski

Final approval and acceptance of this dissertation is contingent upon the candidate's submission of the final copies of the dissertation to the Graduate College.

I hereby certify that I have read this dissertation prepared under my direction and recommend that it be accepted as fulfilling the dissertation requirement.

_____ Date: 12 May 2008
Dissertation Director: Daniel Eisenstein

STATEMENT BY AUTHOR

This dissertation has been submitted in partial fulfillment of requirements for an advanced degree at The University of Arizona and is deposited in the University Library to be made available to borrowers under rules of the Library.

Brief quotations from this dissertation are allowable without special permission, provided that accurate acknowledgment of source is made. Requests for permission for extended quotation from or reproduction of this manuscript in whole or in part may be granted by the head of the major department or the Dean of the Graduate College when in his or her judgment the proposed use of the material is in the interests of scholarship. In all other instances, however, permission must be obtained from the author.

SIGNED: Richard Jacob Cool

ACKNOWLEDGMENTS

DEDICATION

To my father, Marlene, and my grandparents. Without your love and support none of this would have been possible.

TABLE OF CONTENTS

LIST OF FIGURES

LIST OF TABLES

ABSTRACT

Using new wide-area galaxy redshift surveys, we explore the evolution of the most massive galaxies and the most luminous quasars in the universe over much of cosmic history. Quasars and massive red galaxies both are extremes; the most luminous high redshift quasars likely play a key role in shaping their nearby environment and the universe as a whole. The most massive galaxies represent the end points of galaxy evolution and contain a fossil record of the galaxy evolution process.

Using the AGES redshift survey completed with the MMT and the Hectospec multi-object spectrograph as well as new z-band observations of the NOAO Deep Wide-Field Survey Bootes field, we report the discovery of three new quasars at $z > 5$. We explore new mid-infrared selection in light of these three new quasars and place constraints on the slope of the high-redshift quasar luminosity function.

At lower redshift ($0.1 < z < 0.4$) we measure the scatter in red galaxy colors around the optical red-sequence using imaging and spectroscopy from the Sloan Digital Sky Survey. With our sample of nearly 20,000 massive early-type galaxies ($L \gtrsim 2.2L^*$), we find that the scatter around the color-magnitude relation is quite small in colors studied. Each of three model star formation histories can reproduce the scatter we measure, none of the models produce color distributions matching those observed.

We measure the evolution of the LRG luminosity function in the redshift range $0.1 < z < 0.9$. We find that the LRG population has evolved little beyond the passive fading of its stellar populations since $z \sim 0.9$. The most massive ($L > 3L^*$)red galaxies have grown by less than 50% (at 99% confidence) since $z = 0.9$

in stark contrast to the factor of 2 to 4 growth observed in the L^* red galaxy population over the same epoch.

Finally, we introduce the PRIsm MUlti-object Survey (PRIMUS), a new redshift survey aimed at collecting $\sim 300,000$ galaxy spectra over 10 deg^2 to $z \sim 1$. We summarize the current status of PRIMUS observations and data reductions and present several survey statistics. PRIMUS is the largest existing redshift survey at intermediate redshift and holds the largest sample of redshifts for *Spitzer* and X-ray detected objects.

CHAPTER 1

INTRODUCTION

Man has constantly strived to understand his place in the Universe. The driving questions of how the universe began, its composition, and its global history are central to current cosmology experiments. Cosmology strives to answer these questions and put our current position in the Universe in the context of the initial conditions seeded in the moments after the Big Bang. Galaxy evolution experiments, on the other hand, probe the 13 billion years between the Big Bang and the present epoch in order to understand the physical processes that convert the gas in the early universe into the stars and galaxies we observe today. This dissertation centers on several projects focused on understanding the evolution galaxies and quasars over much of cosmic history.

1.1 Historical Background

Before the early twentieth century, it was widely thought that all of the stars, gas, dust, and large nebulae observed on photographic images resided in the Milky Way. By the 1920's this issue culminated in the Shapley-Curtis debate which posed the question of whether or not the large diffuse nebulae were distant galaxies like our own or closer nebulae within the Milky Way itself. This question was answered definitively in 1925 when Edwin Hubble, using the 60-inch and 100-inch reflectors at Mount Wilson Observatory, measured the photometric variability of Cepheids in M33 and M31. Using the known relationship between Cepheid period and luminosity (Leavitt, 1908), Hubble concluded that these galaxies must be located at quite large distances and are not part of the Milky Way (Hubble, 1925). With this discovery, the size of known universe increased dramatically; in-

stead of a single island of stars, the Universe was found to be populated by vast number of island galaxies similar to out own.

By measuring the apparent velocities of nearby galaxies, Hubble found that galaxies in all directions from the Milky Way appear to be receding with a velocity was was directly proportional to their distances (Hubble, 1929). The constant of proportionality, H_0, bears his name today and is currently thought to have a value of 70 km s^{-1} Mpc^{-1} (Komatsu et al., 2008). Hubble's critical observation was the first indication that the Universe is expanding; following this idea backward, it was hypothesized that the Universe began in a very dense and hot state and has since expanded and cooled over cosmic history. The discovery of the cosmic microwave background (CMB; Penzias & Wilson, 1965), the remnant radiation from the hot, dense, universe at high redshift, provided further observational confirmation of this theory. Theory predicts variations on the scale of one part in $10^4 - 10^5$ in the temperature of the CMB due to small density fluctuations in the early universe (Harrison, 1970; Peebles & Yu, 1970; Zeldovich, 1972; Sunyaev, 1978; Hu & Dodelson, 2002, and references therein) which were observed directly by the COBE mission (Smoot et al., 1992; Bennett et al., 1996) resulting in the second Nobel Prize based on measurements of the CMB (the first being to Penzias & Wilson). The WMAP mission (Bennett et al., 2003) has measured the power spectrum of CMB anisotropies with exquisite resolution and has measured the Universe to be composed of 4% normal baryonic matter, 74% dark energy, 22% dark matter (Spergel et al., 2007; Komatsu et al., 2008).

With the knowledge the cosmological parameters from the CMB, we have a firm hold on the composition of the the universe. Combined with Einstein's theory of General Relativity (Einstein, 1915, 1916), the evolution of the purely gravitationally influenced dark matter can be calculated with high precision (Springel

et al., 2005a, 2006, and references therein). As baryonic matter only contributes 4% of the total mass density to the universe, these simulations provide a guide of the total gravitational evolution of the universe but lack the resolution and physical models to simulate the processes which initiate and regulate star formation and other gastrophysical processes which control the growth of galaxies.

1.2 Galaxy Formation and Evolution

Classically, galaxy formation was thought to occur in one of two modes. Perhaps galaxies are formed largely from one initial cloud of gas. In this monolithic collapse model, originally posed by Eggen, Lynden-Bell, & Sandage (1962), galaxies are thought to form from the rapid collapse of a single gas cloud which, in order to conserve angular momentum, slowly collapses into a disk; the oldest stars present in the galaxy form while the cloud contracts leading to a gradient in stellar metallicity in the halo. This model was originally posed to explain the apparent correlation between metallicity and orbital parameters in a sample of high-velocity stars. This model also predicts a very small dispersion in globular cluster ages as they all form quite early during the initial collapse.

The monolithic collapse hypothesis was challenged by Searle & Zinn (1978) based on the lack of an observed metallicity gradient and large age spread in the ages of globular clusters. Instead of a single formation event, Searle & Zinn (1978) advocated a scenario in which the halo was built up over several billion years from the accretion of many independent low-mass galaxies. This hypothesis has been backed up observationally by more precise measurements of stellar ages and abundances in the halo and the discovery of several tidal streams and structures in the halo likely remaining from past accretion events (Majewski et al., 1994; Helmi et al., 1999; Duffau et al., 2006; Newberg et al., 2002; Belokurov

et al., 2006, 2007; Dinescu et al., 2002; Majewski et al., 2003; Newberg et al., 2007, and references therein).

The accretion scenario for galaxy growth is also supported by the growth of dark matter halos in cold dark matter simulations. In these calculations, halos are seen to grow hierarchically wherein haloes flow along filamentary structures and merge into progressively larger systems (e.g Moore et al., 1999). In the current model for galaxy formation, these dark matter haloes accrete gas from the interstellar medium (e.g Katz & Gunn, 1991; Navarro & White, 1994; Steinmetz & Mueller, 1994; Dekel & Birnboim, 2008) and forms a disk. Massive spiral galaxies are destroyed through major mergers resulting in a spheroidal bulge or elliptical galaxy (e.g Toomre, 1974; Kauffmann et al., 1996).

This scenario for galaxy growth does not completely mimic nature, however; early models of galaxy formation in this context were unable to reproduce the full range of galaxy populations. As noted by Thoul & Weinberg (1995), the amount of cooling provided by models tuned to match the number of Milky Way-like galaxies is insufficient to produce the paucity of blue, luminous, galaxies and over produces massive, old, galaxies. This mismatch with observations has led to the introduction of strong feedback processes such as from supernovae or nuclear activity (e.g. Benson et al., 2003; Croton et al., 2006). The extent of this feedback and the processes that couple energy from these phenomena to the large-scale gas in galaxies and the processes that lead to the formation and growth of the most massive galaxies is a topic of much current research and a central theme in this dissertation.

Numerous lines of reasoning indicate that the conditions under which galaxies form stars has significantly changed over cosmic history. With the advent of numerous large-area and deep pencil-beam surveys of the high-redshift uni-

verse, numerous measurements of the global star formation rate density have been made extending to $z \sim 6$. Observations generally agree that the star formation rate density of the universe has decreased significantly from $z = 1$ to the present day with a nearly constant star formation rate density at higher redshifts (e.g., Wilson et al., 2002; Haarsma et al., 2000; Flores et al., 1999; Cowie et al., 1999; Hogg et al., 1998; Hammer et al., 1997; Lilly et al., 1996; Madau et al., 1996; Hopkins, 2004; Hopkins & Beacom, 2006). Similarly, the cosmic stellar mass density has increased steadily over the past 12 Gyr (Pérez-González et al., 2008; Brinchmann & Ellis, 2000; Dickinson et al., 2003; Glazebrook et al., 2004; Drory et al., 2005; Fontana et al., 2006). The decline in star formation rate density appears to affect the most massive galaxies earliest with progressively less massive galaxies dominating the star formation rate density of the universe at lower redshifts (Cowie et al., 1996; Heavens et al., 2004; Juneau et al., 2005; Bauer et al., 2005; Pérez-González et al., 2005; Bundy et al., 2006; Tresse et al., 2007). This mass dependence, often referred to as "downsizing", may indicate a star formation efficiency that is a strong function of stellar mass such that the most massive galaxies are quite efficient at converting gas into stars whereas dwarf galaxies only form stars inefficiently resulting in much more extended star formation histories. While studying the gross averages in the galaxy populations leads to insight about the global evolution of ensemble galaxy population, details about differential evolution in galaxies of different kinds are hidden. It is still unclear, for example, how much the growth of galaxies since $z \sim 1$ has been fueled by new star formation or through the simply the assembly of stellar material through mergers without new star formation. Two of the key goals of this disseration is to understand the relative importance of these two processes in the most massive galaxies since $z \sim 1$ and thus over half of cosmic history. Under-

standing how much new star formation has contributed to the growth of the most massive galaxies is the focus of Chapter 4 and constraining the total stellar mass growth of these galaxies is the focus of Chapter 5.

1.3   The Host Galaxy/Supermassive Black hole Connection

Early observations of quasars (or quasi-stellar objects) and the confirmation that these objects reside at cosmological distances with extreme luminosities gave the first indication that supermassive black holes may play an important role in cosmic history. The discovery of rapid variability in quasar brightnesses implies that quasar luminosity must be fueled by accretion onto a massive compact object (Salpeter, 1964; Lynden-Bell, 1969). Modern observations of the nearby universe find that supermassive black holes with masses of $10^6 - 10^9 M_\odot$ are quite common; spectroscopic observations find that 50-70% of bulge dominated galaxies in the nearby universe show evidence for an accreting supermassive black hole (Ho et al., 1997). In order to infer the presence of an inactive black hole, however, only its gravitation effects on the host can be used and thus high spatial resolution spectroscopy of the sphere of influence of the black hole is required. With the advent of the *Hubble Space Telescope*, spectroscopic observations at the required spatial resolution became possible and it was discovered that every bulge-dominated galaxy in the local universe showed dynamical evidence for a supermassive black hole at its core (see Kormendy, 2004, for a review).

The vast amount of energy injected by active galactic nuclei (AGNs) likely plays a significant role in the formation and evolution of the galaxy itself. This link is highlighted by the existence of a number of tight correlations between black hole mass and both the luminosity (Kormendy & Richstone, 1995) and velocity dispersion (Gebhardt et al., 2000; Ferrarese & Merritt, 2000; Tremaine et al.,

2002) of the host galaxy bulge. The velocity dispersion of the stars in the bulge is determined by the large scale potential in the bulge and are not in the sphere of influence of the central black hole; the existence of these correlations indicates that the black hole must "know" about the halo in which it lives. These correlations suggest that the growth of the black hole is strongly tied to the growth of the galactic bulge itself.

In order to understand the coupling between the properties of the host galaxy bulge and those of the central super massive black hole, several AGN feedback models have been proposed. In these models, as the accretion onto the black hole increases, the black hole grows and heats the gas around it. If the deposited energy exceeds the binding energy of the surrounding gas, the gas is removed as a fuel supply for the AGN as well as a reservoir of fuel for star formation in the bulge of the galaxy. While several models have been proposed to use AGN feedback models to explain the origin of the tight scaling relations between black holes and their bulges (e.g., Silk & Rees, 1998; Wyithe & Loeb, 2002; Di Matteo et al., 2005; Robertson et al., 2006; Hopkins et al., 2006a,b, 2007a,b), many of the details are still poorly understood. It is clear, however, that a detailed understanding of both AGN and galaxy populations as a function of redshift is needed in order to quantify the effects that the two populations have on each other throughout cosmic history. In Chapters 2 and 3, we present a new survey to find examples of quasars, the most powerful AGNs, to $z = 6$. These very luminous quasars at high redshfit are likely the seeds

1.4 The Role of Redshift Surveys in Galaxy Evolution Studies

Understanding the global properties and evolution of galaxies is not unlike undertaking a global anthropological study of the human race and how it has changed

over human history. As with humans, galaxies come in a wide variety of appearances, live in a wide variety of environments, are shaped both by in-situ processes and by interactions with their surroundings, and can change during their history both due to the passage of time and through interactions with others. Large imaging and spectroscopic surveys covering several square degrees of sky have become the tool of choice for collecting large samples of objects, be they stars, galaxies, or quasars, and have opened many new areas of astrophysics previously unexplored. While there are many motivations for large redshift surveys, in this dissertation, we capitalize on three key niches in which wide-areas are required.

1.4.1 Statistics

Statistics form the basis for all modern studies of galaxy evolution. Consider randomly selecting one individual human and studying them in exquisite detail. While it may be possible to perfectly understand the characteristics of that individual, the breadth of human culture, appearance, and ideals will be completely missed. Shortly after it was realized that galaxies were located at large distances from the Milky-Way it also became clear that galaxies come in a wide variety of types (Hubble, 1936). From galaxies with majestic spiral arms to galaxy resembling large spherical collections of red stars, galaxies span a variety of morphological types and optical colors. Any attempt to understand the galaxy population as a whole must consider these various types of galaxies and to understand the physical connections between each.

Even beyond measuring the mean properties of galaxy populations, galaxy evolution studies strive to measure the full distribution of galaxy properties and theoretical work focuses on reproducing these observed distributions. The full suite of galaxy properties are too numerous to list here, so consider, as an exam-

ple, the distribution of optical luminosities and colors of nearby galaxies. Early systematic investigations of the integrated galaxy colors found two types of galaxies: blue galaxies which span a broad range of luminosity and color and red galaxies with lie on a tight relationship between their optical colors and luminosity such that more luminous galaxies are redder than their less massive counterparts (the color-magnitude relation; de Vaucouleurs, 1961; Faber, 1973). This observation alone hints at some of the processes at work in galaxy evolution; the fact that more massive galaxies appear to be redder implies there must be a mass-dependent process that governs the age, metallicity, or dust content of red galaxies (Ferreras et al., 1999; Terlevich et al., 1999; Poggianti et al., 2001). The observed bimodality in optical galaxy colors has been a topic of much recent research both in understanding the origin of observed distribution (Strateva et al., 2001; Ellis et al., 2005; Baldry et al., 2006; Ball et al., 2006; Croton et al., 2006; Kang et al., 2005; Menci et al., 2005; Springel et al., 2005b; Menci et al., 2006; Bower et al., 2006; Cattaneo et al., 2006; Dekel & Birnboim, 2006; Perez et al., 2006) and in quantifying the existence of a color bimodality at high-redshift (Willmer et al., 2006; Bell et al., 2004; De Lucia et al., 2007; Blakeslee et al., 2003; Holden et al., 2004).

With the massive statistics of modern galaxy evolution studies, even more pieces of the puzzle come together. Hogg et al. (2004) showed that other galaxy properties are strongly correlated with its luminosity and color. For example, more compact galaxies tend to be red galaxies whereas blue galaxies tend to be more extended with disk-like surface brightness profiles. Similarly, galaxies which reside in dense regions with more neighbors tend to be red galaxies whereas less-dense areas are populated by both red and blue galaxies. This is a clear example of the necessity for massive statistics in modern empirical studies

of galaxy evolution; with modest samples of galaxies, it became clear that there was a large dispersion in galaxy properties, but only after many thousands of galaxies were observed could the detailed distribution in the galaxy properties be measured as well as the correlations between galaxy properties.

1.4.2 Cosmic Variance

Returning to the anthropology analogy, the location one conducts their research will dramatically influence the inferred result. For example, consider a sample of 100 people selected at random from New York City compared to 100 people chosen from Casper, Wyoming. While these people all fall under the "American" title, the average political, cultural, and economic positions of the two groups are quite different. The local environment from which the sample was drawn has a major impact on the outcomes of the study. The same holds true for galaxy evolution studies.

Comparisons of cluster and field galaxies at low redshift have shown that clusters of galaxies have a higher fraction of early-type, elliptical, galaxies compared to the field (Dressler, 1980; Postman & Geller, 1984; Whitmore & Gilmore, 1991; Goto et al., 2003). Thus a survey of only cluster galaxies would result in a severe under-accounting of spiral galaxies if extrapolated to the galaxy population as a whole. To make the problem more complicated, the range of galaxy environments is a continuum ranging from very dense clusters to nearly-empty voids. In this sense, no single area on the sky is representative of the galaxy population as a whole; any truly global statement about galaxy populations must sample the full range of galaxy environments in order to be unbiased to the environmental dependence of galaxy properties.

If we consider the luminosity function discussed in Section A, it is quite clear that sampling systematically over- or under-dense regions will result in system-

atic biases to the inferred normalization of the luminosity function. The angular correlation function $\omega(\theta)$, quantifies the excess probability of finding a second galaxy an angle θ away from another compared to a random distribution of galaxy positions. Given a galaxy population with angular correlation function $\omega(\theta)$, the expected variance in galaxy counts in a field is given by

$$\left\langle \frac{n_i - \langle n_i \rangle}{n_i} \right\rangle^2 = \frac{1}{\langle n_i \rangle} + \frac{1}{\Omega} \int \int \omega(\theta) \, d\Omega_1 d\Omega_2 \tag{1.1}$$

where θ is the angular separation of two solid angle elements $d\Omega_1$ and $d\Omega_2$ (Groth & Peebles, 1977; Efstathiou et al., 1991). This field-to-field variation in galaxy number counts, also known as cosmic variance in the population, is the dominant source of uncertainty in most modern studies of galaxy evolution.

A number of methods can help minimize the impact of large scale structure in the galaxy population on measurements. Simply increasing the area surveyed increases the range of environments sampled. This possibility has its limitations, however. Large scale structure is highly correlated and thus increasing the size of a single field can lead to a large survey still dominated by a large void or over-density. The 2 deg^2 COSMOS field, for example, contains a large over density of galaxies at $z \sim 0.7$ covering nearly 20% of the field (Guzzo et al., 2007; Scoville et al., 2007). Alternatively, one can divide their survey into several small blocks of sky which are widely separated in order to minimize the effects of a single large scale filament or void being sampled in many subfields. This may be difficult for very deep surveys, however, where the depth needed is reached by spending many hours on one pointing. Observationally, care must be taken when analyzing data from very disjoint areas, as well, as observational completeness and dust extinction likely vary from field to field and, if left uncorrected, will lead to inaccurate statistics.

1.4.3 Rare Objects

If one were interested in studying the culture and characteristics of the extremely wealthy, a large sample of people would need to be interviewed to find a single example of this very rare caste. In much the same way, the rarest objects in the universe can only be found by probing large volumes.

Even with perfect selection algorithms, a class of objects with small densities on the sky require that large areas be sampled in order to find even a handful of objects let alone a statistically robust sample. Often, rare objects are not trivially selected based on colors alone and thus not only is a large sample of object needed to find few examples, but each candidate must be followed up in order to confirm its classification. Consider the example of high-redshift ($z > 6$) quasars. Based on wide-area imaging from the Sloan Digital Sky Survey (SDSS) and follow-up spectroscopy, 19 high-redshift quasars have been discovered over 6600 deg^2 (Fan et al., 2001c, 2003, 2004, 2005). Simultaneously, these searches have increased the number of known brown dwarfs due to the similarity between high-redshift quasars and brown dwarf optical colors. With this density on the sky, at least 360 deg^2 on sky must be imaged in order to find a single quasar of comparable brightness; large area surveys are critical for finding these objects.

1.5 Historical Wide-Area Surveys

1.5.1 The Nearby Universe

Any study of galaxy populations and their evolution suffers from viewing our three dimensional universe on a two dimensional projection. In order to determine the intrinsic properties of galaxies, one needs distances to every galaxy in the sample; imaging alone is insufficient to allow high-precision measurements of galaxy evolution. Measurements of each galaxy's redshift, combined with our

understanding of the cosmological world model, allows for these distance measurements. The last quarter of the twentieth century paved the way for the rich diversity in wide-field imaging and spectroscopic surveys present today.

The Harvard-Smithsonian Center for Astrophysics (CfA) Redshift Survey (Huchra et al., 1983) was the first systematic attempt to catalog the distances to a large, homogeneous, sample of galaxies with the intent of studying the three dimensional distribution of galaxies in the local universe. Work from this survey set the standard for future work including detailed measurements of the clustering of nearby galaxies (Davis et al., 1982) and measurements of the local mean galaxy density and luminosity function (Davis & Huchra, 1982).

Subsequent projects grew in scope, both by observing larger areas on the sky but also by targeting to fainter magnitudes. The Las Campanas Redshift Survey (Shectman et al., 1996) measured nearly 25,000 redshift over 700 deg^2 with a median redshift of $z = 0.1$. The three dimensional structure in the galaxy distribution traced by this survey showed exquisite structure on all scales, clearly highlighting all galaxy environments from clusters to large, nearly-empty, voids. Data from this survey allowed for the detailed measurements of the galaxy luminosity function and found that faint end of the galaxy luminosity function is dominated by emission line galaxies (Lin et al., 1996). The large sample size of LCRS allowed for further subdivision of the galaxy samples and allowed for detailed quantification of the galaxy luminosity function as a function of spectral type (Bromley et al., 1998) and to characterize, for the first time, the influence the local galaxy density has on star formation rates over the full range of galaxy environments (Hashimoto et al., 1998). Capitalizing on the large sample of galaxies to create a sample of rare "E+A" (or post-starburst) galaxies (Dressler & Gunn, 1983), Zabludoff et al. (1996) studied the environments in which galaxies which

have recently ended their star formation activity live. These post-starburst galaxies are likely the missing link between the actively star-forming blue spiral galaxies and the massive red spheroids and seem to be associated with recent galaxy interactions.

The current standard bearer for low-redshift galaxy redshift surveys is the Sloan Digital Sky Survey (SDSS; York et al., 2000; Stoughton et al., 2002b; Abazajian et al., 2003, 2004a, 2005; Adelman-McCarthy et al., 2006a, 2007a,b). SDSS has imaged a quarter of the sky, primarily in the Northern Galactic Cap, through five bandpasses ($ugriz$; Fukugita et al., 1996) and obtained spectroscopy for nearly one million galaxies. The statistical precision made possible with SDSS is unparalleled by any other existing sky survey and has allowed more studies than can be adequately summarized here. The clustering of galaxies has been measured with unprecedented accuracy (Zehavi et al., 2005a) and significant deviations from a power-law in the real-space correlation function have been quantified and interpreted in terms of populating haloes with galaxies using halo occupation distribution modeling (HODs; Zehavi et al., 2004; Zheng et al., 2005). The luminosity function of galaxies has been quantified in exquisite detail (Blanton et al., 2003) and the local relationship between stellar mass and galaxy gas-phase metallicity has been measured with superb statistics (Tremonti et al., 2004). SDSS has allowed for statistically robust measurements of the properties of post-starburst galaxies and comparisons between the "E+A" galaxy luminosity function and the mean galaxy luminosity function (Quintero et al., 2004) and provided the statistics to derive empirical classification schemes for active galaxies (Kauffmann et al., 2003). SDSS, with its wide area, revolutionized samples of rare objects such as broad absorption line quasars (Trump et al., 2006), white dwarfs (Eisenstein et al., 2006a,b), and supernovae (Sako et al., 2008). Quite simply, SDSS now provides

the low-redshift anchor for a wide variety of future galaxy evolution surveys focused on observing more distant galaxies. No future low-redshift galaxy survey will surpass SDSS in terms of cosmic variance as the area useful for galaxy evolution work (areas away from the galactic contamination near the galactic plane) can only increase by a factor of 2 through the addition of a replica of SDSS covering the southern sk.

1.5.2   Probing the Universe to $z = 1$

Large area surveys focused on understanding the universe to $z = 1$ are a recent development in astrophysics. During the 1990s, several studies were completed to characterize galaxies at intermediate redshifts, but all of these surveys suffered from small sample sizes over small areas on the sky. The Canada-France Redshift Survey (Lilly et al., 1995) surveyed 600 galaxies over 0.14 deg^2, the Norris Redshift Survey (Small et al., 1997) obtained redshifts for ~ 800 galaxies by very sparsely sampling 20 deg^2, Cohen et al. (1999) measured spectra for ~ 1200 galaxies in two very small fields, and Carlberg et al. (1997) published a survey of ~ 250 galaxies in an area of 27 arcmin^2. While all pioneering at the time, each of these surveys were strongly hindered by cosmic variance in the small fields and small number statistics.

The COMBO-17 survey (Wolf et al., 2003a) attempted to fill the niche of an intermediate redshift survey without the use of observationally expensive spectroscopic observations. Instead, they used a combination of 5 broad band filters and 12 narrow and medium-band filters to measure the flux of $\sim 25,000$ galaxies across the full optical spectrum. In essence, the photometry measures a low-resolution spectral energy distribution (SED) for each galaxy in the field which can be fitted using models for the stellar continua and emission lines observed in nearby galaxies to recover an estimate of the redshift and stellar mass of each

galaxy in the sample. While redshifts recovered with this method are less precise due to the low-resolution spectral information, the $3 - 5\%$ errors in redshift (in $\sigma_z/(1 + z)$) are sufficient to derive rest-frame colors and luminosities and study the gross evolution of galactic properties to $z \sim 1$. On the other hand, the low-resolution redshifts limit the scales which can be studied in detail. Clusters of galaxies can be identified with photometric redshifts but the velocity structure within the cluster, and thus the tracer of cluster mass, is completely overwhelmed by redshift inaccuracy.

The Deep Extragalactic Evolutionary Probe (DEEP2) Galaxy Redshift Survey marked the first spectroscopic survey at $z = 1$ with large, homogeneously se-lected, samples of galaxies over modest areas on the sky (Davis et al., 2003). Using the Deep Imaging Multi-object Spectrograph (DEIMOS) on Keck, built specifically for this project, redshifts were obtained for $\sim 50,000$ galaxies color selected to reside at $z > 0.7$ over 3.5 deg^2. DEEP2 revolutionized the study of the high-redshift universe as it, for the first time, allowed for detailed subdivision of galaxy populations based on the local galaxy environment, spectral features, and AGN activity without losing statistical fidelity.

Clustering analysis from DEEP2 show that redder galaxies are more clus-tered than blue galaxies at $z = 1$ in much the same way that SDSS demon-strated galaxies cluster locally (Coil et al., 2008; Zehavi et al., 2005a). Cooper et al. (2008) explored the importance of galaxy environment on its star formation rate and found, in general agreement with earlier low-redshift results, that galax-ies in over-dense environments tend to show less star formation activity than field galaxies. Based on galaxy luminosity functions from DEEP2 (Willmer et al., 2006), Faber et al. (2007) found that the number density of all galaxies was ap-proximately constant from $z = 0$ to $z = 1$. When they split the sample into blue

and red galaxies, the number density of blue galaxies appears to remain constant over the same epoch while the number of red galaxies appears to have grown by factor of two. Detailed comparisons between samples of galaxies at $z \sim 0.1$ from SDSS and $z \sim 1$ from DEEP2 suggest that red sequence is likely built up through gas-poor mergers of red galaxies (so-called "dry" mergers) which result in no new star formation (Blanton, 2006).

While a revolutionary survey at $z = 1$, DEEP2 covers only 3.5 deg^2 on the sky. Even at $z = 1$, this probes an order of magnitude less volume than SDSS at $z = 0.1$ and contains 20x fewer redshifts. Furthermore, in all but 0.5 deg^2, DEEP2 targets were prescreened based on their observed BRI colors to remove objects at $z < 0.7$ and increase the sample density of $z = 1$ galaxies. In order to best quantify the evolution of all galaxies since $z = 1$, one needs a spectroscopic sample of galaxies covering a larger area and without a color preselection in order to minimize the effects of cosmic variance and to allowed for measurements of galaxy evolution completely within a single sample. We will present the first in the next generation of redshift surveys in Chapter 6 designed with these goals in mind.

1.6   Overview

The processes that convert gas into stars and those involved in shaping collections of stars, gas, and dust, and molding them into the nearby universe we live in are still very uncertain. This is a vibrant area of modern inquiry with each new insight into the physics involved in galaxy formation and evolution opening new lines of research. In this dissertation, we focus on the formation and evolution of the most massive galaxies in the $z < 1$ universe and try to place empirical constraints on the processes and time scales involved in their creation.

In Chapters 2 and 3, we add to the wealth of multi-wavelength imaging avail-

able in the 9 deg^2 NOAO Deep Wide-Field Survey Boötes Field and leverage this photometry and a new wide-area spectroscopic survey to search for rare high-redshift quasars. These quasars have extreme luminosities in the early universe and likely seed the growth of the most massive galaxies we observe locally. Chapters 4 and 5 are focused on constraining the amount of star formation and assembly through mergers which occurs at $z < 1$ in the most massive galaxies. While existing high-redshift galaxy surveys provide large samples of galaxies near L^*, they are hindered by small number statistics at the brightest magnitudes; Chapter 5 presents a new survey of high-redshift massive galaxies and measurements of the massive galaxy luminosity function over half of cosmic history.

We describe a the first in a new generation of redshift surveys aimed at very efficient spectroscopic of thousands of galaxies simultaneously at the expense of redshift precision in Chapter 6 . This chapter focuses on the motivation behind such a survey as well as a description of our targeting strategy, data processing, and redshift determinations. Finally, we concluded in 7 and offer paths forward in the next several years.

CHAPTER 2

ZBOÖTES : Z-BAND PHOTOMETRY IN THE NOAO DEEP WIDE-FIELD SURVEY
BOÖTES FIELD

We present zBoötes , a new z-band photometric imaging campaign of 7.62 square
degrees in the NOAO Deep Wide-Field Survey (NDWFS) Boötes field. In this pa-
per, all of the images for this survey are released as well as the associated catalogs.
The final zBoötes catalogs are complete (at the 50% level) to 22.7 mag over 50% of
the field. With these depths, the zBoötes images should be sensitive to L^* galaxies
to $z \sim 1$ over much of the survey area. These data have several possible applica-
tions including searching for and characterizing high-redshift quasars and brown
dwarfs and providing added constraints to photometric redshift determinations
of galaxies and active galaxies to moderate redshift. The zBoötes imaging adds
photometric data at a new wavelength to the existing wealth of multi-wavelength
observations of the NDWFS Boötes field.

2.1   Introduction

In recent years, a number of multi-wavelength surveys have been completed in
order to understand the evolution of the multi-wavelength properties of galaxies
and active galactic nuclei (AGNs) throughout cosmic history. Deep observations
spanning from the ultraviolet to the radio are time consuming and obtaining
spectroscopic follow-up observations of cataloged galaxies and AGNs requires
many nights on the largest telescopes available. Thus, the area covered by many
of the deepest multi-wavelength surveys is fairly small. With the advent of new
wide-field optical and near-infrared imagers and multi-object spectrographs, as
well as superb new space facilities such as *GALEX* and *Spitzer*, the amount of the

sky observed at all possible wavelengths is growing steadily.

One of the early deep, wide area, optical surveys, the NOAO Deep Wide-Field Survey [1] (NDWFS; Jannuzi et al. *in prep.*, Dey et al., *in prep.*) consists of two ~ 9 square degree fields (the Boötes and Cetus fields) with excellent optical (B_W, R, and I) and near-infrared (K_s) photometry. The NDWFS Boötes field has become a popular target for many investigators and now has been observed across the full electromagnetic spectrum. Deep GALEX pointings provide near and far-ultraviolet photometry for the field; the NDWFS images consist of optical and near-infrared coverage, and the FLAMINGOS Extragalactic Survey (FLAMEX; Elston et al., 2005) observed the field to deep limits in J and K_S. *Spitzer* has imaged the Boötes field with both IRAC (Eisenhardt et al., 2004, Spitzer Shallow Survey;) and MIPS. Radio observations include deep Westerbork observations at 1.4 GHz (de Vries et al., 2002) and imaging by the Faint Images of the Radio Sky at Twenty-Centimeters survey (FIRST; Becker et al., 1995). *Chandra* has observed the Boötes field for 5 ksec (XBoötes; Murray et al., 2005; Kenter et al., 2005). Optical spectroscopy for several highly complete samples of galaxies and AGN has been completed with the Hectospec multi-object spectrograph on the MMT as part of the AGN and Galaxy Evolution Survey (AGES; Kochanek in prep). A small region in the Boötes field was observed as part of the LALA survey to search for galaxies at very high redshifts (Rhoads et al., 2000). These data sets have allowed searches for high-redshift quasars and low mass stars using mid-infrared selection techniques (Stern et al., 2006), studies of the quasar luminosity function (Brown et al., 2006, Chapter 3), the clustering of high-redshift galaxies (Brown et al., 2005; Stanford et al., 2005; Rhoads et al., 2004; Brown et al., 2003), Lyman alpha emitting galaxies (Wang et al., 2004; Dey et al., 2005; Dawson et al.,

---

[1]http://www.archive.noao.edu/ndwfs
http://www.noao.edu/noao/noaodeep

2004; Rhoads et al., 2003), the broad band properties of AGNs (Brand et al., 2006, 2005; Stern et al., 2006, 2005), the X-ray properties of AGNs (Brand et al., 2006; Kollmeier et al., 2005), the spectral properties of infrared sources (Weedman et al., 2006; Desai et al., 2006; Khan et al., 2005; Higdon et al., 2005) and many other topics.

In this paper, we present new z-band observations of 7.6 square degrees in the NDWFS Boötes region. These catalogs reach several magnitudes deeper than the public imaging released by the Sloan Digital Sky Survey (SDSS) and will provide a useful intermediate photometric measurement between the I band data from NDWFS and near-infrared photometry from FLAMEX. We release the catalogs and reduced images for public use. Throughout this paper, all magnitudes are AB magnitudes (Oke , 1974).

2.2   Observations

The zBoötes imaging survey was completed with the 90Prime wide-field imager (Williams et al., 2004) at prime focus on the Bok 2.3m Telescope located on Kitt Peak. This instrument consists of four 4096x4096 thinned CCDs, providing excellent quantum efficiency in the blue, read out using eight amplifiers. The chips are arranged in a windowpane pattern with 10′ gaps between each of the CCDs. Each CCD images a 30′x30′ field on the sky with 0.45″ pixels. The south-east CCD has a large electron trap, making 13% of the area on that chip unusable for photometric measurements. These pixels are masked throughout the reduction process and are excluded when images are stacked.

The data were obtained between 28 Feb 2005 and 31 Mar 2005. Sky conditions varied from photometric to moderate levels of cirrus throughout the observations. The typical seeing during these observations was 1.6 arcsec. In total, we

completed observations for eight 90Prime pointings within the NDWFS Boötes region. At each location, we obtained several dithered 300s exposures (typically 12 exposures per field). The telescope was moved $\sim 1'$ for each dither. The total number of exposures for each field was determined by the conditions at the time of the observations. All of the exposures for a single field were obtained on the same night. As the gaps between CCDs on 90Prime are rather large, we did not attempt to make our dither pattern large enough the fill the regions between each CCD. This strategy avoids having non-uniform depth across a single field but results in gaps in our photometric coverage of the NDWFS survey field. Figure 2.1 shows the region covered in the zBoötes survey compared to the NDWFS Boötes Survey area. Throughout the rest of this paper, each of the fields imaged by a single 90Prime CCD is treated independently.

2.3 Reductions

All of the raw zBoötes images were processed using a combination of home-grown IDL routines and various tasks available within the Image Reduction and Analysis Facility (IRAF). Each image was bias and overscan corrected and known bad columns are removed by interpolating neighboring columns. On each night of clear skies, observations of the twilight sky were taken to generate a flat field image that was divided into each object frame to correct for pixel-to-pixel variations in the CCD sensitivity.

While the thinned-chip nature of the CCDs on 90Prime allows for high efficiency in the blue, it also results in strong fringing in the reddest bands where the night sky spectrum is dominated by a forest of emission lines. On each night of observation, between 12 and 42 individual dithered images were obtained for this project in the z-band. To generate a master fringe frame, we first removed
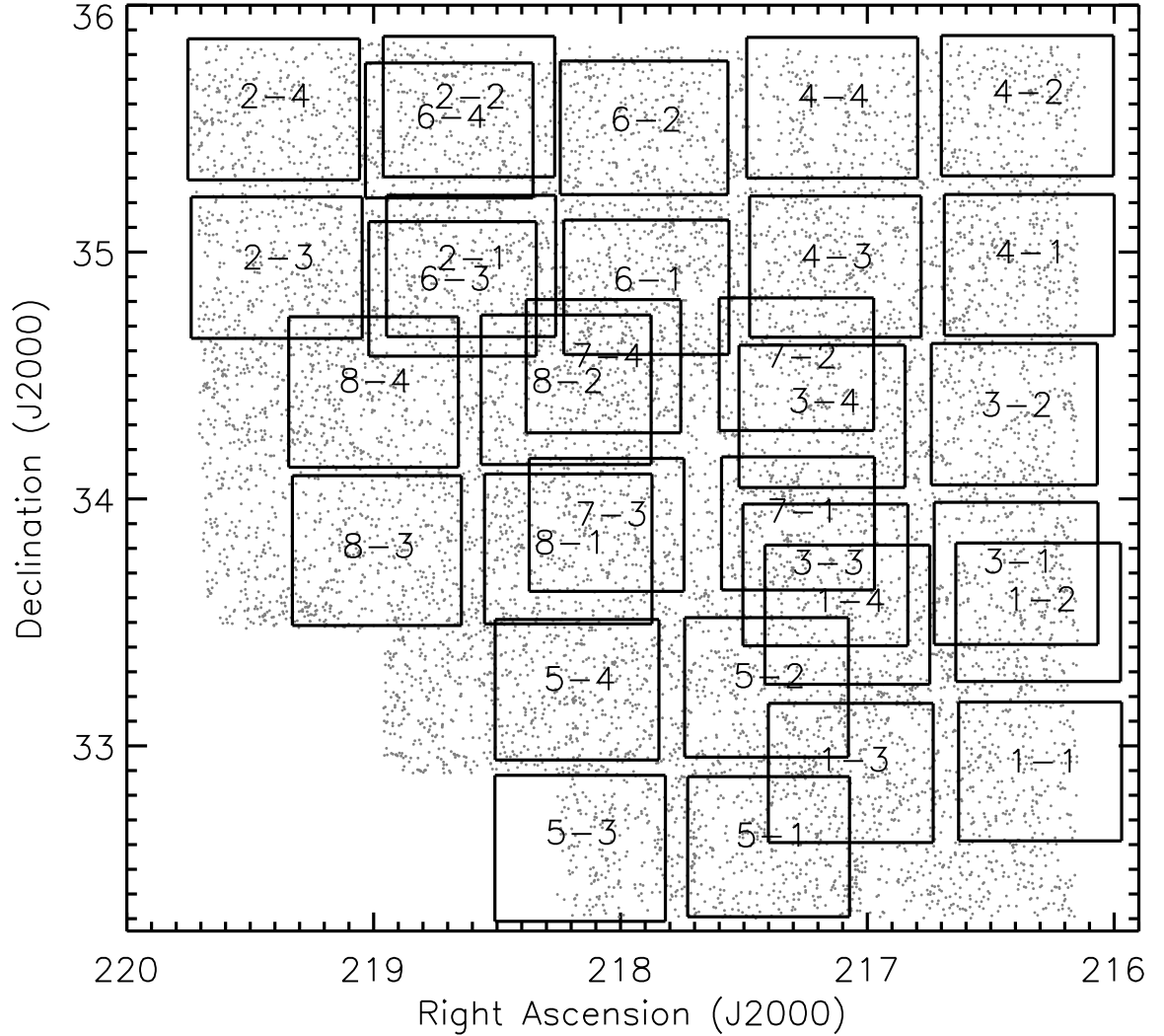
Figure 2.1 Map of the NDWFS survey area with the coverage of the
zBoötes catalog overlayed. The grey points illustrate the distribution of 25%
of the $I < 21.5$ galaxies in the NDWFS catalogs. Each of the subfields of the
zBoötes imaging is labeled with the field number. The zBoötes imaging covers
7.6 square degrees centered on the NDWFS Boötes Field, providing another set
of data to the current suite of multi-wavelength observations completed in this
region.

any large scale gradient in the background of each input image. The strength of the fringe pattern was then measured on each image and a multiplicative scale factor was applied to correct for any differences from the mean. We generated a master fringe frame by taking the median of all of the individual images taken on a single night of observations. This fringe frame was scaled to match the average strength of the fringes in each individual exposure and subtracted. This process was iterated (typically twice) until the fringe pattern was no longer present in each individual exposure. Figure 2.2 (a) and (b) shows a region of a single exposure before any processing and after the fringe pattern was been removed.

The astrometry of each image was calibrated by locating stars with $17 < z < 19$ from the Sloan Digital Sky Survey (SDSS) DR4 (Adelman-McCarthy et al., 2006a). We fit the astrometric solution with a 5th order TNX world-coordinate system (WCS) using the IRAF task CCMAP. The images were then de-projected onto a rectilinear pixel system using the task MSCIMAGE in the MSCRED package in IRAF. Finally, aperture photometry of several stars in the magnitude range $17 < z < 19$ was performed on each of the input frames in order to determine offsets in the background level and photometric zeropoint between each of the frames. Any variations in the mean background or transparency were corrected before the individual images were stacked to create the final coadded frame for each field. Pixels with values more than 3σ from the mean were clipped when creating the final mosaic; this clipping rejected any cosmic rays present in the individual frames. Figure 2.2 shows a portion of a final stacked image.

The photometric zeropoint for each stacked image was determined by comparison with photometry publicly available from the SDSS (Adelman-McCarthy et al., 2006a). Aperture photometry for stars with $18 < z < 19$ was compared to SDSS PSF magnitudes. The mean magnitude offset between the two photo-
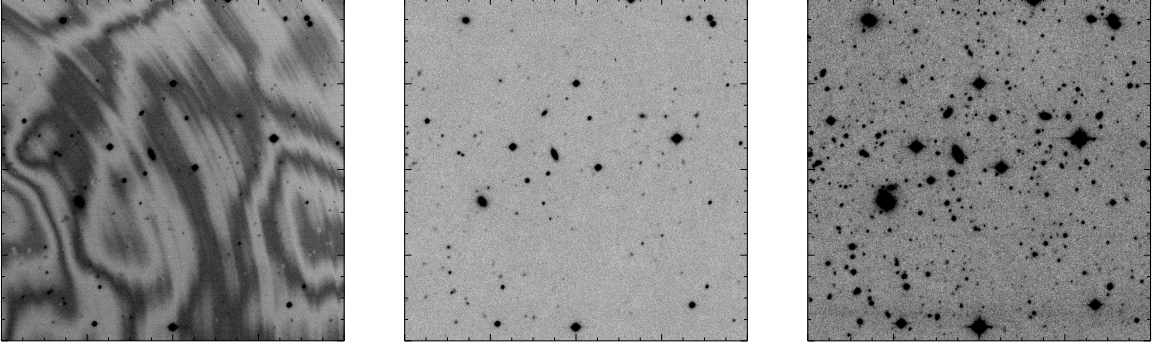
Figure 2.2 Example of the reduction steps performed on the zBoötes imaging data. Frame (a) shows a portion of a raw data frame taken with 90Prime. Frame (b) illustrates the same frame after flat-fielding and fringe correction. The final coadded frame, including all of the observations for this field, is shown in frame (c). Each of the images is 800 pixels on a side corresponding to ~ 6 arcminutes. The total exposure time for this field was one hour.

metric measurements was adopted as the magnitude zeropoint of the field. In general, the dispersion around this median was on the order of $\sigma_z \sim 0.03$ mag, comparable to the photometric scatter expected due to errors in the SDSS photometry (Ivezić et al., 2004). As the effective response of the z-band filter used in our work (including the effects of mirror reflectance and sky absorption) is likely different from that of the SDSS system, we examined the residuals between the zBoötes photometry and the SDSS photometry as a function of the SDSS $i - z$ color of each object. The photometric residuals showed no correlation with the object color, and thus no color term has been applied to the zBoötes photometry.

Several of the zBoötes fields overlapped significantly. These regions of significant overlap were coadded, weighted by seeing and signal-to-noise in each input frame, to create mosaiced images of the overlap regions. Before coadding the individual images in the overlap regions, each of the input images were background subtracted and the measured counts per pixel were converted to a true flux density per pixel measurement using the photometric zeropoint determined from comparison with public SDSS photometry discussed above. Figure 2.3 illus-

trates the area of the zBoötes field included in these coadded observations compared to the object distribution in the NDWFS optical catalogs.

2.4 Source Catalogs

2.4.1 Catalog Generation

We constructed catalogs for each zBoötes field using Source Extractor (SExtractor) version 2.3 (Bertin & Arnouts, 1996). We detected objects using a 0.9″ FWHM Gaussian convolution kernel and enforced a 3σ detection threshold. Pixels were weighted according to the number of input exposures that contributed to each in order to prevent the detections of a large number of spurious sources around the edges of each field which have fewer average observations and thus higher background noise than the centers. For each object detected in the catalog, we measured the flux in ~ 100 apertures (with diameter 3″, 5″, and 7″) in a 6 arcminute radius around the object. We used the interval containing 68.7% of the measurements as a measurement of the photometric error for each object. The simulated photometric errors we calculate from this method are about a factor of 2 larger than those measured by SExtractor.

Catalogs were also constructed for each of the stacked images created for the overlapping zBoötes fields using the same process as used for individual subfields. The final zBoötes catalog was constructed by checking each object for duplicate observations. For any object that was observed multiply, we define the best observation to be the measurement with the smallest simulated photometric errors. The final zBoötes catalogs consists of over 200,000 objects.

Objects in the final zBoötes catalogs were matched to detections in the NDWFS catalogs (DR3). For each NDWFS subfield, we checked for systematic offsets in both right ascension and declination between the zBoötes astrometric system
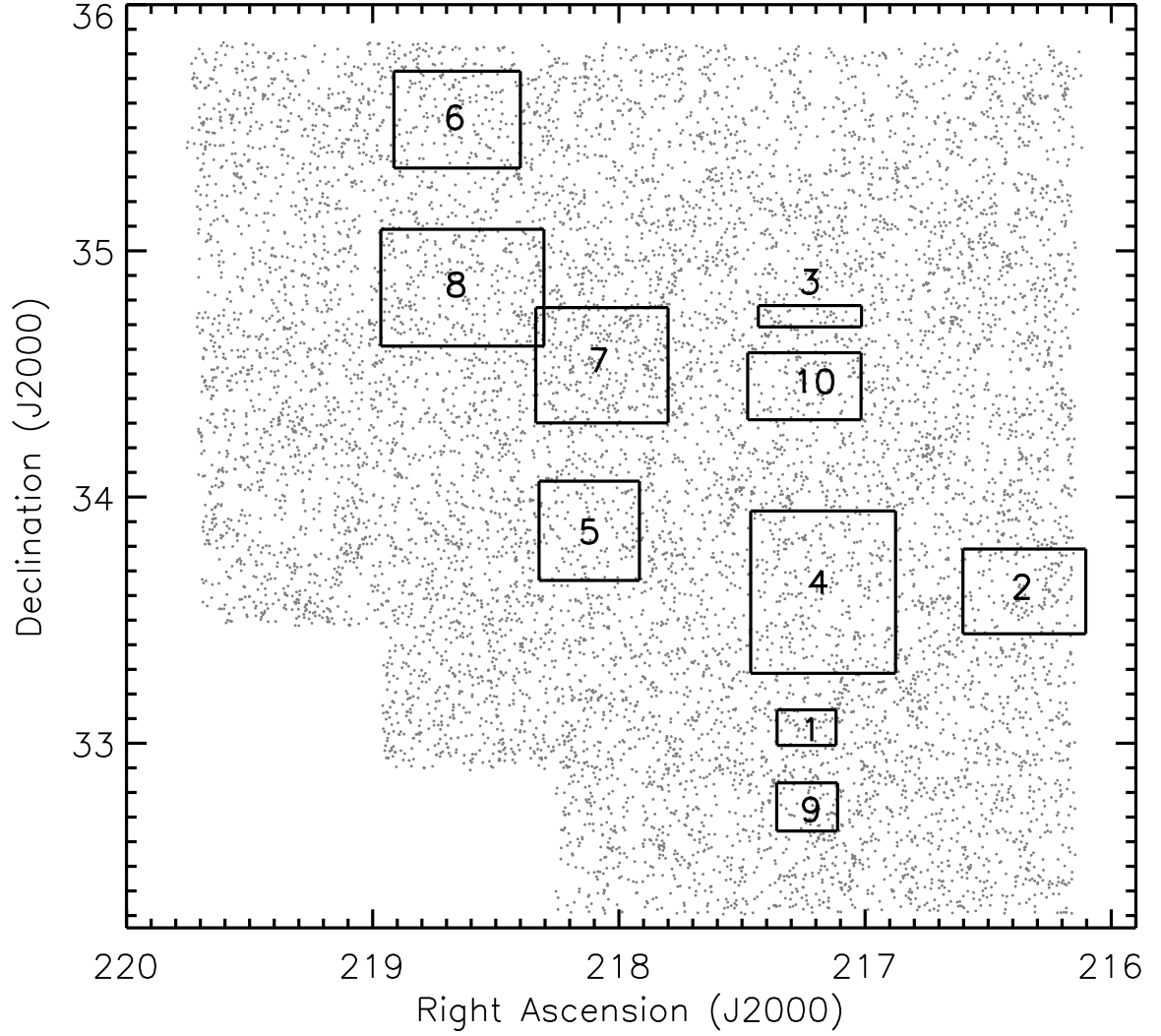
Figure 2.3 Map of the NDWFS survey area with the coverage of the coadded zBoötes fields overlayed. As in Figure 2.1, the grey points show the distribution of 25% of the $I < 21.5$ extended sources from the NDWFS catalogs. The number marking each of the coadded subfields denotes the field number assigned to that subfield. The coadded imaging covers 1.24 square degrees of the 7.62 square degree zBoötes region.

and the NDWFS reference frame. After removing any net offset between the ND-WFS catalogs and our zBoötes catalogs (which are discussed in more detail in §2.4.3), the two object lists were matched with a 1″ match tolerance and the name and coordinates of the closest match NDWFS detection were recorded in the final zBoötes catalog.

2.4.2 Photometric Accuracy

The final residuals between zBoötes and SDSS photometric measurements for well detected stars whose photometry is not affected by non-linearity in the 90Prime CCDS are centered around zero with a 1σ dispersion of 0.035 mag. The average quoted photometric error for the SDSS stars is 0.03 mag and thus the majority of the final calibration error in the zBoötes catalog can be attributed to photometric scatter in the SDSS photometry. The remainder of the scatter in the photometric calibration is likely due to errors in the large-scale flatfield corrections to each frame and imperfect subtraction of the strong fringing the 90Prime CCDs.

Since 1.25 square degrees were observed more than once in the zBoötes imaging, we can quantitatively estimate the error in our photometric measurements, both from calibration errors and reduction imperfections. The distribution of fluxes for the ~ 7200 stars with $17 < z < 20$ observed two or more times within zBoötes itself has zero mean and a 1σ dispersion of 0.03 mag, in good agreement with the scatter in photometric calibration estimated above.

2.4.3 Astrometric Precision

As the zBoötes astrometry was calibrated to the SDSS reference system, the agreement between SDSS and zBoötes astrometry is quite good. Figure 2.4 shows the differences between SDSS, zBoötes , and NDWFS astrometry. The dispersion between the zBoötes and SDSS coordinates is ~ 50 milliarcsec (mas) per coordinate

while the agreement with NDWFS is poorer with a dispersion of nearly 130 mas per coordinate. SDSS astrometry has a 45 mas dispersion per coordinate (Pier et al., 2003), so the zBoötes astrometric error is dominated by astrometric errors in the SDSS catalogs. Also, notice that the NDWFS and zBoötes astrometric have systematic offsets in both directions, likely due to the different astrometric reference systems used by NDWFS and SDSS imaging. Robust comparisons between NDWFS and zBoötes (or SDSS) thus require the removal of these offsets to properly match objects in each catalog. Table 2.1 lists the average shifts between the astrometry of each zBoötes field and the NDWFS catalog.

2.4.4 Survey Depth

The depth of the zBoötes images varies between each field and as a function of position in each field itself due to the variable number of exposures taken for each field and variable conditions during the observations. In order to quantify the depth of our catalogs near each detected object, we added fake point sources with the same point spread function as measured from nearby unsaturated stars in the zBoötes images. For each field, we perform ten simulations with each simulation consisting of 3000 fake stars added to the coadded frame of each field. We then record the average 50% completeness in a 10 arcminute diameter region around each object detected in our catalogs. Figure 2.5 illustrates the variations in the survey depth within a single zBoötes field. As illustrated in the figure, the variations in survey depth can be as large as 0.5 mags across the field.

Figure 2.6 shows the fraction of the zBoötes coverage area as a function of the 50% completeness depth and as a function of the 3σ detection limits of the catalogs. The final zBoötes catalog is 50% complete to 22.4 mag over 90% of the survey area and 50% of the survey area is complete to 22.7 mag. Thus, the zBoötes catalogs reach more than 2 mag fainter than SDSS over the entire survey

Table 2.1.   Astrometric Offsets Between zBoötes and NDWFS

Field Name	$\Delta\alpha$	$\Delta\delta$	Field Name	$\Delta\alpha$	$\Delta\delta$
	$''$	$''$		$''$	$''$
b1-1	-0.37	-0.31	b6-2	-0.25	-0.17
b1-2	-0.30	-0.37	b6-3	-0.31	-0.12
b1-3	-0.22	-0.18	b6-4	-0.24	-0.09
b1-4	-0.29	-0.15	b7-1	-0.22	-0.12
b2-1	-0.30	-0.05	b7-2	-0.26	-0.10
b2-2	-0.22	-0.04	b7-3	-0.28	-0.11
b2-3	-0.24	-0.08	b7-4	-0.30	-0.13
b2-4	-0.21	-0.09	b8-1	-0.35	-0.10
b3-1	-0.20	-0.13	b8-2	-0.37	-0.17
b3-2	-0.23	-0.10	b8-3	-0.26	-0.04
b3-3	-0.25	-0.15	b8-4	-0.33	-0.12
b3-4	-0.27	-0.13	mos-01	-0.17	-0.10
b4-1	-0.03	-0.05	mos-02	-0.25	-0.22
b4-2	-0.01	0.01	mos-03	-0.21	-0.10
b4-3	-0.11	-0.10	mos-04	-0.20	-0.17
b4-4	-0.11	-0.11	mos-05	-0.33	-0.11
b5-1	-0.17	0.02	mos-06	-0.21	0.07
b5-2	-0.30	-0.12	mos-07	-0.30	-0.12
b5-3	-0.20	0.08	mos-08	-0.32	-0.00
b5-4	-0.28	-0.18	mos-09	-0.13	0.04
b6-1	-0.32	-0.13	mos-10	-0.21	-0.07
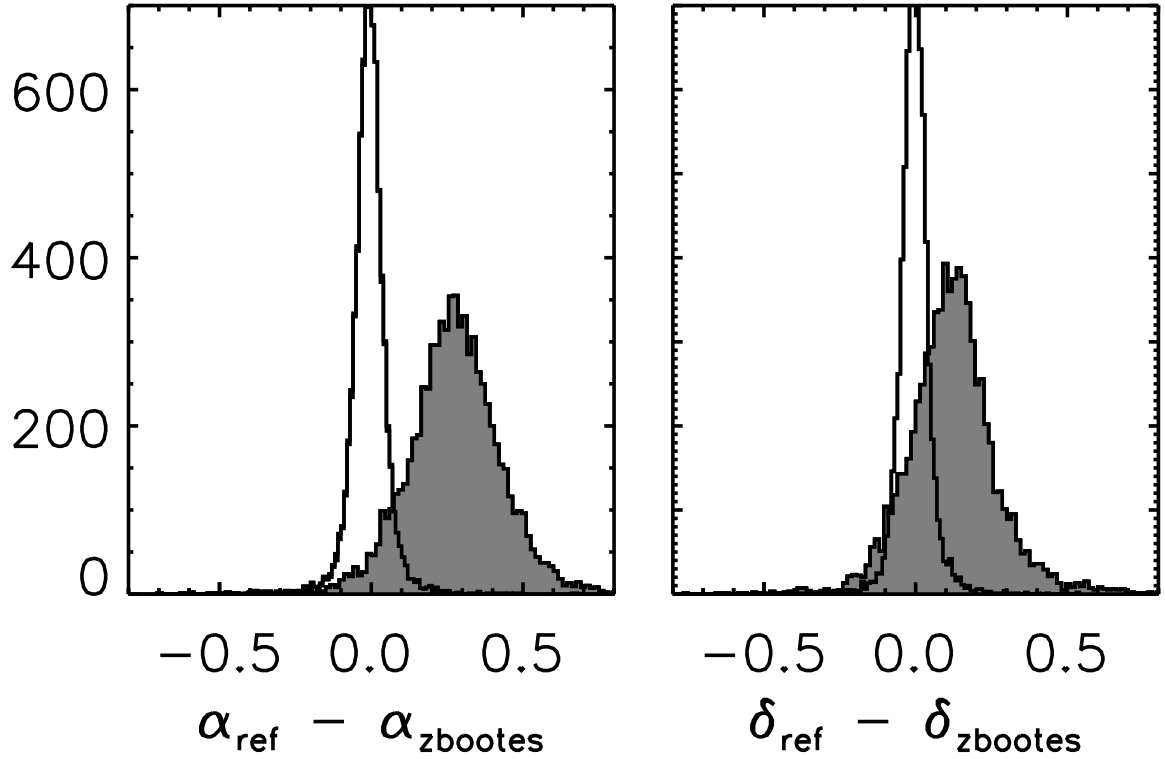
Figure 2.4 Histogram of astrometric offsets (in arcseconds) between sources reported by zBoötes and SDSS (unfilled) and zBoötes and NDWFS (filled). Only well-detected stars are used in this plot, so photon noise is not the dominant source of uncertainty in the astrometry. In general, SDSS and zBoötes agree quite well (50 mas rms). There are offsets between the zBoötes and NDWFS for each of the subfields, resulting in a overall mean offset and larger dispersion seen in the comparison between the zBoötes and NDWFS coordinates.

region. The mosaiced images of the overlapping zBoötes fields reach fainter limits than the single frames. Of the 1.24 square degrees covered in the overlapping fields, 50% of the area is complete to 23.3 mag and 90% is complete to 23.1 mag. Table 2.2 lists the average 50% completeness limit of each of the zBoötes subfields. The zBoötes data are thus sensitive to L^* galaxies to $z \sim 1$ and should provide extra constraint on photometric redshifts measurements for galaxies at $0 < z < 1$.

2.5 Data Products

2.5.1 Images

- Images and weight maps: [`fieldname.fits, fieldname-weight.fits`] We release the final coadded images and the associated weight map for each. The images are in ADU counts per pixel and the magnitude zeropoint of the photometry of each image is stored in the `MAGZERO` header keyword. The weight maps are normalized such that each pixel reflects the number of exposures that contributed to the image. All of these images have world-coordinate system information in the headers. Note that the orientation of these images corresponds to the orientation of the 90Prime images on the sky (north is to the right and east is upward) and not the standard image orientation.

  Regions of the sky that were observed in multiple zBoötes fields were coadded as described in §2.3. The resulting images are flux calibrated and have units of nano-maggies per pixel. A nanomaggie is a flux-density unit equal to 10^{-9} of a magnitude zero source. Since we calibrated the zBoötes photometry to SDSS, and SDSS is nearly an AB system, 1 nanomaggie corresponds to $3.631\,\mu$Jy or 3.631×10^{-29} erg s^{-1} cm^{-2} Hz^{-1}. As above, the weight maps associated with each of the mosaic images reports the total number of 300s

Table 2.2.   Average Completeness Limits (50%) of zBoötes Fields

Field Name	Depth mag	Field Name	Depth mag
b1-1	22.35	b6-2	22.93
b1-2	22.50	b6-3	22.95
b1-3	22.54	b6-4	22.88
b1-4	22.52	b7-1	22.81
b2-1	22.59	b7-2	22.91
b2-2	22.68	b7-3	22.95
b2-3	22.79	b7-4	22.80
b2-4	22.72	b8-1	22.63
b3-1	22.56	b8-2	22.68
b3-2	22.69	b8-3	22.73
b3-3	22.67	b8-4	22.69
b3-4	22.63	mos-01	22.87
b4-1	22.58	mos-02	23.13
b4-2	22.50	mos-03	23.05
b4-3	22.76	mos-04	23.25
b4-4	22.63	mos-05	23.17
b5-1	22.39	mos-06	23.35
b5-2	22.48	mos-07	23.33
b5-3	22.46	mos-08	23.38
b5-4	22.41	mos-09	22.84
b6-1	22.85	mos-10	23.33

Note. — Depth is estimated by the 50% completeness limit of the catalogs.
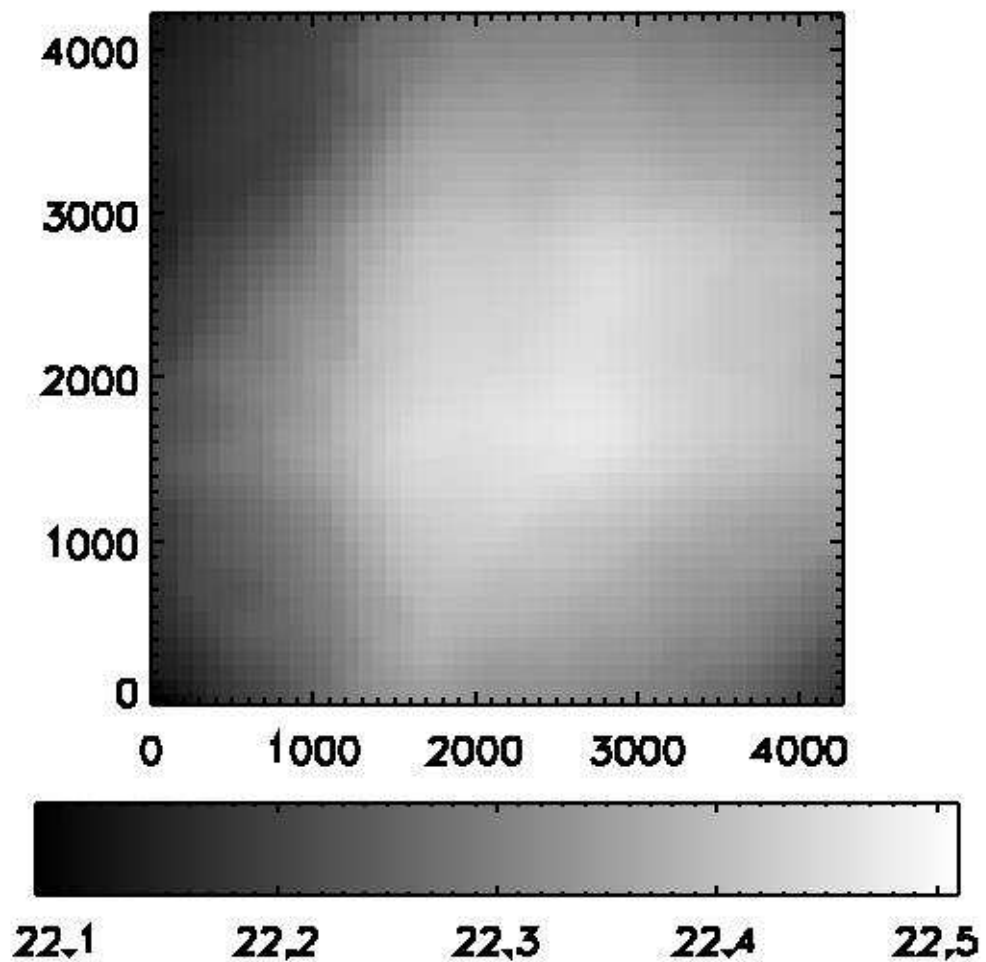
Figure 2.5 Map of the 50% completeness limit of the b4-1 field in pixel coordinates. The depth of the catalogs are a strong function of position in the final mosaiced image. This is primarily due to the decreased number of exposures that were coadded near the edge of the mosaiced field. The completeness can vary as much as 0.5 mag from the center of the field to the edge.
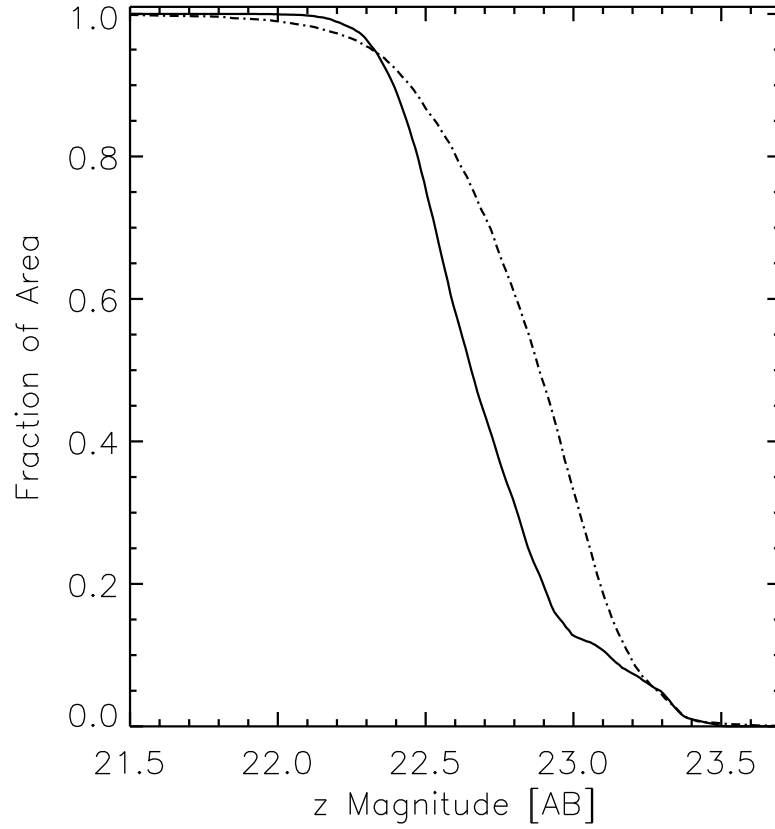
Figure 2.6 Fraction of the zBoötes survey area as function of the 50% complete-
ness limit and 3σ detection limit of the zBoötes catalogs. The solid line shows the
fraction of the zBoötes 7.6 square degree area as a function of the 50% complete-
ness while the dot-dashed line shows the fraction of the survey area versus the
3σ detection limit in a 3 arcsecond aperture. The zBoötes catalog is complete to
22.4 mag over 90% of the survey area and 50% of the area is complete to 22.7 mag
or deeper. The knee in the distribution of 50% completeness limit near $z = 23.0$
is due the deeper limits present in the coadded zBoötes fields as discussed in the
text.

exposures that contributed to each pixel.

- Photometric Catalogs: [`fieldname-cat.fits`] We also release binary FITS files of the SExtractor catalog for each zBoötes field as well as overlapping regions. In each file, we report the measured properties of each of the objects detected in the zBoötes imaging. A majority of the parameters listed in the catalogs are standard SExtractor outputs, so we will not repeat the definitions. The aperture fluxes and magnitudes reported in the zBoötes catalogs are measured at 12 diameters. The diameters run from 1″ to 10″ in steps of 1″; the final two apertures have diameters of 15″ and 20″. The non-standard parameters included in each of the catalogs are :

  - `NOBS` – [integer] Mean number of observations (300s exposures) that contribute to the pixels each object falls on. Objects with less than `NOBS` $\lesssim 5$ should be used with caution.

  - `ERR_[1,3,5,7]` – [float] Photometric error in a [1,3,5,7] arcsecond diameter aperture determined from the dispersion in the local sky background within a 6 arcminute radius around each object.

  - `COMP50` – [float] The 50% completeness limit determined by inserting $\sim 30,000$ fake point sources into the images and measuring the fraction recovered using the same analysis procedure as that used when constructing the catalogs. The local completeness is calculated within a 10 arcminute region around each object.

  - `DETECT_3SIG_3ARC` – [float] The local 3σ detection limit determined in a 3 arcsecond diameter aperture around each object based on measurements of the local variation in the sky background.

  - `PHOTFLAG` – [integer] For each object, this flag is set if any of the pixels

contributing to the object detection were in the non-linear or saturated regime on the 90Prime CCDs. Photometry for objects with this flag set should be used with caution.

- Final Merged Catalog : [zbootes-cat.fits] The final catalog represents the merged catalog for the zBoötes imaging. For objects included in multiple individual catalogs, the observation with the smallest photometric error is declared the primary observation and included in the final catalog. Objects in the final catalog were cross-matched to the NDWFS optical catalogs using a 1 arcsecond search radius. Before the cross-matching was performed, the locally determined astrometric offsets between the zBoötes and NDWFS astrometric systems (reported in Table 1) were removed. The following parameters are included in the final catalog which are not in the individual catalogs:

    - FIELDNAME – [string] Name of the zBoötes field in which the photometric quantities for each object were measured.

    - DUPLICATE – [integer] Flag which is set if a given object was detected in multiple catalogs. If an object was detected in multiple frames, then the observation with the lowest photometric error was declared to be the best and included in the final merged catalog; each object is listed in the final catalog only once.

    - NDWFS_NAME – [string] Name of the nearest NDWFS object to each zBoötes detection. The catalogs were compared with a 1 arcsecond search radius; if there were no NDWFS objects within the search radius of the zBoötes object, this entry is empty.

    - NDWFS_RA – [double] Right ascension of the nearest NDWFS object to

the zBoötes detection in decimal degrees.

– NDWFS_DEC – [double] Declination of the nearest NDWFS object to the zBoötes detection in decimal degrees.

2.6   Catalog availability

The zBoötes catalogs described in this paper are available for download online. [2]. Any use of these data should include references to this paper. If any of the cross-identifications to the NDWFS catalogs are used, the appropriate citations should be made to the papers describing those data.

---

[2]http://archive.noao.edu/nsa/zbootes.html

CHAPTER 3

THE DISCOVERY OF THREE NEW $z > 5$ QUASARS IN THE AGN AND GALAXY
EVOLUTION SURVEY

We present the discovery of three $z > 5$ quasars in the AGN and Galaxy Evolution Survey (AGES) spectroscopic observations of the NOAO Deep Wide-Field Survey (NDWFS) Boötes Field. These quasars were selected as part of a larger *Spitzer* mid-infrared quasar sample with no selection based on optical colors. The highest redshift object, NDWFS J142516.3+325409, $z = 5.85$, is the lowest-luminosity $z > 5.8$ quasar currently known. We compare mid-infrared techniques for identifying $z > 5$ quasars to more traditional optical techniques and show that mid-infrared colors allow for selection of high-redshift quasars even at redshifts where quasars lie near the optical stellar locus and at $z > 7$ where optical selection is impossible. Using the superb multi-wavelength coverage available in the NDWFS Boötes field, we construct the spectral energy distributions (SEDs) of high-redshift quasars from observed B_W-band to 24μm (rest-frame 600 Å - 3.7μm). We show that the three high-redshift quasars have quite similar SEDs, and the rest-frame composite SED of low-redshift quasars from the literature shows little evolution compared to our high-redshift objects. We compare the number of $z > 5$ quasars we have discovered to the expected number from published quasar luminosity functions. While analyses of the quasar luminosity function are tenuous based on only three objects, we find that a relatively steep luminosity function with $\Psi \propto L^{-3.2}$ provides the best agreement with the number of high-redshift quasars discovered in our survey.

3.1   Introduction

Understanding the evolution of quasars through cosmic time allows us to study the history of accretion of matter onto supermassive black holes in the nuclei of galaxies. In addition, quasars at high redshift provide the lighthouses needed to probe the conditions under which galaxies initially formed near the epoch of reionization. Samples of quasars at high redshift, however, are still quite small and most high-redshift quasar surveys are only sensitive to the most luminous examples of these objects. We know very little about the population of low-luminosity quasars at these early times.

Surveys for low-redshift quasars have been quite successful and have led to quasar samples suitable for detailed statistical studies of the evolution of the quasar luminosity function to moderate redshifts (Schmidt & Green, 1983; Boyle et al., 2000; Fan et al., 2001b,a; Wolf et al., 2003b; Croom et al., 2004; Richards et al., 2005; Barger et al., 2005; Brown et al., 2006; Jiang et al., 2006; Richards et al., 2006). Censuses of high-redshift objects have opened the Universe even back to the era of reionization, but the number of such objects is still small. Deep spectroscopic follow-up of i-dropout objects in the Sloan Digital Sky Survey (SDSS) (York et al., 2000) have found 19 quasars at $z > 5.7$ (Fan et al., 2001c, 2003, 2004, 2005). Zheng et al. (2000) and Chiu et al. (2005) found 7 quasars at $z \gtrsim 5$ based on SDSS photometry which complement the 17 quasars at $5 < z < 5.4$ found in SDSS DR3 (Abazajian et al., 2005) spectroscopy selected as outliers from the stellar locus (Schneider et al., 2005). SDSS imaging, however, is relatively shallow ($z_{AB} < 20.5\,\mathrm{mag}$) and thus the quasars found using SDSS photometry probe only the luminous tail of the quasar luminosity function. Furthermore, the use of optical photometry for selecting high-redshift quasars is biased against heavily reddened objects, as the observed optical flux from objects at $z > 3$ probes the

rest-frame ultraviolet emission which is most heavily affected by dust and the strong absorption from neutral hydrogen in the intergalactic medium.

The difficulty of conducting deep, wide-area multi-color surveys has meant that only a handful of lower-luminosity sources have been reported. Stern et al. (2000) found a faint quasar ($M_B = -22.7$) at $z = 5.50$ in a small area imaged approximately 4 magnitudes deeper than SDSS. A quasar at $z = 5.189$ ($M_B \sim -23.2$) was selected based on 1 Ms of X-ray imaging in the *Chandra* Deep Field North (Barger et al., 2002). Djorgovski et al. (2003) imaged the field around the quasar SDSS J0338+0021 at $z = 5.02$ and discovered a second quasar at $z = 4.96$, a magnitude fainter than the SDSS detection limit ($M_B = -25.2$). Mahabal et al. (2005) imaged the field around the $z = 6.42$ quasar SDSS J1148+5251 and report the discovery of a faint ($M_B = -24.3$) $z = 5.70$ quasar.

Unfortunately, the number of successful searches for faint high-redshift quasars is comparable to the number of surveys with negative results. Barger et al. (2003) found no additional high-redshift quasars in the full 2 Ms imaging of the *Chandra* Deep Field North that were not detected in 1 Ms of observation and Cristiani et al. (2004) found no high-redshift objects based on deep X-ray imaging of the *Hubble* Deep Field North and *Chandra* Deep Field South. Willott et al. (2005) imaged 3.8 deg^2 of sky in i and z and Sharp et al. (2004) imaged 1.8 deg^2 in VIZ reaching 3 and 2 magnitudes deeper than SDSS, respectively, but neither survey detected any new low-luminosity, high-redshift quasars.

In this paper, we present photometry and spectroscopy of three new high-redshift ($z > 5$) quasars using the multi-wavelength photometry available in the NOAO Deep Wide-Field Survey (NDWFS; Jannuzi & Dey, 1999, Dey et al., *in prep.*) Boötes field and spectroscopic observations from the AGN and Galaxy Evolution Survey (AGES; Kochanek et al., *in prep*), which provides redshifts for

several highly-complete samples of quasars to $I_{\rm AB} = 22$ mag, nearly 2 mag fainter than SDSS selects high-redshift objects. With our three newly discovered $z > 5$ quasars, we compare the number density inferred from this survey to predictions based on quasar luminosity functions in the literature.

This paper is organized as follows: in §3.2, we summarize all the multi-wavelength photometry used in the paper and in §3.3 we discuss our spectroscopic observations. We compare the mid-infrared selection of quasars utilized in this work to optical criteria used in the past in §3.4. Finally, we place our survey in context with past studies of the quasar luminosity function and consider future high-redshift quasar searches in §3.5. All optical photometry presented here are corrected for foreground galactic reddening using the dust maps of Schlegel et al. (1998). We use AB magnitudes for all bands (Oke , 1974), although the photometric catalogs from the NDWFS and FLAMINGOS Extragalactic Survey (FLAMEX; Elston et al., 2005) present Vega magnitudes[1]. Flux measurements from *Spitzer* are converted to AB magnitudes using $m_{AB} = 23.9 - 2.5 \log(f_\nu / 1\mu{\rm Jy})$. Also, when quoting optical, near-infrared, and IRAC photometry, we use SExtractor (Bertin & Arnouts, 1996) MAG_AUTO magnitudes (which are comparable to Kron total magnitudes; Kron, 1980) due to their small systematic errors and uncertainties at faint fluxes. When calculating luminosities, we use a $(\Omega_m, \Omega_\Lambda) = (0.3, 0.7)$ flat cosmology and $H_0 = 70$ km s^{-1} Mpc^{-1}.

3.2 Multi-wavelength Photometry

3.2.1 NOAO Deep Wide-Field Survey

We utilize the deep optical ($B_W RI$) and near-infrared (K_s) imaging of the 9.3 deg^2 Boötes field provided by the third data release from the NOAO Deep Wide-Field

---

[1] $B_{W,AB} = B_{W,\rm Vega}$, $R_{AB} = R_{\rm Vega} + 0.20$, $I_{AB} = I_{\rm Vega} + 0.45$, $J_{AB} = J_{\rm Vega} + 0.91$, and $K_{s,AB} = Ks_{,\rm Vega} + 1.85$

Survey (Jannuzi & Dey, 1999). A full description of the observing strategy and data reduction will be presented elsewhere (Jannuzi et al., *in prep*; Dey et al., *in prep*) and the data can be obtained publicly from the NOAO Science Archive[2]. The NDWFS catalogs reach $B_{W,\text{AB}} \sim 26.5$, $R_{\text{AB}} \sim 25.5$, $I_{\text{AB}} \sim 25.3$, and $K_{s,\text{AB}} \sim 23.2$ at 50% completeness.

3.2.2 zBoötes

We imaged 8.5 deg^2 of the sky, covering 7.7 deg^2 of the NDWFS Boötes field, between 29 January 2005 and 31 March 2005 in the z'-band with 90Prime (Williams et al., 2004) on the Bok 2.3m telescope on Kitt Peak. The 90Prime imager offers a 1 deg^2 field of view when mounted at prime focus on the Bok telescope. Exposure times range from 1–2.5 hours throughout the field with typical seeing of $1''\!.8$. Images were flatfielded using observations of the twilight sky. For each night of observations, we stack all of the dithered z'-band images to produce a high signal-to-noise ratio image of the fringing pattern in the detector. This master fringe image is then scaled and subtracted from each object frame to remove the strong fringing pattern.

We calibrate the astrometry and photometry of these z'-band images using public imaging from the Sloan Digital Sky Survey DR4 (York et al., 2000; Adelman-McCarthy et al., 2006a). Cross comparisons between zBoötes and SDSS show a $0''\!.1$ rms dispersion in the astrometry and a 5% scatter in the photometry for bright stars ($z < 19$). This 5% scatter is likely a combination of photometric calibration errors in SDSS (expected to be on the order to 2%; Ivezić et al., 2004) and imperfect fringe removal and flat fielding in the zBoötes imaging. Furthermore, we find that objects observed in overlapping zBoötes fields have an rms scatter of

---

[2]http://www.archive.noao.edu/ndwfs
http://www.noao.edu/noao/noaodeep

5% in the final photometry. The astrometry between the NDWFS and zBoötes are slightly offset ($\Delta\alpha \approx 0\rlap{.}''4, \Delta\delta \approx 0\rlap{.}''1$). When matching objects in each zBoötes field to the NDWFS catalogs, we remove the local mean astrometric offsets in both right ascension and declination from zBoötes positions, resulting in astrometry that agrees to $0\rlap{.}''2$ rms. As the exposure times and observing conditions were variable throughout the survey field, the limiting depth of the catalog depends on location in the survey area. The typical 3σ depth is 22.5 mag for point sources in a 5 arcsecond diameter aperture. Full details of the data reduction and a full release of the z'-band imaging catalogs are be presented in Chapter 2.

3.2.3   FLAMEX

The FLAMINGOS Extragalactic Survey (FLAMEX) (Elston et al., 2005) provided some of the J and K_s photometry used in this work. The Florida Multi-object Imaging Near-IR Grism Observational Spectrometer (FLAMINGOS) on the Kitt Peak 2.1m telescope was used to image 4.7 deg^2 of the NDWFS Boötes field to a limiting depth of $K_{s,AB} \approx 21.1$ detecting approximately 150,000 sources (5σ). The FLAMEX catalogs are publicly available[3].

3.2.4   IRAC Shallow Survey

The IRAC Shallow Survey (Eisenhardt et al., 2004) observed 8.5 deg^2 of the sky in the NDWFS Boötes region at 3.6, 4.5, 5.8, and 8.0 μm with the IRAC instrument (Fazio et al., 2004) on *Spitzer*. This survey found $\approx$ 270,000, 200,000, 27,000, and 26,000 sources brighter than 5σ limits of 12.3, 15.4, 76, and 76 μJy (corresponding to limits of 21.2, 20.9, 19.2, and 19.2 AB mag) in each of the four IRAC bands (Eisenhardt et al., 2004; Stern et al., 2005).

---

[3]http://flamingos.astro.ufl.edu/extragalactic/overview.html

3.2.5   MIPS Imaging

The NDWFS Boötes field was also observed at 24, 70, and 160 μm with the Multi-band Imaging Photometer for *Spitzer* (Rieke et al., 2004) as part of the *Spitzer* IRS team's Guaranteed Time Observing programs (Houck et al., 2005); only the 24 μm photometry is considered here. The 24 μm imaging covers 8.22 deg^2 of the NDWFS Boötes field and reaches a 80% completeness limit of 0.3 mJy (Brown et al., 2006).

3.3   Spectroscopic Observations

3.3.1   AGN and Galaxy Evolution Survey

The AGN and Galaxy Evolution Survey (AGES, Kochanek et al., *in prep*) has obtained complete spectroscopic samples of galaxies and quasars using several multi-wavelength selection techniques in the NDWFS Boötes field. Spectra of $\approx 20,000$ objects were taken with Hectospec, a 300 fiber robotic spectrograph on the MMT 6.5m telescope (Fabricant et al., 1998, 2005; Roll et al., 1998). Data reduction was completed using HSRED, a modified version of the SDSS spectroscopic pipeline. Dome flat spectra were used to correct for the high-frequency flat-field variations and fringing in the CCD, and, when available, twilight sky spectra provided a low-frequency flat-field correction for each fiber. Each Hectospec configuration has approximately 30 fibers dedicated to measuring the sky spectrum which is subtracted from each object spectrum. Simultaneous observations of F-type stars in each configuration are cross correlated against a grid of Kurucz models (Kurucz, 1993) to derive a sensitivity function for each observation, thus linking the observed counts to absolute flux units. The final reduced spectra cover the 3700Å to 9200Å spectral range at resolution $R \approx 1000$.

AGES quasar target selection occurred in two stages. In the first phase of the

project, AGES obtained redshifts of nearly all point sources with $R_{AB} < 21.7$ mag that were either X-ray sources with 4 or more counts in the the XBoötes survey (Murray et al., 2005) or were MIPS 24μm sources brighter than 1mJy with non-stellar 24μm to J-band colors. This led to a sample of roughly 900 spectroscopically identified AGNs as well as redshifts of nearly 9000 galaxies selected using a variety of other techniques. By combining the AGES galaxy and AGN redshift samples, Stern et al. (2005) confirmed the ease with whichJiang2006 quasars could be recognized using mid-infrared colors. In the second phase of AGES spectroscopy, we extended the optical flux limit to $I_{AB} = 22$ and added IRAC color selection to our methods of identifying quasars. In detail, mid-infrared selected objects considered here were required to have $[3.6]-[4.5] > -0.1$ and either $[3.6] < 20.8$ or a detection at 5.8 or 8.0μm and be classified as point-sources in the NDWFS imaging. In AGES, targets were classified as point sources if their SExtractor CLASS_STAR parameter was larger than 0.8 for at least one of the B_W, R, or I-bands. The AGES mid-infrared selection cut used for point sources dispenses with the $[5.8] - [8.0]$ color restriction given in Stern et al. (2005) which is intended to minimize the contribution of $z > 1$ galaxies which are not common to our optical flux limits. While we only consider the sample of point-sources selected in the mid-infrared from AGES in this paper, it is worth noting that when selecting AGN from extended source in AGES, the vertical selection cuts from Stern et al. (2005) are imposed to reduce contamination of star-forming galaxies on the AGN sample. The shift from an R-band to an I-band spectroscopic limit led to a significant increase in the number of $z > 4$ quasars in the AGES database, including three $z > 5$ objects. The second phase of AGES target selection also included a 24μm -selected quasar sample. These objects were required to be point sources, have $f_{24\mu m} > 0.3$mJy, and have I-band 3″0 diameter aperture magni-

tudes, $I_{3,AB}$, such that $I_{3,AB} > 18.45 - 2.5\log(f_{24\mu m}/\mathrm{mJy})$. This I-band selection criterion rejects normal stars from the sample but retains AGNs. Two of the three $z > 5$ quasars selected based upon their IRAC colors were also selected based upon their 24μm photometry.

3.3.2 Auxiliary Observations

In order to augment the AGES discovery spectra, spectroscopic observations of two of the high-redshift objects discovered in this work were completed with the Multi-Aperture Red Spectrograph (MARS) on the 4-m telescope on Kitt Peak and the DEIMOS spectrograph (Faber et al., 2003) on the Keck-II telescope under poor observing conditions. These data were reduced using standard techniques. Also, to achieve higher quality data, two of the objects described in this paper were observed multiple times within AGES itself. Coaddition of all of the available spectra for each object was performed to improve the final signal-to-noise ratio of the data.

3.4 Results

We have identified three new high-redshift ($z > 5$) quasars observed as part of the $I_{\mathrm{AB}} \leq 22$ AGES spectroscopic sample. Figures 3.1 and 3.2 show the I-band finding chart and spectra for each of the three high-redshift objects. Tables 3.1 and 3.2 list the observed photometry and redshifts of the three new high-redshift quasars and Table 3.3 shows the derived rest-frame B-band luminosity and the luminosity of each object at 1450 Å. In calculating the rest-frame luminosities, we assume a power-law SED of the form $f_\nu \propto \nu^{\alpha_\nu}$ where $\alpha_\nu = -0.5$. The spectra shown in Figure 3.2 are the coadded spectra from all the observations of each object: ND-WFS J142516.3+325409 was observed three times in AGES as well as with MARS and DEIMOS, NDWFS J142937.9+330416 was observed once in AGES and with
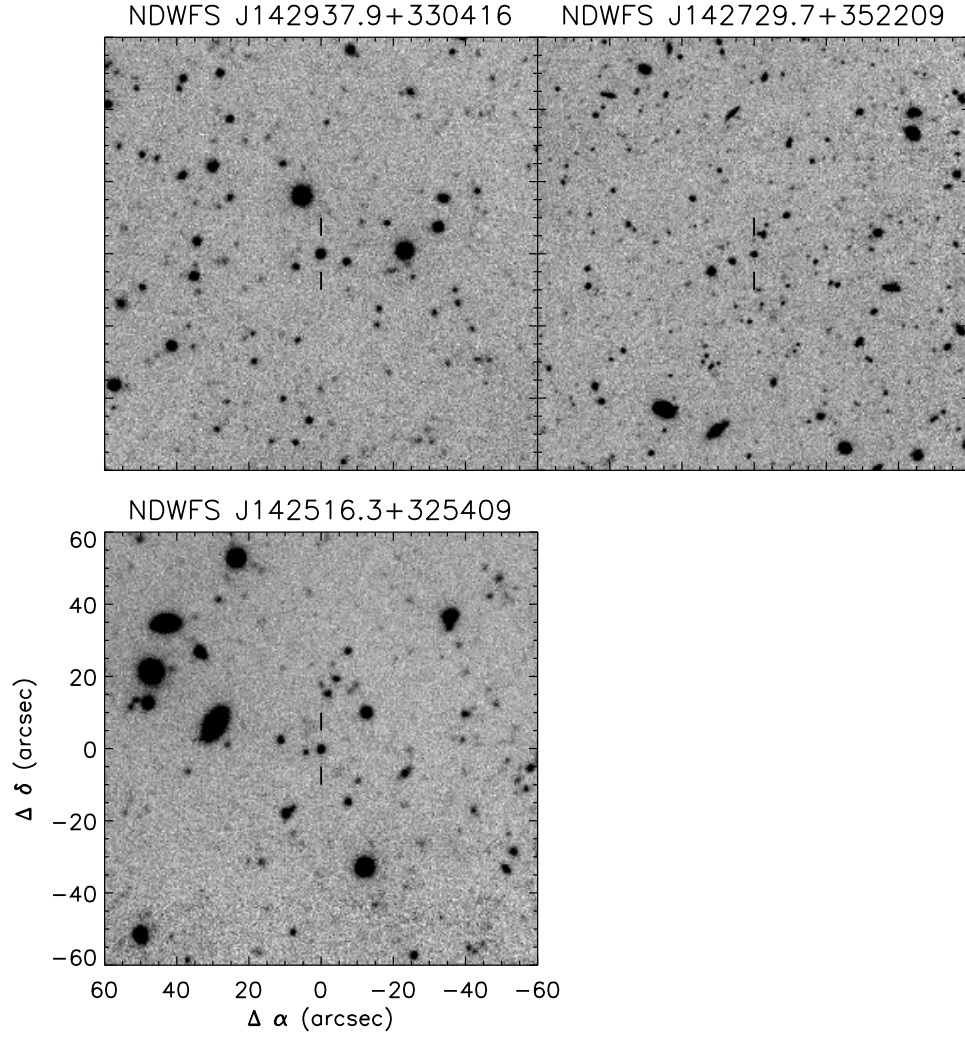
Figure 3.1 Finding charts for the three $z > 5$ quasars discovered in the AGES survey. The images are drawn from the NDWFS I-band imaging of the Boötes region and are each 2 arcminutes on a side. North is up and East is left. The location of the quasar is marked by vertical lines in each panel.

MARS, and NDWFS J142729.7+352209 was observed twice within AGES. Each of the discovered objects show the clear signature of a broad asymmetric Lyα emission line. As the signal-to-noise ratios of the final spectra are only modest, redshifts for each object were determined based upon the break in the Lyα line profile rather than on weak emission lines which are poorly detected. Quoted redshifts thus have errors of order $\Delta z \sim 0.02$.

The quasars included in this paper were not selected with standard dropout techniques which identify objects with very red optical colors indicative of a strong spectral break. These techniques have been successful in identifying quasars at redshifts above 5 (e.g. Fan et al., 2000, 2001c, 2003, 2004, 2005; Stern et al., 2000; Djorgovski et al., 2003; Mahabal et al., 2005), but have several weaknesses. At $z \gtrsim 5.5$, quasars cross the stellar locus in optical color-color space making optical selection problematic. The inclusion of near-infrared photometry can break this degeneracy to some extent, but obtaining this data can be time consuming.

The high-redshift quasars studied here were all selected on the basis of their mid-infrared colors using a scheme similar to that presented in Stern et al. (2005). In brief, quasars, with their roughly power-law spectra, have redder mid-infrared colors than $z < 1$ galaxies. The IRAC color-color space for AGES objects shown in Figure 3.3 illustrates the separation of the high-redshift objects discovered here from stars and low-redshift galaxies. We also indicate the criteria used for AGN selection given by Stern et al. (2005) (dashed line) and the AGES point-source mid-infrared selection criterion (dot-dashed line). Extended sources are targeted as AGN in AGES if they meet the full Stern et al. (2005) criteria. Low-redshift ($z < 0.5$) objects, which are predominately extended galaxies, are shown with x-marks while objects with $z > 1$ are marked with circles and are dominated by unresolved AGN. At $[5.8] - [8.0] \gtrsim 1$, the locus of low-redshift galaxies clearly

Table 3.1.   Optical and Near-Infrared Photometry

Object Name	Redshift	B_W	R	I	z'	J	K_s
NDWFS J142937.9+330416	5.39	> 27.1	22.84 ± 0.09	21.24 ± 0.05	21.02 ± 0.07	20.40 ± 0.12	20.81 ± 0.19
NDWFS J142729.7+352209	5.53	> 26.3	24.20 ± 0.21	21.85 ± 0.07	21.93 ± 0.11	$\cdots$	20.41 ± 0.19
NDWFS J142516.3+325409	5.85	> 25.8	23.99 ± 0.11	21.57 ± 0.06	20.68 ± 0.06	$\cdots$	$\cdots$

Note. — All magnitudes are on the AB system

Table 3.2.   *Spitzer* Photometry

Object Name	Redshift	$[3.6\,\mu m]$	$[4.5\,\mu m]$	$[5.8\,\mu m]$	$[8.0\,\mu m]$	$[24\,\mu m]$
NDWFS J142937.9+330416	5.39	20.81 ± 0.08	20.24 ± 0.09	> 19.2	19.65 ± 0.13	17.31 ± 0.15
NDWFS J142729.7+352209	5.53	20.27 ± 0.06	19.84 ± 0.07	> 19.2	19.88 ± 0.14	17.53 ± 0.18
NDWFS J142516.3+325409	5.85	20.36 ± 0.06	19.91 ± 0.07	> 19.2	20.74 ± 0.18	> 17.7

Note. — All magnitudes are on the AB system

Table 3.3.   Luminosities of Discovered Quasars

Object Name	Redshift	M_B	M_{1450}
NDWFS J142937.9+330416	5.39	-26.00	-25.52
NDWFS J142729.7+352209	5.53	-25.15	-24.67
NDWFS J142516.3+325409	5.85	-26.52	-26.03
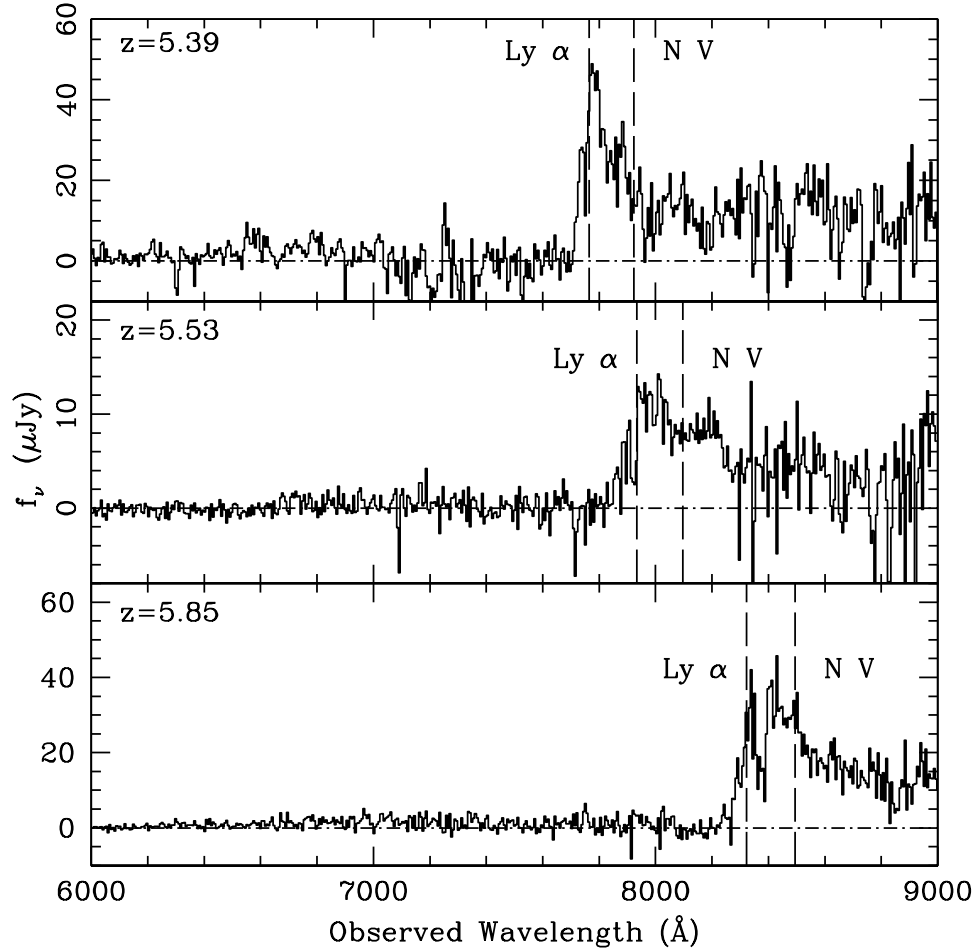
Figure 3.2 Final stacked spectra for each of the high-redshift quasars discovered by our work. These spectra represent the coadded spectra for the repeated observations with Hectospec as well as observations with MARS and DEIMOS. Two prominent quasar emission lines, Lyα and NV, are marked with vertical dashed lines and the measured redshift of each object is listed in the upper left corner of each panel. All three of the quasars show the strong Lyα emission line truncated by neutral hydrogen absorption blueward of the emission line center characteristic of high-redshift quasars.

crosses the AGES point-source mid-infrared selection criterion but remains outside the Stern et al. (2005) selection region, illustrating the need for the separate point-source and extended-source selection criteria used by AGES. The three high-redshift quasars studied here (diamonds with error-bars) are well-separated from low-redshift galaxies throughout this color-color space.

One obvious question arises due to our mid-infrared selection of high-redshift quasars: does the population of mid-infrared selected quasars differ from quasars selected using more traditional optical techniques? The spectra in Figure 3.2, though of only modest signal-to-noise ratio, show no obvious differences from objects presented in the literature and would suggest no strong difference between high-redshift quasars selected based upon their optical or mid-infrared colors. Figure 3.4 shows the $I - z$ versus $R - I$ color-color space for point sources observed in AGES as well as the color track of high-redshift quasars predicted using the Vanden Berk et al. (2001) SDSS quasar composite modified by the addition of absorption blueward of Lyα using the prescription of Songaila & Cowie (2002). The three quasars discovered here reside in the region traditionally used to select quasars with $z > 4.5$ (e.g. Richards et al., 2002) further indicating that the quasars selected in this study are similar to those selected in the past. Both NDWFS J142516.3+325409 and NDWFS J142937.9+330416 lie quite close to the stellar locus in these colors, however, illustrating one of the main difficulties of traditional optical color selection techniques.

Figure 3.5 shows the spectral energy distribution from the observed B_W-band to 24 μm (approximately rest-frame 600 Å - 3.7 μm) for each of the high-redshift quasars identified in this work. Again, all three of these objects were selected based upon their mid-infrared colors; the two lowest-redshift quasars were also selected based on their 24μm fluxes. For comparison, we have also plotted the
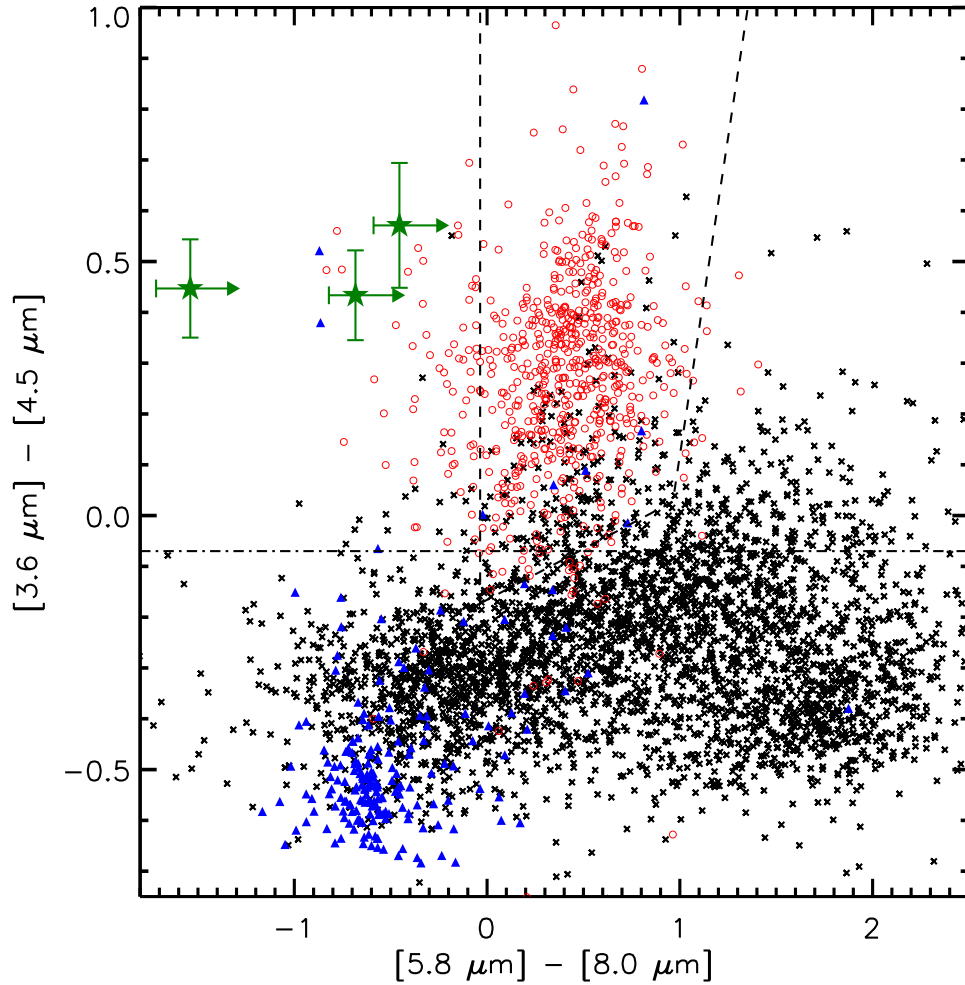
Figure 3.3 The mid-infrared colors of objects detected in the AGES spectroscopic survey. The symbol type and color denote the redshift of each object. The x-marks show the $0.01 < z < 0.5$ objects in AGES. This sample is primarily composed of galaxies, although some low-redshift AGNs are also included. The empty circles (red) show objects with $z > 1.0$ and are dominated by AGNs. The triangles (blue) mark the location of stars in this color-color space. The filled diamonds (green) show the location of the $z > 5$ quasars in this color-color space. The dashed line shows the region used by Stern et al. (2005) to select AGNs. The vertical lines are used to protect against the presence of $z > 1$ galaxies in the AGN sample, but as galaxies at $z > 1$ are fainter than our optical flux limits, these cuts are not used in the AGES mid-infrared point-source quasar selection shown by the dot-dashed line. When selecting AGN from extended objects in AGES, the vertical lines are used to reduce contamination from low-redshift star-form ing galaxies.

average quasar SEDs from two studies in the literature; the top line shows the Elvis, Risaliti, & Zamorani (2002) radio-quiet quasar composite while the lower line shows the average SED of *Spitzer*-observed SDSS quasars from Richards et al. (2006b). The broad photometric properties of the high-redshift quasars are quite similar to each other as well as to the low-redshift composite spectra. The main difference between the low- and high-redshift objects is the lack of absorption due to neutral hydrogen at the highest frequencies in the composite spectra. The highest redshift object, NDWFS J142516.3+325409, shows a strong break between observed 4.5μm and 8.0μm, but this is likely due to poor signal-to-noise ratio in the 8.0μm photometry as this object is near the flux limit of the 8.0μm imaging. The rest-frame UV to optical color of NDWFS J142729.7+352209 is redder than the other two quasars studied here as well as both of the comparison composites, possibly indicating enhanced dust extinction in this object. Compared to a sample of 58 quasars at $3 < z < 3.5$ from AGES, the rest-frame UV to optical color of NDWFS J142729.7+352209 is not unique; it falls well within the distribution of colors of lower-redshift objects.

Figure 3.6 shows the optical versus mid-infrared color-color space for AGES point sources. In this color space, all three of the discovered $z > 5$ quasars are separated from the locus of low-redshift galaxies, Galactic stars, and $z < 5$ quasars. We show one possible selection method for high-redshift quasars by the dot-dashed line in Figure 3.6. Within this region, the AGES source catalog contains 19 point sources with $I < 22$ mag; 14 of these were spectroscopically observed. Of these 14 targets, 9 objects are stars, 2 are lower-redshift ($z = 2.11, 3.57$) quasars, and 3 have $z > 5$. Assuming the 4 objects without redshifts are not located at high redshift, this selection results in a minimum efficiency of $\sim 17\%$, though with only 3 quasars, this efficiency measurement is rather uncertain. The

large contamination from stars arises due to increasing photometric errors in the $[3.6] - [4.5]$ colors as the stars approach the IRAC flux limit and thus much of the contamination could be mitigated with a deeper IRAC imaging survey.

3.5   Discussion

The quasars reported here add three new low-luminosity, high-redshift quasars to the slowly growing catalog of these objects. All three of these objects are fainter than quasars at similar redshifts found in the SDSS, and NDWFS J142516.3+325409 is the lowest luminosity $z > 5.8$ quasar currently known. The number of these objects should grow quickly as the next generation of deep wide-area surveys are completed, opening the door to understanding the nature of low-luminosity quasars near the epoch of reionization.

As the number of low-luminosity $z > 5$ quasars is still small, the details of the luminosity function of these objects is poorly constrained. Extrapolating the Fan et al. (2001b) quasar luminosity function (QLF), determined using $3.5 < z < 5$ quasars with $-27.5 < M_{1450} < -25.5$, to higher redshifts and lower luminosities, we would expect a density of 0.28 deg^{-2} to the optical flux limit of the AGES spectroscopy or 2.2 quasars with $z > 5$ in the AGES survey area for a complete, optically limited, survey.

In order to estimate the effect of the IRAC flux limits on the expected number of quasars in our survey, we create a sample of 58 quasars at $3 < z < 3.5$ from the full AGES catalog with existing FLAMEX photometry. These objects include quasars selected using the full suite of AGES selection techniques including X-ray, radio, or 24μm fluxes or their optical or mid-infrared colors and thus likely exhibit a broad range of broad-band photometric properties. We augment this sample with 17 quasars in the same redshift range listed in the SDSS Third

Quasar catalog (Schneider et al., 2005) which were also detected in 2MASS. For each object in this sample, we convert the observed $R - K_s$ (or $r - K_s$ for SDSS quasars) to a rest-frame ultraviolet-to-optical spectral slope, α_{UO}, by assuming the measured broad-band colors are the result of a pure power-law SED with $f_\nu \propto \nu^\alpha$. Next, we create a mock catalog of high-redshift quasars using the Fan et al. (2001b) QLF to assign each mock object a redshift and UV luminosity at 1450 Å. The observed distribution of UV-to-optical spectral slopes defines the distribution of k-corrections that are applied to the mock catalog to convert the rest-frame luminosity at 1450Å to the observed flux at 3.6μm for each object. We then use the observed distribution of mid-infrared spectral indices, $\alpha_{MIR} = 0.73 \pm 0.84$, measured by Stern et al. (2005), to assign each mock quasar a flux at 4.5, 5.8, and 8.0 μm. Finally, we apply the AGES mid-infrared flux limits and selection criteria to measure the fraction of high-redshift objects which are missed by the AGES mid-infrared selection criteria. We find that approximately 35% of the mock quasars that pass the $I < 22$ mag optical flux limits are missed when the IRAC flux limits are included. It may be a concern that the addition of the SDSS quasars, which, unlike the AGES sample, were all selected based on their optical colors, may bias this estimate; we have verified that omitting these objects from the calculation does not affect the final completeness more than a few percent. It should be noted that the above calculation assumes quasars at $z > 5$ have the same broad-band photometric properties as $z \sim 3$ objects; this assumption can only be tested after a large sample of high-redshift quasars with multi-wavelength photometry is collected. In the $I < 22$ AGES sample of 2153 mid-infrared selected objects, 83% of the targets obtained valid redshifts. Combining this 83% spectroscopic completeness with the effects of the mid-infrared flux limits, we estimate that our overall completeness is 54% and thus we would expect to find only 1.2 quasars at $z > 5$

for a QLF with a slope of $\Psi \propto L^{-2.6}$. To then find three quasars is somewhat unlikely, since the Poisson probability of finding 3 or more objects when 1.2 are expected is only 12%.

Based on a sample of 12 quasars at $z > 5.8$, Fan et al. (2004) found that the high-redshift QLF was best fit by a steeper QLF ($\Psi \propto L^{-3.2}$) than that measured by Fan et al. (2001b). If we instead use the best fit bright-end slope and normalization from Fan et al. (2004) but keep the redshift evolution of the quasar number density determined by Fan et al. (2001b), we would expect to find 6.2 quasars at $z > 5$ in a complete optically-limited survey of the AGES area. This value drops to 3.5 when the effects of our mid-infrared flux limits and spectroscopic incompleteness are added. This value agrees quite well with the 3 objects found in our survey, but, at this point, this agreement is only suggestive due to the small number of quasars in our sample and the small sample size and luminosity range used by Fan et al. (2004) to determine this QLF slope. Richards et al. (2006) found the QLF slope to evolve from $\beta = -3.1$ (where $\Psi \propto L^{\beta}$) at $z < 2.4$ to progressively flatter slopes at higher redshift such that at $z \sim 5$, one would predict $\beta \gtrsim -2.4$. If the QLF at $5 < z < 6$ is, indeed, as steep at L^{-3}, the trend measured by Richards et al. (2006) must break down beyond $z \sim 4.5$, but a larger sample of low-luminosity objects is required to place any robust constraints on the evolution of the QLF to $z \sim 5$.

We have shown that mid-infrared selection of quasars can be useful in the search for high-redshift objects to $z \sim 6$, thus avoiding some of the key problems inherent in optically based high-redshift quasar searches. At $z \gtrsim 7$, optical selection of quasars is impossible as the Lyα emission from objects at these redshifts is shifted out of the z'-band. In the near-infrared, the existing large area surveys (primarily 2MASS) are too shallow to detect even the brightest high-

redshift quasars found by the SDSS. In the near future, the UKIDSS survey will image 4000 deg^2 of the sky to 3 mag deeper than 2MASS and should find about 10 quasars with $5.8 < z < 7.2$ (Warren & Hewett, 2002). While near-infrared spectroscopy is ultimately the only means by which one can ensure any candidate is located at high redshift, the use of mid-infrared colors in the selection of these objects may provide a valuable tool in separating stars from quasars at the highest redshifts. Figure 3.7 illustrates the expected $[3.6] - [4.5]$ color of quasars to $z \sim 8$ based upon the locally determined SDSS quasar composite spectrum (Vanden Berk et al., 2001). We also show the colors predicted from a power-law ($\alpha_\nu = -0.5$) continuum with Balmer emission lines having the same strength and width of those measured on the SDSS composite spectrum.

As the strong emission from the Hα emission line redshifts into the 4.5μm band, the colors of quasars redden quickly near $z \sim 5$. Correspondingly, the sudden drop in color at $z \sim 6.5$ occurs as the strong Hα emission line redshifts out of the 4.5μm band; by $z \sim 7$, the colors of high-redshift quasars redden as Hβ redshifts from the 3.6μm band into the 4.5μm IRAC bandpass. The overall trend toward bluer colors exhibited by the SDSS composite across this redshift range occurs as the IRAC passbands probe the transition between a spectral slope of $\alpha_\nu = -0.5$ measured blueward of 5000Å and of $\alpha_\nu = -2.5$ redward of this wavelength in the SDSS composite spectrum. This transition likely occurs due to contamination of the AGN light by the host-galaxy in the low-redshift AGNs used to construct the composite spectrum. This contamination makes the colors predicted using the Vanden Berk et al. (2001) composite generally redder than those expected using the simple model consisting only of a power-law continuum and Balmer emission lines. For both tracks, the mid-infrared colors of very high-redshift quasars remain redder than stars ($[3.6] - [4.5] \sim -0.5$) and low-redshift galaxies through-

out the redshift range shown. As the large number of deep, wide-area, *Spitzer* fields with corresponding deep optical and near-infrared photometry become available, the ability to build large samples of high-redshift quasars, including low-luminosity objects, will allow us, for the first time, to probe the statistics of low-luminosity quasars at high redshift.
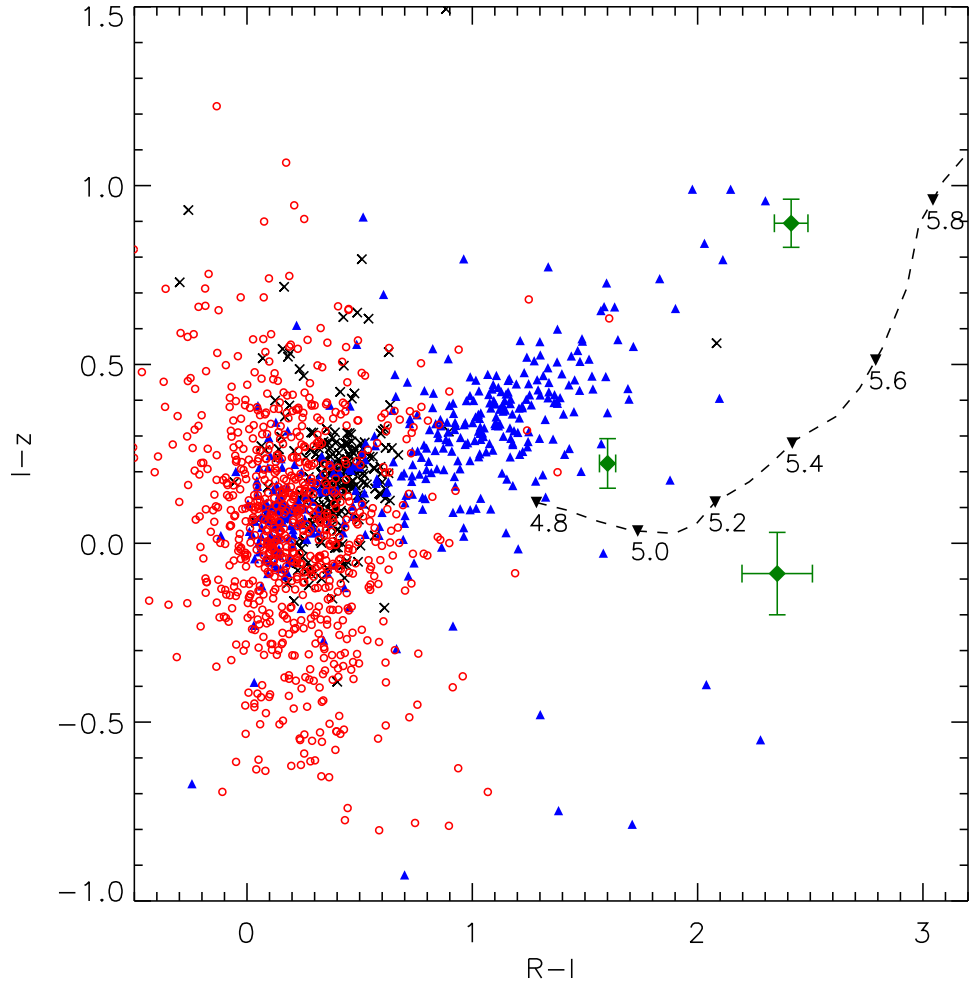
Figure 3.4 Optical color-color space for AGES point sources. The symbols are defined as in Figure 3.3. Additionally, the dashed line shows the expected colors of quasars at $z > 4.8$ predicted using the SDSS quasar composite (Vanden Berk et al., 2001) modified by the addition of absorption blueward of Lyα using the prescription of Songaila & Cowie (2002). The three high-redshift quasars discovered in this work occupy the same location in color-color space used in the past to optically-select $z > 4.5$ quasars. At the same time, two of the three objects lie very near the stellar locus in this color-color space, illustrating one of the main difficulties in using optical colors alone to select high-redshift quasars.
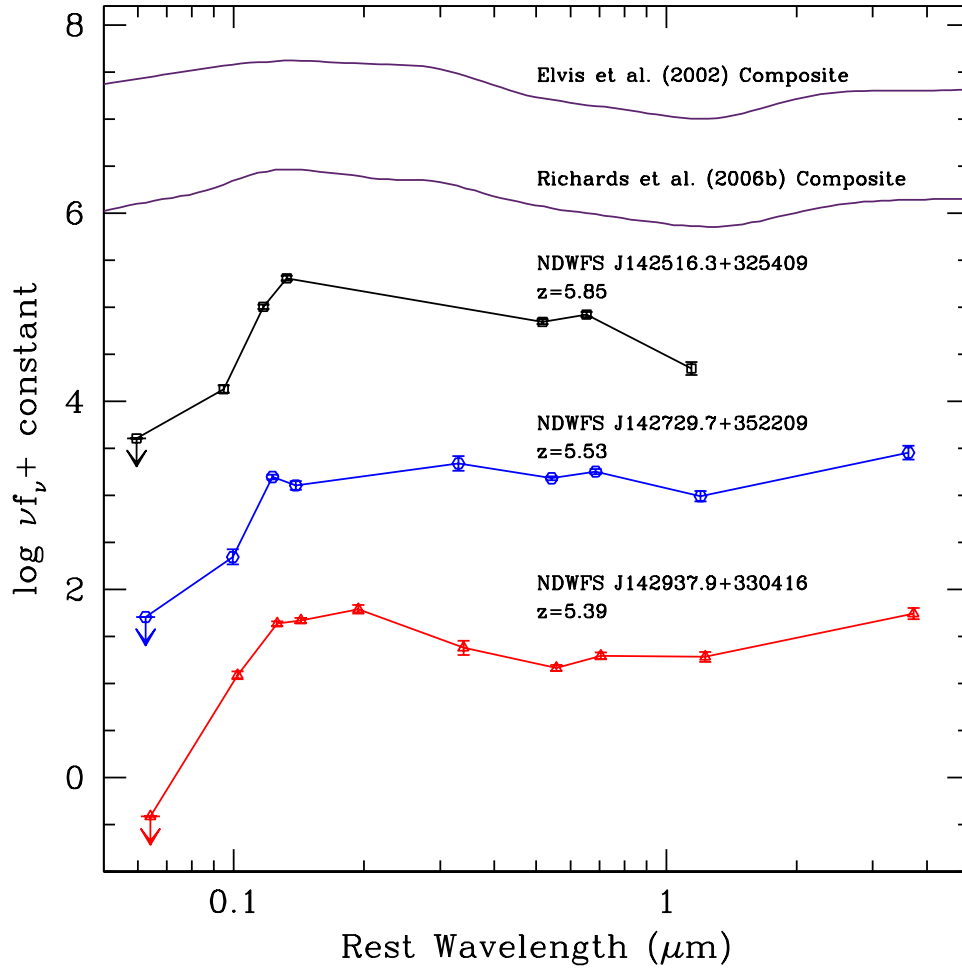
Figure 3.5 Broad-band spectral energy distributions of the three high-redshift quasars presented here. The quasars are ordered by redshift with the highest-redshift object on the top. The top two lines show two composite quasar spectral energy distributions for comparison; the to p line shows the radio-quiet quasar SED from Elvis, Risaliti, & Zamorani (2002) while the bottom comparison shows the composite of *Spitzer* observed SDSS quasars from Richards et al. (2006b). The high-redshift SEDs are very similar to each other and the low-redshift composites are broadly similar to the SEDs of the high-redshift objects although th e SEDs of the three $z > 5$ objects presented here have much stronger breaks in the blue from abso rption from neutral hydrogen. The large ratio between the 4.5μm and 8.0μm flux of the highest-redshift object, NDWFS J142516.3+325409 is likely a result of low signal-to-noise ratio photometry as this object is close to the detection limit in that band .
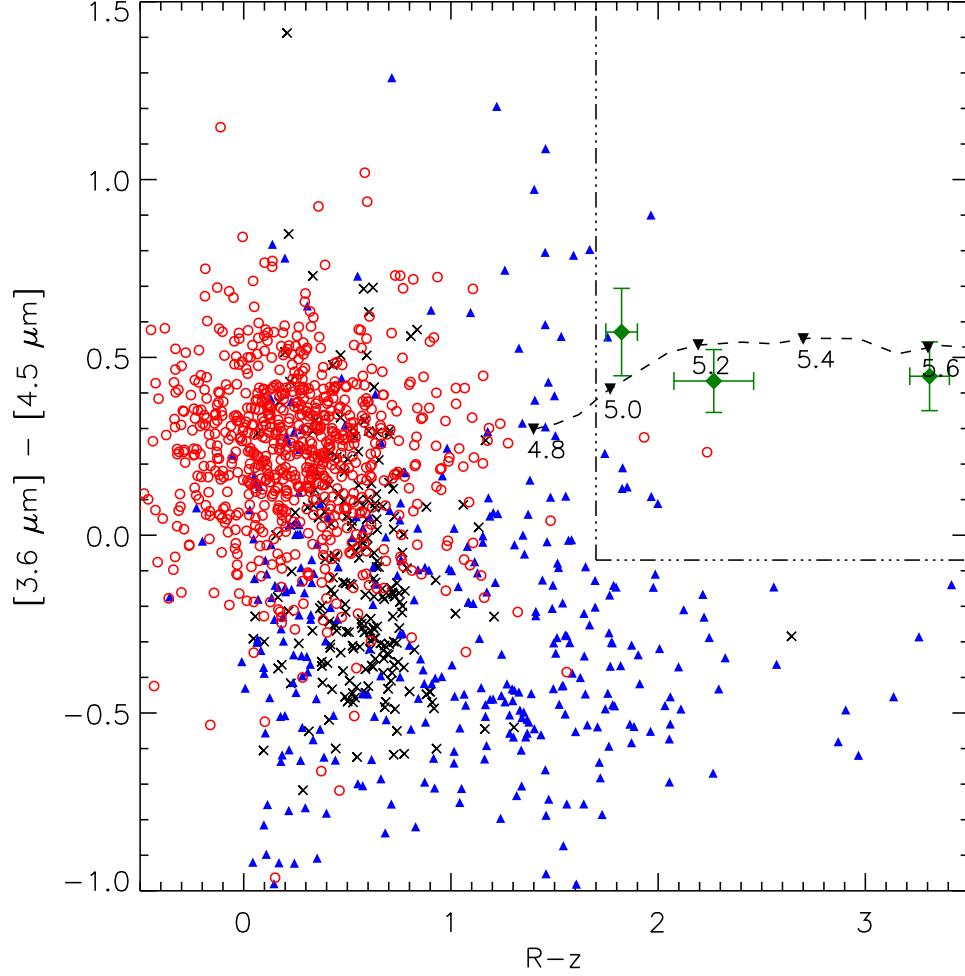
Figure 3.6 Optical versus mid-infrared color-color space of AGES spectroscopically observed point sources. The symbols and colors are as in Figure 3.4. The dashed line illustrates the color track of quasars above $z \sim 4.8$. The $z > 5$ quasars are well-separated from the loci of low-redshift galaxies, stars, and lower-redshift quasars. The region defined by the dot-dashed line illustrates one way to select high-redshift quasars by combining optical and mid-infrared photometry. The minimum efficiency for selecting $z > 5$ quasars in this region is 17% with the l argest portion of the contamination arising due to stars with low signal-to-noise IRAC photometry which scatter to redder $[3.6] - [4.5]$ colors. Deeper mid-infrared imaging would increase the color measurement accuracy, significantly reducin g the stellar contamination and increasing the quasar selection efficiency.
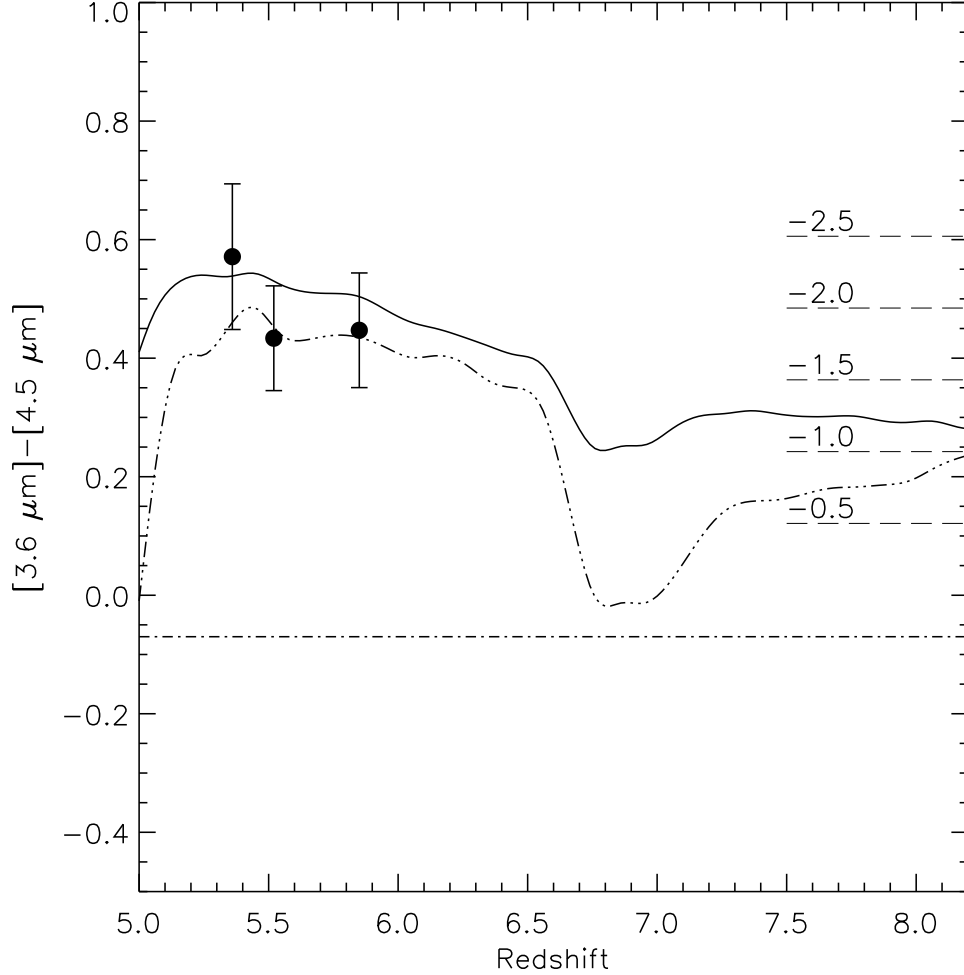
Figure 3.7 [3.6] − [4.5] color of quasars to very high redshift based on the SDSS quasar composite (solid line, Vanden Berk et al., 2001) or a $\alpha = -0.5$ power-law combine d with the Balmer emission lines observed in the SDSS composite spectrum (dash-dot-dot-dot line) . The color cut imposed by the mid-infrared selection of quasars in AGES is shown by the dot-dashed line. Longward of rest-frame 5000Å, the SDSS composite is dominated by low-luminosity AGNs and is l ikely heavily contaminated by host-galaxy light, making the colors slightly redder. For comparison, the location of the three $z > 5$ quasars discovered here are marked and the dotted lines on the right mark the colors of pure power-law spectra with different values of α_ν. The rapid rise at $z = 5$ occurs as the Hα emission line passes from the 3.6μm band in to the 4.5μm bandpass. Similarly, as the Hα emission line redshifts out of the 4.5μm bandpass near $z \sim 6.5$, the colors drop quickly; the colors become redde r again near $z \sim 7$ as the Hβ enters the 4.5μm bandpass. Even at very high redshifts, the colors of quasars predicted by both tracks fall within the region used to mid-infrared select quasars in our survey.

CHAPTER 4

BROADBAND OPTICAL PROPERITES OF MASSIVE GALAXIES: THE DISPERSION

AROUND THE FAINT GALAXY COLOR-MAGNITUDE RELATION OUT TO $z \sim 0.4$.

Using a sample of nearly 20,000 massive early-type galaxies selected from the Sloan Digital Sky Survey, we study the color-magnitude relation for the most luminous ($L \gtrsim 2.2L^*$) field galaxies in the redshift range $0.1 < z < 0.4$ in several colors. The intrinsic dispersion in galaxy colors is quite small in all colors studied, but the 40 milli-mag scatter in the bluest colors is a factor of two larger than the 20 milli-mag measured in the reddest bands. While each of three simple models constructed for the star formation history in these systems can satisfy the constraints placed by our measurements, none of them produce color distributions matching those observed. Subdividing by environment, we find the dispersion for galaxies in clusters to be about 11% smaller than that of more isolated systems. Finally, having resolved the red sequence, we study the color dependence of the composite spectra. Bluer galaxies on the red sequence are found to have more young stars than red galaxies; the extent of this spectral difference is marginally better described by passive evolution of an old stellar population than by a model consisting of a recent trace injection of young stars.

4.1 Introduction

The presence of a tight correlation between the rest-frame optical color and luminosity of early-type galaxies, the so-called color-magnitude relation (CMR) or red-sequence, is well established in the literature (Visvanathan & Sandage, 1977; Larson, Tinsley, & Caldwell, 1980; Lugger, 1984; Zepf, Whitmore, & Levison, 1991; Terlevich et al., 1999; Blanton et al., 2003a; Hogg et al., 2004; Baldry et al., 2004;

López-Cruz, Barkhouse, & Yee, 2004). The relation implies that the properties of the stellar populations in early-type galaxies are strongly dependent on the total stellar mass of the system. The tight correlation observed along this relationship (e.g. Faber, 1973; Visvanathan & Sandage, 1977; Bower et al., 1992) requires a strong coherence between both the age and metallicity of stellar populations present in early-type galaxies. Measurements of the slope, zero-point, and dispersion around the color-magnitude relation probe the star formation histories of early-type galaxies and can provide physical insight into galaxy formation and evolution.

One possible explanation for the slope of the CMR is that massive, and thus more luminous, galaxies retain more metals than less massive ones. The deeper potential wells of massive galaxies may allow fewer metals to be expelled in supernova driven winds (Larson, 1974; Arimoto & Yoshii, 1987; Matteucci & Tornambe, 1987; Bressan, Chiosi, & Tantalo, 1996). Alternatively, Kauffmann & Charlot (1998) have shown that the color-magnitude relation can be reproduced in hierarchical merging models if the epoch of mergers occurs at very early times. Since the age of a stellar population is degenerate with its metallicity on the CMR, however, metallicity may not be the sole parameter behind the relationship (Faber, 1972, 1973; O'Connell, 1980; Rose, 1985; Worthey et al., 1995). While both age and metallicity effects may create the CMR, studies of the evolution of the relationship toward high-redshift argue that the relation is driven primarily by metallicity and cannot be generated by age effects alone (Kodama & Arimoto, 1997).

The color-magnitude relation of galaxies in clusters has been studied extensively. Using high precision U and V photometry, Bower et al. (1992) determined the dispersion around the CMR for early-type galaxies in Coma and Virgo to be

small, $\delta(U - V) \lesssim 40$ milli-mag (mmag). This small scatter implies early-type galaxies in clusters must be uniformly old with formation epochs earlier than a $z \sim 2$. Hogg et al. (2004) found $\delta(U - v) \sim 100$ mmag for clusters at $z \approx 0.54$; this scatter, combined with the early age of the Universe at the observed epoch, indicates that elliptical galaxies must have stopped forming stars in these clusters by a $z \sim 2.7$ for a simple approximation to the color evolution of stellar populations. The cluster MS 1054-03 at a $z = 0.83$ has a 29 mmag dispersion in the $U - B$ color (van Dokkum et al., 2000), while van Dokkum et al. (2001) and Blakeslee et al. (2003) showed that the scatter in single clusters is only 40 and 30 mmag at $z \sim 1.3$. These small dispersions, seemingly independent of redshift, indicate that the coordination of star formation between galaxies in clusters is quite strong. Using a sample of 158 clusters with $0.06 < z < 0.34$ drawn from the Early Data Release of the Sloan Digital Sky Survey (SDSS), Andreon (2003) found that the CMR between clusters is very homogeneous. Locally, the CMR is universal between clusters of various masses as well (McIntosh et al., 2005).

While the mean color of red sequence galaxies in over-dense regions is only slightly redder than for similar galaxies in less dense regions and the slope of the CMR is independent of environment (Hogg et al., 2004), several studies show that the scatter around the CMR is dependent on galaxy environment. A re-analysis of the data presented in Sandage & Visvanathan (1978) indicates the dispersion around the CMR in clusters is 2-σ smaller than that for galaxies in groups or in the field (Larson, Tinsley, & Caldwell, 1980). The scatter in galaxy colors in the core of the cluster CL 1358+62 at $z = 0.33$ have $\delta(B - V) \sim 22$ mmag while early-types at large radii ($R > 1.4h^{-1}$ Mpc) have nearly double that value, indicating that the dispersion of galaxy colors in the field may be larger than that measured in clusters (van Dokkum et al., 1998). Early-type galaxies in the Hubble Deep Field

have a scatter of 120 ± 60 mmag in rest-frame $U - V$ with an average redshift of 0.9 (Kodama, Bower, & Bell, 1999). While this measurement is rather uncertain, it is larger than that measured in clusters, further indicating that field galaxies may have less coordinated star formation than galaxies in clusters.

A majority of the work on the CMR has focused on early-type galaxies in clustered environments with luminosities near L^*. This is natural, as statistically significant samples are more easily selected in these over-dense regions and L^* galaxies are more common than their more massive analogs. In this work, we extend the analysis of the color-magnitude relation to a sample of nearly 20,000 very luminous red field galaxies from the Sloan Digital Sky Survey. These galaxies are not selected to reside in clustered environments and are chosen to be quite luminous with $L \gtrsim 2.2\,L^*$. We create two galaxy samples from the SDSS spectroscopic data. At low-redshifts ($0.1 < z < 0.2$) we use galaxies from the entire survey region while at higher redshifts ($0.3 < z < 0.4$), where the galaxies are apparently fainter, we select galaxies from a 270 deg^2 region which has been imaged an average of 10 times and up to 29 times. The repeated imaging of our moderate-redshift galaxies makes comparisons between the galaxy samples possible with similar fidelity. Our sample allows us to probe a new area in parameter space — luminous galaxies in the field — and compare our results to those found for galaxies in clustered environments.

The paper is organized as follows: §4.2 describes the Sloan Digital Sky Survey and the selection for the galaxies used here. In §4.3, we present our measurements of the slope and scatter of the color-magnitude relations. We discuss simple star formation history models in §4.4 and use our measurements of the scatter around the CMR as a constraint on the evolutionary history of massive early-type galaxies in the field. In §4.5, we discuss the role environment plays on the CMR of

galaxies. We construct the composite spectra of galaxies across the red sequence in §4.6 before closing in §4.7. Throughout this work, we use $H_0 = 100\,h$ km s^{-1} Mpc^{-1} and (Ω_{m}, Ω_{Λ}) = (0.3,0.7) to calculate luminosities and distances. When calculating ages of stellar populations, we set $h = 0.7$. All magnitudes used here have been corrected for reddening using the Schlegel et al. (1998) dust maps.

4.2   Data

4.2.1   The Sloan Digital Sky Survey

The Sloan Digital Sky Survey (York et al., 2000; Stoughton et al., 2002b; Abazajian et al., 2003, 2004a, 2005) is imaging π steradians of the northern sky through 5 passbands (Fukugita et al., 1996). The imaging is conducted with a CCD mosaic in drift-scanning mode (Gunn et al., 1998) on a dedicated 2.5m telescope located at Apache Point Observatory in New Mexico. After the images are processed (Lupton et al., 2001; Stoughton et al., 2002; Pier et al., 2003) and calibrated (Hogg, et al. , 2001; Smith et al., 2002; Ivezić et al., 2004), targets are selected for spectroscopy with two double-spectrographs mounted on the same telescope using an automated spectroscopic fiber assignment algorithm (Blanton et al., 2003b).

Two spectroscopic galaxy samples are created using the SDSS imaging. The MAIN galaxy sample (Strauss et al., 2002) is a complete, flux limited, sample of galaxies with $r < 17.77$. This cut is nearly five magnitudes brighter than the SDSS detection limit of $r \sim 22.5$, and thus the photometric quantities for these galaxies are measured with signal-to-noise of a few hundred. The Luminous Red Galaxy (LRG) sample (Eisenstein et al., 2001) selects luminous early-type galaxies out to $z \sim 0.5$ with $r < 19.5$ using several color-magnitude cuts in g, r, and i. The combination of these two samples allows us to study the broadband colors of luminous field galaxies at moderate-redshifts with statistically significant samples.

While the focal point for the SDSS is a contiguous survey of the Northern Galactic Cap, the SDSS also conducts a deep imaging survey, the SDSS Southern Survey, by repeatedly imaging an area on the celestial equator in the Southern Galactic Cap. Currently, objects in the 270 deg^2 region have been imaged an average of 10 times and up to 29 times, resulting in improved photometric precision for faint galaxies. Objects detected in each observational epoch were matched using a tolerance of 0.5 arcseconds to create the final coadded catalog used here. The photometric measurements from each epoch were combined by converting the reported asinh magnitudes (Lupton et al., 1999) into flux and then calculating the mean value. Errors on each parameter are simply the standard deviation of the flux measurements. The Southern Survey is an ideal region to compare the properties of faint galaxies at moderate-redshift with brighter low-redshift analogs drawn from the entire SDSS survey area with photometry of similar fidelity.

4.2.2   Galaxy Photometric Properties

Several methods are used to measure galaxy fluxes in SDSS. Below, we briefly describe the two flux measurements used throughout this paper. The Petrosian ratio, $\mathcal{R}_P$, the ratio of the local surface brightness at radius θ to the average surface brightness at that radius, is given by

$$\mathcal{R}_P(\theta) \equiv \frac{\int_{\alpha_{\mathrm{lo}}\theta}^{\alpha_{\mathrm{hi}}\theta} d\theta' 2\pi\theta' I(\theta') \big/ \left[\pi(\alpha_{\mathrm{hi}}^2 - \alpha_{\mathrm{lo}}^2)\theta^2\right]}{\int_0^\theta dr' 2\pi\theta' I(\theta') \big/ \left[\pi\theta^2\right]}, \tag{4.1}$$

where $I(\theta)$ is the azimuthally averaged surface brightness profile of a galaxy and α_{lo} and α_{hi} are chosen to be 0.85 and 1.25 for SDSS. The Petrosian flux is given by the flux within a circular aperture of $2\theta_P$, where θ_P is the radius at which $\mathcal{R}_P$ falls below 0.2. In SDSS, θ_P is determined in the r band then subsequently used in each of the other bands. This flux measurement contains a constant fraction

of a galaxy's light, independent of its size or distance, in the absence of seeing. More details of SDSS Petrosian magnitudes can be found in Blanton et al. (2001), and Strauss et al. (2002).

For each galaxy imaged by SDSS, two seeing-convolved models, a pure de Vaucouleurs (1948) profile and a pure exponential profile, are fit to the galaxy image. The best-fit model in the r band is used to measure the flux of a galaxy in each of the other bands. These model magnitudes are unbiased in the absence of color gradients and provide higher signal-to-noise ratio colors than Petrosian colors. A more complete description of model magnitudes is given in Stoughton et al. (2002b). Throughout this paper, we use Petrosian magnitudes when calculating galaxy luminosities while model magnitudes are used to determine galaxy colors.

4.2.3   The k-Correction

We calculate photometric k-corrections using the method of Blanton et al. (2003c) (`kcorrect v3_2`). This program constructs a linear combination of carefully chosen spectral templates in order to best match the observed photometry at the measured redshift of the galaxy. The rest-frame colors of these best-fit spectra are used to derive corrections to the observed galaxy colors. With this method, it becomes simple to transform between bandpasses and, if necessary, photometric systems given a detailed understanding of the filter characteristics. After calculating k-corrections with `kcorrect`, we remove any mean k-corrected color versus redshift trends with a low order polynomial to account for the passive evolution of stellar populations between observed epochs. This evolutionary correction is normalized to a redshift of 0.3, near the median of the LRG redshift distribution. The color evolution correction is small (less than 2% for all bands in both samples) and does not affect any of the results presented here. We further

assume a galaxy dims by one magnitude per $\Delta z = 1$ change in redshift in the g-band due to the passive evolution of its stellar populations. Again, this correction is normalized to $z = 0.3$. In the remainder of this paper, all of the color and luminosity measurements refer to quantities which have been adjusted for the k-correction and evolution.

Throughout this paper, we work in the $^{0.16}g$, $^{0.16}r$, $^{0.16}i$, $^{0.16}z$ and $^{0.37}g$, $^{0.37}r$, $^{0.37}i$, $^{0.37}z$ systems for the low- and moderate-redshift galaxy samples, respectively. Here, the notation ^{z_0}g indicates the reported AB magnitudes are derived through a standard g filter that has been blueshifted by z_0. For a filter system which has been shifted by z_0, the k-correction for galaxies at that redshift is trivial, $-2.5\log(1 + z_0)$, and is independent of the galaxy spectral energy distribution. In choosing shifts which nearly match the median redshift of each sample, we minimize the uncertainty introduced through the k-corrections (Blanton et al., 2003c). Table 4.1 lists the effective wavelengths for each of the bandpasses used here.

4.2.4 Sample Construction

In order to investigate the color-magnitude relation of massive galaxies in the range $z \sim 0.1 - 0.4$, we create two samples from the SDSS spectroscopic database to be analyzed separately; Figure 4.1 shows the selection cuts used to define each of these samples. From the MAIN sample of galaxies, we extracted 16622 galaxies in the redshift range $0.1 < z < 0.2$ satisfying the rest-frame color cut

$$^{0.16}(g - i) > 8.374 + 0.32\,(M_g - 5\log h) \tag{4.2}$$

which approximates a cut of constant stellar mass (Bell & de Jong, 2000). This selection criterion results in a cut diagonally across the red sequence, which could bias our measurements of the scatter in red sequence colors and will greatly affect

Table 4.1.   Effective Wavelengths of Shifted Bandpasses

Filter	λ_{eff}
(1)	(2)
$^{0.16}g$	4026
$^{0.16}r$	5307
$^{0.16}i$	6441
$^{0.16}z$	7687
$^{0.37}g$	3408
$^{0.37}r$	4494
$^{0.37}i$	5454
$^{0.37}z$	6509
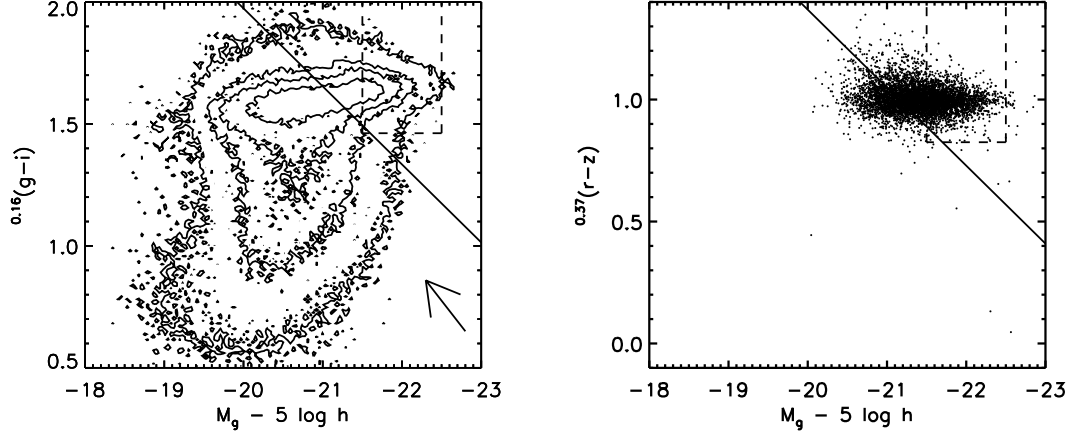
Figure 4.1 Sample definition for the galaxies used in this paper. The left panel shows the low redshift selection regions; contours encapsulate 25%, 50%, 75%, and 95% of the considered galaxies. The right panels shows the target selection for our high-redshift galaxies overlayed on the LRG galaxies in the SDSS Southern Survey. In each panel, the solid line shows the selection cut which approximates a cut at constant stellar mass using the relations of Bell & de Jong (2000). The regions defined by the dashed lines were used to create control samples which do not have a strong cut across the red sequence to test the effects of sample selection on our scatter measurements. The arrow in the lower right of the left panel shows the reddening vector. Note the dearth of very luminous blue galaxies which could contaminate our red-sequence samples if heavily reddened.

any slope measurement of the color-magnitude relation. In order to avoid biased slope measurements and test the consistency of our scatter measurements, we also construct a sample of 5100 galaxies in the luminosity range $-22.5 < M_g - 5 \log h < -21.5$ with $^{0.16}(g - i) > 1.46$ for comparison (shown by the dashed region in Figure 4.1).

We further select 2782 LRG galaxies from the SDSS Southern Survey in the redshift range $0.3 < z < 0.4$ which satisfy

$$^{0.37}(r - z) > 7.769 + 0.32 \, (M_g - 5 \log h) \qquad (4.3)$$

and have been imaged 6 or more times. Equation 3 is the same rest-frame color cut applied to the low-redshift galaxies (Equation 2) shifted to the $^{0.37}(r - z)$ color

— the effective wavelengths of the filters that define each of these colors are similar, and thus these colors probe similar regions in the rest-frame galaxy spectrum (see Table 4.1). Of these 2782 sample galaxies, 62% were imaged more than 9 times while 20% of the galaxies were imaged more than 12 times in the SDSS Southern Survey. As in the low-redshift sample, we adopt a simple constant color cut, $^{0.37}(r - z) > 0.825$ and $-22.5 < M_g - 5 \log h < -21.5$, to define a subsample of 1380 high-redshift galaxies to test the consistency of our scatter measurements and allow us to determine the slope of the color-magnitude relation without a strong cut across the red sequence.

We find no differences within our quoted error between the dispersion around the CMR measured from galaxies defined using the stellar mass cut and the constant color cut; throughout the remainder of this paper, scatter measurements will be based upon galaxies drawn in the first manner while all slope measurements are referenced to samples created using the latter method. Figure 4.2 shows the redshift distribution of the galaxies used to measure the scatter around the color-magnitude relation in this paper.

In detail, the red sequence is populated by elliptical and S0 galaxies as well as late-type galaxies reddened by dust. The arrow in the lower right of Figure 4.1 shows the reddening vector given by the O'Donnell (1994) extinction curve. In order for a dusty late-type galaxy to scatter into our sample, it must have a large unobscured luminosity as we only consider the most luminous red-sequence galaxies in this work. There is a clear paucity of very luminous blue galaxies in Figure 4.1 and thus the contamination from dusty spiral galaxies is likely small in our sample. Furthermore, Eisenstein et al. (2003) constructed the average spectrum of massive galaxies, such as those used in our analysis, and found that only 5% of the galaxy spectra in the $-22.5 < M_r < -22$ luminosity range were contaminated
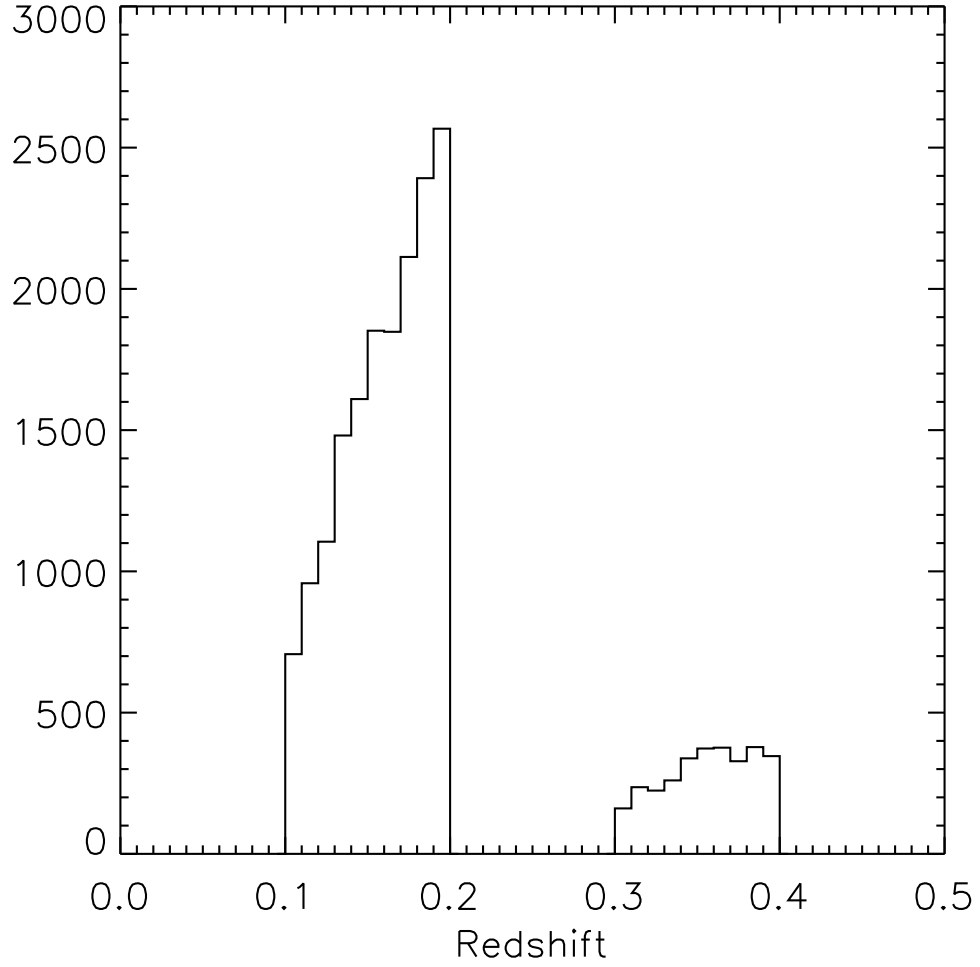
Figure 4.2 Redshift distribution of the galaxies selected for this work is shown. The low-redshift sample was drawn from the MAIN SDSS galaxy sample while the moderate-redshift sample is composed of LRG galaxies selected from the SDSS Southern Survey. The low-redshift sample has robust photometry in one observation epoch as the galaxies are upwards of five magnitudes brighter than the SDSS detection limit while the higher redshift galaxies, which extended two magnitudes fainter, have been imaged repeatedly allowing for more precise photometric measurements.

by emission lines uncharacteristic of early-type galaxies. In the remainder of this paper, we will use the red-sequence and early-type classifications synonymously.

Throughout this paper, we will refer to the galaxies considered here as field galaxies as they are not specifically selected to reside in clustered environments. It is important to note, however, that galaxies which are of similar color and luminosity as those in our sample tend to lie in over-dense environments (Hogg et al., 2003). Zehavi et al. (2005b) found the clustering strengths and mean separations of LRGs are comparable to those of poor clusters or rich groups. For comparison, of the LRGs in the volume surveyed by Bahcall et al. (2003) to find galaxy clusters with 13 or more detected cluster members, 16% are projected less than 500 kpc from the inferred location of a cluster and within 0.05 of the photometric redshift for that cluster. A detailed examination of the density dependence of the scatter around the CMR is conducted in §4.5.

4.3   The Color-Magnitude Relation

When determining the slope of the color-magnitude relation, we only consider the galaxies selected with our simple luminosity and constant color cuts as any slope measurements based on samples with a strong cut across the red sequence will be quite biased. The galaxy samples considered in this work only span a small range of luminosities and thus are not ideally suited for measurements of the slope of the CMR – we simply use our measurement of this quantity to remove the mean relationship before determining the scatter around it. The slopes and zero-points for the CMR for several colors are listed in Table 4.2. Figure 4.3 shows the measured slopes of the CMR as a function of the effective wavelengths of the two bandpasses used to define the color. The slope in bluer colors is more pronounced than that for redder bands which tend to show small or negligible

slopes. This trend is consistent with a metallicity sequence as the primary driver along the red-sequence. As noted by Gladders et al. (1998) using models from Kodama (1997), the flattening of the color-magnitude relation toward redder colors can also be reproduced by an age trend along the red sequence but only if a very specific relationship between galaxy mass and star formation time holds with very little scatter. In the bluest colors, which have been used historically in the literature, the slopes measured here are in general agreement with past work; for comparison, Hogg et al. (2004) report a slope of -0.022 mag mag^{-1} in the $^{0.1}(g - r)$ color for a large sample of galaxies at $z \sim 0.1$.

Figure 4.4 illustrates the typical scatter about the mean color-magnitude relation for the $^{0.16}(r - i)$ and $^{0.37}(r - i)$ colors; the measured dispersion about this relationship is quite small. The second column of Table 3 lists the measured dispersion around the CMR for each of the colors used in this study. For each color studied, we fit a Gaussian to the observed color distribution using Poisson errors on each color bin and define the dispersion of the best-fit Gaussian to be the scatter in galaxy colors on the red sequence. By fitting the histograms rather than calculating the standard deviation directly, we place more weight on the core of the distribution compared to the wings. Thus, our scatter measurements will not be heavily affected by any non-red-sequence interlopers in the wings of the color distributions. As this method could potentially depend on the binning used, we are careful to vary the bin size for each fit and ensure the measured scatter is not dependent on our choice of bin size. It should be noted that past work has used the standard deviation to quantify the scatter in galaxy colors. While the standard deviation and Gaussian widths may give systematically different dispersions in the case of non-Gaussian distributions, Figure 4.4 shows the color distribution on the red sequence is well described by a Gaussian and thus the two measurements

Table 4.2.   Slope of the Color-Magnitude Relation

Color	Total Sample		Field Sample		Cluster Sample	
	Zero-point[a]	Slope	Zero-point[a]	Slope	Zero-point[a]	Slope
	mag	mmag/mag	mag	mmag/mag	mag	mmag/mag
(1)	(2)	(3)	(4)	(5)	(6)	(7)
$^{0.16}(g-r)$	1.162	-15.6 ± 5.2	1.162	-10.5 ± 6.7	1.164	-12.4 ± 7.8
$^{0.16}(r-i)$	0.449	-8.10 ± 2.6	0.449	-6.7 ± 3.4	0.451	-7.6 ± 4.3
$^{0.16}(i-z)$	0.329	3.50 ± 6.4	0.329	4.2 ± 8.2	0.329	5.5 ± 10.4
$^{0.16}(g-i)$	1.611	-26.1 ± 5.5	1.610	-21.5 ± 7.4	1.612	-22.9 ± 8.2
$^{0.37}(g-r)$	1.750	-23.3 ± 12.1	1.750	-15.5 ± 16.1	1.754	-10.6 ± 19.5
$^{0.37}(r-i)$	0.613	-3.8 ± 4.3	0.612	0.41 ± 6.2	0.614	-3.6 ± 8.4
$^{0.37}(i-z)$	0.379	5.0 ± 6.1	0.377	0.58 ± 7.7	0.381	7.21 ± 9.9
$^{0.37}(r-z)$	0.991	1.8 ± 8.5	0.989	3.4 ± 3.5	0.983	8.1 ± 1.4

[a]The zero-point is defined at $M_g - 5 \log h = -21.8$.

are comparable. Bootstrap resampling of the data (e.g. Press, 2002) was employed to determine the uncertainty on our scatter measurements. It is important to note that the scatter measurements in the second column of Table 4.3 represent upper limits to the intrinsic scatter in galaxy colors as these values are not corrected for systematic or experimental effects, which could be significant.

In order to investigate the level of skewness of the observed color distribution, we define β_n to be the absolute value of the color difference between the $n\%$ quantile and the median of the distribution. The level of asymmetry in the distribution is then estimated using

$$\gamma = \frac{\beta_{10} - \beta_{90}}{\beta_{10} + \beta_{90}}. \tag{4.4}$$

For this statistic, a maximally skewed distribution would have $\gamma = \pm 1$ such that a tail of galaxies to the red would result in $\gamma < 0$. A symmetric distribution would have $\gamma = 0$. We adopt this approach rather than a traditional third moment calculation as the calculation of higher moments of a distribution is strongly dependent on the wings of the distribution where contamination may be important. For the histograms shown in Figure 4.4, we find that $\gamma = -0.027 \pm 0.019$ for the $^{0.16}(r-i)$ color and $\gamma = -0.064 \pm 0.048$ for the $^{0.37}(r-i)$ color. Both of these measurements reflect the slight over-abundance of red galaxies compared to a Gaussian in both panels of Figure 4.4. This red tail is due to the diagonal cut across the red sequence imposed by our stellar mass selction criterion; red galaxies are selected to lower luminosities than blue galaxies. Since the luminosity function of galaxies is steeply rising toward lower luminosities in this range, more red galaxies are selected than blue galaxies. For comparison, we measure $\gamma = 0.001 \pm 0.029$ for the $^{0.16}(r-i)$ color and $\gamma = -0.005 \pm 0.057$ for the $^{0.37}(r-i)$ color when the simple luminosity cuts are used to select our sample galaxies.

Since our intermediate redshift sample is drawn from regions that have been

Table 4.3. Scatter Around the Color-Magnitude Relation

Color	Measured Scatter	Instrumental Scatter	Intrinsic Scatter	Field[a]	Clustered[a]
	mmag	mmag	mmag	mmag	mmag
(1)	(2)	(3)	(4)	(5)	(6)
$^{0.16}(g-r)$	39.6 ± 0.4	17.6 ± 3.6	35.4 ± 3.7	40.5 ± 0.4	35.9 ± 0.8
$^{0.16}(r-i)$	18.7 ± 0.2	15.1 ± 3.9	11.0 ± 4.0	19.1 ± 0.2	17.3 ± 0.3
$^{0.16}(i-z)$	26.6 ± 0.4	20.9 ± 4.2	20.9 ± 4.2	26.7 ± 0.5	23.4 ± 0.8
$^{0.16}(g-i)$	40.0 ± 0.4	21.2 ± 4.1	34.4 ± 4.1	42.0 ± 0.5	36.1 ± 0.7
$^{0.37}(g-r)$	48.0 ± 1.2	20.4 ± 6.1	43.5 ± 6.2	48.8 ± 1.4	47.3 ± 2.2
$^{0.37}(r-i)$	19.7 ± 0.5	12.3 ± 3.1	14.6 ± 3.1	20.1 ± 0.6	18.9 ± 1.0
$^{0.37}(i-z)$	27.9 ± 0.7	21.6 ± 4.5	17.6 ± 4.6	29.2 ± 0.8	24.4 ± 1.4
$^{0.37}(r-z)$	35.9 ± 1.1	18.4 ± 5.2	30.8 ± 5.2	38.1 ± 1.2	28.4 ± 2.1

[a]Field and clustered values are *measured* scatter, not the intrinsic scatter in the galaxy colors.

repeatedly imaged by the Sloan Digital Sky Survey, we can assess the level to which the dispersion we observe in the color-magnitude relation is dependent on measurement noise. If the scatter is contaminated by measurement noise, we would expect the squared scatter to decrease inversely with the number of observations :

$$\sigma_{\text{obs}}^2 = \sigma_{\text{intrinsic}}^2 + \frac{A}{N_{\text{obs}}} \ . \tag{4.5}$$

Figure 4.5 shows the results of this test; the methods used for the ensemble sample were used in the same manner to calculate the scatter and error for each bin. In each bin of N-measurements, we include galaxies which were imaged a total of N times, and thus each bin contains a unique subsample of galaxies. For the moderate-redshift sample, the third and fourth columns in Table 4.3 lists the instrumental contribution and intrinsic galaxy scatter predicted by extrapolating the fits to Equation 2 to infinite observations for each of the three colors.

While the intrinsic dispersion around the color-magnitude relation at moderate redshift can be extracted from the measured scatter based on subsamples of galaxies with different number of measurements, the low-redshift galaxies do not allow for this test as most galaxies in this sample have been imaged only once. In order to estimate the intrinsic scatter in galaxy colors for this sample, we identified 5839 of our low-redshift galaxies that have been imaged more than once under photometric conditions. We adopt the average root-mean squared variation of each photometric measurement as the instrumental error for each color of interest. We find the mean measurement uncertainty to be 17.6, 15.1, and 20.9 mmag in the $^{0.16}(g-r)$, $^{0.16}(r-i)$, and $^{0.16}(i-z)$ bands, respectively. The internal dispersion in each color is the difference, in quadrature, between the measured scatter and inferred mean uncertainty in our single pass photometry. For the low-redshift galaxies, the third and fourth columns of Table 4.3 lists the observational

error and intrinsic scatter determined by this correction. While our estimate of the instrumental contribution to the observed color dispersion corrects for uncorrelated errors on each independent measurement, we do not correct for systematic errors common to all observations which could cause an overestimation of the intrinsic dispersion in galaxy colors.

Figure 4.6 shows our scatter measurements as a function of the effective wavelength of the filters used to construct each color. The scatter about the CMR is clearly wavelength dependent; the bluest colors, which are most affected by small changes in the age, metallicity, or dust attenuation of the system, have systematically larger dispersions than the reddest colors where changes in metallicity and age have less impact.

4.4   Star Formation History of Massive Galaxies

Here, we consider three simple star formation histories and derive the range of permitted parameters for these histories following a method similar to that of van Dokkum et al. (1998). In these toy models, we will assume that only age variations between red-sequence galaxies creates the scatter in early-type galaxy colors. In reality, the scatter across the CMR is likely driven by some combination of age, metallicity, dust, and possibly α-enhancement variations across the red-sequence. These models will thus illustrate the broadest range of ages allowed by our measurements; the inclusion of any variation in the other galaxy properties will only constrain the age more strongly.

In this section, we will primarily consider the high-redshift sample, as these are the intrinsically youngest galaxies in our sample and hence should provide the tightest constraints on the past star formation history of massive early-type galaxies. An identical analysis of the low-redshift sample provides results con-

sistent with those presented below. In all three model cases, the low-redshift galaxies provide looser constraints than the high-redshift sample; star formation is allowed to continue to slightly later times.

First, we consider a star formation history composed of a single delta-function burst. The probability of a burst occurring is distributed uniformly between the earliest allowed time for galaxy formation, t_0, set to $z = 10$, and t_{max}, the time at which the youngest early-type galaxies form. Using a grid of Monte-Carlo simulations with 5000 galaxies per realization, we create samples of galaxy spectra synthesized using the method of Bruzual & Charlot (2003) with solar metallicity, a Salpeter (1955) initial mass function, and varying values of t_{max}. We find that realizations allowing galaxies younger than 8.8 Gyr ($z \sim 1.4$) generate color distributions with standard deviations larger than that measured.

We perform a similar test using a scheme in which 80% of the stars in a galaxy are formed in a single burst at $z = 10$ and 20% are formed in a second burst which occurs at a random time between $z = 10$ and a minimum age, as done by van Dokkum et al. (1998). For this scenario, the secondary bursts must occur between $10 > z > 0.9$ to reconstruct the observed scatter in the color-magnitude relation. For bursts that generate less than 5% of a galaxy's stars, the time scale for the secondary burst is unconstrained - small amounts of star formation can occur at late epochs without violating the constraints placed by our measurements.

Finally, we create a grid of models in which star formation begins at $z = 10$ and continues at a constant rate until it is truncated at t_f. For each realization, we allow t_f to range from $z = 10$ to a critical cutoff time at which all galaxies have stopped forming stars. Star formation in this manner must have ended by $z \sim 0.8$ in order to reproduce the observed scatter in the color-magnitude relation at $z = 0.37$.

The allowed range of parameters and the distribution of galaxy colors found in each model are shown graphically in Figure 4.4. To allow comparison with Figure 4.4, typical observational errors have been included in the color distributions in the lower panels of the figure. Interestingly, all of these models predict similar scatter trends to those seen in Figure 4.6. In all three cases, the scatter in the $^{0.37}(g-r)$ color is nearly double that predicted for the $^{0.37}(r-i)$ and $^{0.37}(i-z)$ colors. While each of the three models succeeds in reproducing the observed scatter in early-type galaxy colors, none of the models adequately recreates the color distribution measured from real galaxies, a sign that the models chosen do not perfectly track the true evolution of the star formation history of early-type galaxies. The γ parameter, as defined in Equation 4, for each of the model distributions is shown in Figure 4.4. The three models produce color distributions with $\gamma = (0.165, 0.508, 0.313)$ compared to the value of -0.064 calculated for the observed sample of galaxies at the same redshift. The difference between the observed skewness and that determined from our simple models reiterates the mismatch between the observed and predicted color distributions. In our simulations, we assume all galaxies have the same metallicity and no dust attenuation. Also, the onset of star formation is uniform in the second two models. In reality, these parameters are not constant, and thus the sharp truncations seen on the red edges of model color distributions will be blurred by the addition of other complications to the models. However, any of these corrections will increase the observed scatter in galaxy colors thus driving the last epoch of star formation needed to satisfy our constraints to earlier times.

4.5   Comparison with Clustered Environments

A majority of the work on the color-magnitude relation of early-type galaxies has focused on cluster galaxies at various redshifts. While some work (e.g. Sandage & Visvanathan, 1978; Larson, Tinsley, & Caldwell, 1980; Kodama, Bower, & Bell, 1999) tackles the problem in the field, these studies suffer from small numbers of galaxies. The measurement of the scatter around the CMR presented here, on the other hand, focuses on the most massive field galaxies at moderate redshifts using a statistically significant sample. We can now, for the first time, statistically compare the dispersion around the CMR in both clustered and field environments.

In order to explore the environmental dependence of the color-magnitude relation within our data set, we use SDSS imaging of 5305 $\deg^2$ to identify a comparison sample of 16 million normal galaxies down to $r = 21$. At the location of each LRG galaxy in our sample, we count the number of neighboring galaxies within a $1\,h^{-1}$ Mpc (proper) aperture which have colors similar to those expected for an L^* galaxy on the red sequence, and luminosities in the $M^* - 0.5$ to $M^* + 0.4$ range; the details of the luminosity and color cuts are given in Eisenstein et al. (2005).

Using the number of neighbor galaxies as a proxy for the environment of each LRG in our sample, we divide each of our galaxy sets into a clustered subsample and a low density subsample. We define LRG galaxies with more than 5 (7) neighboring galaxies in the low- (moderate-) redshift samples to be in clustered environments while a field subsample is comprised of galaxies with fewer neighbors. This threshold was chosen such that the clustered sample in both redshift bins composes 30% of the total galaxy sample at that redshift. To place these values in physical context, at $z = 0.16$ ($z = 0.37$) there are 25.3 (170) tracer galaxies

per square degree. Given the angular diameter distance of 398 (712) h^{-1} Mpc to that redshift, this yields a total of 1.65 (3.46) background galaxies per aperture on average. The average number of neighbors in the field sample is 2.3 (3.9) galaxies while the clustered galaxies have a mean of 9.1 (11.4) neighbors. Thus our clustered samples are over-dense by a factor of 4 (3) compared to the field galaxies.

Hogg et al. (2004) found that the slope and zeropoint of the color-magnitude relation do not depend strongly on the local galaxy environment. We find the same result; Table 4.2 lists the measurements of the slope and zeropoint of the relationship for the ensemble sample as well as for the field and clustered subsamples. The variation between the two samples is small. In the following calculations, we use the ensemble slope and zeropoint measurements as these are measured with the highest signal-to-noise. The results are unaffected if the individual measurements of the slope and zeropoint are used for each subsample.

The fifth and sixth columns of Table 4.3 list the measured scatter in galaxy colors for the field and clustered galaxies respectively. In all of the bands, the scatter for the field subsample is larger than that in clustered environments. If we assume the scatter introduced by instrumental effects is the same for both the field and clustered subsamples, the same correction determined for the ensemble galaxy sample can be applied to these subsamples, as well. With this correction, we find that the scatter in galaxy colors in dense environments is $11 \pm 2\%$ smaller than for that of isolated systems in both redshift intervals studied here.

Our clustered galaxies reside in a range of densities, not simply rich clusters, as have often been used for similar studies, and thus we likely underestimate the significance of the difference in scatter between the field and strongly clustered environments. Furthermore, our field sample is not completely composed of isolated galaxies as the average number of neighbor galaxies in this sample is larger

than the average density of background galaxies. Again, this leads to an under-estimation of the true difference in the dispersion around the color-magnitude relation for field and clustered galaxies.

The larger scatter in field galaxy colors supports previous claims of an environmental dependence for the scatter around the color-magnitude relation for early-type galaxies (e.g. Larson, Tinsley, & Caldwell, 1980; Kodama, Bower, & Bell, 1999), though the effect measured here is weak. Comparisons of the scatter in galaxy colors for clustered galaxies often draw on galaxies from a single cluster whereas our clustered sample is created by combining galaxies from a number of clustered environments. It is possible that the star formation histories of galaxies in a single cluster are more highly coordinated than the star formation histories between different clusters, thus the scatter measured using galaxies from a single cluster would be smaller than when several clusters are combined. As the fraction of blue galaxies is larger in the field compared to clustered environments, the field subsample may have a larger contamination fraction compared the the clustered subsample. This would also cause an increased scatter in field galaxies colors compared to the galaxies in more dense environments.

4.6   Average Galaxy Spectrum Across the Red Sequence

Having measured the scatter in galaxy colors, we next investigate the spectral differences between galaxies by examining the average spectrum of massive early-type galaxies across the red sequence. The composite early-type galaxy spectrum has been investigated as a function of environment, luminosity, redshift, size, and velocity dispersions (Eisenstein et al., 2003; Bernardi et al., 2003); here, we construct the composite spectrum for red sequence galaxies of different mean colors. Since the galaxies in our low-redshift sample are brighter, and thus have higher

quality spectra, and are more numerous than the higher redshift galaxies, we only consider these galaxies in our analysis.

To construct the average spectrum of the galaxies in each color bin, we first shift the spectra according to the observed redshift and then normalize the observed SDSS spectrum by the flux at rest-frame 5000 Å. We augment the SDSS pixel mask to include all pixels within 10 Å of the bright sky lines at 5577, 5890, 5896, 6300, 6364, 7245, and 7283 Å. Since the galaxies of interest are in the redshift range $0.1 < z < 0.2$, the masked pixels occur at different rest-frame wavelengths for each galaxy, leaving the mean spectrum unaffected. We then find the number-weighted mean of the spectra, ignoring all masked pixels in the mean.

Galaxies are divided into two distinct color bins – red galaxies having $^{0.16}(g - r)$ colors between 1-σ and 3-σ redward of the mean and a blue sample in the same range blueward of the mean. The red galaxy bin contains 1321 galaxies with a mean $^{0.16}(g - r)$ color of 1.20 and $M_g - 5 \log h = -21.3$ while the blue sample contains 1161 galaxies with mean color and luminosity of 1.09 and $M_g - 5 \log h = -21.5$. Figure 4.8(a) shows the coadded spectra of the red and blue galaxies. The gross properties of each composite spectrum are similar. Figure 4.8(b) shows the difference between the blue and red spectra. This difference spectrum shows clear signs of enhanced Balmer absorption in the blue galaxies compared to the red composite, indicating that, on average, the blue galaxies contain more young stars, in agreement with past studies (e.g. Trager et al., 2000b; Bernardi et al., 2005). While the red composite shows stronger [N II] emission lines relative to the blue composite, no other prominent emission lines, such as [O II], [O III], and Hα are present; this emission line difference is likely due to a larger fraction of AGN in the red galaxies compared to the blue.

We consider two possible evolutionary scenarios to explain the spectral differ-

ences between the blue and red galaxies on the red sequence: pure age (i.e. passive) evolution of a single age stellar population and a recent epoch of star formation mixed with an existing old population. In the first scenario, we fit each composite spectrum with a solar metallicity, single age, stellar synthesis model created using the method of Bruzual & Charlot (2003). The red and blue spectra are best fit by 6.3 Gyr and 3.7 Gyr populations, respectively. In the second scenario, we find the blue composite spectrum is well fit by a 6.3 Gyr old stellar population mixed with a 1 Gyr population containing 3.5% of the stellar mass and we model the red composite with a simple 6.3 Gyr population. The difference spectra for both scenarios are shown in Figure 4.8(b). While each of the two model hypotheses would suggest quite different evolutionary histories for massive early-type galaxies, the predicted difference spectra are remarkably similar. The model consisting of a recent burst of star formation slightly over-estimates the continuum in the difference spectrum near 3900 Å and thus provides a marginally poorer fit to the data than the passive evolution model.

The residuals between the data and the model difference spectra are shown in Figure 4.8(c). Both of the models fail to match the strengths of the CN_2 and Mg b features near 4140 and 5160 Å. Eisenstein et al. (2003) interpret these differences between observations and synthetic spectra as a enhanced α-to-iron ratio present in the galaxies but not included in the synthetic models. Also, several weak iron features are evident in the two model spectra near 4300 and 5300 Å which are missing in the observed difference spectrum. In a pure-age model for the evolution across the red sequence, the enhanced blue continuum provided by the hotter stars in the young population dilutes the metal lines seen in the older population. This dilution leads to differences in the strengths of the metal lines of the two population models, thus causing the residual iron features in

both model difference spectra. The absence of these residuals in our observed difference spectrum indicates that a pure-age model for the spectral differences between red and blue galaxies on the red sequence is an incomplete model. In order to match the variations of the spectral features across the red sequence, a more detailed model is required. This model should include both age and metallicity variation and, more importantly, non-solar abundance ratios. Until spectral synthesis models with realistic α-enhancement prescriptions are available, more quantitative analysis of our observed difference spectrum is difficult as the interplay between age, metallicity, and α-to-iron ratio variations must be included for a full understanding of the physical differences between these galaxies.

Another clear difference between the models and the data is the strong Na D feature near 5892 Å. Here, the red composite spectrum has considerably more Na D absorption than predicted by the stellar synthesis models. As the model spectra do not contain absorption due to the interstellar medium, this discrepancy may indicate that the red galaxies contain more neutral gas than their blue counterparts.

4.7   Conclusions

We present new multi-color observations of a large sample of galaxies in the range $0.1 < z < 0.4$ gathered from the Sloan Digital Sky Survey. These galaxies represent the most massive galaxies in the Universe and are not selected to be in clustered environments. Past studies of the color-magnitude relationship have focused on L^* galaxies in clusters, thus our work focuses on an area of parameter space previously unexplored. Using the robust photometry of bright galaxies provided by the SDSS as well as multiple observations of moderate-redshift galaxies, we are able to construct the color-magnitude relations for massive field

galaxies in several colors. While our data only span one magnitude in luminosity, and thus are not ideal for in-depth analysis of the slope and zeropoint of the CMR, our large sample of galaxies allows us to measure the dispersion about this relationship quite well. The scatter around the red sequence is 20 mmag in the reddest bands while the bluest colors have nearly double this value.

We construct several toy model star formation histories in order to place constraints on the evolutionary processes at work in massive galaxies. We find that the majority of star formation in these early-type galaxies must have occurred before $z \sim 1$, in agreement with other authors. For secondary bursts of star formation with strengths less than 5% of the total stellar mass of the system, our data are consistent with bursts of star formation at any epoch. However, one should note that none of the toy models reproduce the observed distribution of galaxy colors.

Furthermore, we make comparisons between our new measurement of the scatter around the color-magnitude relation for massive field galaxies and early-type galaxies in clusters. An internal comparison shows that the scatter around the CMR in dense environments is $11 \pm 2\%$ smaller than that measured using more isolated galaxies.

The composite spectra of LRG galaxies redward and blueward of the mean galaxy color are physically distinct. The blue galaxies show stronger Balmer absorption than the red galaxies, consistent with the presence of a younger stellar population. Simple models slightly favor passive evolution of stellar populations as the cause of the observed differences in spectra across the red sequence compared to a more recent injection of young stars onto an old stellar population, though the difference between the predicted spectra from these models is small.
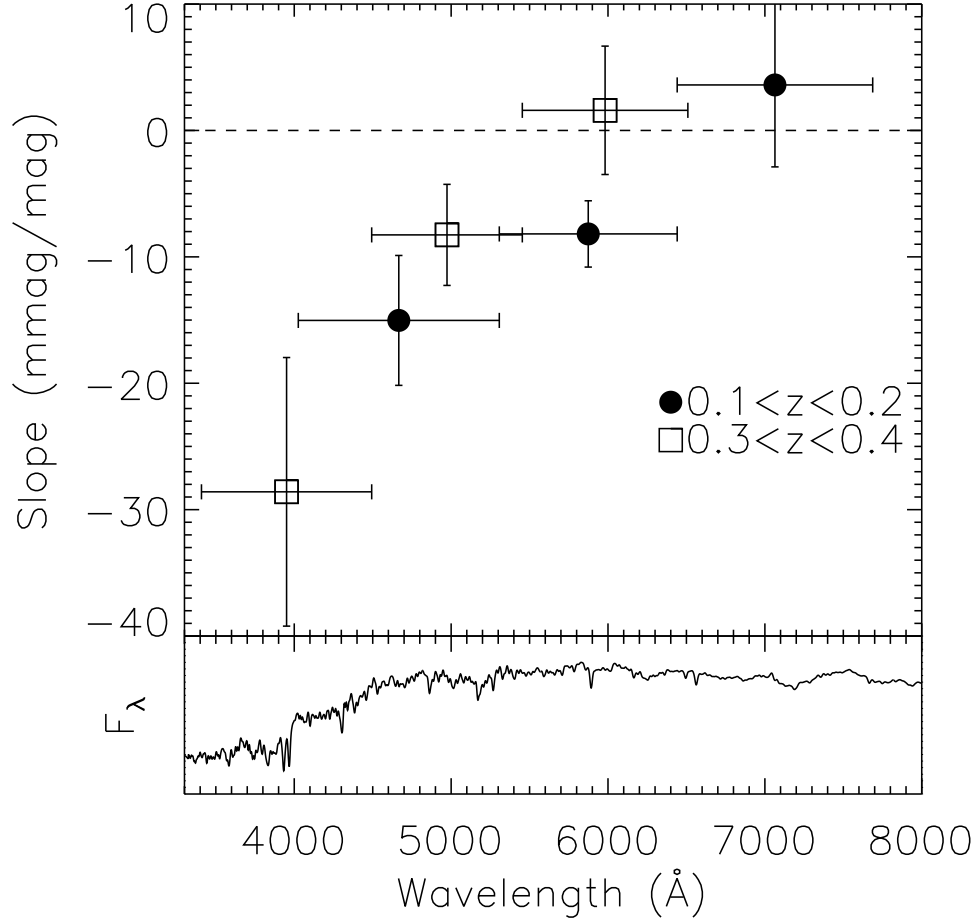
Figure 4.3 Measured slope of the CMR as a function of the rest-frame bandpass. The endpoints of the horizontal error bars mark the effective wavelengths of the filters used to define the bandpass while the vertical error bars show the measured uncertainty on each slope measurement. The spectrum of an early-type galaxy is plotted as a reference. The two symbols represents the two galaxy samples - the hollow squares mark measurements on the moderate-redshift ($0.3 < z < 0.4$) sample while the filled circles show the data from low-redshift ($0.1 < z < 0.2$) galaxies.
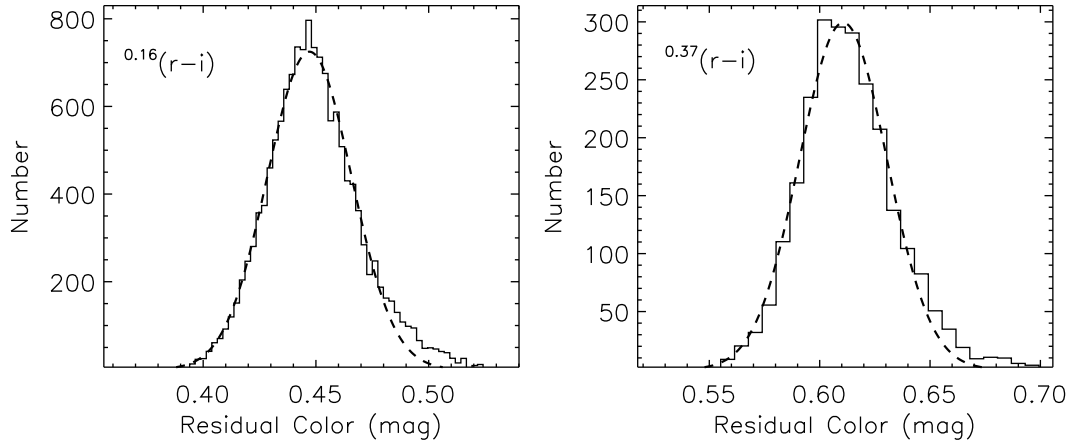
Figure 4.4 Scatter around the color-magnitude relation for both galaxy samples. The $^{0.16}(r-i)$ and $^{0.37}(r-i)$ residual colors, normalized to the characteristic color of a galaxy with $M_g - 5\log h = -21.8$ are shown for the low and intermediate redshift galaxies respectively. Note that the dispersion of this relation is quite small. The dashed line is the best-fit Gaussian to the data. Table 4.3 lists the measured scatter around the CMR for all of the colors measured in this paper.
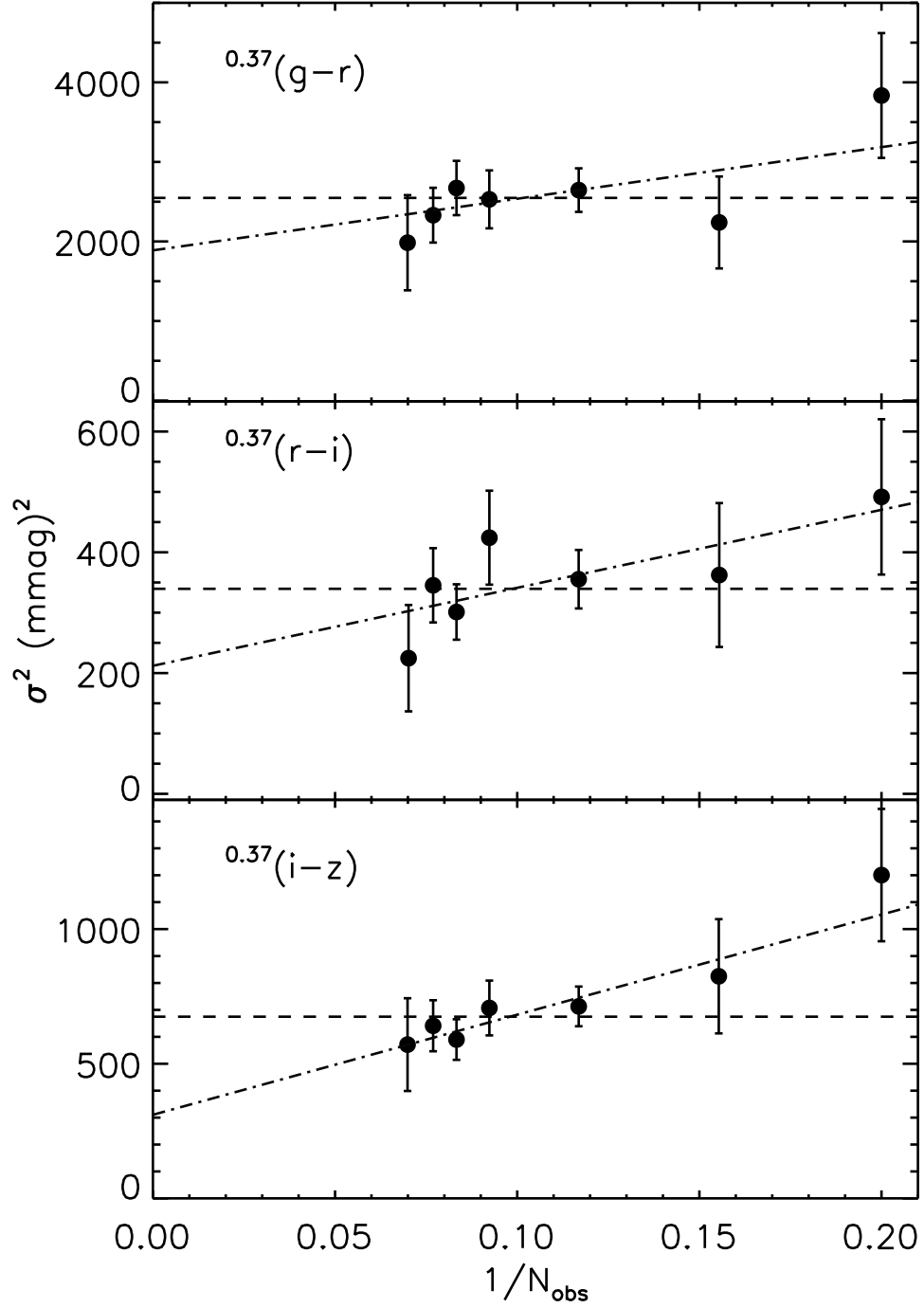
Figure 4.5 Relationship between the number of observations and the measured scatter around the color-magnitude relation. The dotted line shows the weighted mean of the data while the dot-dashed line marks the best fit line to the data. The data for each color are not statistically consistent with a constant value but are well described by a line, as is expected. We extrapolate the best fit line to infinite measurements to find the intrinsic scatter in galaxy colors; these values are listed in the fourth column of Table 4.3.
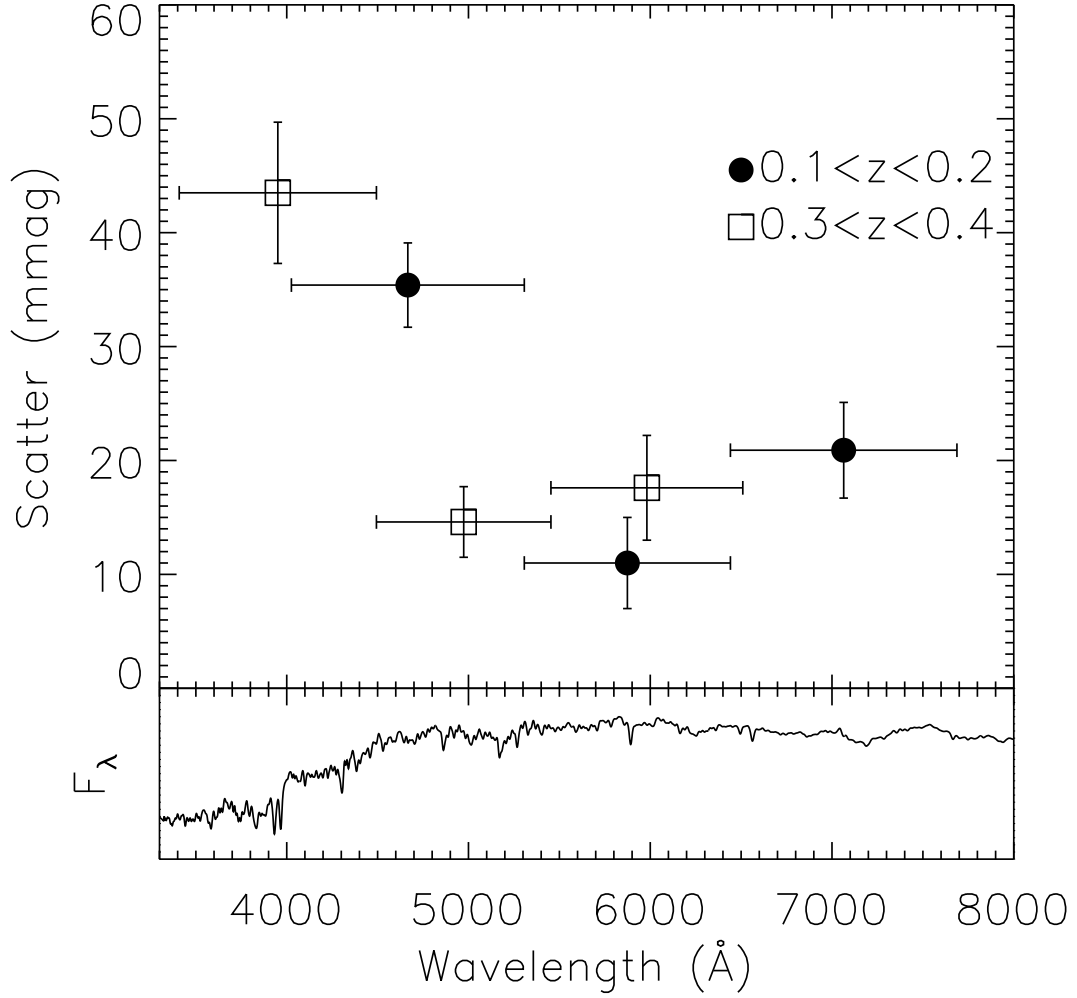
Figure 4.6 Intrinsic scatter in the color-magnitude relation as a function of the observed bandpass. The error bars and symbols are defined as in Figure 4.3. The spectrum of an early-type galaxy is shown for comparison. The scatter in redder bands tends to be smaller than in blue bands. This is not unexpected, as small changes in a galaxy's age, metallicity, or dust attenuation affect the blue portion of a its spectrum more than the red.

Figure 4.7 Reproduction of the observed scatter in rest-frame color of early-type galaxies using Monte-Carlo simulations following a method similar to that of van Dokkum et al. (1998). For each simulation, the top panel shows several examples of star formation histories drawn from the simulation. The shaded region denotes the allowed epoch of star formation for that simulation. Each of the bottom panels shows the distribution of residual colors around the color-magnitude relation for the realization that most closely matches the observed scatter. The γ parameter, as defined in the text, is listed for each of the distributions. For comparison with the color distributions in Figure 4.4, we have added typical observational errors to the color distributions. The dashed line in each panel shows a Gaussian with the same mean and dispersion as the simulated colors. The left-most panel illustrates the allowed epoch of star formation for a SFH composed of a single delta function burst. For galaxy formation beginning at a redshift of 10, the youngest early-type galaxies must have formed by $z \sim 1.13$. The middle panel illustrates the allowed range of times for a secondary burst which contributes 20% of the stars to the galaxy. This secondary burst must have occurred before a $z \sim 0.84$. Finally, for a constant star formation history, all star formation must have ended by $z \sim 0.62$ to reproduce the observed scatter in the color-magnitude diagram at $z = 0.37$. For reference, the lookback time at $z = 0.37$ is 3.89 Gyr. A comparison with Figure 4.4 shows that the color distributions predicted by these models do not match the observed colors of massive galaxies, a sign that the models used here are overly simple. This is echoed by the mismatch between the γ value measure from the data and those measured for each of the model distributions.

Lookback Time (Gyr)

Lookback Time (Gyr)

Lookback Time (Gyr)

$\gamma=0.165$

$\gamma=0.508$

$\gamma=0.313$

$\Delta^{0.37}(r-i)$

$\Delta^{0.37}(r-i)$

$\Delta^{0.37}(r-i)$
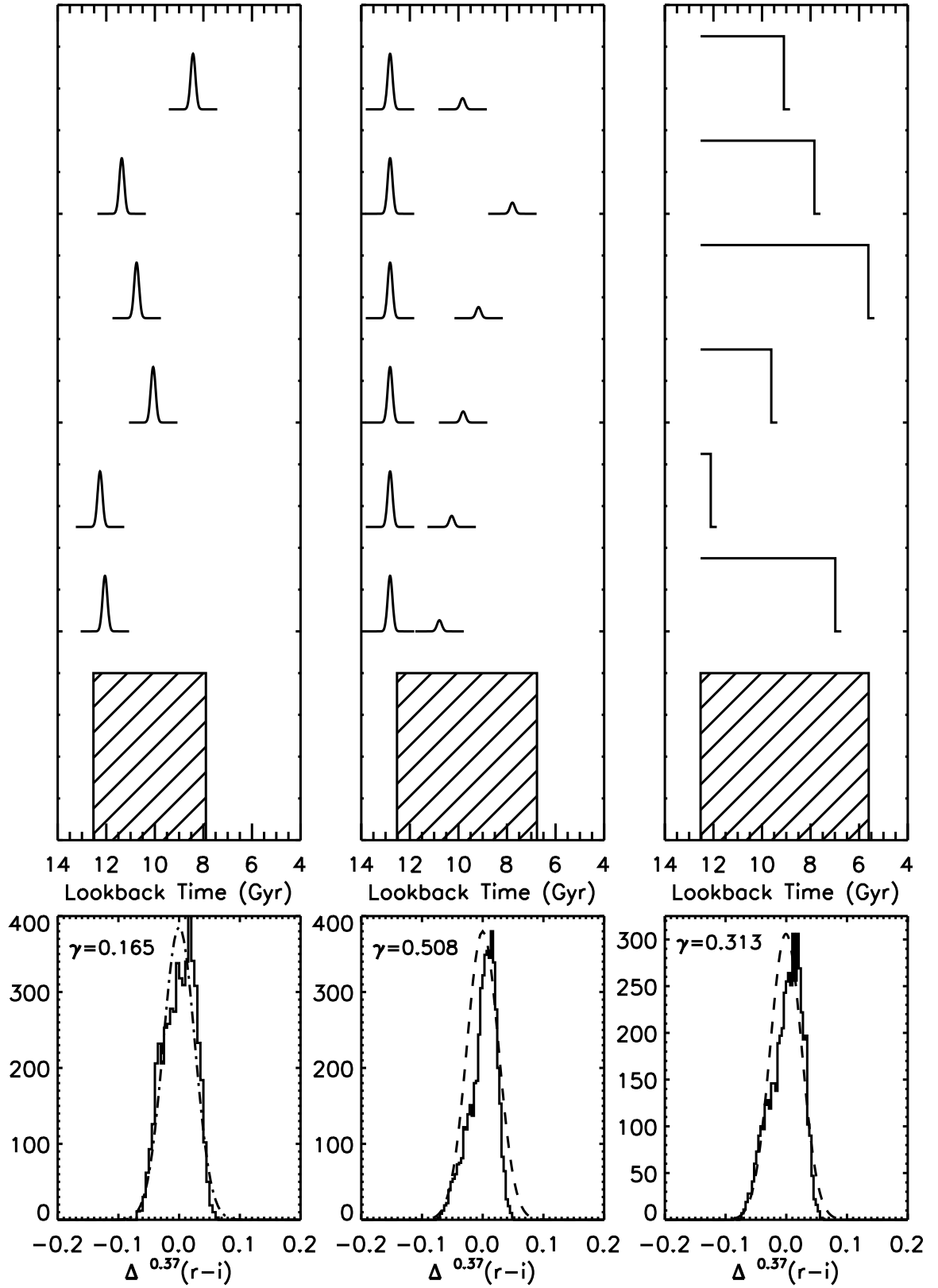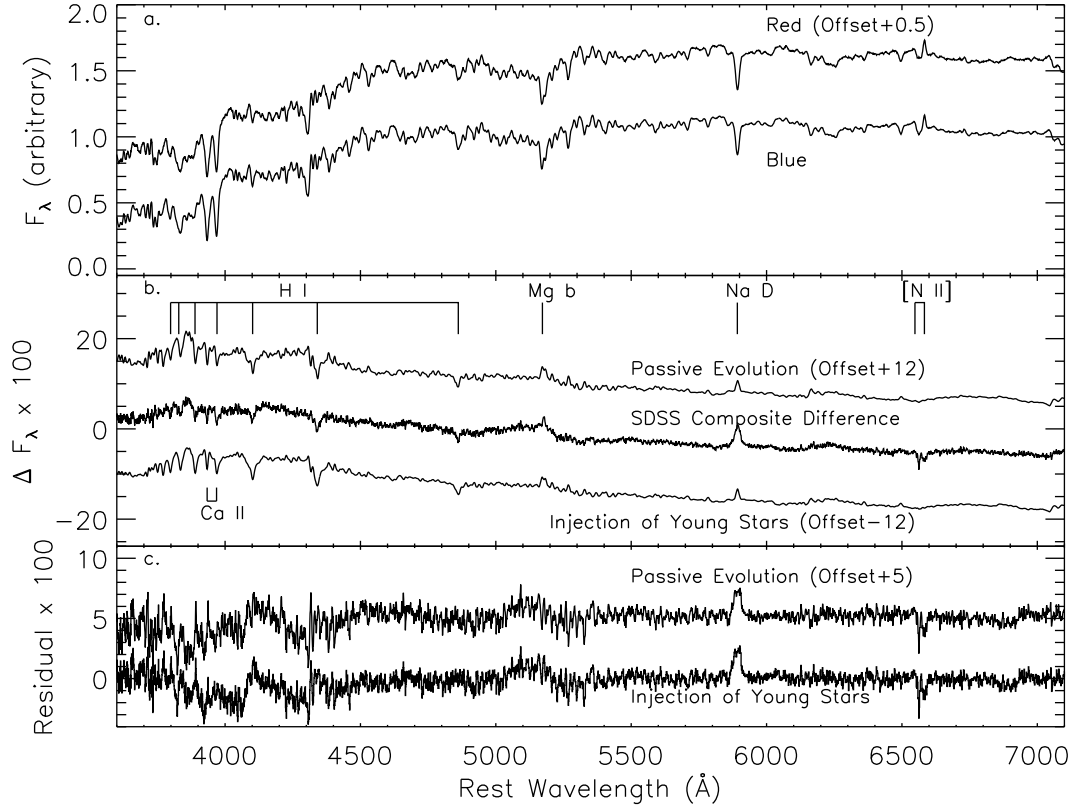
Figure 4.8 (a) Composite spectra of galaxies between 1-σ and 3-σ of the mean $^{0.16}(g-r)$ color. The gross properties of the composite red and blue spectra are quite similar. (b) The difference spectrum between the blue and red galaxies (middle) compared to the difference spectrum predicted for a passively evolving population (top) and an old population with a recent injection of young stars (bottom). The difference spectrum shows clear signs of enhanced Balmer absorption lines in the blue galaxies as well as stronger molecular features in the red galaxies. The red galaxies have stronger sodium absorption, leading to the "emission" feature in the difference spectrum. (c) Residuals between the data and comparison synthesis spectra. The general properties of the observed difference spectrum are matched in both comparisons, though the model consisting of an old galaxy with a small amount ($\sim 3\%$) of star formation in the past 1 Gyr slightly over-predicts the continuum strength in between 3900 Å and 4100 Å compared to the passively evolving model.

CHAPTER 5

LUMINOSITY FUNCTION CONSTRAINTS ON THE EVOLUTION OF MASSIVE RED GALAXIES SINCE $z \sim 0.9$

We measure the evolution of the luminous red galaxy (LRG) luminosity function in the redshift range $0.1 < z < 0.9$ using samples of galaxies from the Sloan Digital Sky Survey as well as new spectroscopy of high-redshift massive red galaxies. Our high-redshift sample of galaxies is largest spectroscopic sample of massive red galaxies at $z \sim 0.9$ collected to date and covers 7 deg^2, minimizing the impact of large scale structure on our results. We find that the LRG population has evolved little beyond the passive fading of its stellar populations since $z \sim 0.9$. Based on our luminosity function measurements and assuming a non-evolving Salpeter stellar initial mass function, we find that the most massive ($L > 3L^*$) red galaxies have grown by less than 50% (at 99% confidence), since $z = 0.9$, in stark contrast to the factor of 2-4 growth observed in the L^* red galaxy population over the same epoch. We also investigate the evolution of the average LRG spectrum since $z \sim 0.9$ and find the high-redshift composite to be well-described as a passively evolving example of the composite galaxy observed at low-redshift. From spectral fits to the composite spectra, we find at most 5% of the stellar mass in massive red galaxies may have formed within 1Gyr of $z = 0.9$. While L^* red galaxies are clearly assembled at $z < 1$, $3L^*$ galaxies appear to be largely in place and evolve little beyond the passive evolution of their stellar populations over the last half of cosmic history.

5.1   Introduction

The favored model for the evolution of galaxies is through the hierarchical merging of smaller satellite galaxies into larger systems. The details of the frequency and efficiency of the merging process are poorly constrained, especially in the densest environments. As the endpoint of the hierarchical merging process, the most massive galaxies are most sensitive to various merger models assumptions and thus offer a strong opportunity to constrain models of galaxy formation and evolution.

Observations of the evolution of early-type galaxy stellar populations have shown that the stars in these galaxies formed at $z > 2$ and that the galaxies have had little star formation since that epoch (Bower et al., 1992; Ellis et al., 1997; Kodama et al., 1998; de Propris et al., 1999; Brough et al., 2002; Holden et al., 2005; Wake et al., 2005; Pimbblet et al., 2006; Jimenez et al., 2006; Bernardi et al., 2003a,b,c,d; Glazebrook et al., 2004; McCarthy et al., 2004; Papovich et al., 2005; Thomas et al., 2005; Bernardi et al., 2006). While the average population of massive galaxies appears to be quite old and passively evolving, a number of studies have indicated that local massive early-type galaxies show signs of recent star formation activity (Trager et al., 2000a; Goto et al., 2003; Fukugita et al., 2004; Balogh et al., 2005). The fraction of early-type galaxies with evidence of recent star formation seems to increase to high redshift and decreases with increasing stellar mass (Le Borgne et al., 2006; Caldwell et al., 2003; Nelan et al., 2005; Clemens et al., 2006).

At $z < 1$, early-type galaxies form a tight relationship between their rest-frame color and luminosity (the so-called color-magnitude relation or red-sequence of galaxies) wherein more luminous (and hence more massive) galaxies have redder colors then less-massive counterparts (Visvanathan & Sandage, 1977; Bower et

al., 1992; Hogg et al., 2004; McIntosh et al., 2005; Willmer et al., 2006). The tight dispersion around this relationship implies that, at fixed luminosity, galaxies on the red-sequence share very similar star formations histories. If massive galaxies have undergone any mergers since $z \sim 1$, the mergers must have resulted in very little star formation; the addition of even a small fraction of blue stars would result in a larger intrinsic scatter than observed (Chapter 4).

The extent to which gas-poor mergers that result in no new star formation are involved in the build-up of massive galaxies is a topic of much current research. While examples of these mergers have been observed at low redshift (Lauer, 1988; van Dokkum, 2005; McIntosh et al., 2007) and at intermediate redshifts (van Dokkum et al., 1999; Bell et al., 2006b; Tran et al., 2005; Rines et al., 2007; Lotz et al., 2008), the extent to which massive galaxies participate in these merger events is controversial. Bell et al. (2006) and Le Fèvre et al. (2000) estimate that L^* red galaxies experience 0.5-2 major mergers since $z \sim 1.0$ based on pair counts of galaxies. van Dokkum (2005) identified galaxies which have likely undergone a recent gas-poor merger based on the presence of diffuse emission extended from the main galaxies and found that 35% of today's bulge dominated galaxies have experienced a merger with mass ratio greater than 1:4 since $z \sim 1$. Based on the very small-scale correlation function of luminous red galaxies from SDSS, Masjedi et al. (2006) concluded that mergers between these very massive systems occur quite rarely at $z \sim 0.3$ with rates $< 1/160\,\mathrm{Gyr}^{-1}$. Masjedi et al. (2007) calculate that massive early-type galaxies have grown by 1.7% per Gyr on average since $z \sim 0.2$ due to mergers with all other galaxies.

Studies based on the number counts of galaxies from COMBO-17, DEEP2, and the NOAO Deep Wide-Field Survey (NDWFS) all agree that the stellar mass averaged all red-galaxies has at least doubled since $z \sim 1$ (Brown et al., 2007;

Willmer et al., 2006; Bell et al., 2004). While the truncation of star formation in blue galaxies and subsequent passive fading of the stellar populations can explain the growth of L^* galaxies since $z \sim 1$, the lack of very massive blue galaxies at redshift of unity (Bell et al., 2004) indicates that any evolution of the most massive galaxies must be fueled by mergers of less luminous red-galaxies and not from pure passive evolution of massive star forming galaxies. While red galaxies with $L \approx L^*$ appear to grow substantially since $z \sim 1$, results from Brown et al. (2007) indicate that very luminous ($L \gtrsim 4L^*$) galaxies have grown by only 25% since $z \sim 1.0$. Similarly, Wake et al. (2006), used a combination of the SDSS and 2dF-SDSS LRG and QSO (2SLAQ) sample to measure the evolution of the massive galaxy luminosity functions to $z = 0.6$ and found that at least half of the massive early-type galaxies present at $z = 0.2$ must have been well assembled by $z \sim 0.6$. These investigations agree with a number of studies which have suggested little or no evolution in the most massive galaxy populations (Lilly et al., 1995; Lin et al., 1999; Chen et al., 2003; Bundy et al., 2006; Willmer et al., 2006; Cimatti et al., 2006).

In this paper, we present new observations of massive red galaxies at $0.7 < z < 0.9$ and augment it with samples of massive red-sequence galaxies from SDSS in order to quantify the evolution of the massive galaxy luminosity function over half of cosmic history. Our high-redshift spectroscopic survey is unaffected by possible systematic errors from photometric redshifts and covers 7 square degrees, minimizing the effects of cosmic variance due to large-scale galaxy clustering.

After describing our galaxy sample selection criteria in §5.2, we discuss the construction of our massive red galaxy luminosity functions in §5.3. In §5.4, we interpret out luminosity function measurements and examine the compos-

ite spectrum of massive red galaxies since $z \sim 0.9$ in §5.5 before closing in §5.6. All magnitudes discussed in the text are AB (Oke & Gunn, 1983). When calculating luminosities and volumes, we use the cosmological world model of $\Omega_m = 0.25, \Omega_m + \Omega_\Lambda = 1$, and $H_0 = 100\,h$ km s^{-1} Mpc^{-1} (Spergel et al., 2007). When calculating time, for example when considering the aging of stellar populations, we use $h = 0.7$. All magnitudes are corrected for dust extinction using the dust maps of Schlegel et al. (1998).

5.2   Sample Construction

5.2.1   SDSS Galaxy Sample

The Sloan Digital Sky Survey (SDSS; York et al., 2000; Adelman-McCarthy et al., 2007b) has imaged π steradians of the sky in five bands, $ugriz$, (Fukugita et al., 1996) with a dedicated 2.5m telescope located at Apache Point Observatory (Gunn et al., 2006). Imaging is performed with a CCD mosaic in drift-scan mode (Gunn et al., 1998) with an effective exposure time of 54s. After images are reduced (Lupton et al., 2001; Stoughton et al., 2002; Pier et al., 2003) and calibrated (Hogg, et al. , 2001; Smith et al., 2002; Ivezić et al., 2004; Tucker et al., 2006), objects are chosen for follow-up spectroscopy using an automated spectroscopic fiber assignment algorithm (Blanton et al., 2003b). Two galaxy samples are selected for spectroscopy from SDSS imaging. The MAIN galaxy sample (Strauss et al., 2002) is a complete, flux-limited ($r < 17.77$), sample of galaxies with an average redshift of 0.1. The Luminous Red Galaxy (LRG) sample (Eisenstein et al., 2001) selects luminous early-type galaxies out to $z \sim 0.5$ with $r < 19.5$ using several color-magnitude cuts in g, r, and i. The average redshift of the LRG sample is ~ 0.3.

In addition to its contiguous coverage of the Northern Galactic cap, the SDSS

also conducts a deep imaging survey, SDSS Southern Survey, by repeatedly imaging an area on the celestial equator in the Southern Galactic Cap. The data we utilize here includes 300 deg^2 of imaging that has been observed an average of 20 times and up to 30 times. Objects detected in each observational epoch were matched using a tolerance of 0.5 arcseconds to create the final coadded catalog. The measured photometry from each epoch were combined by converting the reported asinh magnitudes (Lupton et al., 1999) to flux and then calculating the mean value. Errors on each parameter are reported as the standard deviation of the flux measurements.

While the LRG color selection criteria identify massive red galaxies at moderate redshifts, at redshifts below $z \sim 0.2$ the LRG color selection becomes too permissive – under-luminous blue galaxies are allowed into the sample (Eisenstein et al., 2001). In order to construct a sample of galaxies at $0.1 < z < 0.2$, we thus rely on the MAIN galaxy sample; in this redshift range, the massive galaxies of interest pass the $r < 17.77$ flux limit of the MAIN sample. We utilize a simple rest-frame color-luminosity cut, $M_g < -21$ and $(g - i)_{\rm rest} > 2$ to select low-redshift galaxies on the red-sequence. These cuts result in 23,854 LRGs at $0.1 < z < 0.2$. At $0.2 < z < 0.4$, the LRG selection provides a clean sample of 46,856 massive red galaxies which we consider our intermediate redshift galaxy sample. Our low- and intermediate- redshift samples clearly have quite different selection functions in their rest-frame colors which must be considered when measuring the evolution between samples; we will address this when we present our luminosity function measurements in §5.3.

5.2.2 SDSS Photometry

As described in detail in Stoughton et al. (2002), Strauss et al. (2002), and Blanton et al. (2001), SDSS galaxy photometry is reported using two systems. Each galaxy

in SDSS is fit by two seeing-convolved models, a pure de Vaucouleurs (1948) model and a pure exponential profile. The best-fitting model in the r-band is used to determine the flux of the galaxy in each of the other bands by adjusting the normalization to the model while leaving all other parameters fixed to those derived in the r-band. Alternatively, the Petrosian magnitude is defined to be the flux within $2\theta_P$ where θ_P is defined to be the radius at which point

$$\mathcal{R}_P(\theta) \equiv \frac{\int_{0.85\theta}^{1.25\theta} d\theta' 2\pi\theta' I(\theta') \Big/ \left[\pi(1.25^2 - 0.85^2)\theta^2\right]}{\int_0^\theta dr' 2\pi\theta' I(\theta') \Big/ \left[\pi\theta^2\right]} \tag{5.1}$$

falls below 0.2. Here, $I(\theta)$ is the azimuthally averaged surface brightness profile of the galaxy. The Petrosian radius is determined in the r-band and then applied to each of the other bands. While the Petrosian flux measurement contains a constant fraction of the galaxy's light in the absence of seeing, independent of its size or distance, model magnitudes are unbiased in the absence of color gradients and provide a higher signal-to-noise ratio color measurement than Petrosian colors. As the Petrosian flux aperture is defined based on the shape of the light distribution, it doesn't require measuring the faint, low-surface brightness, isophotes of the galaxy at large radius which is quite difficult with shallow photometry. Throughout this paper, we use model magnitudes when discussing colors of galaxies and Petrosian quantities when calculating luminosities.

As has been noted by Lauer et al. (2007), SDSS photometry of very large ($r_{\mathrm{eff}} > 10$") galaxies at low redshift have large systematic differences from measured photometry in the literature. For very large galaxies, the automated photometric pipeline includes galaxy light in the estimation of the local sky background and thus underestimates the total galaxy flux. At $z > 0.1$, we expect this effect to play a minimal role and thus perform no correction to our photometry. In order to ensure that this is a valid approach, we simulate 2,000 galaxies at $0.1 < z < 0.4$

with properties of observed massive early-type galaxies. Specifically, we simulate a $M_r - 5\log h = -22.5$ galaxy with a half-light radius of $12h^{-1}$ kpc and Sersic parameter of $n = 4$. Galaxies were assigned colors assuming a passively evolving simple stellar population (SSP) that was formed in a single burst at $z = 3$. For each galaxy, we convolve the simulated postage stamp with the local seeing, apply the flat field, bias, and bad column corrections in reverse, and add it to a raw SDSS image. Each image is then reduced using the standard SDSS PHOTO pipeline. Figure 5.1 shows the result of this test. We find no significant trend with redshift of the measured flux compared to the total galaxy flux, indicating that our photometry is not biased strongly due to sky subtraction errors. The mean flux ratio found in our simulations, 80%, is quite close to that expected as the Petrosian flux systematically estimates the total flux of a galaxy with a $n = 4$ surface brightness profile to be $\sim 82\%$ of its total flux (Graham et al., 2005). Throughout this work, we use the luminosity derived from the measured Petrosian flux directly, and thus if comparisons are done to luminosity functions based on total flux measurements, care must be taken to account for this systematic effect.

While Petrosian fluxes are unbiased in the absence of seeing, as a galaxy becomes unresolved, the Petrosian flux will report a systematically smaller fraction of the galaxy light (Blanton et al., 2001). Similarly, when working near the detection limit of our imaging, one may worry that a given object only scatters above the detection threshold a fraction of the time; an average flux across many epochs can systematically overestimate the flux of such a source. At $z > 0.7$, the sizes of our sample galaxies are approaching the size of the typical SDSS seeing disk and are quite faint relative to typical SDSS applications. To ensure that photometry of these high-redshift galaxies are unbiased, we simulate 10,000 galaxies at $z > 0.7$ with $M_r - 5\log h = -21.5$ (corresponding to the faintest galaxies used in our lu-
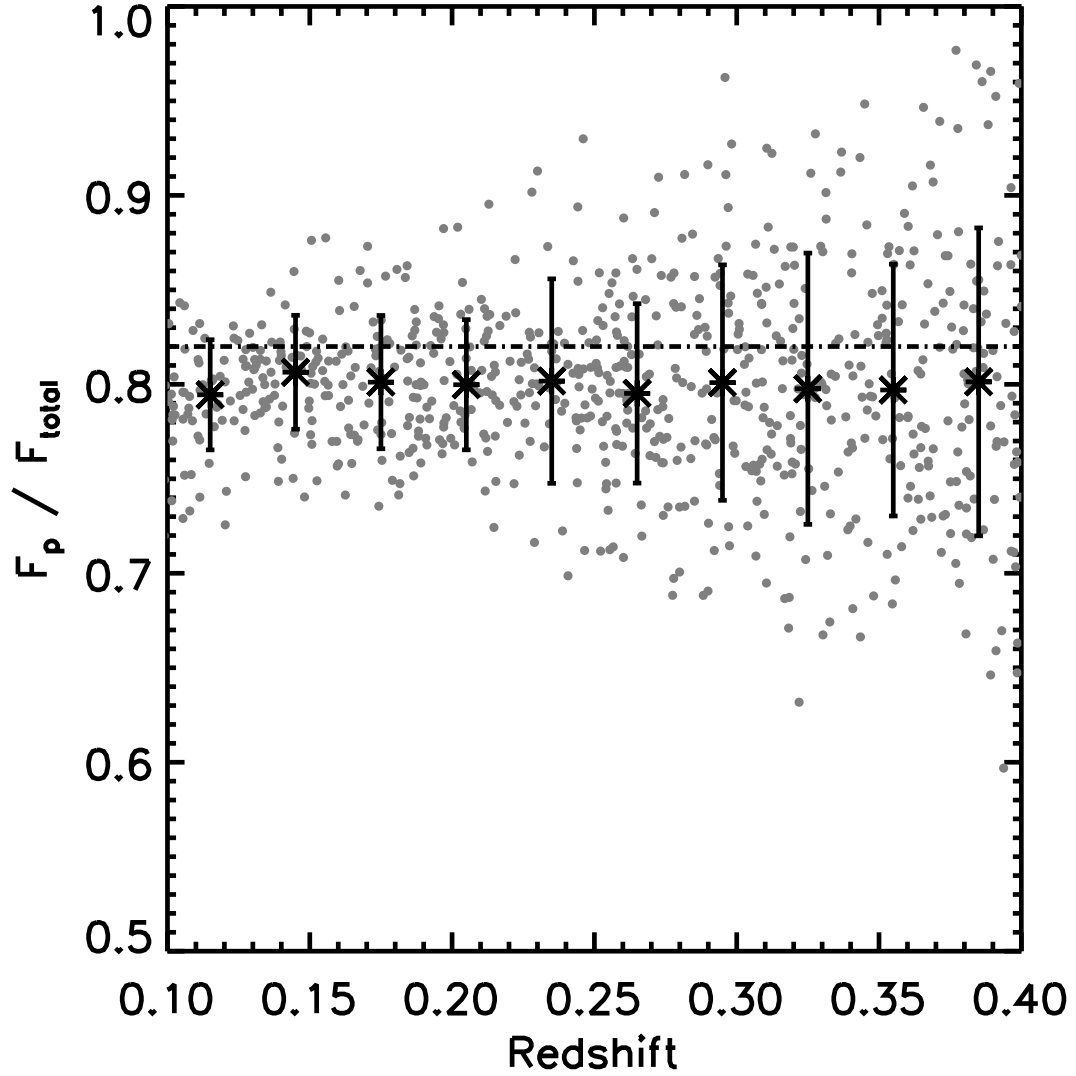
Figure 5.1 Ratio of reconstructed Petrosian flux to the total galaxy light for 2,000 simulated galaxies with $M_r - 5\log h = -22.5$, half-light radii of $12h^{-1}$kpc, and colors of a passively fading SSP formed at $z = 3$. The dark asterisks mark the mean and 1σ dispersion of the simulations while the gray points show each of the fake galaxy trials. We find no mean trend in the recovered flux with redshift and thus our galaxies are unaffected by overestimates of the local sky background which lead to underestimated galaxy fluxes for very large galaxies at low redshift.

minosity function calculations in §5.3), half-light radii of $8h^{-1}$ kpc, and colors characteristic of a passively fading SSP which formed at $z = 3$. Using an identical procedure to that described in §5.2.2, we add simulated images to raw SDSS frames and measure their photometry using PHOTO. We generate 30 realizations of the simulations with the galaxy parameters and positions held constant but allowing the Poisson noise of the fake stamp to vary between realizations. We then coadd the photometric measurements in each fake observation epoch to generate a mock coadded catalog of massive high-redshift galaxies using the same method described in §5.2.1 to generate the SDSS coadded catalog. Figure 5.2 shows the results of this test for the SDSS z-band which is the basis of our high redshift luminosity measurements. The grey points show each galaxy simulated in this experiment while the stars show the mean in bins of input total flux. The mean ratio of Petrosian flux to input total flux is consistent with the ratio of 80% measured for low-redshift simulations above and thus we do not expect our use of Petrosian quantities when measuring luminosities to bias our results to the flux limit of our survey (shown by the vertical dashed line). Below our selection limit, galaxies become unresolved and the total recovered flux begins to decline.

5.2.3 High-redshift Galaxy Sample

The 54s exposure time of SDSS imaging is not sufficient to select galaxies at $z \sim 0.9$ based on their colors. The added depth of the SDSS Southern Survey, however, allows for the selection of massive galaxies to $z \sim 1.0$. Using a similar method utilized to select LRGs at moderate redshifts from SDSS, we employ color cuts in $griz$ to isolate high-redshift LRGs for spectroscopy. In designing this selection, we capitalize on the fact that the strong 4000Å break of early-type galaxies moves through the i-band at $0.6 < z < 1$ resulting in progressively redder $i - z$ colors while the $r - i$ color shows less variation. Figure 5.3 illustrates
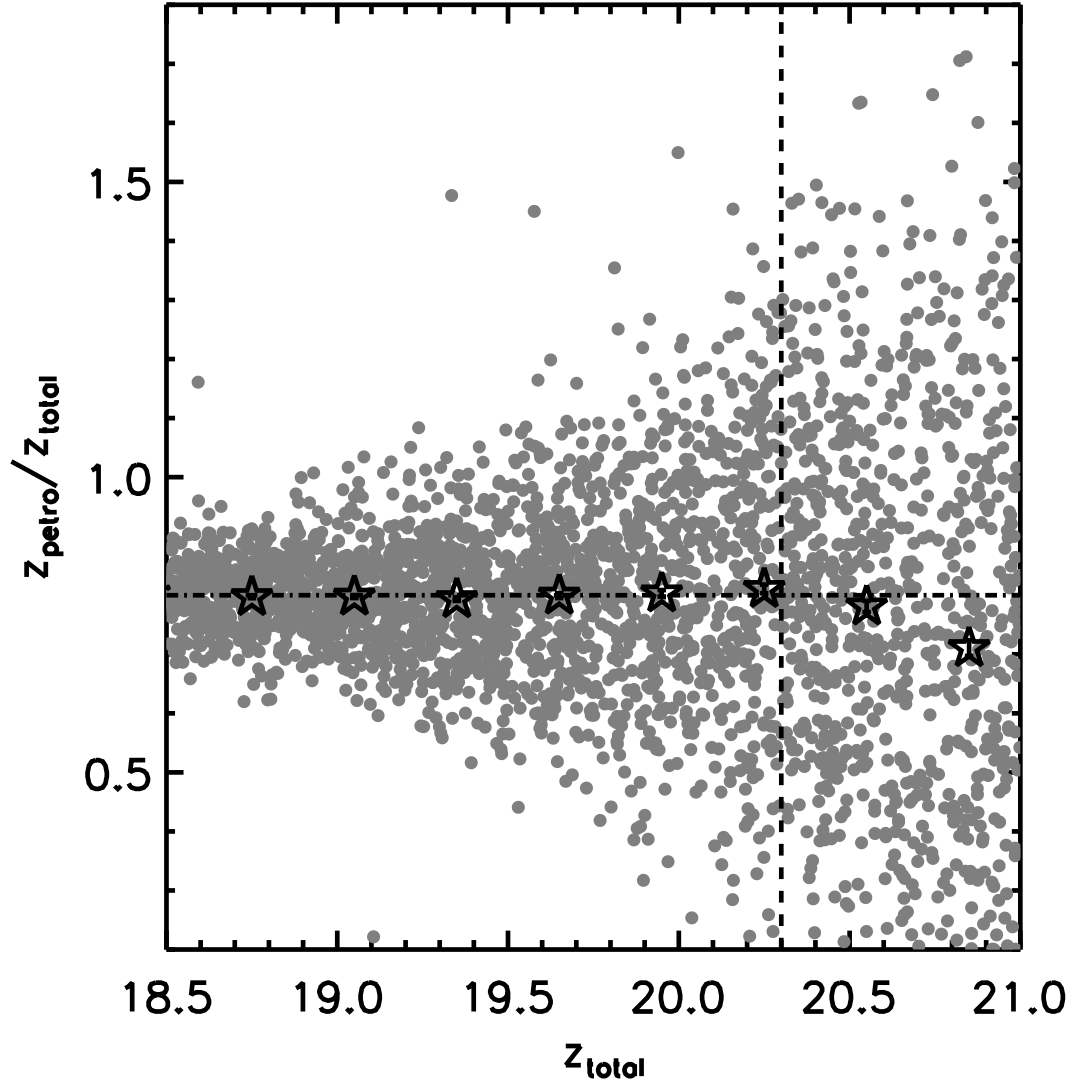
Figure 5.2 Simulation of coadded Petrosian flux measurements in high-redshift photometric data. Each grey point represents the coadded Petrosian flux from 30 realizations measured with the same method used to coadd the individual SDSS photometric epochs to generate our deep photometric catalog. The mean in bins of total flux are shown as stars. Each photometric galaxy has properties of known high-redshift massive galaxies and thus the input flux, color, and size are all correlated – the faintest galaxies in this figure are also the smallest. We find that galaxies above the z-band flux limit (vertical dashed line) are not strongly affected by the seeing disk; the g,r,and i bands follow similar trends. The horizontal dashed line shows the mean flux ratio measured for low-redshift simulations.

the expected color evolution of massive galaxies at $z > 0.5$. The gray scale shows the locus of galaxy colors from the deep SDSS imaging. The solid curves show the expected evolutionary tracks for three different star formation histories; the reddest curve in $r - i$ is a very early-type SED while the bluest track in $r - i$ is roughly an early-type spiral (e.g. an Sa) from Bruzual & Charlot (2003). Galaxies with later spectral types never get comparably red in $r - i$; for comparison, the dot-dashed track shows the color evolution of an Sc type galaxy. The open circles are separated by $\Delta z = 0.1$ with the break in the color tracks occurring at $z \sim 0.7$. Above $z \sim 0.7$, the $r - z$ color measures the distance from the turn in the color tracks and thus provides a good estimate of the photometric redshift of early-type galaxies.

We construct two regions in this color-color space to select galaxies for deep spectroscopic observations. Similarly to Eisenstein et al. (2001), we define

$$c_\perp = (r - i)_{\mathrm{model}} - (g - r)_{\mathrm{model}}/4 - 0.177. \tag{5.2}$$

We require every galaxy candidate to satisfy

$$i_{\mathrm{psf}} - i_{\mathrm{model}} > 0.2, \tag{5.3}$$

$$0.15 < c_\perp < 1.2 \tag{5.4}$$

$$0 < (r - i)_{\mathrm{model}} < 1.7 \tag{5.5}$$

$$0.3 < (i - z)_{\mathrm{model}} < 1.5 \tag{5.6}$$

$$17 < z_{\mathrm{model}} < 20.3 \tag{5.7}$$

$$1.5 < (r - z)_{\mathrm{model}} < 2.5 \tag{5.8}$$

Here, the magnitude and color subscripts mark if the magnitude was based on SDSS PSF magnitudes or MODEL magnitudes (Stoughton et al., 2002). Equation
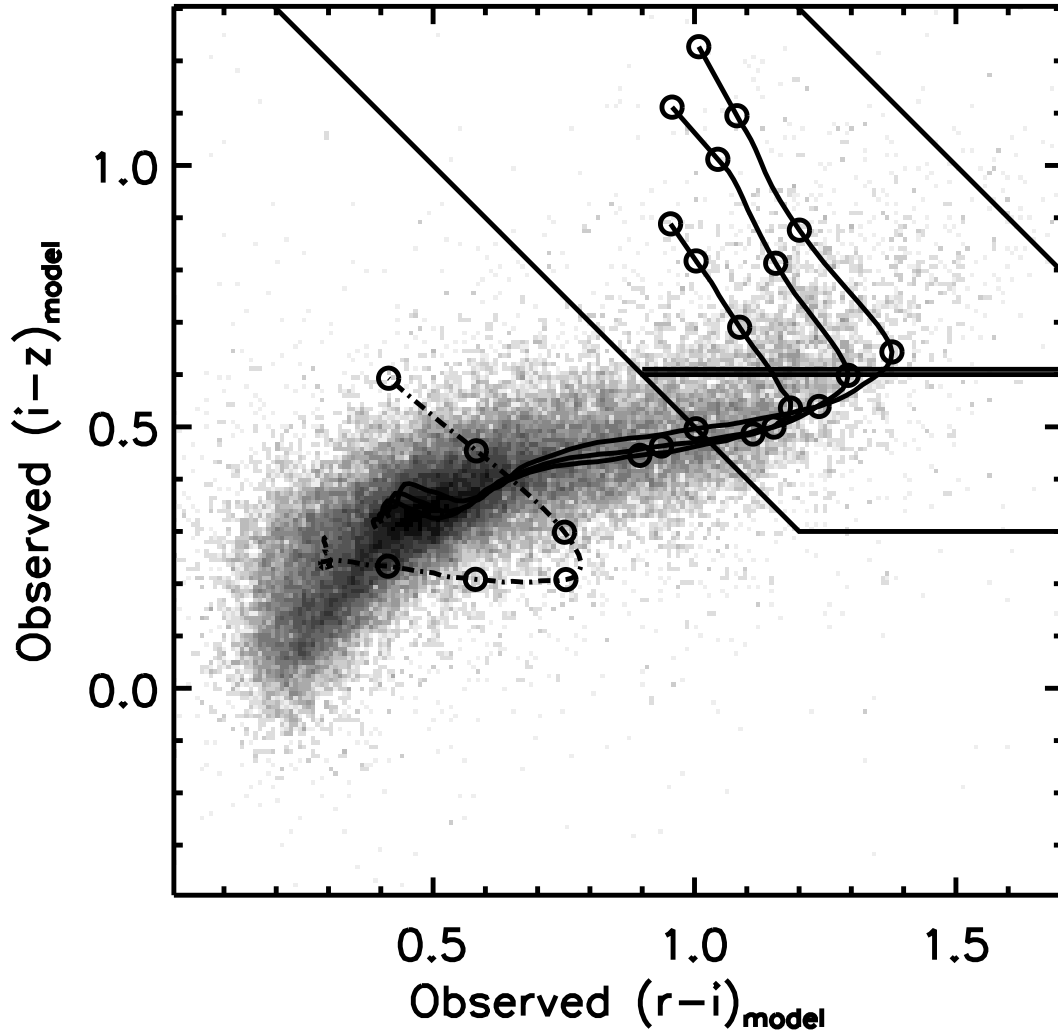
Figure 5.3 Selection of massive red galaxies at $z > 0.5$. The greyscale illustrates the observed galaxy locus for galaxies brighter than $z_{\mathrm{model}} = 20.3$ from the SDSS Southern Survey. The three solid tracks show the expected colors of passively fading galaxies from Bruzual & Charlot (2003). The reddest track in $r - i$ shows the expected colors of a very early-type galaxy and the bluest solid track shows those of an early-type disk galaxy (such as an Sa). The dot-dashed track shows the colors of an Sc type galaxy, for comparison. The tracks are marked by open circles at $\Delta z = 0.1$ intervals between redshifts of 0.5 and 1.0; the strong break in the colors occurs at $z \approx 0.7$. The boxed regions illustrate our photometric color selection. As detailed in section §5.2.3, galaxies at $i - z > 0.6$ are targeted at higher priority than galaxies with $0.3 < i - z < 0.6$ as the redder galaxies are most likely to reside at $z > 0.7$.

(5.3) limits targets to objects in which at least 20% of the flux arises outside a central point source to select only extended objects in the SDSS photometry. At $z = 0.9$, 1.2 arcseconds (the median seeing of our deep photometry) corresponds to 6.7 h^{-1} kpc, smaller than the typical luminous red galaxy, and thus we do not expect galaxies of interest to be unresolved at $0.7 < z < 0.9$. The definition of $c_\perp$ follows that of Eisenstein et al. (2001) and is designed to be parallel to the low-redshift galaxy locus in $g-r$ versus $r-i$ color-color space; Equation (5.4) removes $z < 0.45$ interlopers from the sample.

Equations (5.4) - (5.8) limit our sample to red galaxies at $0.5 < z < 1.0$ and the flux limit imposed by Equation (5.7) isolates only the most luminous galaxies in this redshift range. We divide our selection into two groups based on their $i - z$ color. Galaxies with $i - z > 0.6$ are given higher priority than galaxies with $0.3 < i - z < 0.6$ as the redder subset of galaxies are more likely to lie at $z > 0.7$ as shown in Figure 5.3. Based on early observations and data simulations, we found that our redshift success would degrade at fluxes fainter than $z_{\mathrm{model}} = 20$. In order to maximize the number of high-quality redshifts obtained, we targeted galaxies at $z_{\mathrm{model}} < 20$ at a higher priority than galaxies with $20 < z_{\mathrm{model}} < 20.3$. After target selection, fibers were allocated to 20% of the available galaxy candidates in the field.

If there are unresolved galaxies that were untargetted with our algorithm, we can quantify this sample bias by comparing the galaxy angular correlation function to the star-galaxy cross correlation function from our targeting data. As the locations of distant galaxies are uncorrelated with Galactic stars, the presence of unresolved galaxies in our star sample will result in an apparent signal in the star-galaxy cross-correlation function due to the correlated galaxy interlopers in the sample. We construct a sample of stars which meet identical selection criteria
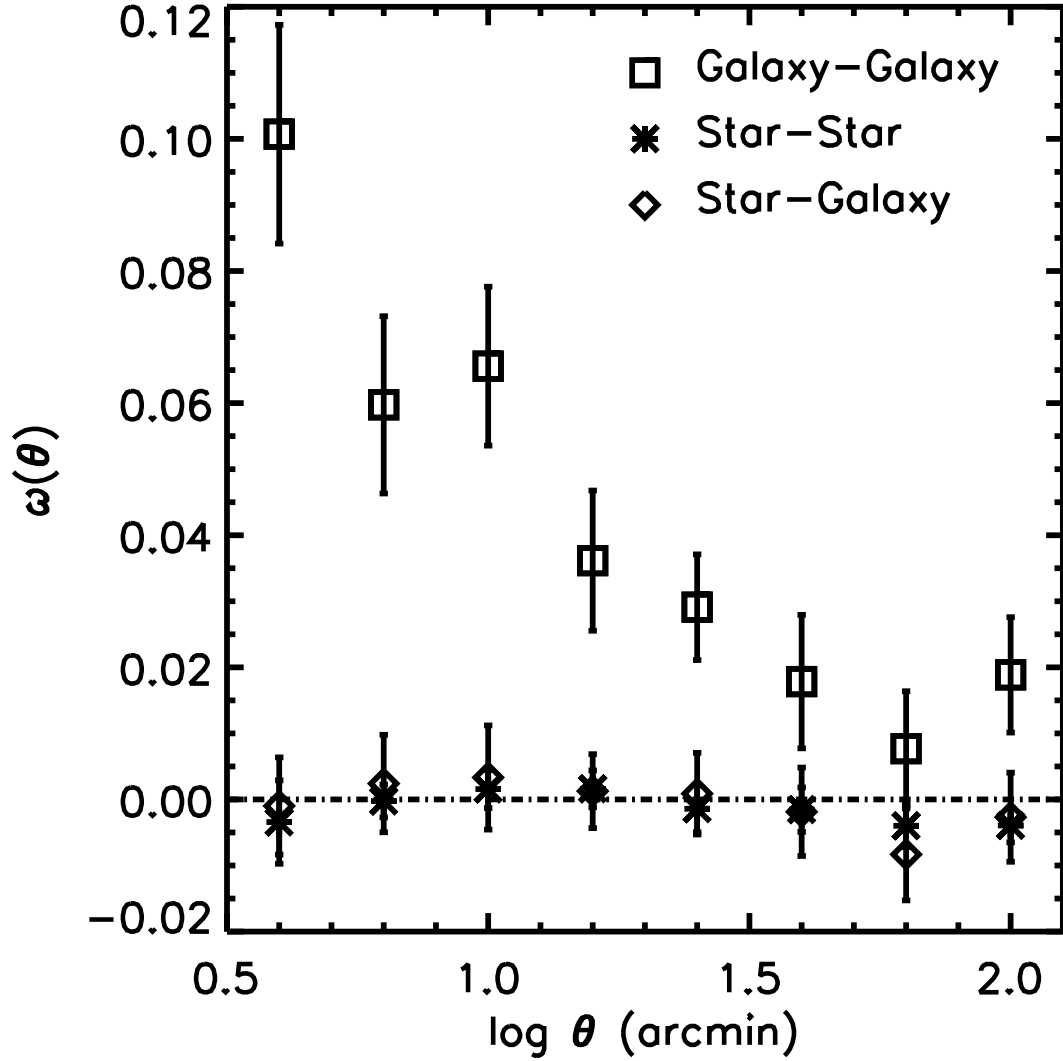
Figure 5.4 Angular correlation functions for stars and galaxies selected with our high-redshift galaxy color criteria. The galaxy-galaxy correlation function (squares) shows strong clustering on all scales while both the star-star auto-correlation function (asterisks) and star-galaxy cross-correlation function (diamonds) show very little clustering signal on several arcminute scales. If many galaxies were lost from our sample due to being unresolved by our star-galaxy separation, the star-galaxy cross correlation function would mirror that of the galaxy-galaxy auto-correlation function. Thus, the lack of signal at small separations in the star-galaxy cross correlation function indicates we lose, at most, 2% of our galaxy targets due to our star-galaxy separation errors.

used to select galaxies with the exception of Equation (5.3). After masking out 2′ regions around bright ($r < 12$) stars, we count the number of galaxy-galaxy, star-galaxy, and star-star pairs as a function of separation compared to the expected number of pairs derived from a mock catalog of objects over the same area and subject to the same bright star mask. Our spectroscopic observations directly probe the contamination by stars in our galaxy sample; we use this known contamination rate to correct for the dilution of the galaxy-galaxy auto-correlation function arising from the addition of an uncorrelated stellar sample and create the average correlation function shown in Figure 5.4. As expected, the star-star auto-correlation function (asterisks) shows little power on several arcminute scales whereas the galaxy-galaxy auto-correlation (squares) function shows significant clustering. The lack of strong signal in the star-galaxy cross-correlation function implies only a small fraction of galaxies can be lost to the star sample. Based on our measurements, we find that a maximum of 3% of the star sample can be contributed by interloper galaxies at 99% confidence. As the average number density of stars in our fields is about 40% larger than galaxy targets, we find that we lose, at most, 2% of our galaxy targets due to our star-galaxy separation.

5.2.4 MMT Spectroscopy Observations and Data Processing

We observed selected galaxies using Hectospec (Fabricant et al., 1998, 2005; Roll et al., 1998), a 300-fiber spectrograph on the 6.5m MMT telescope between Mar 2004 and Oct 2005. Hectospec offers a 1 deg^2 field of view and covers from 4000-9000 Å with 6Å resolution. Observations were completed using seven pointings with Hectospec. For each field, approximately half of the fibers were used to target high-redshift massive red galaxy candidates and half were used to measure the faint quasar luminosity function (Jiang et al., 2006). Exposure times varied due to conditions, but each field was observed for an average of 3 hours.

All Hectospec data were reduced using the HSRED [1] package which is based upon the SDSS spectroscopic pipeline. Data were flat-fielded using observations of an illuminated screen in the dome to remove pixel-to-pixel sensitivity variations as well as to correct for the strong fringing in the Hectospec CCDs in the red. When possible, spectra of the twilight sky were taken to provide a secondary correction to account for any low-order residuals between fibers after the flat field derived from the dome flat corrections were applied. Wavelength solutions were obtained each night using observations of HeNeAr calibration lamps and the location of strong emission lines in the spectrum of the night sky were used to correct for any drift in the wavelength solution between the observations of the calibration frames and the data frames.

Observations of each field included approximately 30 sky fibers which we used to construct the master sky spectrum from each exposure and subtract that from each object spectrum. Additionally, 3-5 photometrically selected F stars were targeted in each field. The extracted spectra of these stars are compared to a grid of Kurucz (1993) model atmospheres to determine the spectral type of each star. Once we have determined the spectral type of each F star, we measure the average ratio between the observed spectra and the model prediction to determine the global calibration to convert counts $pixel^{-1}$ to ergs s^{-1} cm^{-2} Å^{-1}. Figure 5.5 shows three fully-processed spectra from this survey.

To determine the redshift of each object we compare the observed spectra with stellar, galaxy, and quasar template spectra and choose the template and redshift which minimizes the χ^2 between model and data. As many of our spectra have low signal-to-noise ratios, every spectrum is examined by eye to ensure that the fitted redshift was correct. In cases in which the automated routine failed to con-

---

[1]http://mizar.as.arizona.edu/hsred/index.html
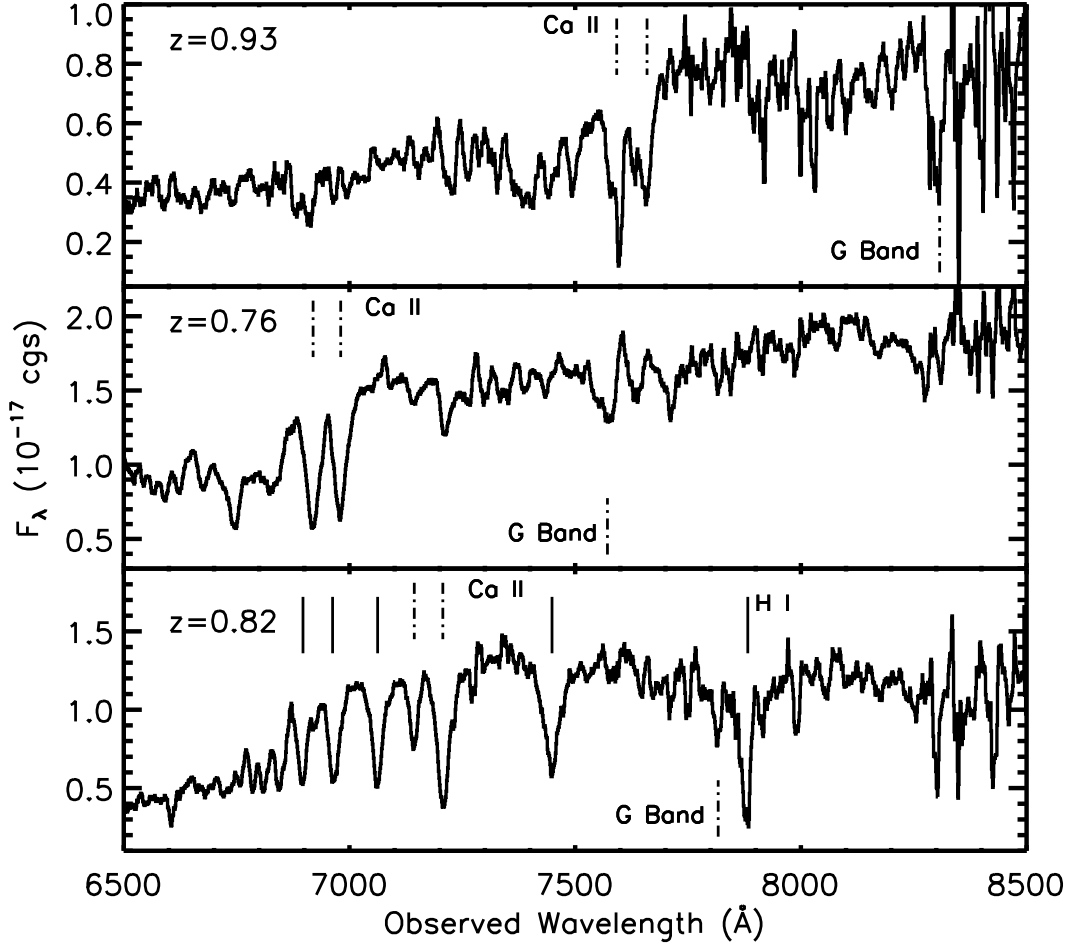
Figure 5.5 Example of MMT spectra of high-redshift galaxies. Each spectrum has been smoothed by 2 resolution elements for display; the spectra each have resolution of 6Å. In each panel, vertical lines highlight prominent spectral features to guide the eye. The top panel shows a $z = 0.92$ galaxy with moderate signal-to-noise. The strong Ca II H+K absorptions lines and G-band at 4300Å allow for accurate redshift determination even at low signal-to-noise ratio. The middle panel shows a high signal-to-noise ratio $z = 0.76$ spectrum and the bottom panels shows a $z = 0.82$ galaxy with strong Balmer absorption features characteristic of 1 Gyr populations. The spectral range plotted was chosen to highlight the key features of our spectra; Hectospec observes considerably further into the blue but those data are generally of quite low signal-to-noise for the high-redshift galaxies studied here.

verge to the correct redshift, a hand-measured redshift is used in its place. Our spectroscopy resulted in redshifts for 470 galaxies at $0.6 < z < 1.0$ over 7 deg^2 and 302 galaxies at $0.7 < z < 0.9$ which will be used in our analysis, here. Figure 5.6 shows the color distribution of the confirmed galaxies at $0.7 < z < 0.9$ which are used for our luminosity function calculations at high redshift. Of the 890 galaxy candidates that were targeted for spectroscopy, 12% of the spectra did not result in a redshift measurement.

5.3 Luminosity Function Construction

5.3.1 Calculation of Rest-frame Luminosities

In order to compare the populations of massive red galaxies as a function of redshift, we first need to transform the observed photometry to the rest-frame of each galaxy to remove the effects of redshift on the observed properties. A number of approaches have been developed to perform k-corrections to the rest-frame system; each approach has its advantages and drawbacks. In order to minimize errors introduced due to errors in the stellar synthesis models used to calculate our k-corrections, we consider the rest-frame properties of our galaxies through a modified SDSS filter set. This system, denoted $^{0.3}u^{0.3}g^{0.3}r^{0.3}i^{0.3}z$, consists of the SDSS $ugriz$ filters which have been blueshifted by a redshift of 0.3 similar to the approach used in Blanton et al. (2003) and Wake et al. (2006). In this system, a galaxy at a $z = 0.3$ will have a k-correction that is independent of its spectral energy distribution and will equal $-2.5\log_{10}(1 + 0.3)$. We choose a shift of 0.3 to draw upon the fact that at $z \sim 0.8$ (near the median redshift of our high-redshift galaxy sample), the observed z-band probes a similar portion of the spectrum as probed by the r-band observing a $z = 0.3$ galaxy. In the following sections, we will measure the $M_{0.3_r}$ luminosity function of massive galaxies; for comparison,
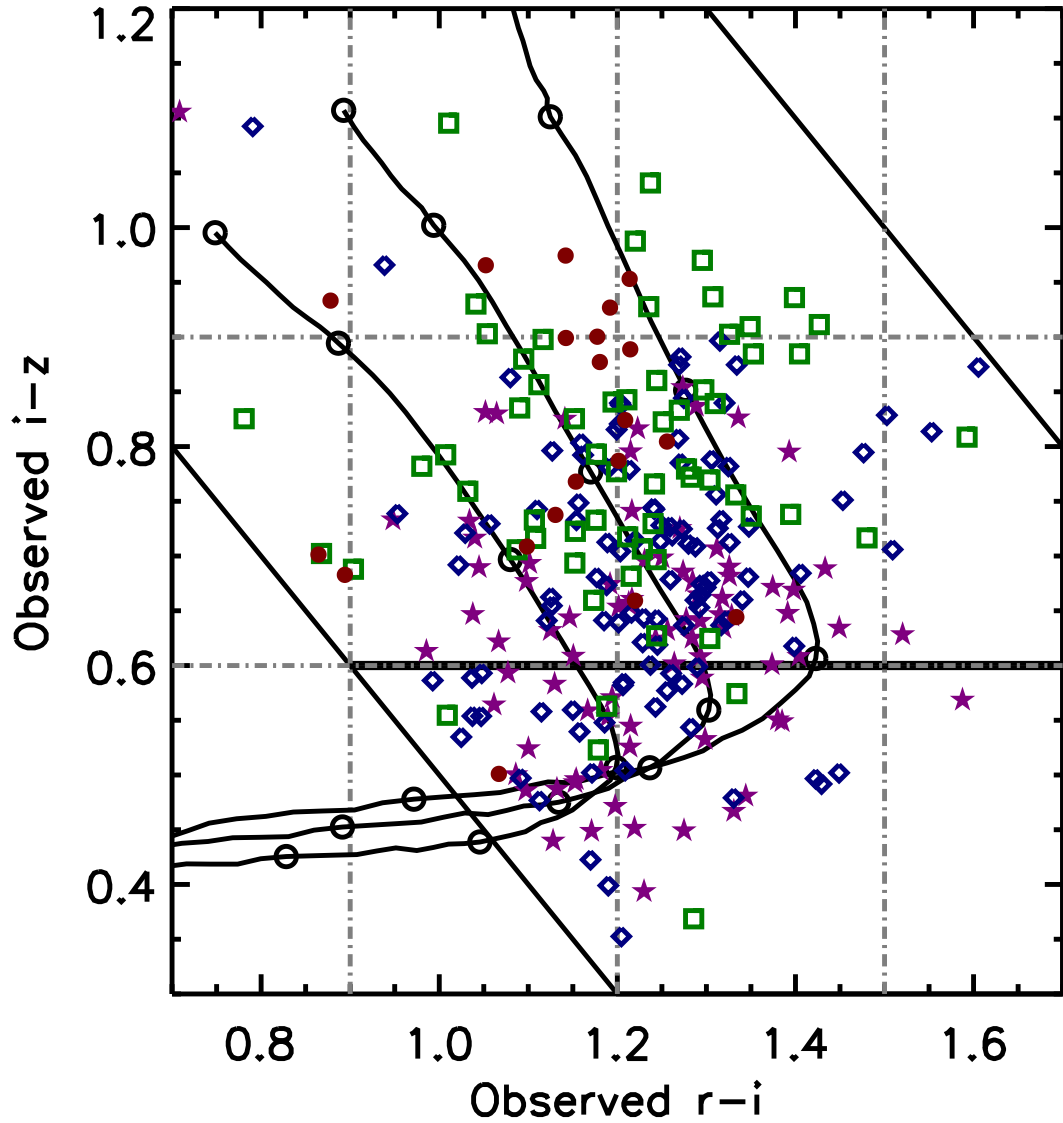
Figure 5.6 Colors of confirmed galaxies at $0.7 < z < 0.9$ from our MMT spectroscopy. The early-type galaxy color tracks and color selection criteria are as shown in Figure 5.3. The colored points show the location of each of our sample galaxies in this color space; the shape (color) of each point denotes its redshift. Stars (magenta) show $0.70 < z < 0.75$ galaxies, diamonds (blue) mark $0.75 < z < 0.80$ objects, and the squares (green) and filled circles (red) illustrate $0.80 < z < 0.85$ and $0.85 < z < 0.90$ galaxies respectively. The grey dot-dashed lines show the sub-regions of color-color space used to measure the fraction of spectroscopically observed galaxies which were excluded when evolved to our lower-redshift bins. We use this correction factor when bootstrapping to our full photometric sample as described in §5.3.2.

$B - ^{0.3}r \approx -0.01$ for an old stellar population. Based on luminosity function fits from Brown et al. (2007), $M^*_{0.3_r} - 5\log h = -20.3$ and thus our sample focuses on galaxies with $L > 3L^*$. For reference, a $3L^*$ SSP at $z = 0.3$ which formed its stars at $z = 3$ has an approximate stellar mass of $3 \times 10^{11} M_\odot$.

To construct the k-corrections for galaxies in each of our samples, we create a grid of evolving and non-evolving SSP at solar metallicity with formation redshifts ranging from 1 to 10 from Bruzual & Charlot (2003) based on a Salpeter (1955) initial mass function (IMF). We find that this set of models adequately span the range of observed colors for all of our galaxies. Each galaxy is assigned a template based on a maximum likelihood comparison of the predicted colors and observed SDSS photometry.

While the k-corrections based on non-evolving models assume that the underlying stellar population remains unchanged from the observed epoch, our $k + e$ corrections include the passive evolution, normalized to $z = 0.3$, of the stellar populations in the galaxies between the observed epoch and the rest-frame redshift. For each galaxy, we use the best fitting SSP to predict the SED the galaxy would have at $z = 0.3$; a galaxy fit by a SSP with age τ will age into a SSP with age $\tau + \Delta\tau(z_0)$ where $\Delta\tau(z_0)$ is the lookback time difference between $z = 0.3$ and z_0, the observed redshift of the galaxy. We include both types of models in order to compare the affects of passive evolution on the inferred evolution of the luminosity function of massive galaxies since $z \sim 0.9$.

5.3.2 Luminosity Functions

Luminosity functions are calculated using the standard $1/V_{\max}$ method (Schmidt, 1968). For each galaxy, we calculate the redshifts at which the galaxy would have been selected and observed in our survey. In this calculation, we utilize the best-fit template chosen when calculating k-corrections, as described above, to esti-

mate each galaxy's colors as a function of redshift. Based on these predicted colors, we assign a probability (0 or 1) that a given galaxy would have been selected at each redshift. The maximum available volume is then the integral over the redshift range weighted by the selection probability at each redshift.

Each sample is corrected independently for the spectroscopic completeness of the observations. The low-redshift SDSS MAIN and intermediate-redshift SDSS LRG galaxies were corrected to account for the spatially-dependent incompleteness of SDSS spectroscopy. As we have several priority classes in our high-redshift target selection, we must correct our sample with more detail than merely the fraction of the galaxies that received fibers. Instead, we break our sample into four regions in color-magnitude space and calculate the completeness in each region independently. As described in §2.2, galaxies were given priority based both on their $i - z$ color and z_{model} flux. This results in four color-magnitude regions in which we then calculate the photometric completeness by counting the number of photometrically selected galaxies which were given a fiber compared to the number of galaxies in the parent catalog in that color and magnitude bin. Our completeness correction was calculated independently for each of our seven Hectospec fields. In each field, we compare the number of spectroscopically observed objects to the total number of photometric objects within a 2 deg^2 square box around the field center when calculating our incompleteness. In doing this, we bootstrap our spectroscopic sample to 9000 photometrically selected galaxies over twice the area observed with Hectospec, thus minimizing the effects of cosmic variance on our sample. The inclusion of this photometric sample doesn't change the normalization of the high-redshift luminosity function we measure, but results in smaller errors due to field-to-field variations in the galaxy number counts.
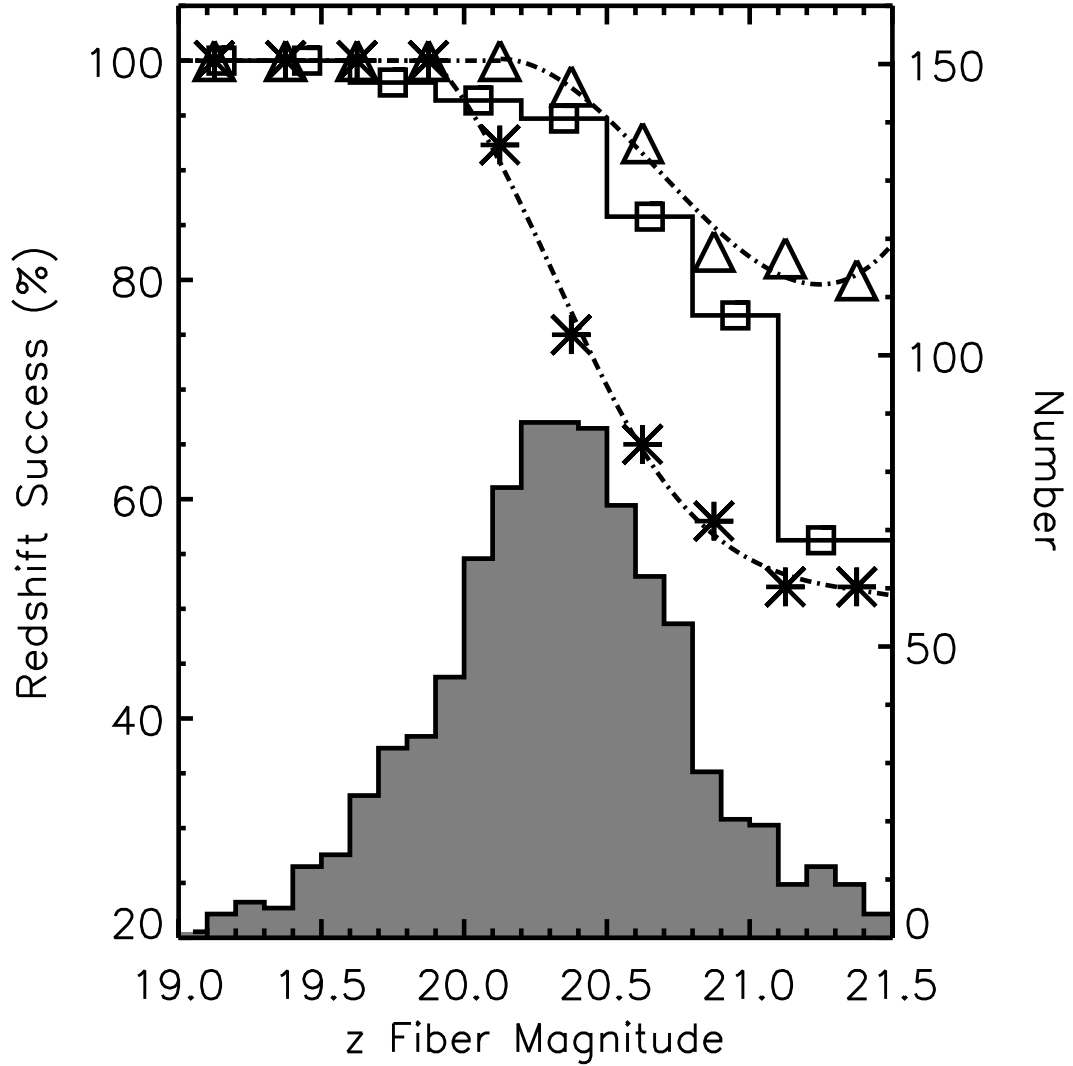
Figure 5.7 Redshift success versus the z-band flux in a 1.5 arcsecond aperture for two of our targeted fields. The triangles show a high quality mask observed under photometric conditions and excellent ($\approx 0.5''$) seeing. The asterisks show a poor-quality mask affected by clouds and poor seeing leading to degraded success at the faintest fluxes. We correct for this incompleteness in each of our Hectospec fields before computing the luminosity function using low-order fits as show by the dot-dashed lines. The grey histogram illustrates the distribution of fiber magnitudes for all of our spectroscopic targets. The sharp decline in objects at $z_{\mathrm{fiber}} = 20.8$ corresponds to our sparser sampling of objects with $z_{\mathrm{model}} > 20$. The squares mark the redshift completeness of our full spectroscopic sample.

Signal-to-noise ratio variations in our high-redshift galaxy spectroscopy result in approximately 12% of our observed objects with no measurable redshift. In order to correct for this effect, we measure the fraction of observed galaxies with viable redshifts as a function of the z-band flux within an 1.5 arcsecond aperture centered on our fiber location to estimate the flux available to the spectroscopic fiber. We then fit this relationship with a low-order polynomial for each Hectospec field and apply the derived correction before calculating the the final luminosity function. Figure 5.7 shows an example of this technique on two different fields spanning the full range of data quality. The triangle symbols show the completeness for a field with high signal-to-noise observed under photometric conditions and superb seeing ($\approx 0\rlap{.}''5$) while the asterisks show a field observed under less photometric conditions. The range in data quality leads to significant completeness variations between each of our spectroscopically observed fields; neglecting this would bias our final inferred luminosity function. The square symbols in the figure show the composite completeness for the full galaxy sample as a function of fiber magnitude.

We make a further correction to ensure that the galaxies utilized in the construction of the luminosity function in each redshift bin probe a homogeneous population of objects. Using the best-fit stellar population template derived when calculating the $k + e$-corrections, we estimate the colors of each galaxy as a function of redshift from $z = 0.1$ to $z = 0.9$. We then require that every galaxy included in our calculation of the luminosity function would have been selected in each of our redshift samples thus ensuring that the population of galaxies we consider at $0.1 < z < 0.2$ are consistent with galaxies at $0.7 < z < 0.9$ after the passive evolution of their stellar populations has been included. When bootstrapping to the entire photometric sample of galaxies at high redshift, we grid

the $r - i$ versus $i - z$ color-color plane into 12 subsections as shown in Figure 5.6 and calculate the fraction of galaxies in each subregion that would be excluded based on this criterion. The size of these sub regions was chosen to sample both the $i - z < 0.6$ and the $i - z > 0.6$ subsamples with similar detail. The final results are not strongly dependent on the exact subregions chosen for this correction.

When target selection is based on noisy photometry, the effects of photometric scattering of objects into or out of the nominal color- and flux-limits can be quite significant (Wake et al., 2006). As our high-redshift sample of galaxies is selected from SDSS stacked photometry, we perform an empirical test of this photometric scattering on our sample. Using the full sample of SDSS main galaxies observed at $0.1 < z < 0.2$ we create a mock sample of $0.7 < z < 0.9$ galaxies based on the best-fit $k + e$-corrections described in §5.3.1. We then subject this mock galaxy sample to representative photometric errors present in our coadded photometric catalog and determine the fraction of mock galaxies that would have been selected in the presence of photometric errors. For galaxies brighter than $z = 20$, we find that $\sim 2\%$ of selected galaxies have colors that would fall outside our color-cuts but scatter into the sample when photometric errors are included. At fainter magnitudes, $20 < z < 20.3$, approximately 10% of the galaxies included in the mock high-redshift galaxy sample have scattered above the survey flux-limit due to photometric errors. When calculating our high-redshift luminosity functions, we include these contamination rates as a statistical weight assigned to each galaxy based on its observed z-band flux.

In order to estimate the error on our high-redshift luminosity function measurements, we remove each of our spectroscopic fields (and ancillary photometric data), in turn, from our calculation of the ensemble luminosity function and repeat our calculations; we use the measured variation in the luminosity functions

created with this test as an estimate of the large scale structure error on our luminosity function measurements. Similarly, for our SDSS samples, we divide the SDSS survey area into 20 subregions and perform the same experiment. These jack-knife errors are $\sim 25\%$ larger than those based on Poisson errors alone in the lowest-luminosity bins and are comparable to those estimated from counting statistics at the bright end. While subsampling can result in an underestimate of the error if a single large scale feature is present in multiple subfields, the large area surveyed by SDSS at low redshift and the several degree separation between our spectroscopic fields at high-redshift minimize this effect and thus jack-knife errors are a robust estimate of the cosmic variance errors for our samples. Throughout this paper, we utilize the larger of the two errors when doing calculations with our measured luminosity functions.

Table 5.1.   Luminous Red Galaxy Luminosity Functions With No Evolutionary

Correction

$M_{0.3_r} - 5\log h$	$\log_{10}$ Galaxy Number Density[a]			$M_{0.3_r} - 5\log h$	$\log_{10}$ Galaxy Number Density[a]
	$0.1 < z < 0.2$	$0.2 < z < 0.3$	$0.3 < z < 0.4$		$0.7 < z < 0.9$
(1)	(2)	(3)	(4)	(5)	(6)
-21.55	-3.66 ± 0.01	-3.64 ± 0.03	-3.78 ± 0.05	-21.59	-3.26 ± 0.08
-21.65	-3.75 ± 0.01	-3.56 ± 0.07	-3.66 ± 0.04	-21.77	-3.30 ± 0.07
-21.75	-3.89 ± 0.01	-3.85 ± 0.01	-3.64 ± 0.04	-21.95	-3.44 ± 0.06
-21.85	-4.04 ± 0.02	-3.92 ± 0.04	-3.73 ± 0.03	-22.13	-3.53 ± 0.06
-21.95	-4.21 ± 0.02	-4.06 ± 0.03	-3.87 ± 0.02	-22.31	-3.89 ± 0.09
-22.05	-4.38 ± 0.03	-4.25 ± 0.01	-4.02 ± 0.02	-22.49	-4.28 ± 0.13
-22.15	-4.53 ± 0.04	-4.41 ± 0.02	-4.18 ± 0.01	-22.67	-4.64 ± 0.24
-22.25	-4.79 ± 0.04	-4.57 ± 0.02	-4.34 ± 0.02	-22.85	-5.40 ± 0.43
-22.35	-4.94 ± 0.05	-4.77 ± 0.02	-4.63 ± 0.01	$\cdots$	$\cdots$
-22.45	-5.15 ± 0.06	-4.97 ± 0.03	-4.83 ± 0.01	$\cdots$	$\cdots$

<div align="center">Table 5.1—Continued</div>

$M_{0.3_r} - 5\log h$	log$_{10}$ Galaxy Number Density[a]			$M_{0.3_r} - 5\log h$	log$_{10}$ Galaxy Number Density[a]
	$0.1 < z < 0.2$	$0.2 < z < 0.3$	$0.3 < z < 0.4$		$0.7 < z < 0.9$
(1)	(2)	(3)	(4)	(5)	(6)
-22.55	-5.36 ± 0.08	-5.16 ± 0.04	-5.01 ± 0.02	$\cdots$	$\cdots$
-22.65	-5.65 ± 0.12	-5.38 ± 0.05	-5.19 ± 0.02	$\cdots$	$\cdots$
-22.75	-5.74 ± 0.13	-5.78 ± 0.07	-5.41 ± 0.03	$\cdots$	$\cdots$
-22.85	-6.18 ± 0.22	-5.88 ± 0.08	-5.68 ± 0.03	$\cdots$	$\cdots$
-22.95	-6.13 ± 0.22	-5.99 ± 0.09	-5.88 ± 0.04	$\cdots$	$\cdots$

[a]All number densities are expressed in units of h^3 Mpc^{-3} Mag^{-1}

Table 5.2.   Luminous Red Galaxy Luminosity Functions After Passive

Evolution Correction

| $M_{0.3r} - 5 \log h$ | $\log_{10}$ Galaxy Number Density[a] | | | $M_{0.3r} - 5 \log h$ | $\log_{10}$ Galaxy Number Density[a] |
| | $0.1 < z < 0.2$ | $0.2 < z < 0.3$ | $0.3 < z < 0.4$ | | $0.7 < z < 0.9$ |
(1)	(2)	(3)	(4)	(5)	(6)
-21.55	-3.52 ± 0.01	-3.64 ± 0.07	-3.71 ± 0.04	-21.59	-3.48 ± 0.06
-21.65	-3.56 ± 0.01	-3.60 ± 0.02	-3.62 ± 0.04	-21.77	-3.68 ± 0.07
-21.75	-3.66 ± 0.01	-3.60 ± 0.03	-3.66 ± 0.04	-21.95	-3.96 ± 0.11
-21.85	-3.74 ± 0.01	-3.72 ± 0.02	-3.81 ± 0.02	-22.13	-4.25 ± 0.12
-21.95	-3.90 ± 0.01	-3.90 ± 0.01	-3.94 ± 0.02	-22.31	-4.55 ± 0.16
-22.05	-4.05 ± 0.02	-4.05 ± 0.01	-4.12 ± 0.01	-22.49	-4.79 ± 0.22
-22.15	-4.21 ± 0.02	-4.21 ± 0.01	-4.24 ± 0.02	-22.67	-5.41 ± 0.43
-22.25	-4.40 ± 0.03	-4.37 ± 0.02	-4.45 ± 0.01	-22.85	-5.40 ± 0.43
-22.35	-4.57 ± 0.03	-4.57 ± 0.02	-4.61 ± 0.02	$\cdots$	$\cdots$
-22.45	-4.75 ± 0.05	-4.74 ± 0.03	-4.81 ± 0.02	$\cdots$	$\cdots$

Figure 5.8 and Table 5.1 show the non-evolving luminosity function measured from our samples. The symbol (color) denotes the redshift bin : diamonds (black) $0.1 < z < 0.2$, asterisks (magenta) $0.2 < z < 0.3$, squares (green) $0.3 < z < 0.4$, and circles (red) $0.7 < z < 0.9$. The figure shows a clear separation between each luminosity function with higher-redshift galaxies having higher luminosities (or larger number density). This characteristic behavior is expected due to the passive fading of the stellar populations in these massive red galaxies. We must remove this effect in order to understand any true changes in the underlying population of massive galaxies since $z \sim 0.9$. The turnover at low-luminosities is an artifact of the color-selection of these galaxies. As shown in Eisenstein et al. (2001), the LRG sample selection results in a diagonal cut across the red-sequence at low luminosities which is being reflected here as the turn over at low-luminosities in our luminosity function. This should not be interpreted as a characteristic luminosity of the sample. The luminosity functions of galaxies in our survey are shown in Figure 5.9 and recorded in Table 5.2 after the effects of evolution are included. After the effects of passive evolution are accounted for, the luminosity functions show little variation between redshift bins. The integrated luminosity densities for both the evolutionary-corrected and k-corrected luminosity functions are listed in Table 5.3. Analysis of these luminosity functions is the focus of §5.4.

5.4   Luminosity Function Analysis

5.4.1   Evolution in the Massive Galaxy Population Since $z \sim 0.9$

The agreement between the luminosity function measurements at $0.1 < z < 0.9$ as illustrated in Figure 5.9 indicates that the massive galaxy population has evolved little since $z \sim 0.9$. In order to quantify this evolution, we have adopted a similar

Table 5.2—Continued

| $M_{0.3_r} - 5\log h$ | log$_{10}$ Galaxy Number Density[a] | | | $M_{0.3_r} - 5\log h$ | log$_{10}$ Galaxy Number Density[a] |
| | $0.1 < z < 0.2$ | $0.2 < z < 0.3$ | $0.3 < z < 0.4$ | | $0.7 < z < 0.9$ |
(1)	(2)	(3)	(4)	(5)	(6)
-22.55	-5.06 ± 0.06	-4.92 ± 0.03	-4.97 ± 0.03	$\cdots$	$\cdots$
-22.65	-5.23 ± 0.07	-5.12 ± 0.04	-5.17 ± 0.03	$\cdots$	$\cdots$
-22.75	-5.33 ± 0.08	-5.50 ± 0.06	-5.42 ± 0.04	$\cdots$	$\cdots$
-22.85	-5.73 ± 0.13	-5.70 ± 0.08	-5.82 ± 0.07	$\cdots$	$\cdots$
-22.95	-5.89 ± 0.15	-5.85 ± 0.09	-5.96 ± 0.08	$\cdots$	$\cdots$

[a]All number densities are expressed in units of h^3 Mpc^{-3} Mag^{-1}

Table 5.3.   Integrated Luminosity Density

| | $j(M_{0.3r} < -21.50)$[a] | | $j(M_{0.3r} < -22.25)$[a] | |
| Redshift | k[b] | $k + e$[c] | k[b] | $k + e$[c] |
(1)	(2)	(3)	(4)	(5)
0.15	2.63 ± 0.04	5.45 ± 0.06	0.24 ± 0.02	0.54 ± 0.03
0.25	3.54 ± 0.06	5.22 ± 0.09	0.33 ± 0.01	0.54 ± 0.02
0.35	5.18 ± 0.11	4.58 ± 0.09	0.50 ± 0.01	0.48 ± 0.01
0.80	34.32 ± 10.00	5.47 ± 1.00	2.46 ± 0.62	0.71 ± 0.29

[a] Luminosity densities in units of $10^6 h^3 \, L_\odot \, \mathrm{Mpc}^{-3}$

[b] Integrated luminosity densities based on luminosity functions derived without correcting for the passive fading of stellar populations

[c] Integrated luminosity densities based on luminosity functions calculated after correcting for stellar evolution based on Bruzual & Charlot (2003) stellar population synthesis models and a Salpeter IMF as discussed in §5.3.2.
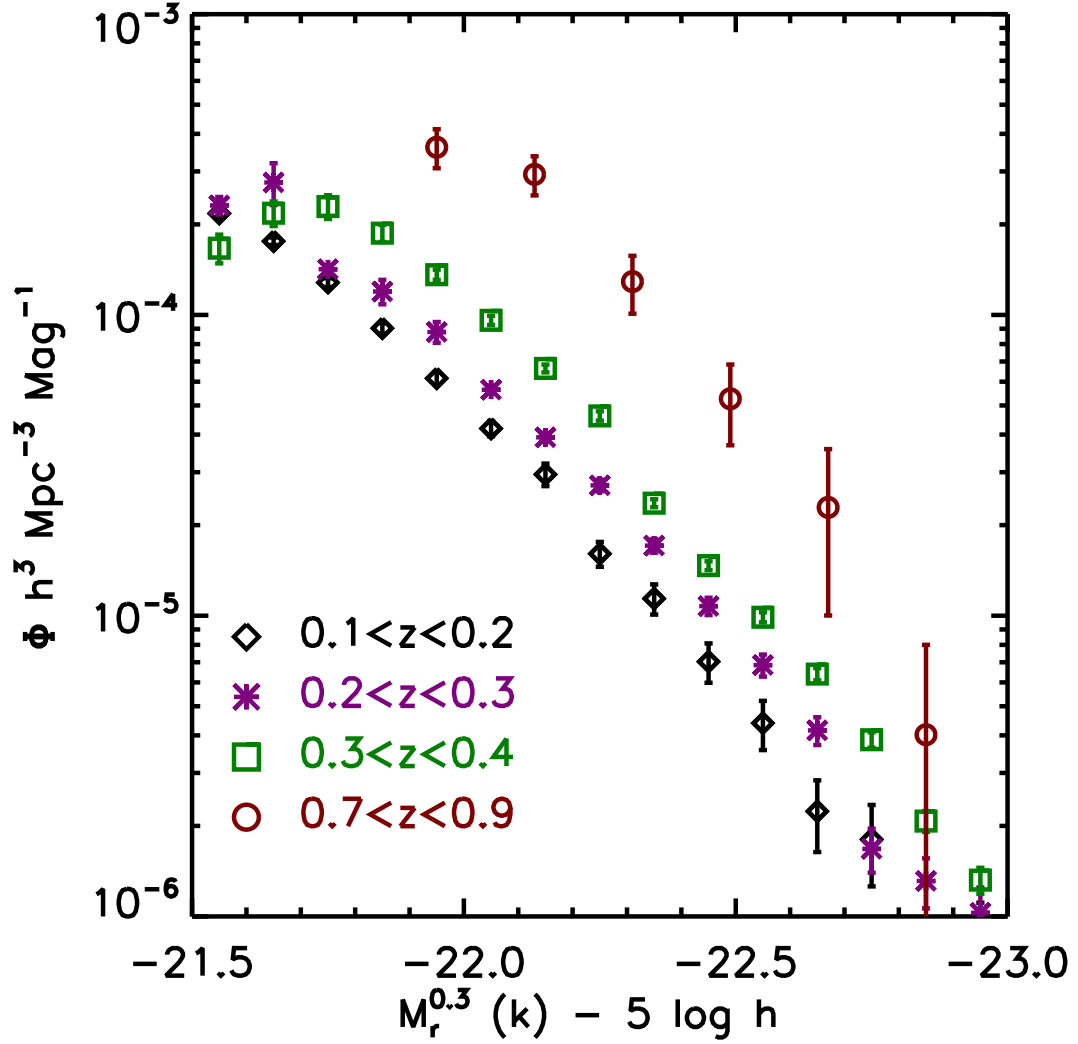
Figure 5.8 Luminosity function of massive galaxies with only a k-correction applied to account for the redshifting of galaxy light. The symbols (color) mark the four redshift bins used : diamonds (black) $0.1 < z < 0.2$, asterisks (magenta) $0.2 < z < 0.3$, squares (green) $0.3 < z < 0.4$, and circles (red) $0.7 < z < 0.9$. The luminosity functions show the characteristic brightening toward higher redshifts due to the passive aging of stars. We must correct for the passive evolution of stellar populations in order to measure the evolution in the underlying galaxy population.
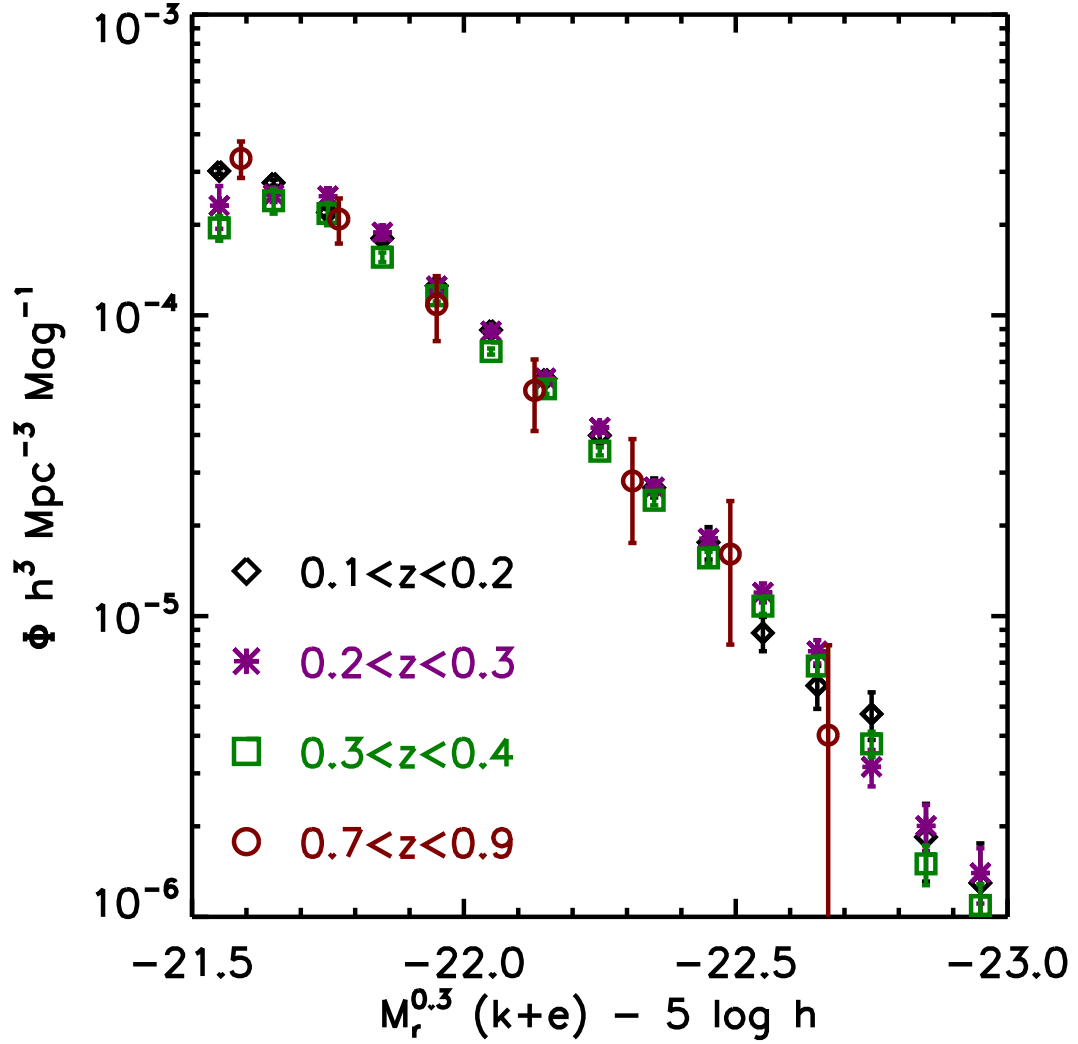
Figure 5.9 Luminosity function of massive galaxies after both the redshifting of their spectra and the passive evolution of their stellar populations have been accounted for when calculating galaxy luminosities. The symbols are as described in Figure 5.8. We find very little evolution in the number counts of massive galaxies to $z \sim 0.9$, indicating that the most massive galaxies have grown little over the latter half of cosmic history.

parameterization to that discussed by Brown et al. (2007). Instead of measuring the evolution in the total luminosity density contained in massive galaxies, we instead measure the magnitude at which the integrated number density reaches a certain value. As massive galaxies populate the exponential tail of the luminosity distribution, small photometric errors can result in significant errors in the total luminosity density derived. For example, a shift of 3% in the luminosity threshold corresponds to a 10% change in the inferred number density of the population. Thus, if the integrated number or luminosity density at a given magnitude is used to measure the evolution of a population, results are quite sensitive to the magnitude threshold utilized. Here, we use the inverse; we measure the magnitude at which the integrated number density reaches a threshold of $10^{-4.5}$ and $10^{-5.0} h^3$ Mpc^{-3}. These magnitudes are denoted by $M_{0.3_r}(10^{-4.5})$ and $M_{0.3_r}(10^{-5.0})$ throughout this discussion.

In order to measure $M_{0.3_r}(10^{-4.5})$ and $M_{0.3_r}(10^{-5.0})$, we fit each of our luminosity functions with a quadratic polynomial in the logarithm. We then integrate the best fitting polynomial and determine the magnitude at which the integrated number density reaches $10^{-4.5}$ and $10^{-5.0} h^3$ Mpc^{-3}. Error bars were calculated by repeating this calculation while removing one of our subfields in turn in the same manner we calculated jack-knife errors on our luminosity function measurements. The exact form we use to fit the luminosity function has little effect on our final results. Figure 5.10 shows the evolution in $M_{0.3_r}(10^{-4.5})$ and $M_{0.3_r}(10^{-5.0})$ before the passive evolution of stellar populations is removed from our galaxies and columns (2) and (4) of Table 5.4 reports these measurements. Tables Table 5.5 and 5.6 and Figures 5.11 and 5.12 show the same critical magnitudes recalculated after the affects of passive evolution have been removed from our galaxy luminosity measurements. In both figures, the differences between the number

Table 5.4.   Evolution of the Massive Red Galaxy Population Without Correcting

for Passive Evolution

| | $M_{0.3r}(10^{-5.0}) - 5\log h$[a] | | $M_{0.3r}(10^{-4.5}) - 5\log h$[b] | |
| Redshift | Petrosian Luminosity | $20h^{-1}$ kpc Aperture Luminosity[c] | Petrosian Luminosity | $20h^{-1}$ kpc Aperture Luminosity[c] |
(1)	(2)	(3)	(4)	(5)
0.15	-22.08 ± 0.008	-21.84 ± 0.005	-21.79 ± 0.005	-21.63 ± 0.005
0.25	-22.16 ± 0.010	-21.91 ± 0.010	-21.87 ± 0.010	-21.69 ± 0.010
0.35	-22.25 ± 0.010	-22.04 ± 0.010	-21.98 ± 0.010	-21.84 ± 0.010
0.80	-22.60 ± 0.090	-22.37 ± 0.020	-22.33 ± 0.052	-22.20 ± 0.033

[a]The magnitude at which the integrated number density of LRGs reaches $10^{-5.0}h^{-3}$ Mpc^{-3}.

[b]The magnitude at which the integrated number density of LRGs reaches $10^{-4.5}h^{-3}$ Mpc^{-3}.

[c]See §5.4.5 for a full description of the aperture luminosity functions

Table 5.5.   Evolution of the Massive Red Galaxy Population After Correcting

for Stellar Evolution

	$M_{0.3_r}(10^{-5.0}) - 5\log h$[a]		
Redshift	Petrosian Luminosity	$20h^{-1}$ kpc Aperture Luminosity[b]	Maraston Luminosity[c]
(1)	(2)	(3)	(4)
0.15	-22.27 ± 0.008	-22.23 ± 0.007	-22.00 ± 0.005
0.25	-22.30 ± 0.010	-22.26 ± 0.010	-22.04 ± 0.010
0.35	-22.25 ± 0.010	-22.24 ± 0.010	-21.99 ± 0.010
0.80	-22.28 ± 0.056	-22.25 ± 0.080	-22.04 ± 0.060

[a]The magnitude at which the integrated number density of LRGs reaches $10^{-5.0}h^{-3}$ Mpc^{-3}.

[b]See §5.4.5 for a description of the $20h^{-1}$kpc aperture luminosity function.

[c]Maraston luminosities are Petrosian flux measurements which have been $k + e$-corrected using Maraston (2005) models and are described in §5.4.2

Table 5.6.   Evolution of the Massive Red Galaxy Population After Correcting
for Stellar Evolution

	$M_{0.3_r}(10^{-4.5}) - 5\log h$[a]		
Redshift	Petrosian Luminosity	$20h^{-1}$ kpc Aperture Luminosity[b]	Maraston Luminosity[c]
(1)	(2)	(3)	(4)
0.15	-21.99 ± 0.005	-21.81 ± 0.005	-21.94 ± 0.005
0.25	-22.02 ± 0.010	-21.85 ± 0.010	-21.97 ± 0.010
0.35	-21.96 ± 0.010	-21.80 ± 0.010	-21.94 ± 0.010
0.80	-22.01 ± 0.053	-21.81 ± 0.037	-21.96 ± 0.075

[a]The magnitude at which the integrated number density of LRGs reaches $10^{-4.5}h^{-3}$ Mpc^{-3}.

[c]See §5.4.5 for a description of the $20h^{-1}$kpc aperture luminosity function.

[d]Maraston luminosities are Petrosian flux measurements which have been $k + e$-corrected using Maraston (2005) models and are described in §5.4.2

density measured in each redshift bin are significant within our errors. The large area probed by SDSS makes cosmic variance between the redshift bins smaller than the observed differences at $0.1 < z < 0.4$, so large scale structure is unlikely the cause. We fit the measured critical magnitudes with a linear evolution with redshift. The best fit relation is shown as dot-dashed lines in Figures 5.11 and 5.12; the shaded region shows the one sigma confidence of the fit. Fits to both critical magnitude thresholds find similar evolution; the critical magnitudes have evolved by 0.03 ± 0.08 mag between $z = 0$ and $z = 1$. When fitting this value, we add systematic floor of 0.02 mag in quadrature to each magntiude threshold. As shown by the dotted lines in the figures, the best fit to our data does not rule out pure passive evolution in the massive galaxy population.

5.4.2   Importance of k-corrections on the Result

Central to any study of the rest-frame photometric properties of extragalactic sources are the k-corrections used to convert the observed quantities to the rest-frame properties of the galaxy. There are a number of inherent problems with this method, in particular when applied to the massive galaxies of interest here. As demonstrated in Eisenstein et al. (2003) and Chapter 4, popular stellar synthesis models such as Bruzual & Charlot (2003) and PEGASE.2 (Fioc & Rocca-Volmerange, 1999) do not match the spectral properties of LRGs, especially α-element features; LRGs are α-enhanced compared to solar while the synthesis models do not include non-solar α-abundances. Furthermore, a number of studies (e.g. Eisenstein et al., 2001; Wake et al., 2006) demonstrate that the current generation of stellar synthesis models poorly reconstruct the observed broad-band colors of galaxies on the red-sequence over a variety of redshifts.

To explore the importance of the k-correction models on our inferred results, we employ a second set of k-corrections based on the Maraston (2005) models
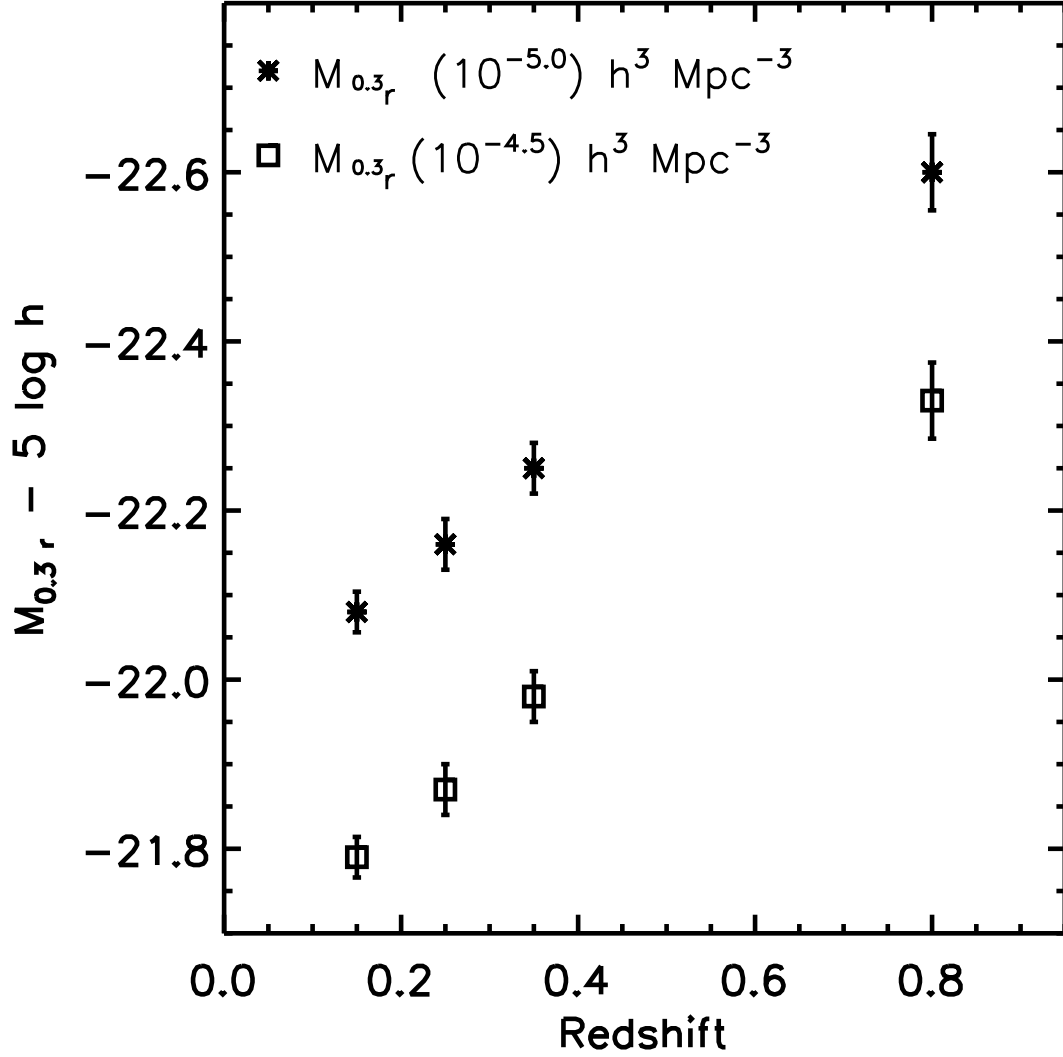
Figure 5.10 The evolution of $M_{0.3r}(10^{-4.5})$ and $M_{0.3r}(10^{-5})$, the magnitudes at which the integrated luminosity density reaches values of $10^{-4.5}h^3$ Mpc^{-3} (asterisks) and $10^{-5.0}h^3$ Mpc^{-3} (squares) respectively. Here, we show the evolution of this parameter if the passive fading of stellar populations is not removed when calculating galaxy luminosities. Both measurements show the characteristic brightening toward higher redshifts. Without removing the luminosity evolution induced by the passive evolution of stars in these massive galaxies, the observed trends may be due to both the passive fading of galaxies over time or the build up in the number density of these galaxies over cosmic history.
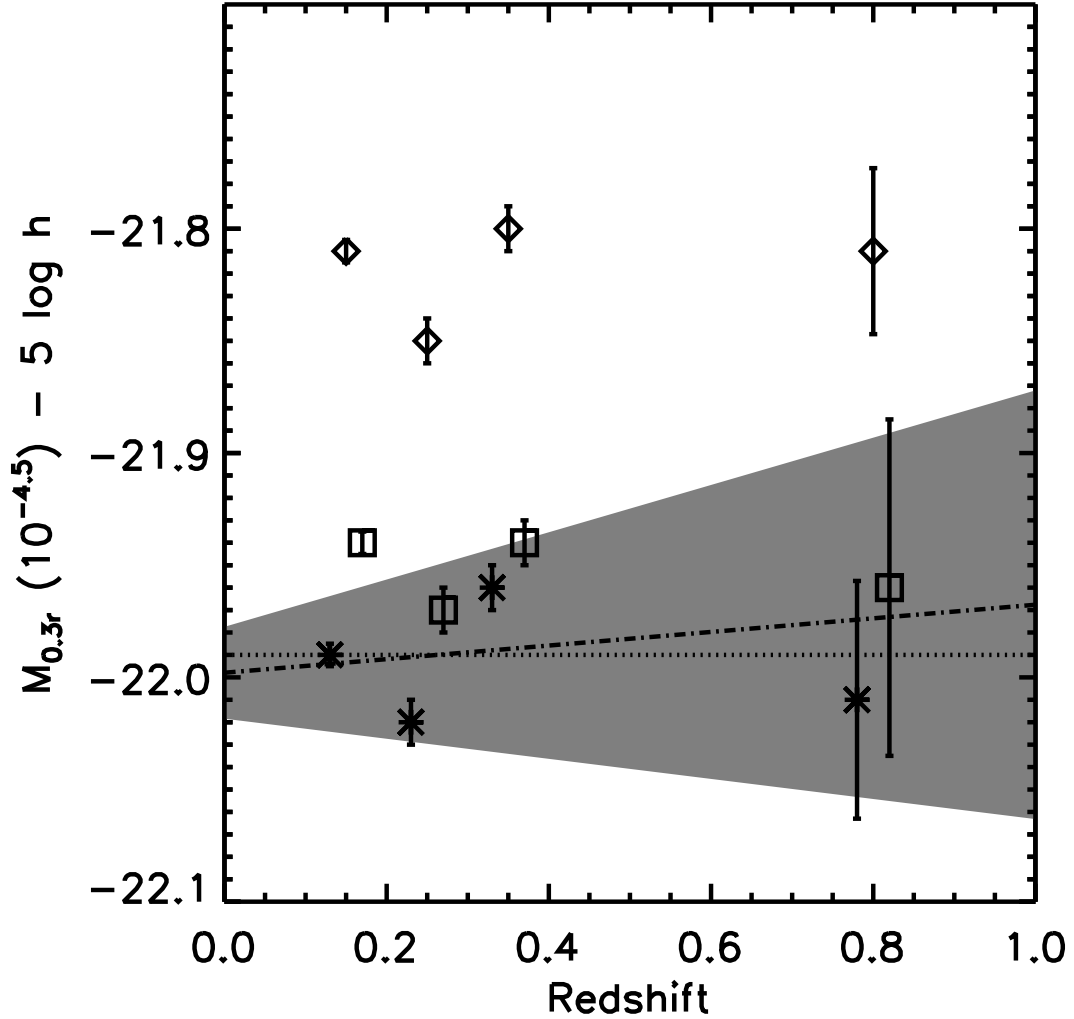
Figure 5.11 The evolution of $M_{0.3r}(10^{-4.5})$, the magnitude at which the integrated luminosity function reaches a number density of $10^{-4.5}h^3$ Mpc^{-3}. This parameter is used to quantify the evolution of the LRG population as these galaxies populate the exponential tail of the luminosity function and small changes to the magnitude threshold chosen may lead to significant errors when calculating the total number or luminosity density in these objects. The asterisks show measurements using the Bruzual & Charlot (2003) stellar templates, the squares show the derived evolution based on Maraston (2005) models (see §5.4.2), and the diamonds show measurements based on the flux within fixed $20h^{-1}$ kpc apertures and Bruzual & Charlot (2003) $k + e$ corrections as described in §5.4.5. For clarity, the Bruzual & Charlot (2003) and Maraston (2005) points have been shifted by -0.02 and +0.02 in redshift, respectively. None of these samples shows a strong evolution in the massive galaxy population since $z = 0.9$. The dot-dashed line shows the best fit linear relationship based upon the Bruzual & Charlot (2003)-derived luminosity functions and the shaded area shows the 1-σ confidence of the fit. The best fitting slope predicts an evolution of 0.03 ± 0.08 mag between $z = 0$ and $z = 1$ and is consistent with no-evolution (shown by the dotted line).
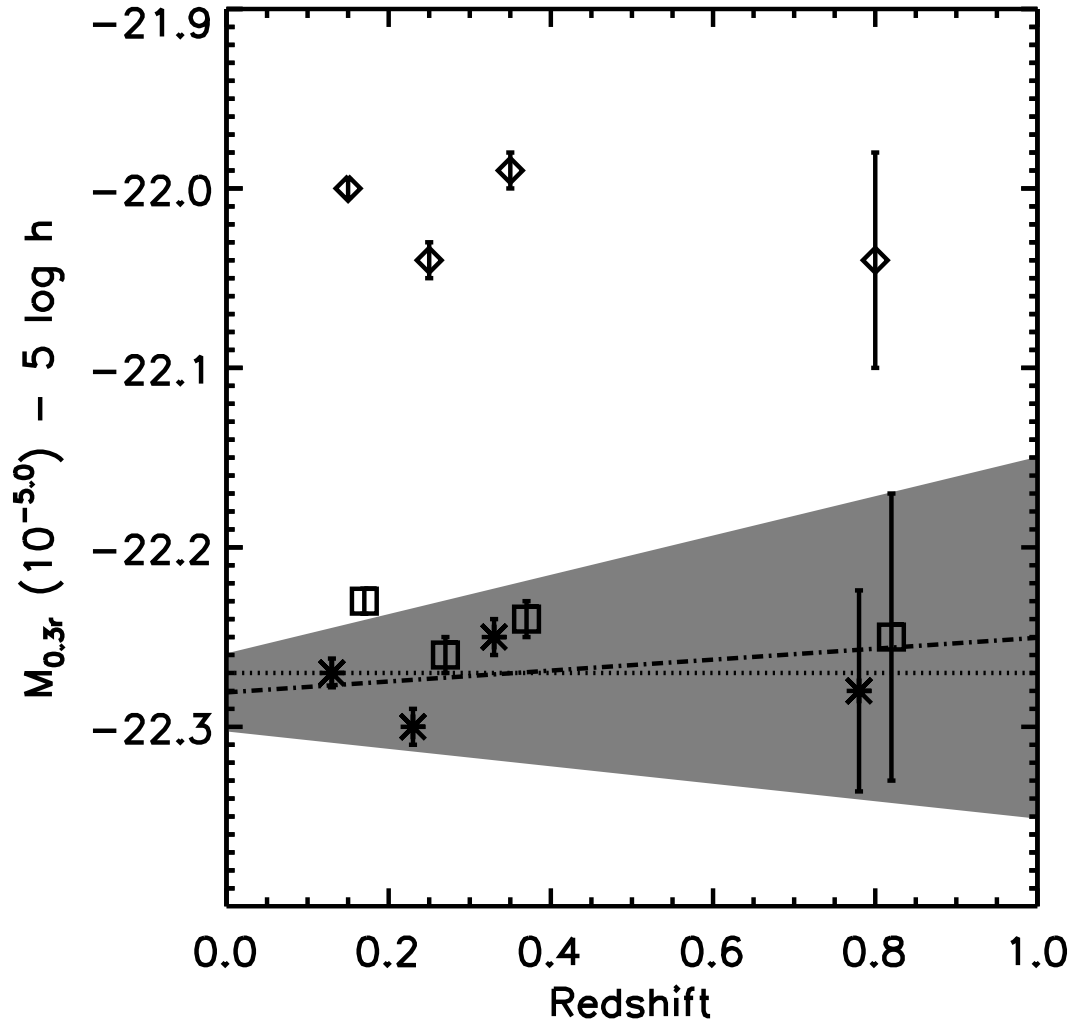
Figure 5.12 Same as Figure 5.11 except showing the evolution of $M_{0.3_r}(10^{-5.0})$. The best fit to the $k + e$-corrected luminosity functions based on Bruzual & Charlot (2003) models is shown, again. The fit here is independently calculated from the one in Figure 5.11, but shows the same slope.

provided by C. Maraston (private communication). These models were created to more accurately track the colors of massive red galaxies than simple stellar populations. The spectrum is modeled as a composite of a metal-rich ($2Z_\odot$) population and a metal poor ($0.005Z_\odot$) population; the metal-poor population holds 10% of the mass in the galaxy.

Figure 5.13 shows the expected colors of a passively fading galaxy from the the Maraston (2005) and Bruzual & Charlot (2003) models utilized in our analysis. As shown in the figure, at $z > 0.6$, the Maraston models predict significantly bluer $g - r$ colors, and more closely follows the observed color locus of galaxies in our sample. While the $g - r$ and $g - i$ colors of galaxies are better matched with the Maraston (2005) models, the $r - i$ colors predicted from both templates are systematically bluer than observed galaxies.

In order to understand any systematics introduced based on the stellar synthesis models used, we re-performed our analysis using the Maraston (2005) models as the basis for our $k-$ and $k + e$-corrections. Figure 5.14 shows the result of this analysis compared to the low-redshift luminosity function derived using Bruzual & Charlot spectral templates. The number density of massive galaxies shows little evolution after the passive evolution of the stellar evolutions are taken into account regardless of the models used to perform the $k + e$-corrections as shown in Figures 5.11 and 5.12 and Tables 5.5 and 5.6. There is, however, a net offset in the measured luminosity of galaxies between the two methods, so care must be taken that k-correction differences are accounted for when comparing galaxy samples from differing analysis techniques. To quantify any difference in the implied evolution based on these two sets of stellar templates, we plot both the Bruzual & Charlot and Maraston derived $M_{0.3_r}(10^{-4.5})$ and $M_{0.3_r}(10^{-5.0})$ in Figures 5.11, 5.12. In both data sets, these quantities have only evolved by less than
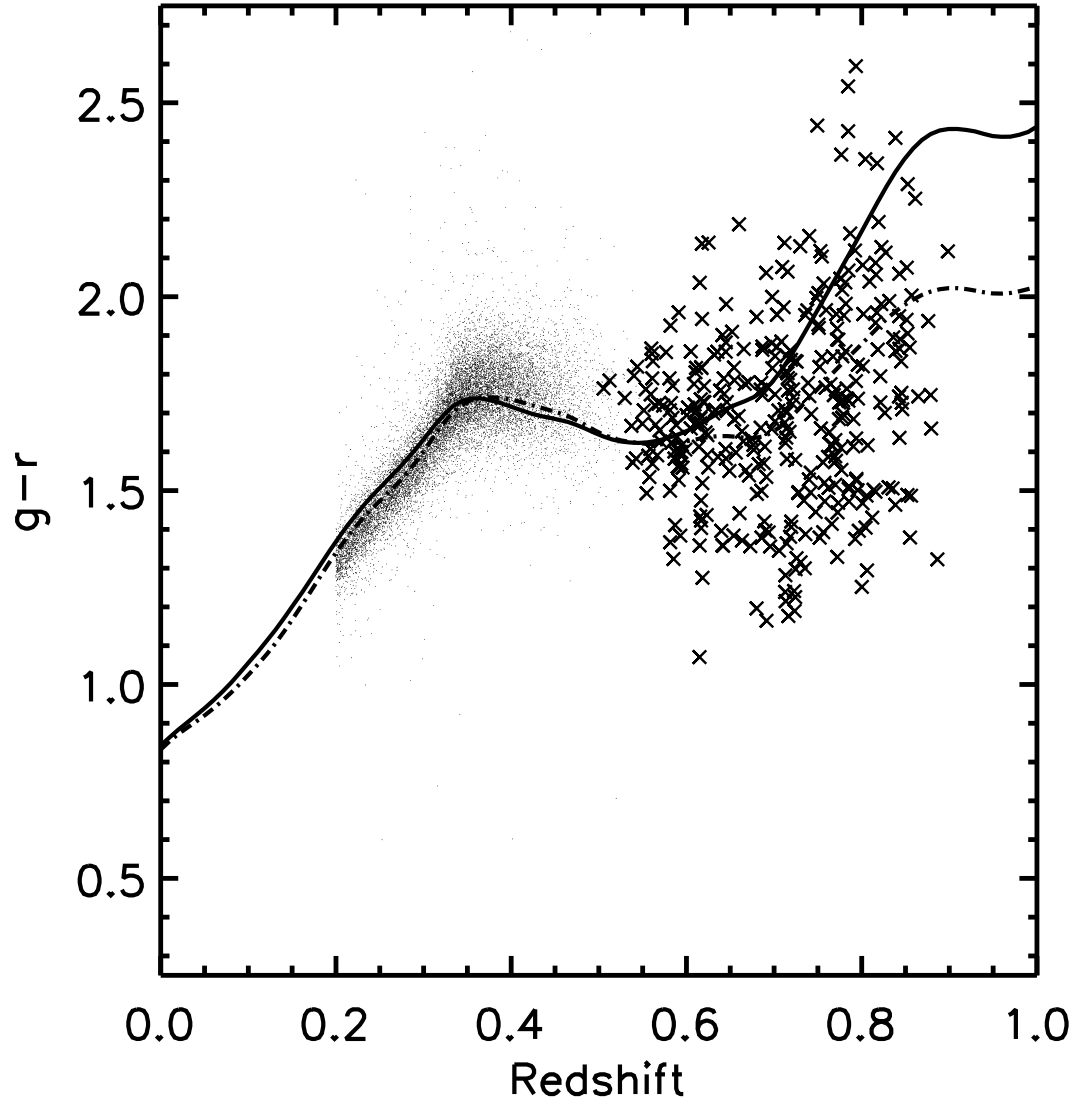
Figure 5.13 Predicted passively evolving color tracks from Bruzual & Charlot (2003) (solid line) and a composite stellar population based on Maraston (2005) models (dot-dashed) as described in §5.4.2. The data show the colors of galaxies in our intermediate and high-redshift samples. The Maraston (2005) models predict significantly bluer $g - r$ colors at high redshifts which follow the observed locus of galaxy colors more closely than Bruzual & Charlot (2003) SSP predictions.

0.05 mag since $z \sim 0.9$, implying that massive galaxies do little more than fade over the latter half of cosmic history.

5.4.3   Merger Fraction from $z \sim 0.9$

Following the method described in Wake et al. (2006), we construct a toy model for the merger history of LRGs to constrain the merger rate of massive red galaxies since $z \sim 0.9$. Using our $0.1 < z < 0.2$ luminosity function, we create a mock sample of galaxies and then allow a fixed fraction of them to have undergone a 1:1 merger since $z = 0.9$. We then compare the luminosity function prediction for this mock sample to the observed luminosity function to determine the probability that both were drawn from the same population. Examples of predicted luminosity functions assuming different merger fractions are shown with the high-redshift data in Figure 5.15.

Our high-redshift luminosity function is best fit by no merging over the latter half of cosmic history. Merger rates greater than 25% are ruled out with 50% confidence and merger rates larger than 40% are excluded at the 99% level based on our measured high-redshift luminosity function. This result agrees with previous studies based on lower-redshift data and photometric redshift surveys (Brown et al., 2007; Masjedi et al., 2006, 2007; Wake et al., 2006). If less massive mergers are considered, more substantial merger rates are permitted. Performing the same experiment but instead considering 1:3 mergers, no merging is still favored, but rates as high as 40% are allowed at 50% confidence and only merger rates larger than 60% are ruled out at 99% confidence. These rate limits imply the total stellar mass in massive red galaxies from $z \sim 0.9$ must not have grown by more than 50% (at 99% confidence) in order to reproduce the observed luminosity functions.

The fact that the most massive red galaxies appear to have evolved very little beyond the passive aging of their stellar populations since $z \sim 0.9$ is quite inter-
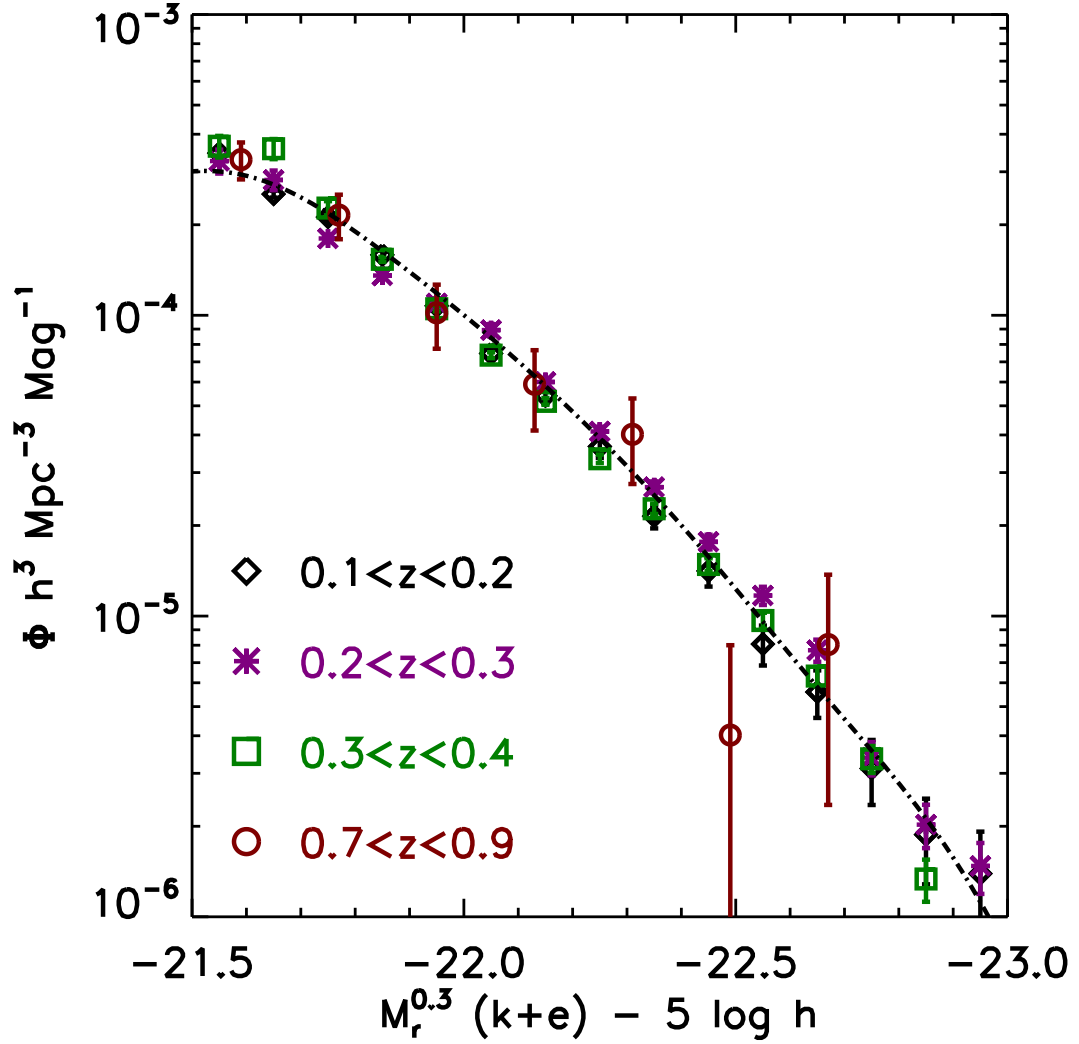
Figure 5.14 Evolution of the massive galaxy luminosity function using Maraston (2005) models when correcting for the redshifting of the galaxy spectra and the passive evolution of their stellar populations. The data points are as in Figure 5.8. The dot-dashed line shows the $0.1 < z < 0.2$ luminosity function calculated using Bruzual & Charlot (2003) templates for comparison. We find no strong difference in the inferred evolution of massive galaxies when different stellar synthesis models are used.
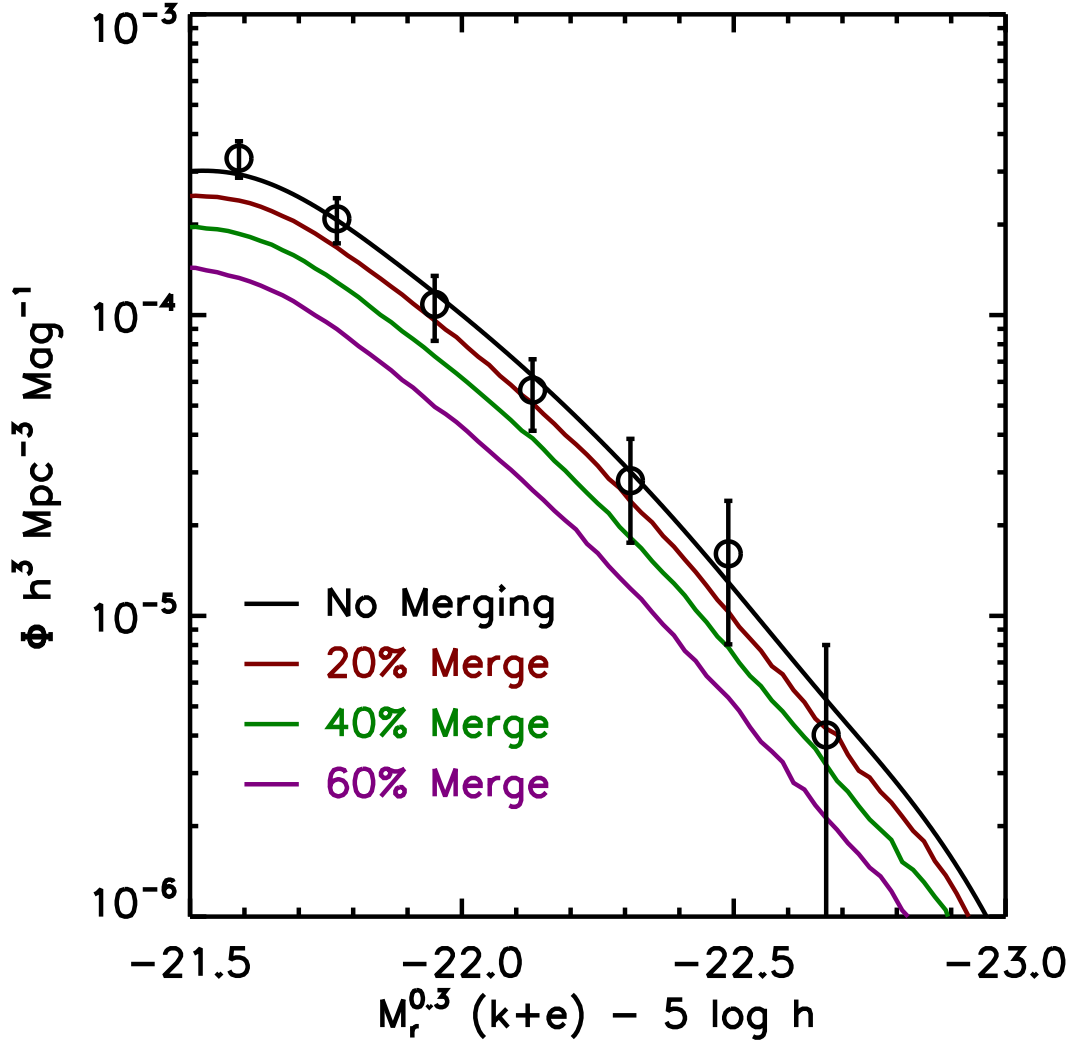
Figure 5.15 Models of the high-redshift luminosity function (points and error-bars). Each of the solid lines shows a simulation in which our $0.1 < z < 0.2$ luminosity functio n is evolved backward assuming a fixed fraction of the LRGs has doubled its luminosity through 1:1 mergers between $z \sim 0.9$ and $z \sim 0.1$. Full details can be found in §5.4.3. Our data are consistent with no growth in the massive red galaxy population since $z \sim 0.9$; merger fractions larger than 25% are ruled out at the 50% confidence level and merger fractions larger than 40% are ruled out at the 99% level.

esting. The most massive galaxies reside in the most massive dark matter halos – these halos have not remained static since $z \sim 1$. In a standard ΛCDM universe, the most massive halos ($M \gtrsim 3 \times 10^{13} M_\odot$) have grown by a factor of two or three since redshift of unity (Seo et al., 2007; Conroy et al., 2007b); one would naively estimate that the galaxies that reside in these halos would have grown, as well.

LRGs at $z = 0.3$ are known to reside in dense environments with mean clustering similar to rich groups and poor clusters (Zehavi et al., 2005a). The formation and assembly of groups and clusters at $z < 1$ would naturally result in a discrepancy between the stellar mass growth of the massive central galaxy and the dark matter halo mass in which it resides. As satellite galaxies are accreted into the group or cluster halo, these satellites contribute stellar mass to the total stellar mass of the halo but not to the stellar mass of the central galaxy. The fact that galaxies with masses $M > 10^{11} M_\odot$ are observed to reside in a broad range of halo masses (McIntosh et al., 2007) may be a natural outcome of group and cluster formation.

If the lack of evolution in the number density of LRGs is due to the growth of clusters rather than the growth of the central LRG, one would expect to observe multiple LRGs within a single cluster halo. To address this hypothesis, Ho et al. (2007) performed a thorough accounting of the number of LRGs which reside in a single halo in the SDSS dataset and Conroy et al. (2007a) used this multiplicity function to conclude that there are fewer LRG satellites of other LRG galaxies than predicted from N-body simulations. Furthermore, White et al. (2007) noted that the apparent lack of evolution in the clustering strength of massive galaxies since $z \sim 1$ implies that these galaxies themselves must be merging as the underlying dark matter distribution has undergone substantial merging during that epoch. Wake et al. (2008) measure the evolution of LRG clustering from

$z = 0.55$ to $z = 0.2$ and find that it is consistent with the idea that LRGs which originally resided in different halos merged to create a single galaxy when their host haloes merged. From the measured clustering of red galaxies in the NDWFS Bootes field, White et al. (2007) estimate that 1/3 of the LRGs which are satellites galaxies of another LRG have merged or been destroyed between $z = 0.9$ and $z = 0.5$.

One model suggested to explain the deficit of LRG satellites suggests that the stars from late mergers onto massive galaxies feed the growth of an intracluster-light (ICL) type of extended envelope rather than the central galaxy. Conroy et al. (2007b) recently simulated the dissipationless evolution of galaxies since $z = 1$ and find that a model in which $\gtrsim 80\%$ of the stars from merged satellites go into a low surface brightness extended stellar halo such as an ICL best predicts measurements of the galaxy stellar mass function and the observed distribution of ICL and brightest cluster galaxies in the local universe. If the total stellar content of the most massive haloes grow considerably at $z < 1$ but the accreted stellar content resides in an extended, diffuse, envelope around the central galaxy, the total luminosity function of massive galaxies as measured by our technique would remain unchanged.

It is clear from our observations that massive red galaxies evolve in a systematically different manner than L^* red galaxies. While the stellar mass in L^* red galaxies has doubled since $z = 1$, our analysis implies the mass in the $L > 3L^*$ red galaxies has grown, at most, by 50% over the same epoch The growth of clusters and groups, including the intracluster light, may play a role in shaping the massive end of the red galaxy mass function while the lower-mass red galaxies are formed through the quenching of star forming galaxies at low redshifts. Alternatively, if the processes that govern star formation at the epoch of massive red

galaxy formation are systematically different from those which govern star formation at $z < 1$, our analysis may underestimate the number density evolution in our sample. In the following section, we explore the impact that an evolving IMF would have on our analysis.

5.4.4 Implication in the Presence of an Evolving Initial Mass Function

Throughout all of our analyses, the slope of the stellar IMF is held fixed. While our dataset is not sufficient to constrain any evolution in the IMF of massive galaxies, if this evolution exists, it can strongly affect our conclusions. Local measurements of the IMF show that at $M \gtrsim 1 M_\odot$ the IMF follows a power-law ($M/M_\odot \propto M^{-x}$; $x = 1.3$) with a turnover at lower masses (Salpeter, 1955; Kroupa, 2001; Chabrier, 2003). For this discussion, we will only consider the IMF at $M \gtrsim 1 M_\odot$; lower-mass stars, while contributing significant stellar mass to the galaxy, do not contribute significantly to the galaxy luminosity and thus play a negligible role in the evolution of the M/L ratio compared to variations in more massive stars. Suggestions of top-heavy IMFs have been found in environments dominated by violent star-formation (Rieke et al., 1993; McCrady et al., 2003; Figer et al., 1999; Stolte et al., 2005; Maness et al., 2007). Also, one may expect the IMF to evolve with redshift as the temperature of the cosmic microwave background begins to dominate over temperatures typically found in Galactic prestellar cores (Larson, 1998). Recently, van Dokkum (2007) compared the luminosity evolution of galaxies in clusters at $0.02 < z < 0.83$, coupled with the color-evolution of these systems, to test models of IMF evolution in early-type galaxies. These data prefer a logarithmic slope of $x = -0.3^{+0.4}_{-0.7}$, considerably flatter than $x = 1.3$ derived in the Milky Way disk. Similarly, Davé (2007) used hydro-dynamical models of galaxy formation and observations of the correlation between galaxy stellar mass and star formation rate to $z = 2$ to suggest that the

characteristic mass at which the IMF turns over, $\hat{M}$, evolves strongly with redshift : $\hat{M} = 0.5(1 + z)^2 M_\odot$.

To explore the importance of the assumed IMF slope on the inferred density evolution in the LRG population, we show luminosity evolution tracks predicted using the fits of van Dokkum (2007) for SSPs formed at $z = 2.0$ and $z = 6.0$ in Figure 5.16; the B-band luminosity evolution in each of the three tracks has been normalized to $z = 0.3$. The details of these models can be found in van Dokkum (2007). Briefly, these tracks show the expected luminosity evolution given three different IMF slopes using Maraston (2005) synthesis models and [Fe/H]=0.35. For slopes shallower than $x = 1.3$, our current passive evolution correction will systematically undercorrect for the passive fading of stars which will lead to significant underestimations of the density evolution experienced by these galaxies. For example, if we underestimate the luminosity evolution from $z = 0.8$ to $z = 0.3$ by 0.2 mag, we would conclude that the massive galaxy population has evolved little since $z = 0.8$ when, in actuality, the number density of these massive systems has grown by a factor of two. Clearly, more detailed constraints are needed on the fraction of high mass to low mass stars in these galaxies in order to place any evolutionary measurement into proper context.

5.4.5 Measurements of Massive Galaxy Luminosity Functions Using Aperture Luminosities

Comparisons of several recent studies of the evolution of the red galaxy luminosity function since $z \sim 1$ have revealed a number of possible systematic differences which have been attributed to differences in the methods used to measure the total galaxy luminosities. For example, Brown et al. (2007) find that the stellar mass of the red galaxy population has grown by of a factor of 2 since $z = 1.0$ while results from DEEP2 suggest growth of a factor of 4 during the same epoch
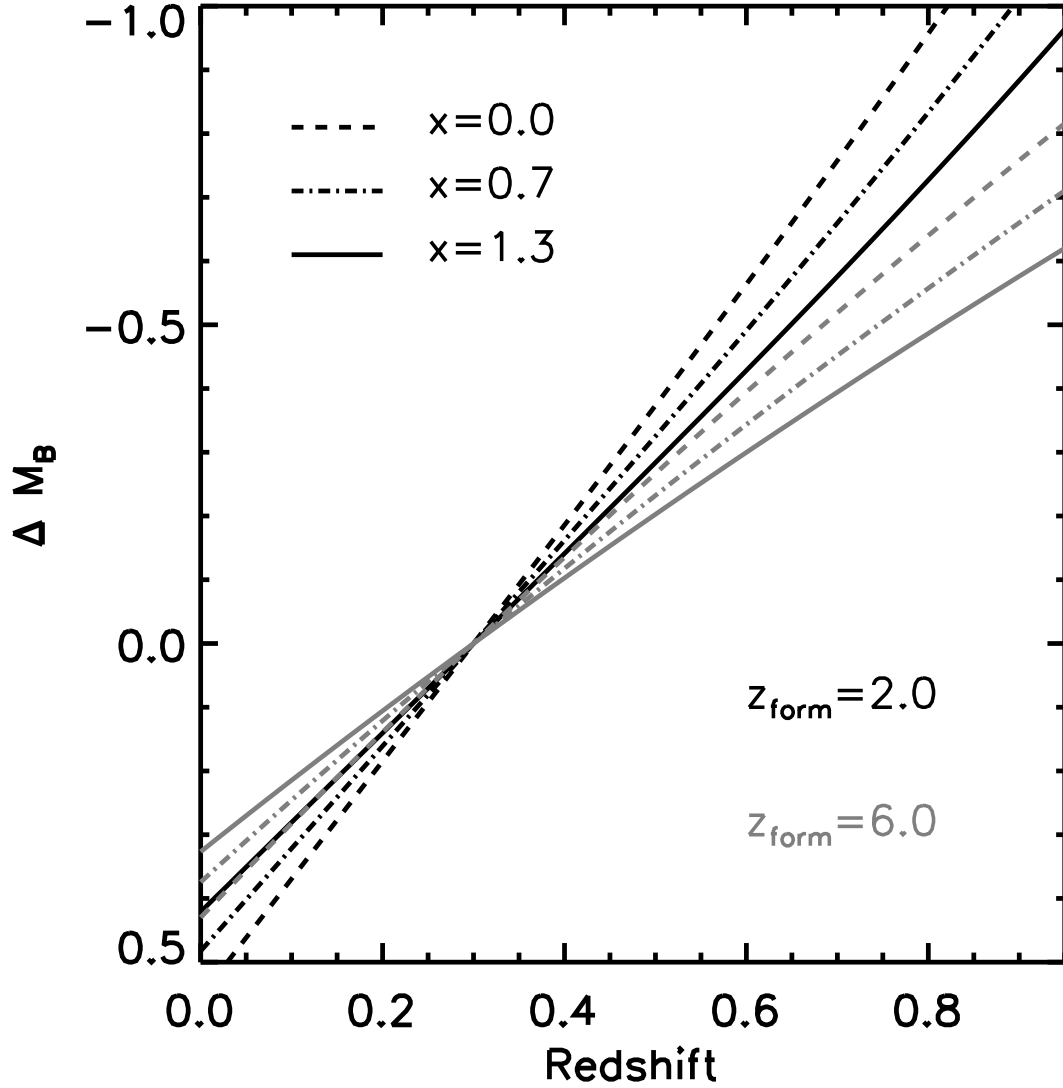
Figure 5.16 B-band luminosity evolution based on initial mass functions with different slopes using the fits presented in van Dokkum (2007). The grey lines show the expected evolution of an SSP formed at $z = 6$ while the black lines show the trends for $z = 2$; all of the tracks have been normalized at $z = 0.3$. If galaxies in our sample have IMF slopes shallower than the traditional $x = 1.3$ Salpeter (1955) value, we would underestimate the evolution of galaxies at $z = 0.8$ by $\gtrsim 0.15$ mag by utilizing synthesis models based on the Salpeter (1955) IMF.

(Willmer et al., 2006; Faber et al., 2007). One alternative is to measure the luminosity of each galaxy in an aperture of fixed physical size and to study the evolution of the luminosity function based on this quantity. This method removes the systematics introduced by comparing analyses done with fixed angular size aperture or extrapolations to the total galaxy flux. Furthermore, extrapolations to a total brightness requires careful treatment of the low surface-brightness outer isophotes which are quite difficult to photometer without very deep imaging. It is important to note, however, that the evolution of the luminosity within a fixed physical aperture size addresses a slightly different question than the total luminosity function; instead of tracking the total contribution of starlight, we instead focus on the growth of the stellar mass only in the inner region of the galaxy. Depending on the physical aperture size chosen, these luminosity measurements will not only be affected by the total starlight in the galaxy but also by the central concentration. Furthermore, the aperture luminosity function and total luminosity function may exhibit different evolution if the ratio of the luminosity within the physical aperture to the total galaxy luminosity changes with time. For example, the aperture to total luminosity ratio may change if significant mass is accreted at large radii or the stellar concentration evolves due to recent merger activity.

To investigate this method, we measure the evolution of the luminosity within the inner $20h^{-1}$ kpc for each galaxy in our sample. We choose $20h^{-1}$ kpc radii apertures as this size will enclose a majority of the galaxy light, thus minimizing the effects on color gradients and galaxy concentration on our results, and yet not be too large such that the photometric errors due to sky subtraction uncertainties become significant. For the low-redshift SDSS galaxy samples, we make use of the measured aperture fluxes at fixed angular sizes output by the SDSS
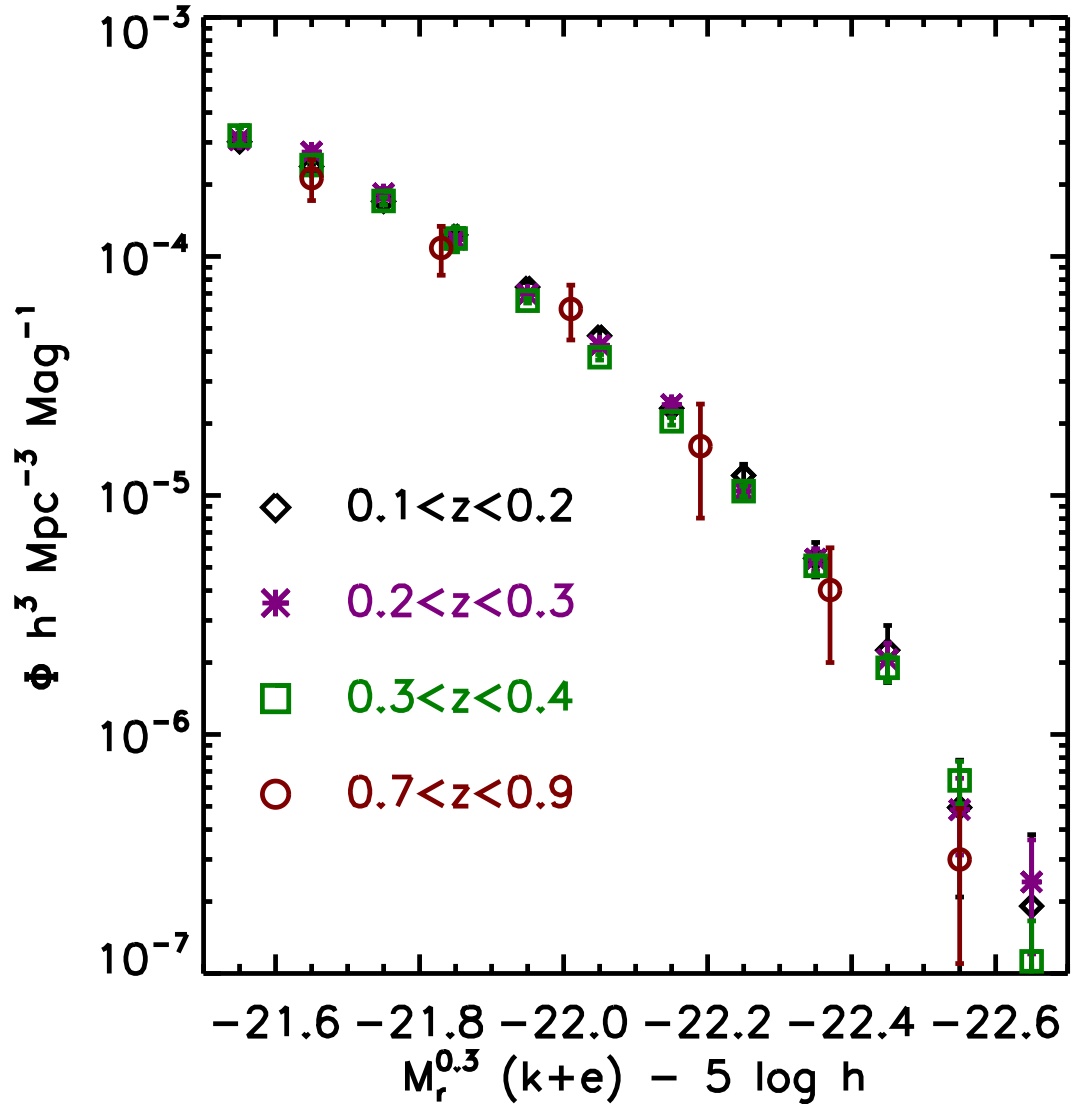
Figure 5.17 Evolution of the luminosity function based upon luminosities contained within the central $20h^{-1}$ kpc of massive galaxies. No significant differences are seen when the evolution of this central flux compared to the total galaxy luminosity functions presented in Figure 5.9. Measuring luminosities in apertures of fixed physical size eliminates systematic differences in estimates of the total galaxy flux and thus will allow for more robust comparisons between future samples.

pipeline. For reference, the SDSS pipeline measures galaxy flux in apertures with radii of 0.23, 0.68, 1.03, 1.76, 3.0, 4.63, 7.43, 11.42, 18.20, 28.20, 44.21, 69.00, 107.81, 168.20, and 263.00 arcseconds (see Table 7 in Stoughton et al., 2002). Based on the measured redshift of each galaxy in our sample, we interpolate the measured aperture photometry to the radius corresponding to $20h^{-1}$ kpc at the redshift of the galaxy. In order to measure the fluxes of our $z \sim 0.9$ galaxies at the highest possible signal-to-noise, we photometer these galaxies directly from the SDSS imaging data. As our high-redshift sample was constructed from galaxies lying in the SDSS Southern Survey region, which has been scanned several times over the course of the survey, we construct a coadded image of $90h^{-1}$ kpc x $90h^{-1}$ kpc around each of our sample galaxies. Only data with seeing less than 1.5 arcseconds was used to construct the postage stamps. Before coadding each of the individual SDSS frames, we do not account for the seeing variations between each run; this has a negligible effect on the aperture fluxes on the scales we consider here. On each coadded postage stamps, known sources were masked out to avoid contamination and the flux of each galaxy was measured in a $20h^{-1}$ kpc radius aperture.

Table 5.7.   LRG $20h^{-1}$kpc Aperture Luminosity Functions with No Evolution

Correction

| $M_{0.3_r} - 5\log h$ | $\log_{10}$ Galaxy Number Density[a] | | | $M_{0.3_r} - 5\log h$ | $\log_{10}$ Galaxy Number Density[a] |
| | $0.1 < z < 0.2$ | $0.2 < z < 0.3$ | $0.3 < z < 0.4$ | | $0.7 < z < 0.9$ |
(1)	(2)	(3)	(4)	(5)	(6)
-21.55	-3.75 ± 0.01	-3.72 ± 0.01	-3.49 ± 0.04	-21.59	-3.27 ± 0.07
-21.65	-3.92 ± 0.01	-3.84 ± 0.01	-3.59 ± 0.03	-21.77	-3.33 ± 0.07
-21.75	-4.09 ± 0.02	-3.99 ± 0.01	-3.73 ± 0.02	-21.95	-3.51 ± 0.08
-21.85	-4.30 ± 0.02	-4.12 ± 0.04	-3.88 ± 0.04	-22.13	-3.74 ± 0.09
-21.95	-4.55 ± 0.03	-4.39 ± 0.01	-4.08 ± 0.05	-22.31	-4.01 ± 0.10
-22.05	-4.93 ± 0.05	-4.62 ± 0.02	-4.33 ± 0.01	-22.49	-4.53 ± 0.15
-22.15	-5.15 ± 0.06	-4.94 ± 0.03	-4.58 ± 0.02	$\cdots$	$\cdots$
-22.25	-5.64 ± 0.12	-5.23 ± 0.04	-4.85 ± 0.02	$\cdots$	$\cdots$
-22.35	-5.93 ± 0.16	-5.52 ± 0.05	-5.18 ± 0.02	$\cdots$	$\cdots$
-22.45	-6.30 ± 0.25	-6.19 ± 0.12	-5.53 ± 0.03	$\cdots$	$\cdots$

Table 5.7—Continued

| $M_{0.3_r} - 5\log h$ | log$_{10}$ Galaxy Number Density[a] | | | $M_{0.3_r} - 5\log h$ | log$_{10}$ Galaxy Number Density[a] |
| | $0.1 < z < 0.2$ | $0.2 < z < 0.3$ | $0.3 < z < 0.4$ | | $0.7 < z < 0.9$ |
(1)	(2)	(3)	(4)	(5)	(6)
-22.55	-6.45 ± 0.43	-6.63 ± 0.19	-5.86 ± 0.04	$\cdots$	$\cdots$
-22.65	-6.64 ± 0.43	-6.63 ± 0.19	-6.20 ± 0.06	$\cdots$	$\cdots$

[a]All number densities are expressed in units of h^3 Mpc^{-3} Mag^{-1}

Table 5.8.   LRG $20h^{-1}$kpc Aperture Luminosity Functions After Passive

Evolution Correction

| $M_{0.3_r} - 5\log h$ | $\log_{10}$ Galaxy Number Density[a] | | | $M_{0.3_r} - 5\log h$ | $\log_{10}$ Galaxy Number Density[a] |
| | $0.1 < z < 0.2$ | $0.2 < z < 0.3$ | $0.3 < z < 0.4$ | | $0.7 < z < 0.9$ |
(1)	(2)	(3)	(4)	(5)	(6)
-21.55	-3.51 ± 0.01	-3.44 ± 0.02	-3.51 ± 0.02	-21.59	-3.61 ± 0.08
-21.65	-3.62 ± 0.01	-3.56 ± 0.02	-3.62 ± 0.02	-21.77	-3.84 ± 0.09
-21.75	-3.77 ± 0.01	-3.74 ± 0.02	-3.77 ± 0.02	-21.95	-4.12 ± 0.11
-21.85	-3.91 ± 0.02	-3.93 ± 0.02	-3.93 ± 0.05	-22.13	-4.51 ± 0.15
-21.95	-4.13 ± 0.02	-4.16 ± 0.01	-4.19 ± 0.01	-22.31	-5.09 ± 0.22
-22.05	-4.33 ± 0.02	-4.37 ± 0.02	-4.42 ± 0.01	-22.49	-5.81 ± 0.23
-22.15	-4.64 ± 0.03	-4.62 ± 0.02	-4.69 ± 0.02	$\cdots$	$\cdots$
-22.25	-4.92 ± 0.05	-4.98 ± 0.03	-4.98 ± 0.02	$\cdots$	$\cdots$
-22.35	-5.26 ± 0.07	-5.27 ± 0.05	-5.29 ± 0.03	$\cdots$	$\cdots$
-22.45	-5.65 ± 0.12	-5.69 ± 0.07	-5.72 ± 0.06	$\cdots$	$\cdots$

Figure 5.17 and Tables 5.7 and 5.8 show the aperture magnitude luminosity functions as a function of redshift. The aperture luminosity functions shown in Figure 5.17 show some systematic differences compared to the total luminosity functions presented in Figure 5.9. At fixed luminosity, the aperture luminosity function reports a systematically smaller number density than the total luminosity function. As the aperture luminosity measurements do not measure the full galaxy flux (with a median $M_{\mathrm{aper}} - M_{\mathrm{total}} \sim 0.15$ mag), the aperture luminosity function is shifted toward fainter magnitudes compared to the total luminosity function. Secondly, the number density falls off more rapidly toward more luminous galaxies when aperture magnitudes are considered rather than total luminosities. This appears to be due to differential aperture losses as a function of luminosity; more luminous early-type galaxies have larger effective radii and thus more flux is missed by a fixed physical size aperture. While the shape and normalization of the aperture luminosity function have systematic differences with the total luminosity function, the aperture luminosity functions show little evolution in the $0.1 < z < 0.9$ range after the effects of passive evolution are removed just as is seen for the total galaxy luminosity function.

The squares on Figure 5.11 and values in columns (3) and (5) of Table 5.4 and Tables 5.5 and 5.6 show the lack of evolution quantitatively - while the luminosities computed using physically sized apertures were systematically fainter than the total galaxy luminosities, as expected, the evolution of the central 20 h^{-1} kpc of these massive red galaxies appears to follow the evolution of the ensemble starlight. These measurements can provide a benchmark for future comparisons of the luminosity function without the need to correct for systematic differences between the photometric methods used.

Table 5.8—Continued

| $M_{0.3_r} - 5\log h$ | log$_{10}$ Galaxy Number Density[a] | | | $M_{0.3_r} - 5\log h$ | log$_{10}$ Galaxy Number Density[a] |
| | $0.1 < z < 0.2$ | $0.2 < z < 0.3$ | $0.3 < z < 0.4$ | | $0.7 < z < 0.9$ |
(1)	(2)	(3)	(4)	(5)	(6)
-22.55	-6.31 ± 0.25	-6.31 ± 0.15	-6.19 ± 0.09	$\cdots$	$\cdots$
-22.65	-6.72 ± 0.43	-6.62 ± 0.22	-6.95 ± 0.21	$\cdots$	$\cdots$

[a]All number densities are expressed in units of h^3 Mpc^{-3} Mag^{-1}

5.5   Spectral Evolution of Massive Galaxies Since $z \sim 0.9$

While each of our individual MMT galaxy spectra have too low signal-to-noise to perform any detailed measurements of line strengths, averaging the entire sample results in a modest quality spectrum which can be used to measure the change in the spectral structure of massive red galaxies since $z \sim 0.9$. We construct the average LRG spectra in each redshift bin used to calculate our luminosity functions presented above : $0.1 < z < 0.2$, $0.2 < z < 0.3$, $0.3 < z < 0.4$, and $0.7 < z < 0.9$. We limit the luminosity of the galaxies used in this analysis to the evolution-corrected magnitude range of $-23 < M_{0.3_r} - 5\log h < -22$ to focus on galaxies for which we are very complete. After masking within 10 Å of each of the strong emission lines arising from the Earth's atmosphere, we shift the observed spectrum of each galaxy to the rest-frame and normalize it by the average flux between 4100-4200Å. We construct the mean spectrum by weighting each individual spectrum with the same weight assigned to that galaxy when calculating the luminosity function (including the $1/V_{\max}$) and thus construct the composite spectrum of a typical galaxy in each of our redshift bins.

Figure 5.18 shows the coadded spectra of massive red galaxies from $z = 0.1$ to $z = 0.9$. Each of the composite spectra look quite similar showing the strong spectral features characteristic to old stellar populations. While the high-redshift composite spectrum clearly shows enhanced [O II] emission compared to the lower-redshift spectra other differences between the spectra are more subtle. Figure 5.19 shows the measured $H\delta$ and G-band at 4300 Å absorption equivalent width, from our composite spectra. A solar-metallicity stellar population formed at $z = 2$ using a Salpeter (1955) IMF with subsequent passive fading is shown with the solid line. Our measurements are broadly consistent with the passive fading of stars since $z \sim 0.9$. Note that we make no claim that since these points lie near the

solar-metallicity track that we expect these galaxies to have solar metallicity or have a given age. It has been shown (e.g. Eisenstein et al., 2003) that LRGs show α-enhancements compared to solar and also that the age and metallicity of the stellar populations one might derive from most spectral indicies are degenerate. Instead, we simply illustrate that the data follow the same trend expected for a passively fading population.

In order to model the amount of recent star formation activity allowed by our high-redshift composite spectrum, we model it as the linear combination of a passively faded version of our low-redshift spectrum plus a frosting of more recent star formation activity. The lowest-redshift composite is well fit by a 7.0 Gyr, solar metallicity, population. Thus, we model our high-redshift composite as the non-negative linear sum of a 1.9 Gyr population – the universe has aged by 5.1 Gyr between $z = 0.8$ to $z = 0.15$ – and a frosting of either 10Myr, 100Myr, or 1Gyr stars. We find that the high-redshift composite is best modeled by a single-age population at 1.9 Gyr with no need for the presence of younger stars save for the [O II] which may be generated by either young stars or enhanced AGN activity. We can constrain the presence of 10Myr, 100Myr, and 1Gyr stars to contribute less than 0.1%, 0.5%, and 5% of the stellar mass based on our spectral fits with 99% confidence. Thus, it appears that high-redshift LRGs have enhanced signatures of youth compared to their low-redshift counterparts due to the passive evolution of their stellar populations. We find no signatures of more recent star formation activity in our high-redshift sample indicative of recent gas-rich mergers at $z \sim$ 0.9.

The evolution of the average spectrum presented here may be underestimated in the event that galaxies with weak absorption lines are preferentially removed from the sample due to redshift determination failures. We do not expect our
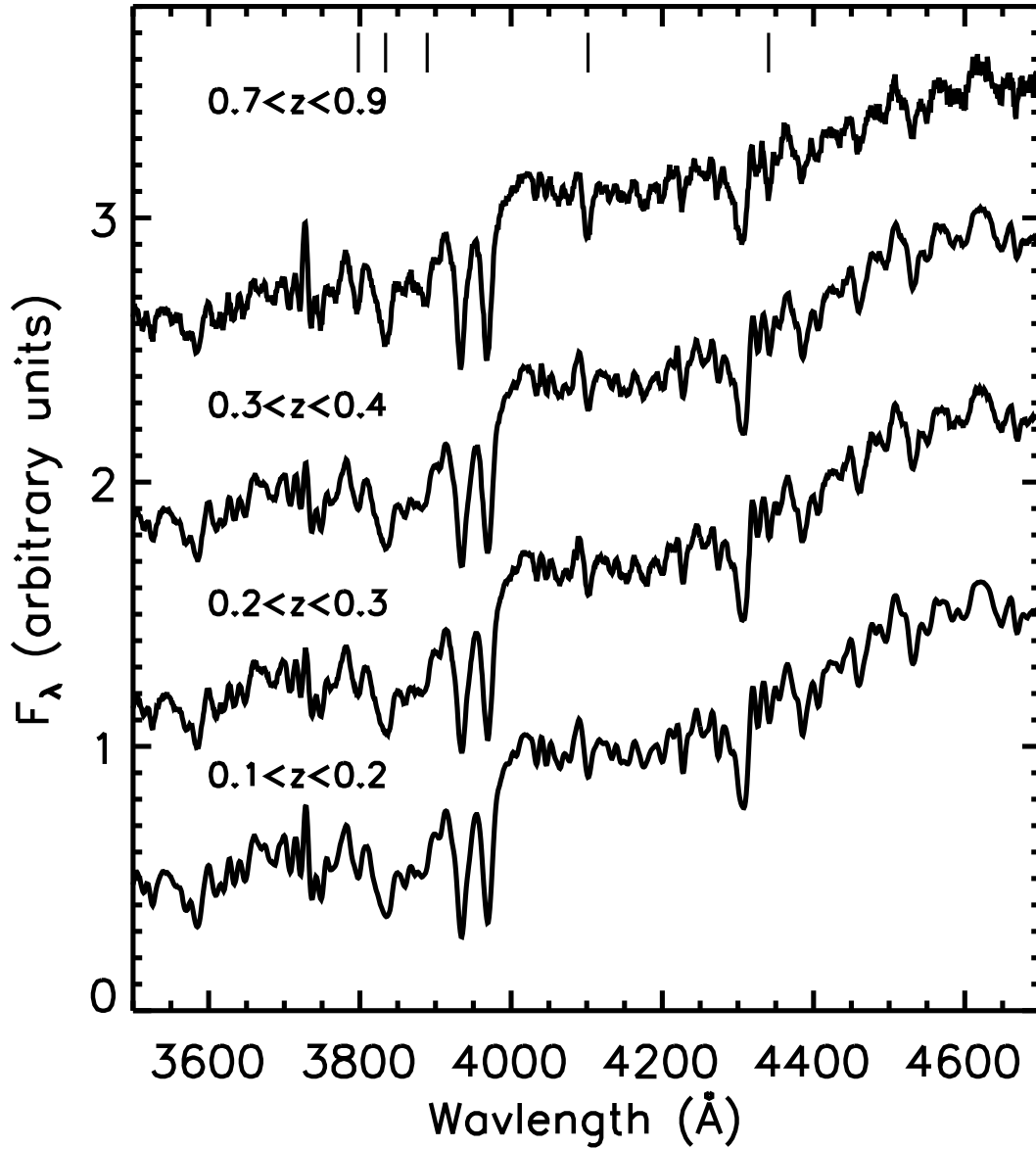
Figure 5.18 Average spectrum of LRGs since $z = 0.9$. Each composite spectrum shows features characteristic of old stellar populations while the highest redshift spectrum shows enhanced [O II]$\lambda 3727$ emission and stronger Balmer absorption indicating the presence of younger stars. The location of Balmer features are marked by vertical bars. As discussed in §5.5 , we model the high-redshift average spectrum with a passively faded version of the low-redshift composite combined with a recent frosting of young stars. We find at most 5% of the stellar mass in the average high-redshift LRG has formed within 1Gyr of $z = 0.9$.
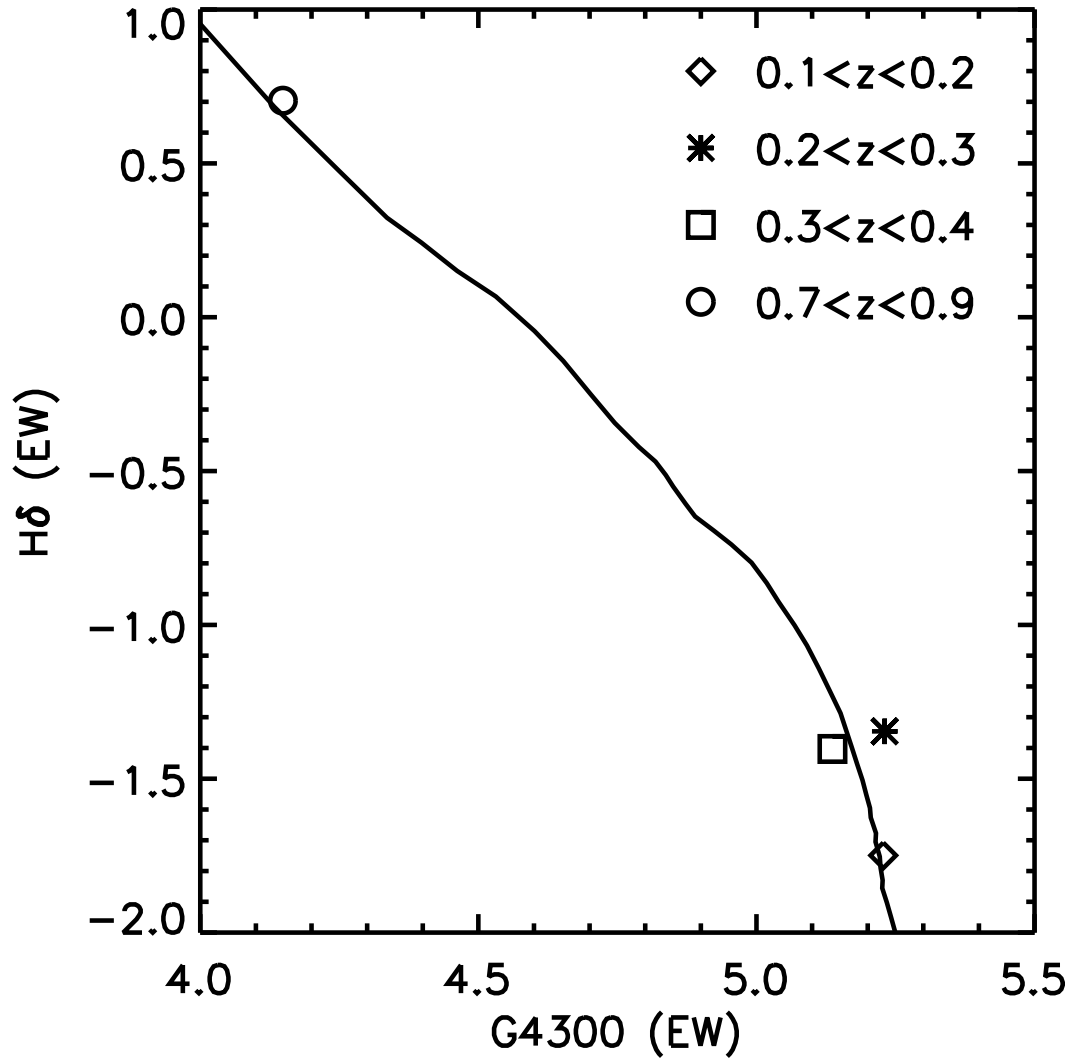
Figure 5.19 Equivalent widths of Hδ and G-band absorption features from the composite galaxy spectra. The style of data point corresponds to the redshift of the composite spectrum; star: $0.1 < z < 0.2$, asterisk: $0.2 < z < 0.3$, square: $0.3 < z < 0.4$, and circle: $0.7 < z < 0.9$. The solid line shows the expected trend for a solar-metallicity galaxy formed at $z = 2$ from Bruzual & Charlot (2003) models. Errors are comparable to the size of each data point. While only illustrative, the observed composite spectra show similar trends as that expected of a passively fading population.

spectroscopy to be biased in this way, however. Primarily, as the absorption line strength is correlated with the total galaxy luminosity, we expect the galaxies with weak lines to have luminosities fainter than the limits imposed in creating our composite spectra. Secondly, we would expect the presence on [O II] emission to allow redshift determination even if the absorption lines were very weak. To examine this effect, we refit each of our galaxies after masking out the wavelengths affected by the [O II] emission line and find that only 3 of the galaxies in our sample had sufficiently weak absorption lines that the presence of [O II] dominated the redshift fitting.

5.6   Conclusions

Massive galaxies serve as probes of the merger history of the universe as these galaxies have participated most heavily in the merger process. Using samples of massive ($L > 3L^*$) red galaxies observed by SDSS at low redshift augmented with a new spectroscopic sample of galaxies targeted from deep SDSS coadded photometry and observed with the MMT, we have measured the evolution of massive red galaxies at $0.1 < z < 0.9$. Our sample is currently the largest collection of massive red galaxies spectroscopically observed at $z \sim 0.9$ and thus provides an excellent tool for constraining the evolution of the most massive galactic systems over half of cosmic history.

After correcting for passive evolution using a non-evolving Salpeter (1955) IMF, we find the magnitude at which the integrated number density of the LRG population has reached $10^{-4.5}h^3$ Mpc^{-3} is consistent with constant with a best-fit evolution of 0.03 ± 0.08 mag from $z = 1$ to $z = 0$. Simple toy models for the merger histories of massive red galaxies indicate that 1:1 merger rates larger than 25% are disfavored at 50% confidence and merger rates larger than 40% are ruled

out at 99% significance. Even if lower-mass mergers are considered, we find that the total stellar mass contained in massive red galaxies must not have grown by more than $\sim 50\%$ since $z = 0.9$. This growth rate starkly contrasts the factor of 2-4 in stellar mass growth observed in L^* red galaxies over the same epoch. The processes that regulate the growth of massive red galaxies and yet allow the large growth observed in the L^* red galaxy population are poorly understood. As the most massive galaxies reside in group and cluster sized haloes, the processes that govern the assembly of clusters or the growth or an intracluster stellar envelope may play an important role in the shaping of LRGs.

The evolution in the average LRG spectrum to high redshift also supports a purely passive fading of LRGs since $z \sim 0.9$. The composite spectrum of our high-redshift LRGs is well-described by a passively faded version of the average galaxy spectrum at $0.1 < z < 0.2$. No recent star formation is needed to explain our composite spectrum at $z = 0.9$; we constrain the mass fraction of 10Myr, 100Myr, and 1Gyr stars to be less than 0.1%, 0.5%, and 5% with 99% confidence. Star formation in these LRGs must have completely ended by $z \sim 0.9$ and very few blue stars must have been accreted since that epoch.

While our sample comprises the largest spectroscopic sample of massive red galaxies at $z \sim 0.9$ collected to date, a sample of 300 galaxies suffers from small numbers of objects per luminosity bin, especially at the highest masses. Future surveys aiming to collect spectroscopic samples of many thousand LRGs at redshifts up to $z \sim 0.7$, while at slightly lower redshifts, will have the statistics to place tighter constraints on the overall density evolution of the massive red galaxy population as well as to study the evolution in the LRG luminosity function shape to constrain the role of mass-dependent processes which regulate LRG growth.

CHAPTER 6

PRIMUS : THE PRISM MULTI-OBJECT SURVEY

6.1   Introduction

The epoch since $z = 1$ has been an era of dramatic galaxy evolution. Over the last half of cosmic history, disk galaxies have faded and grown redder as their star-formation rates have declined and L^* early-type galaxies have doubled in number (Willmer et al., 2006; Faber et al., 2007; Brown et al., 2007). The global star formation rate has declined by a factor of $\gtrsim 10$ and a large fraction of disk galaxies have had their star formation quenched and evolved into the red galaxy population since $z = 1$ (Bundy et al., 2006; Hopkins, 2004). While we have begun to understand some of the mean properties of $z = 1$ galaxies, the current generation of intermediate- and high-redshift surveys are severely limited by cosmic variance and are insufficient to understand how the stellar masses, star-formations rates, quenching from AGN feedback, clustering, and merger rates all fit into a global picture of galaxy evolution since $z \sim 1$. Quantifying evolutionary trends with redshifts requires larger redshift surveys with multiwavelength imaging spanning from the X-ray to the infrared in order to reduce the cosmic variance uncertainties and to minimize systematics associated with determinations of physical parameters.

Astronomy has entered an era of wide-field imaging. Major surveys in the UV, optical, and infrared are mapping wide areas with depth sufficient to detect large numbers of galaxies and AGN to $z \sim 1$. Of particular note are the *Spitzer* Wide-area InfraRed Extragalactic Survey (SWIRE; Lonsdale et al., 2003), the *GALEX* Deep Imaging Survey (DIS), and the *Spitzer* Shallow Survey (Eisenhardt et al., 2004) which are covering about 70 deg^2 to depths that reach below L^* at $z = 1$

from the UV to far-IR. The 2 deg^2 COSMOS field (Scoville et al., 2007) combines high-resolution imaging from the Advanced Camera for Surveys (ACS) on the Hubble Space Telescope (HST) with a rich multiwavelength dataset. Furthermore, many of the deep optical and infrared surveys now have accompanying X-ray imaging from *XMM-Newton* or *Chandra*.

While the area covered by wide-area imaging surveys has grown exponentially in the recent past, imaging alone cannot measure the three dimensional structure of the universe and is limited by observing the three dimensional universe on our two dimensional sky. Wide-field redshift surveys are necessary to effectively leverage multiwavelength imaging datasets and to maximize the scientific return. With the combinations of wide-area imaging and redshifts, we can study the distribution of stellar masses, star formation, and halo masses in diverse types of galaxies, across a wide range of environments, and as a function of redshift.

Locally, the SDSS (York et al., 2000) and 2dF (Colless et al., 2003) surveys have observed a large sample of galaxies which overcomes the cosmic variance of large-scale clustering creating a sample of ~ 1 million galaxies over a quarter of the observable sky. At $z \sim 1$, a number of projects such as the Deep Evolutionary Extragalactic Probe 2 (DEEP2; Faber et al., 2003), the Vimos-VLT Deep Survey (VVDS; Le Fèvre et al., 2004), and COMBO-17 (Wolf et al., 2003a), have mapped large volumes of the distant universe and have provided the data which has shaped our current understanding of galaxy evolution. Existing surveys at $z \sim 1$, while pioneering, do not probe volumes comparable to those observed at low-redshift and are still strongly effected by cosmic variance.

While high-precisions spectroscopic redshifts remain the gold standard for measuring galaxy distances, low-precision photometric redshifts from imaging

datasets alone have become popular because they are less observationally expensive for large samples of galaxies over wide areas (Budavári et al., 2003; Mobasher et al., 2004; Padmanabhan et al., 2005; Blake & Bridle, 2005; Gladders & Yee, 2005). The usual broadband ($R \equiv \lambda/\Delta\lambda \sim 3-5$) photometric redshifts are prone to systematic errors, have a non-trivial fraction of catastrophic failures, and, at best, have uncertainties that are large compared to the clustering lengths of typical galaxies. At $z \gtrsim 0.5$, photometric redshift errors can be large enough to produce significant uncertainty in the inferred physical quantities such as galaxy luminosities, stellar masses, and star-formation rates. To minimize the effects of these errors, the COMBO-17 project increased the spectral resolution of their photometry by measuring galaxy fluxes in 5 broad-band filters and 12 medium-band filters, resulting in $R \approx 15$. These additional filters reduced the redshift errors from 5% to 1% and lowered the fraction of catastrophic redshift failures.

This chapter describes the PRIsm MUlti-object Survey (PRIMUS), a new redshift survey aimed at obtaining redshifts for $\sim 250,000$ galaxies to $z \sim 1$ over a volume comparable to that available from low-redshift surveys at $z = 0.1$. For comparison, Figure 6.1 shows PRIMUS in relation to the volume and number of spectra of other surveys of the universe to $z = 1$. PRIMUS is able to observe large numbers of galaxies simultaneously by observing galaxies only at low-resolution leading to very efficient mapping of large areas of the sky. PRIMUS uses the Baade 6.5m Magellan telescope at Las Campanas in Chile. We replace the traditional grating or grism in the IMACS spectrograph with a specifically designed prism to obtain spectra for ~ 3000 galaxies simultaneously.

The exposure time needed to reach a given signal-to-noise ratio scales as R^2 in narrow-band imaging surveys; one factor of R for the number of filters needed to reach the desired resolution and another for the exposure time needed to reach
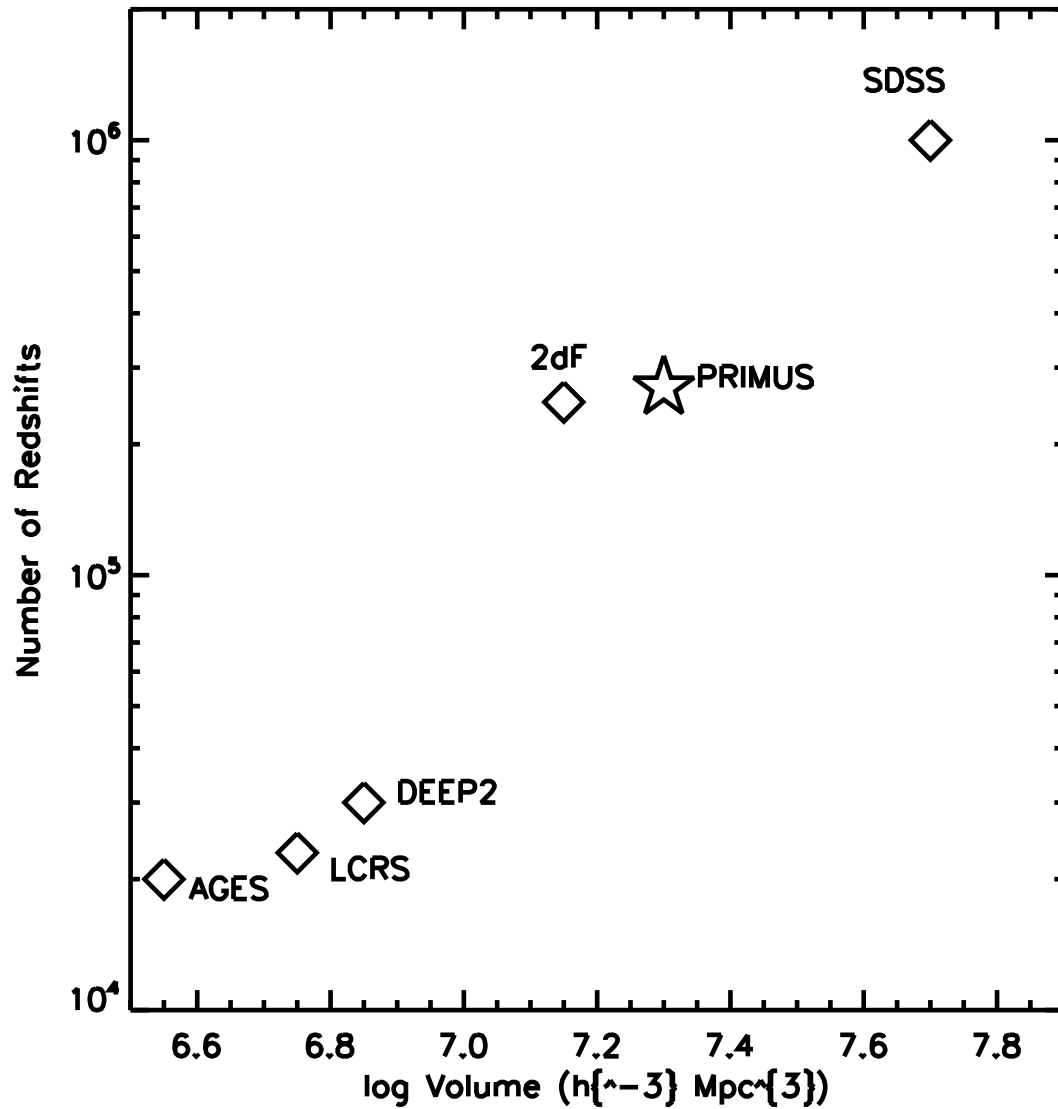
Figure 6.1 The volume and number of redshifts compared amongst several surveys at $z < 1$. PRIMUS, for the first time, probes to universe to $z \sim 1$ with volume and numbers of objects comparable to the largest low-redshift datasets.

a given imaging depth per filter. In PRIMUS, we capitalize on the weakness that imaging surveys spend the majority of their imaging pixels measuring blank sky. It is more efficient to disperse light from each object and fully utilize the detector space available; in this situation, exposure times go as R to reach a given signal-to-noise per resolution element. While this method may require two slit masks to minimize the effects of collisions between traces and has the added inefficiency of spectroscopic optics, at $R \approx 20$, the efficiency gain using low-resolution spectroscopy is more than enough to compensate for these extra overheads.

This chapter summarizes the design, execution, and data processing involved with the PRIMUS project. At the time of this writing, many of the details of the reduction code are in flux; while this chapter will provide an overview of the project, none of the details included here are firmly finalized. The interested reader should read PRIMUS data release publications for full survey details. In §6.2, we detail the target selection, photometric catalogs, and sparse sampling methods used when executing PRIMUS. The two-dimensional data and the processing steps completed in taking the two-dimensional images and producing extracted one-dimensional spectra are described in §6.3 and the calibration procedures used on our one-dimensional spectra are detailed in §6.4. The current implementation of the PRIMUS redshift finder is described in §6.5. We summarize the current status of PRIMUS reductions and conclude in §6.6.

6.2 Target Selection

6.2.1 Photometric Catalogs

One fundamental limitation of any spectroscopic survey is that prior imaging is required to select objects of interest. The strategy for PRIMUS was to capitalize on the wealth of existing wide-field imaging in the optical to create an optically

flux limited survey and to focus most heavily on datasets with existing multi-wavelength imaging from *Spitzer*, *Chandra*, or *GALEX*.

White using pre-existing optical imaging alleviates the need for new imaging observations, using imaging catalogs from separate teams with different cameras on telescopes at various sites leads to inhomogeneous selection functions between each imaging survey. Table 6.1 lists the imaging catalogs used for PRIMUS observations. The filters and photometric reference system vary between surveys, so care must be taken when trying to select homologous samples of objects spanning all the surveys. Even a simple flux limited survey is not trivially created based on this imaging data; no filter is shared between each dataset. Section 6.2.2 discusses the solutions used to address these dataset homogeneities.

The fields listed in Table 6.1 were not chosen randomly. Each of these fields have either publicly available images, catalogs, or existing imaging obtained through new collaborations. Furthermore, we focused on fields with existing multiwavelength data available from *Spitzer*, *Chandra*, XMM-*Newton*, or *GALEX* or high-resolution imaging from *HST*. Table 6.2 highlights the multi-wavelength data available in several of the fields observed with PRIMUS. These multiwavelength data are of great value as the infrared photometry provides robust measures of the stellar masses of sample galaxies, IR+UV photometry probes the total obscured and unobscured star formation rate, and the X-ray imaging serves as a means to isolate active galaxies.

6.2.2 Target Selection Criteria

In choosing PRIMUS targets, we want a full census of all galaxies at $0.2 < z < 1.0$. While we don't formally select against galaxies at $z < 0.2$, the volume probed over tens of square degrees is quite small so the final statistics will be quite poor within PRIMUS at these redshifts. At $z \gtrsim 1$, the 4000Å break and Balmer break

Table 6.1.   Optical Imaging Catalogs Used to Select PRIMUS Targets

Survey	Area (deg^2)	Filters	Photometric System
(1)	(2)	(3)	(4)
CDFS	5.3	$ugriz$	Vega
XMM-SWIRE (CFHTLS)	18.3	$ugriz$	AB
XMM-SWIRE (Subaru)	1.2	BVR_ciz	AB
COSMOS	2.0	ACS814W	AB
DEEP2	2.0	BRI	AB
DLS - D4	3.5	$BVRZ$	Vega
ELAIS S1	1.5	BVR	Vega

Table 6.2.   Multiwavelength Imaging in PRIMUS Fields

Survey	*Spitzer*	*GALEX*	X-Ray
(1)	(2)	(3)	(4)
XMM-Swire	X	X	X
ELAIS S1	X	X	$\cdots$
CDFS	X	X	P[a]
DEEP2	X	X	X

[a]The central region of the CDFS has *Chandra* imaging

redshift into the extreme red making redshift determinations more difficult. At $z > 1.4$, the 4000Å break redshifts out of the optical removing the key feature used when fitting low-resolution spectra or broadband photometry to derive a redshift.

Using a set of color cuts to select galaxies in the redshift range of most interest can also remove galaxies with peculiar colors and requires a homogeneous set of photometry. Given the inhomogeneous optical passbands used in our targeting photometry, variable relative depths of each imaging dataset, and non-aperture matched fluxes in many of the targeting catalogs, color pre-selection would likely result in very inhomogeneous galaxy samples making statistical investigations difficult. Furthermore, in PRIMUS, we would like to measure the evolution of galaxies internally throughout the full $0.2 < z < 1.0$ redshift range and thus any redshift-dependent incompleteness caused by imperfect color cuts would bias our measurements. Instead of a set of optical color cuts, we rely on a simple flux-limited sample for galaxy targets.

Our goal in target selection was to create an $i < 23$ sample of galaxies with which to perform our statistical analyses of galaxy evolution. While early data and signal-to-noise simulations showed that our redshift success for galaxies at $i > 22.5$ would be significantly degraded compared to our goal of $\sigma_z/(1+z) \sim 1\%$, certain classes of galaxies such as emission line objects or AGN may yield redshifts to fainter limits. Thus, our general targeting strategy was to fully sample the $i < 22.5$ galaxies and to target fainter galaxies with an *a priori* known sparse sampling rate. As all targeting weights are known exactly and are saved, we can observe a subset of our full photometric galaxy sample and statistically reconstruct it from our sparsely sampled spectroscopic dataset. The details of the sparse sampling used in PRIMUS is described in §6.2.3.

In general, we use the star-galaxy separation provided by the optical imaging teams to remove point sources from our targeted sample. For fields with existing *Spitzer* imaging, we add additional cuts to remove stars from the sample without also removing AGNs. Objects marked as point sources in the optical imaging but passed any of the following cuts were flagged as AGN candidates and included in our targeting sample.

$$[3.6] - [4.5] > -0.1 \tag{6.1}$$

$$[3.6] - [5.8] > -0.4 \tag{6.2}$$

$$[3.6] - [8.0] > -1 \tag{6.3}$$

$$[3.6] - [24] > -2 \tag{6.4}$$

$$g - r < 0.9 \tag{6.5}$$

$$u - g < 0.7 \tag{6.6}$$

$$(r - i) - 0.45(g - r) - 0.03 > 0.2 \tag{6.7}$$

Equations (6.1)-(6.7) keep point sources with optical or IRAC colors consistent with being an AGN or inconsistent with colors on the stellar locus. In the ELAIS-S1 field, in which we only have BVR optical photometry, we exclude Equations (6.5) - (6.7) but retain the *Spitzer* cuts. Figure 6.2 shows the optical color-color space for point sources in the SWIRE observations of the *Chandra* Deep Field South. The blue asterisks mark objects classified as stars and lie on a well-defined stellar locus in these colors. Similarly Figure 6.3 shows the IRAC color-color space of both galaxies and point sources in the same dataset. In general, AGN have red $[3.6\mu\mathrm{m}] - [4.5\mu\mathrm{m}]$ colors compared to galaxies and stars due to their non-thermal continua. The AGN candidates separated from the main AGN locus are likely either unresolved galaxies or stars with peculiar colors which are included with our broad AGN selection.
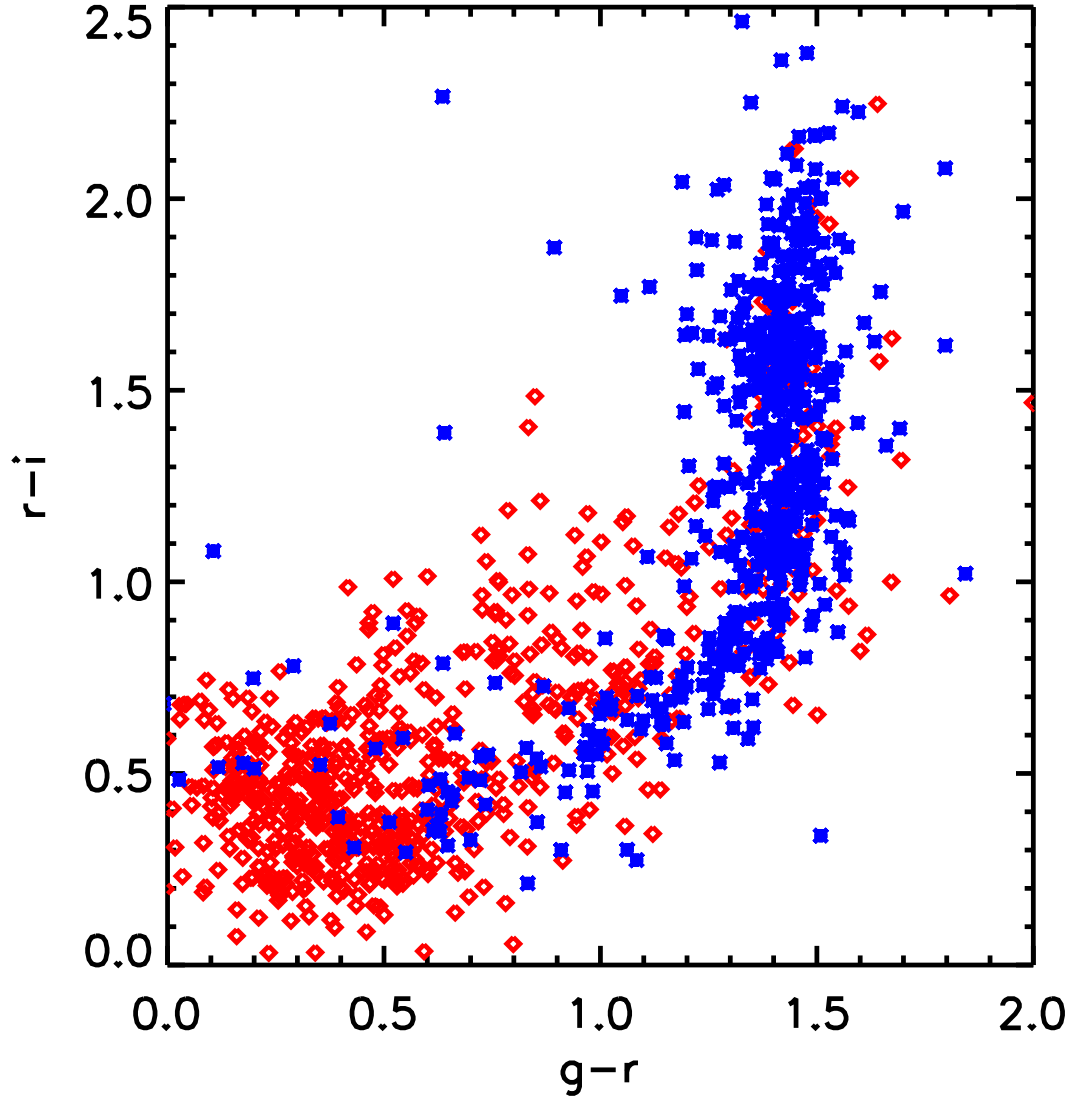
Figure 6.2 Optical $g - r$ versus $r - i$ color-color space for point sources detected in the SWIRE observations of the *Chandra* Deep Field South. The blue asterisks show point sources which are unresolved in the optical i-band imaging and do not display any characteristics suggesting that they might be AGNs as detailed in Equations (6.1) - (6.7). The red diamonds mark the colors of AGN candidates which are targeted for PRIMUS spectroscopy.
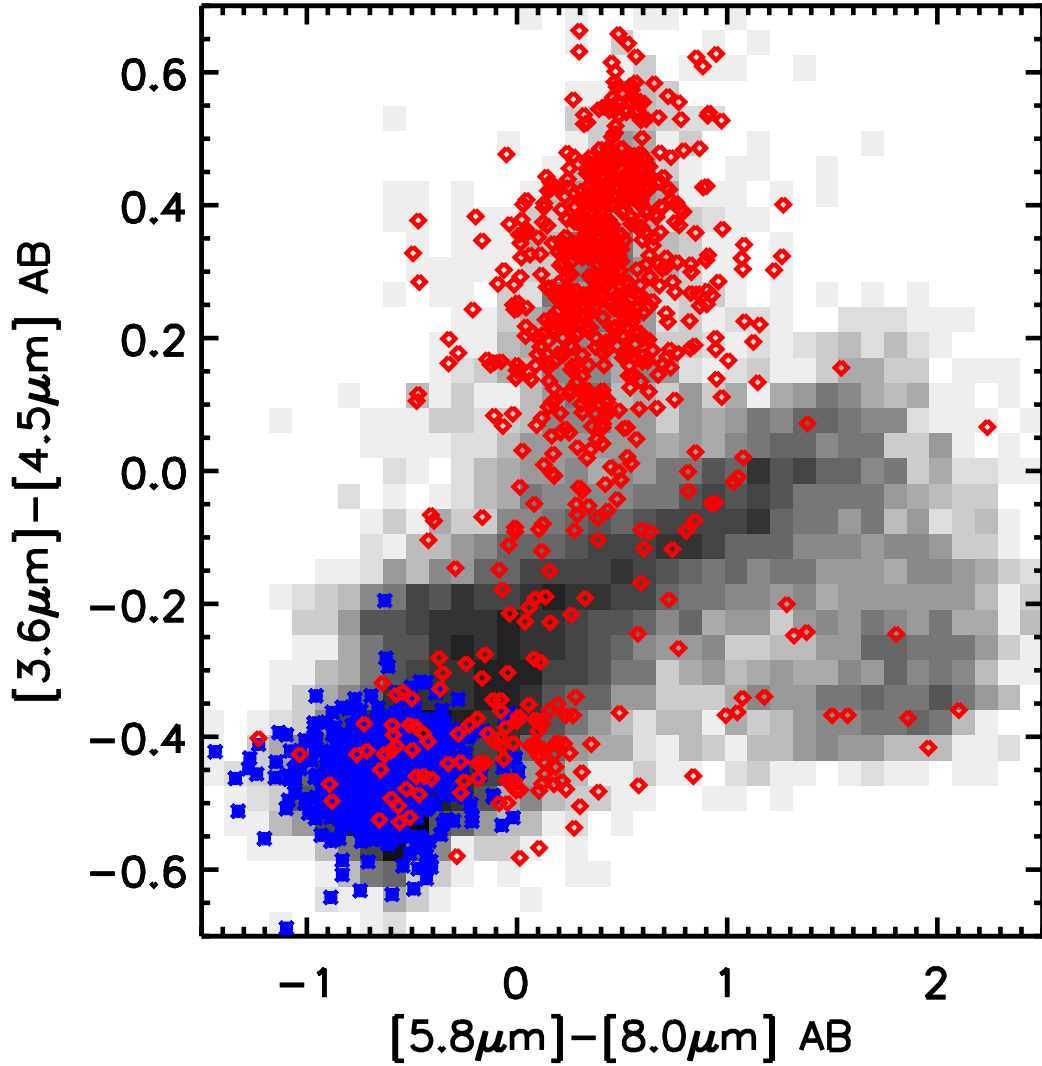
Figure 6.3 Mid-infrared colors of stars, galaxies, and AGN targets from SWIRE observations of the *Chandra* Deep Field South. The greyscale shows the color distribution of all mid-infrared detect objects with $i < 22.5$ and detections in all four *Spitzer* IRAC bands regardless of optical morphology. The red diamonds and blue asterisks show the colors of AGN candidates and stellar contamination as described in Figure 6.2 and the text. As the mid-infrared photometry probes the Rayleigh-Jeans tail of the stellar continua, stars cluster around $[3.6\mu\mathrm{m}] - [4.5\mu\mathrm{m}] \sim -0.45$ and $[5.8\mu\mathrm{m}] - [8.0\mu\mathrm{m}] \sim -0.6$.

While we would like to select our targets based only a simple i-band flux limit, not all of the existing optical imaging datasets has i-band imaging. In the event that i-band photometry was unavailable for a given field, we then create a flux-limited sample based on either $r-$, $R-$, or $I-$band imaging. Table 6.3 lists the flux limits used in each of our fields explicitly. As galaxies, in general, don't have zero color, a flux limited sample of $i < 22.5$ does not translate to $R < 22.5$. In adjusting the flux limits for the different targeting imaging datasets, we chose flux limits such that the cumulative galaxy number counts at the flux limit were comparable between surveys. In essence, this corrects the flux limit for the average color of galaxies in our sample, but individual objects are not targeted to different depths based on their observed colors. Clearly, this will lead to varying selection functions between targets selected from different imaging surveys and will need to be modeled when using the ensemble PRIMUS galaxy sample.

6.2.3 Sparse Sampling

The footprint of PRIMUS spectra covers 30" x 8" on the sky and thus any close pairs of galaxies will have, at maximum, only one galaxy of the pair observed on a given slit mask. In this case, the two-point correlation function will be unrecoverable due to the large spectroscopic incompleteness at small and intermediate scales. To ensure that the two-point correlation function is well-defined on these scales and to increase our completeness, we observe each PRIMUS pointing with two separate masks. This method naturally breaks slit conflicts for close pairs as each galaxy of the pair is observed.

In detail, galaxies are often found in groupings larger than pairs. In this case, two masks cannot fully observe every galaxy in the group and thus targets must be chosen in such as way that the full photometric sample can be reconstructed

Table 6.3.   Flux Limits Used to Select PRIMUS Targets

Survey	PRIMUS Target Name	Flux Range
(1)	(2)	(3)
CDFS	SWIRE_BRIGHT	$i < 22.5$
	SWIRE_FAINT_SPARSE	$22.5 < i < 23.5$
XMM-SWIRE (CFHTLS)	CFHTLS_BRIGHT	$i < 22.5$
	CFHTLS_FAINT	$22.5 < i < 23.5$
XMM-SWIRE (SUBARU)	SWIRE_BRIGHT	$i < 22.5$
	SWIRE_FAINT_SPARSE	$22.5 < i < 23.5$
COSMOS	COSMOS_GALAXY	$I < 22.7$
	COSMOS_GALAXY_FAINT	$22.7 < I < 23.2$
DEEP2	DEEP2_COMP_BRIGHT	$R < 22.8$
	DEEP_COMP_FAINT	$22.8 < R < 23.5$
DLS - D4	DLS	$R < 22.8$
	DLS_FAINT	$22.8 < R < 23.3$
ELAIS S1	SWIRE_BRIGHT	$r < 22.7$
	SWIRE_FAINT_SPARSE	$22.7 < r < 23.7$

statistically from the spectroscopic sample for robust clustering and galaxy evolution studies. In a simple case, one would consider every galaxy in the conflicting group and randomly select the galaxies that would receive slits. In this simple case, however, galaxies in dense environments are systematically chosen more often compared to field galaxies when the conflicts are resolved as they will dominate the number of galaxies in colliding groups. In order to more fully sample the range of galaxy environments, PRIMUS uses a more complex method in resolving conflicts. We divide the galaxy sample into two groups - group A contains the bright galaxies ($i < 22.5$) and group B contains a fainter collection of galaxies ($22.5 < i < 23.5$). The number of A+B collisions is calculated for each galaxy in the two samples. Any galaxy in group B that has more than 2 collisions is then sparse sampled at a rate of 30%. This sparse sampling is done to ensure that the faint galaxies, which will likely have higher redshift incompleteness and less secure redshifts, do not dominate the assigned slits compared to the bright galaxies where we predict better redshift performance.

After the sample of faint galaxies has been sparse sampled, we again count the number of A+B collisions for every galaxy in the surviving A+B superset. Now, we assign a spare sampling probability of

$$p(N_{\text{conflicts}}) = \begin{cases} 1 & N_{\text{conflicts}} \leq 2 \\ \frac{1.8}{N_{\text{conflicts}}} & N_{\text{conflicts}} > 2 \end{cases} \tag{6.8}$$

to each galaxy. This entire sample is then sparse sampled according to this probability. That is, every galaxy is assigned a random number between 0 and 1; if this random number is smaller than $p(N_{\text{conflicts}})$, then the object remains in the galaxy sample. Otherwise, the galaxy is assigned a lower priority, so that is might be added as a filler object after all the high priority targets have been targeted. We consider the sample of surviving sparsely sampled galaxies our primary galaxy

sample. With this density-dependent sparse sampling algorithm, very dense regions are more heavily spare-sampled compared to field areas. This ensures that spectra are taken for large samples of galaxies over a broad range of environments. As all of this density-dependent sparse sampling is done using well-defined weights which are tracked throughout the target selection process, the full photometric sample can be statistically recovered and galaxy environments, clustering, and the evolution of galaxy properties can be derived with robust statistics.

Slits are assigned to each mask from the primary sample with the goal of placing the maximum number of non-overlapping slits possible onto the mask. After the sample of primary galaxies have been selected, any galaxies which did not survive the density dependent sparse-sampling but which can be placed onto the mask without colliding with primary objects are targeted. Finally any filler objects, such as very faint galaxies, galaxies provided from external catalogs as objects of interest, or galaxies which have already been targeted on other PRIMUS masks are added to the mask at the lowest priority.

In addition to galaxy targets, we also target 10-16 bright stars which are used to acquire and align the telescope and instrument on our field. Furthermore, we target 20 to 50 blue point sources per mask for flux calibration. These F-star candidates were used with great success by SDSS and AGES; the simple spectra of F stars in the red and the large surface density of them on the sky make them ideal as instantaneous probes of the throughput of the system and transparency of the sky. The general strategy used to select these objects was to isolate the blue tip of the stellar locus in optical color-color space based on selection used by SDSS and AGES previously.

Figure 6.4 shows the layout of one PRIMUS mask in the XMM-SWIRE field.

The grey circular region shows the usable portion of the IMACS field of view in f/2 mode; there is strong vignetting in the IMACS camera that makes the corners of the field of view unusable. Each of the small points shows a possible target; the colored points each show objects for which a slit was cut on this mask. The blue asterisks show the positions of blank sky slits used as quality assurance checks for our spectral extractions. The red diamonds mark filler objects which were added to the mask after the high priority primary galaxy sample (green circles) and calibration F stars (magenta stars) were assigned slits. The black squares mark the locations of alignment stars used to acquire the field but which are not extracted. Generally, we find that we can assign slits to 95% of the primary galaxy sample. Typical PRIMUS masks have 2500-3000 objects targeted.

6.3   Two-Dimensional Reductions

6.3.1   Prism Characteristics and Data Overview

The resolution of PRIMUS spectra has a strong dependence on wavelength. Figure 6.5 shows the resolution of PRIMUS prism per pixel ($\lambda \backslash \Delta\lambda$) from 4000 Å to $1\mu\text{m}$. With this resolution, the full optical spectrum from $\sim 4200\text{Å}$ to $1\,\mu\text{m}$ covers ~ 150 pixels on the detector. In the red, the night sky spectrum is dominated by a forest of emission lines which are completely unresolved at the resolution of PRIMUS. Figure 6.6 shows both a high-resolution sky spectrum from Gemini North and the same spectrum after it has been convolved to PRIMUS resolution. As the sky is much brighter than the objects considered here, robust sky subtraction is required in order to measure redshifts for the faintest galaxies in our sample. High resolution spectroscopy can resolve the night sky lines in the red and measure the spectrum between these lines, but at the PRIMUS resolution, we do not have any information about individual lines and only the ensemble sky
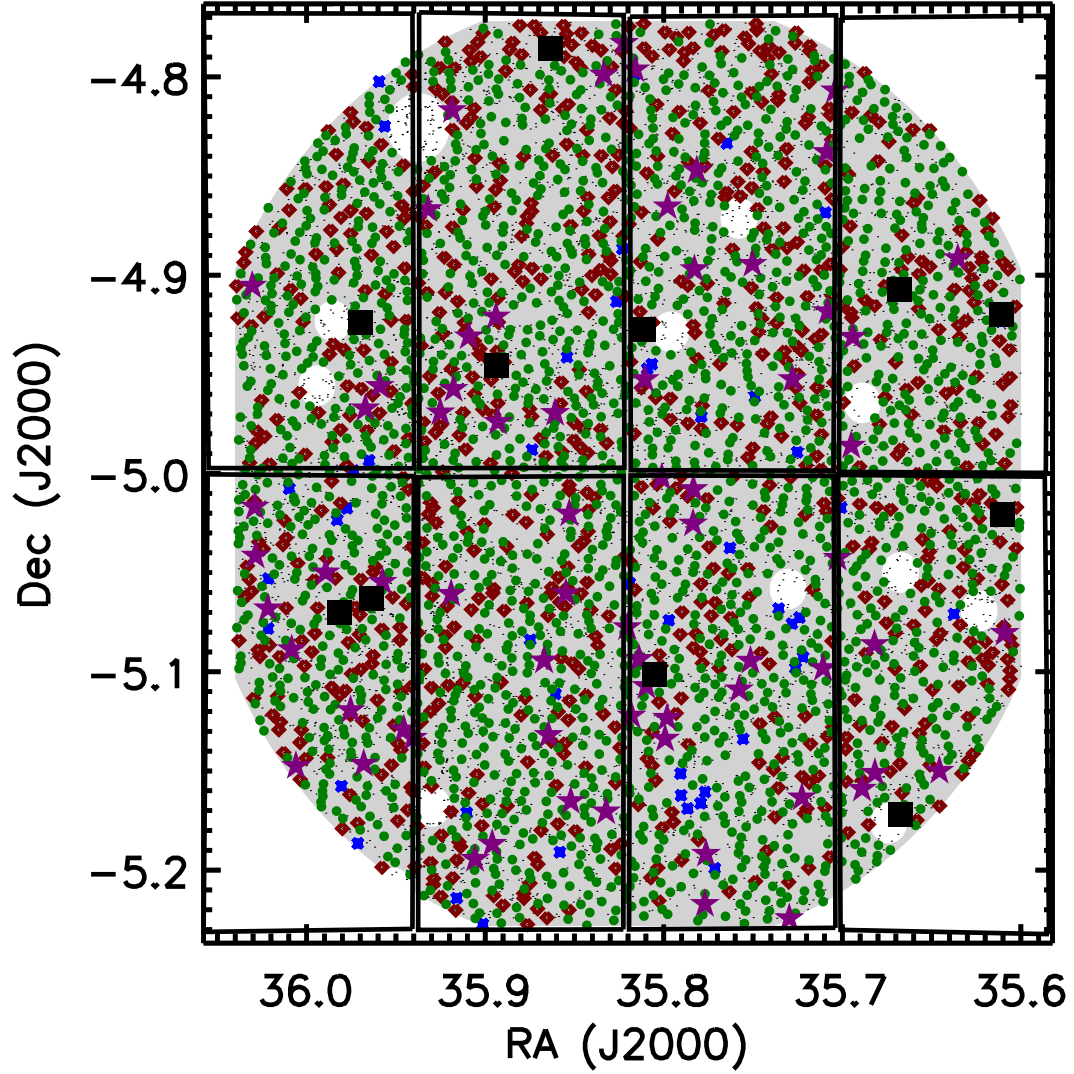
Figure 6.4 Target layout on PRIMUS mask #210. The 8 rectangular boxes mark the locations of the 8 IMACS CCDs on the field; the corners of the IMACS field of view is heavily vignetted, so only the grey shaded region is used when choosing targets and modeling the PRIMUS window function. The small black points show each of the possible targets in the field while the colored points mark the locations of objects which slits on this mask. The high priority objects (magenta stars marking the calibration F stars and green circles marking the primary galaxy sample) are selected first and then any remaining area is filled with either lower priority filler objects (red diamonds) or empty sky slits (blue asterisks).
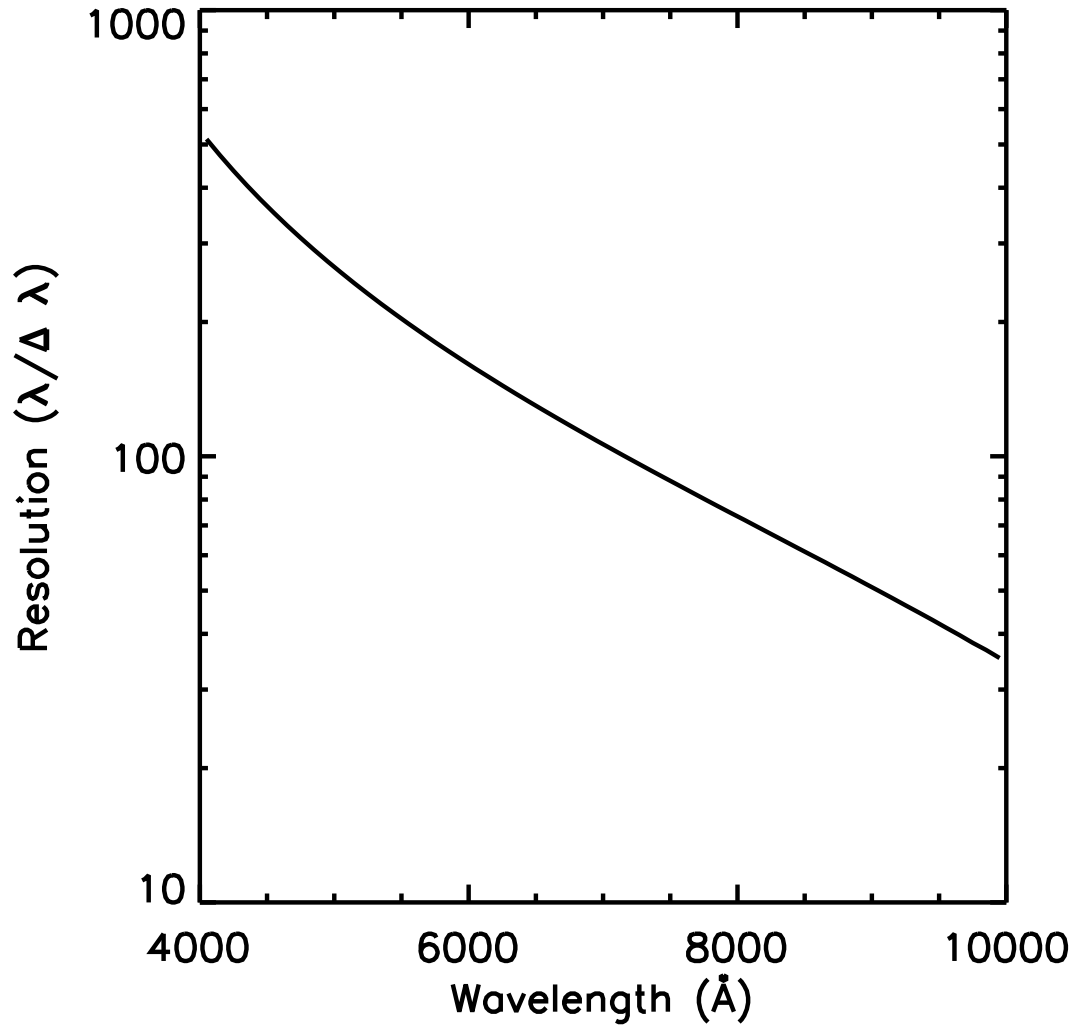
Figure 6.5 Resolution per pixel of the PRIMUS prism ($\lambda \backslash \Delta \lambda$) from 4000Å to 1μm. The strong wavelength dependence results in higher precision spectroscopy in the blue compared to the red. Furthermore, moderate strength emission lines will only be visible if they are in the blue. The strong Balmer and 4000Å breaks of galaxies throughout the $0.2 < z < 1.0$ redshift range are sufficient for redshift determinations even if the break appears in the low-resolution red end of PRIMUS spectra.
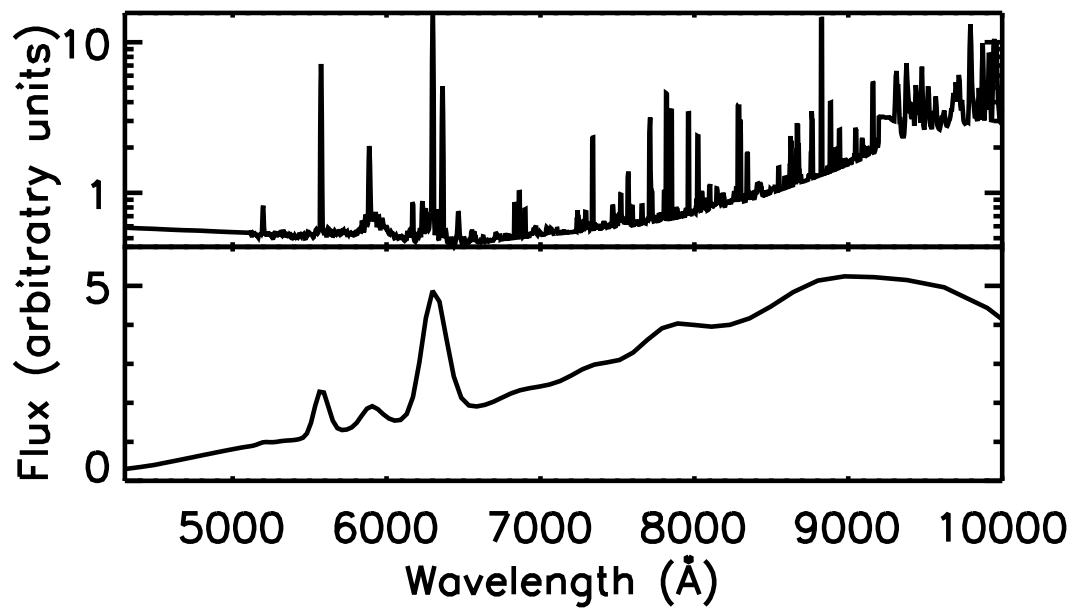
Figure 6.6 The night sky spectrum measured during a dark sky from Gemini compared at both high resolution (top panel) and convolved to the resolution of PRIMUS observations (bottom panel). To show detail in the high-resolution spectrum, the top panel is plotted on a log scale while the low-resolution bottom panel uses a linear range. The strongest sky lines in the blue are still visible at PRIMUS resolution, but the forest of emission lines in the red, where the PRIMUS resolution is quite small, are unresolved.

spectrum.

The CCDs used in the IMACS camera are not thick chips and thus suffer from modest levels of fringing in the red due to the presence of monochromatic emission lines in the night sky spectrum. In order to minimize the effect of flat-fielding imperfections and fringing on our final sky subtraction, we observe in nod & shuffle mode (e.g., Glazebrook & Bland-Hawthorn, 2001). Using this method, we cut two slits for each target object. First, we acquire the field, using the bright alignment stars placed on each CCD. The shutter is opened, usually for 60s, observing the object plus sky light in slit A while slit B only observes the sky. After this 60s exposure, the shutter is closed, the telescope is nodded such that the object now falls in slit B. The charge gathered in the CCD is shifted up on the detector (either 8 or 10 pixels depending on the specifics of our mask design) such that the light from the first exposure is in a non-illuminated portion of the chip. The shutter is then reopened and another 60s is taken with slit A observing only sky and slit B observing both sky and object. The shutter is then closed, the telescope nodded again to return the object to slit A, and the charge shuffled back to its original location. In this way, both the sky and object are observed through each slit so variations in the laser slit cutting and slit size (and thus resolution) differences do not affect the sky subtraction. Furthermore, since the physical pixels which collect the light from slit A in the sky position and the slit A sky+object position are the same, flat-fielding errors and fringing in the CCDs do not lead to sky-subtraction errors. While the nod & shuffle method provides a perfect sky subtraction in the presence of flat-fielding and fringing errors, for a fixed exposure time, the signal-to-noise ratio in the final spectra are degraded by a factor of $\sqrt{2}$ as the sky spectrum that is subtracted has half the exposure time as it would for a standard observation. This shorter effective exposure time leads to a factor

of 2 less photons measured in the sky and thus the sky subtraction errors are increased by Poisson noise. PRIMUS observations typically consist of four to six nod & shuffle exposures with a total on-source exposure time of (60s $\times$ 8 cycles $\times$ 2 apertures) 960s.

Generally, slit A and slit B could have any orientation desired with respect to each other. Often, rather than cutting two slits for each object, the object is nodded between two positions on a single long slit. In PRIMUS, we chose to nod between two slits separated both along the spatial direction and dispersion direction of the IMACS focal plane. By including a nod along the spectral direction, a single bad column affects two different wavelength in slit A compared to slit B. Thus, a single bad column does not remove all information at a given wavelength for an object; wavelengths masked in slit A will correspond to an unmasked pixel in mask B. Panels (a) and (b) of Figure 6.7 shows examples of the slit layout for PRIMUS observations and a portion of a raw data frame showing 2 objects before any processes has been completed.

Before any extraction is performed on raw images, we first create a mask of known bad pixels and cosmic rays. Throughout all of our reduction steps, we track the direct image, a two-dimensional pixel mask, and an inverse variance image to ensure that any information about masked pixels is properly propagated through the extraction and spectral fitting. A global bad column mask is applied to every IMACS image from our survey; bad columns were identified manually. Masked columns are interpolated over and are assigned a mask bit and a zero inverse variance such that they are not used in any spectral fitting. We then construct the median of all of the PRIMUS observations of a single field; this median image is clean from cosmic-rays. Each individual exposure is then compared to the median image and any pixel that deviates from the median im-
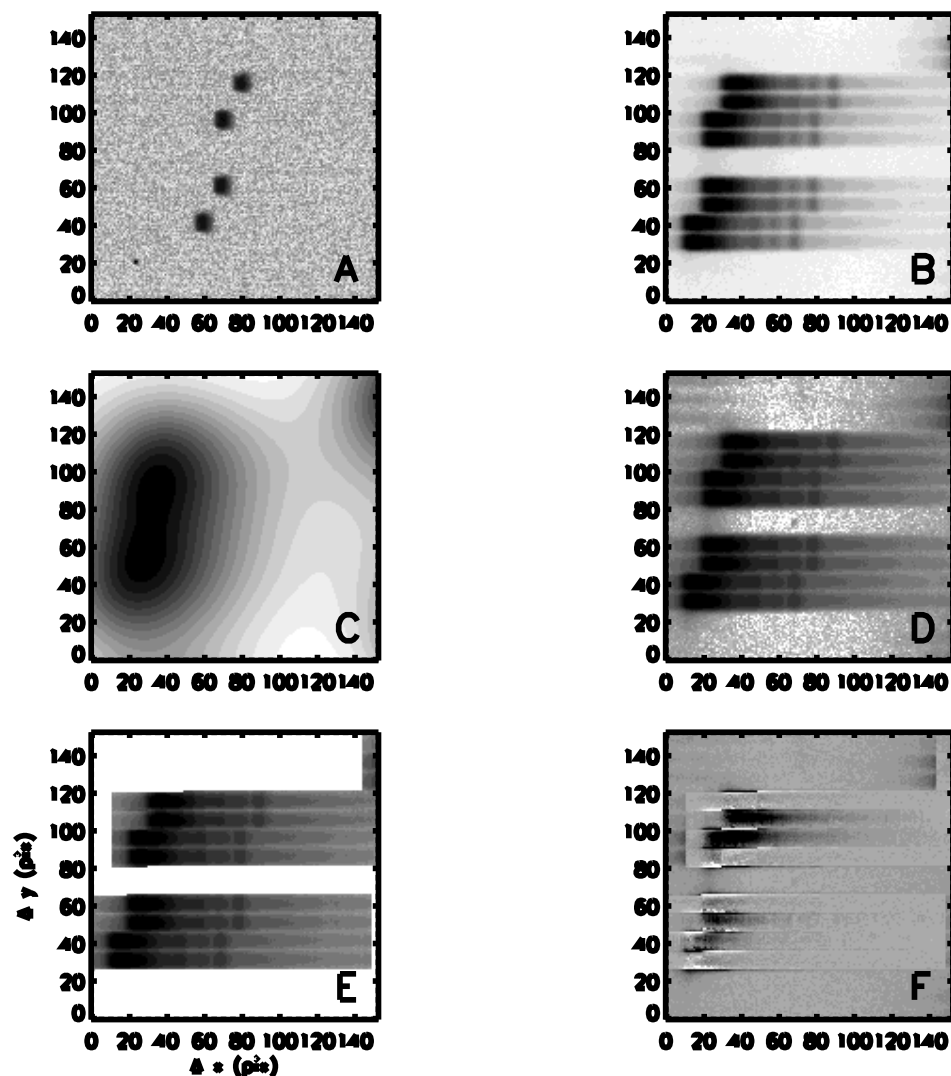
Figure 6.7 Six stages of two dimensional data processing completed in the PRIMUS pipeline. Panel (a): Four slits in a PRIMUS slitmask without a disperser. The four slits mark the A and B positions for two objects targeted for spectroscopy. Panel (b): Raw data frame from IMACS. The four traces for each object (from top to bottom) are the A position sky, A position sky+object, B position sky+object, and B position sky. Panel (c): Scattering light halo image constructed as described in §6.3.2for the same region of the image as shown in panels (a) and (b). The scale in this panel is quite different from the other panels; the peak of the image shows in panel (c) is 2% of the peak in panel (b). Panel (d): Halo-subtracted two-dimensional image after the halo in panel (c) has been subtracted from the raw image. Panel (e): Modeled flux contained in the sky as described in §6.3.3. Panel (f): sky-subtracted two-dimensional image. Only pixels contained within each of the 4 traces for the two objects in the image have been subtracted. Outside these regions, excess light can be seen in the image but this light is not included when objects are extracted.

age at 5σ or more compared to the Poisson noise and read noise expected in the image are masked as cosmic rays. All pixels within 1 pixel of the inferred cosmic ray locations are masked out, as well. All masked pixels are tracked in the bad pixel mask, masked pixels in the raw image are set to zero, and have their inverse variances set to zero. Once each exposure has a cosmic ray mask, we construct the total light image for each mask by adding the the counts from each input image. The average image is then constructed by dividing each pixel in the summed image by the number of unmasked pixels that contributed to the total.

6.3.2 Scattered Light

IMACS images suffer from large diffuse haloes of light around bright sources. The total light contained in this halo is correlated with the flux of nearby bright stars. The halo from one bright star an be seen to cross CCD gaps, indicating that the haloes are likely not due to scattering within the CCDs themselves and are likely created in the camera optics. The presence of excess light that is not subject to the nod & shuffle procedure such as this large scattering halo term will naturally lead to errors in the nod & shuffle sky subtraction and thus it is important that we remove the contribution of the scattered light before performing out sky subtraction.

We quantify the IMACS scattering halo term by choosing a set of well-isolated slits in the PRIMUS images and construct a convolution kernel which describes the light in pixels outside of the object and sky traces in the vertical direction. We find a Lorentzian-like kernel, after being convolved with the raw data frame, reproduces the haloes observed on large scale. Quantitatively, we create a circularly symmetric kernel, s_{circ} such that

$$r^2 = \frac{x_{\text{pix}}^2 + y_{\text{pix}}^2}{800} \tag{6.9}$$

$$s_{\text{circ}} = \frac{1}{(1 + r^2)^{1.08}}. \tag{6.10}$$

While this kernel does a modest job at removing the large scale halo, the wavelength of the incidence light appears to have a modest effect on the shape of the scattering light halo. To parameterize this, we add a dipole-like term to the kernel:

$$\theta = \arctan \frac{y_{\text{pix}}}{x_{\text{pix}}} \tag{6.11}$$

$$s_{\text{dip}} = s_{\text{circ}} \cos \theta. \tag{6.12}$$

This dipole term mimics the behavior of a wavelength-dependent kernel without requiring a detailed understanding of what wavelength of light is contributing to each pixel. Figure 6.8 shows both a one-dimensional cut through the the circularly symmetric halo and the two-dimensional shape of the final halo. Once the halo kernel has been constructed, the raw IMACS image is convolved with the kernel to make a two-dimensional mapping of the scattered light. In order to properly normalize the scattered light image, we mask out any pixels which have light contributions from the object traces themselves. We then fit a two-dimensional quadratic normalization in x_{pix} and y_{pix} by comparing the unmasked pixels to the two-dimensional halo image. The best-fit spatially-dependent normalization is applied to the two-dimensional halo image and then subtracted from the raw image. Figure 6.9 shows the flux along one column in a raw image compared the the flux contained in the halo model subtracted from the data. Panel (c) in Figure 6.7 shows the halo an example of the two-dimensional halo image subtracted from the data and panel (d) shows the IMACS image after halo subtraction has been performed.

The master halo image is generated based on the coadded image for each mask. In order to guard against introducing fluxing errors due to varying trans-
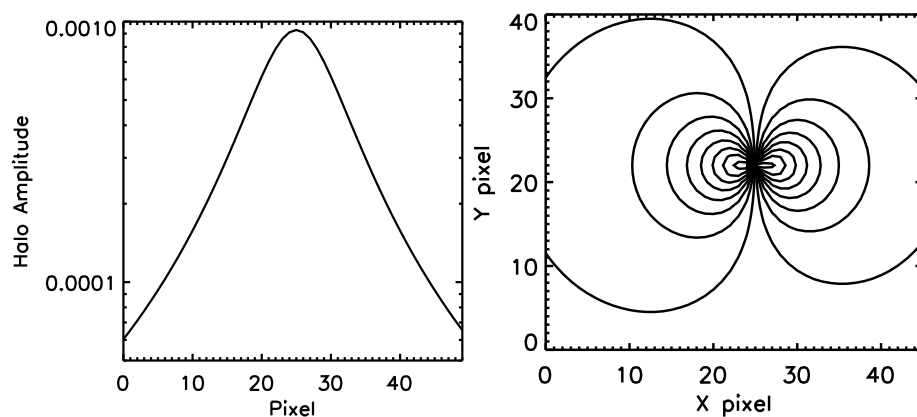
Figure 6.8 Scattering halo model subtracted from PRIMUS images. Panel (a): One dimensional cut through s_{circ}, the circularly symmetric scattered light halo. Panel (b) : Final kernel after the dipole-like term is included. This kernel is convolved with the raw IMACS image to produce a two-dimensional image to be subtracted from the raw image to remove the contribution of scattered light before spectra are extracted. Before this subtraction is performed, the two dimensional image of the halo is compared to the raw image after the pixels on which the spectral traces lie have been masked out. A two-dimensional quadratic fit is performed to determine the best halo amplitude as a function of x and y location on the CCD. After this spatially varying amplitude has been applied to the halo image, it is subtracted from the raw image.
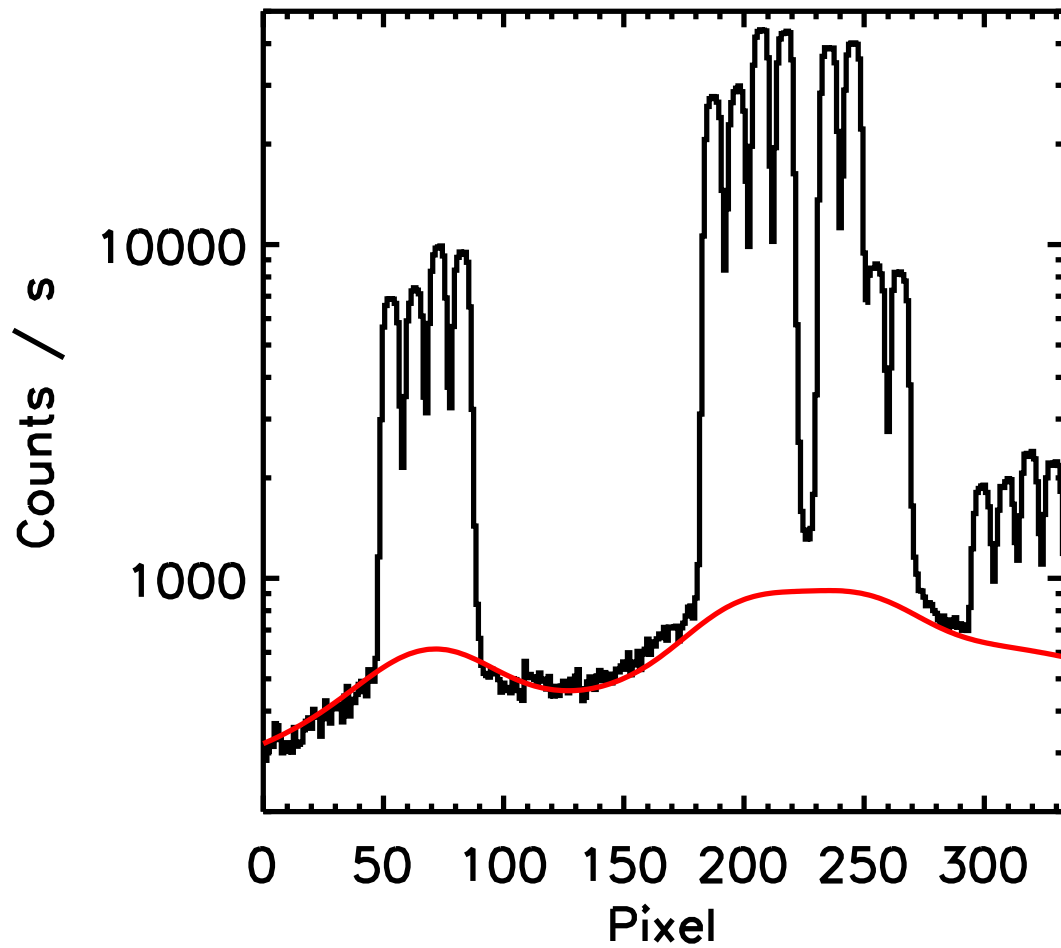
Figure 6.9 IMACS scattered light halo subtraction. The black line show a cut along a column in a raw IMACS frame. The IMACS image has been biased subtracted and thus any light between the spectral traces is due to scattered light in the instrument. The red line shows the halo model that is subtracted from the image before spectra are extracted.

parency, seeing, and atmospheric extinction during the course of observing a single mask, we do not perform extractions on the coadded image. Instead, we use the coadded image to generate the cosmic ray pixel mask for each exposure and generate the scattered light halo correction and then use this mask and correction when extracting each of the individual exposures taken for a given mask.

6.3.3   Spectral Extraction

Once the scattered light contribution has been subtracted from the individual exposures of a mask, we perform a three-stepped extraction to convert the two-dimensional images to one-dimensional spectra for each of the observed objects. Direct imaging flat fields which are produced through observations of the night sky during twilight or an illuminated screen in the dome cannot be directly applied to the nod & shuffle observations used in PRIMUS observations. As the image pixel that received light recorded at position x, y in a raw PRIMUS image could have either been the physical pixel at location x, y on the array or $x, y + N_{\mathrm{shuffle}}$, care must be taken account to account for the nod & shuffle pattern. In the limit that every pixel on the focal plane received photons in both positions A and B, the flatfield appropriate for a nod and shuffled image would be the mean of the direct image flat and the same flat which has been shifted by N_{shuffle} in the readout direction. Correcting for the flatfield when using slitmasks is more problematic each pixel receives some photons in each nod position but the fraction in position A versus position B is not known *a priori*. Without this missing information, we choose to correct each pixel by the mean flatfield in the two nod positions; any pixel with a flatfield blemishes less than 75% of the mean are flagged as suspect due to this flat fielding uncertainty.

During the first stage of spectral extraction, the pipeline has no information about the spatial extent of a given object. The goal for the first pass of extrac-

tion is to develop a spatial profile for each object that will be used in subsequent stages of reduction. In this stage, the sky+object traces are fit as a linear combination of the sky values measured in the sky-only traces and $N_{\mathrm{slitpix}} - 2$ Gaussians separated by 1 pixel and with a width of 0.8 pixels. These Gaussians form an adequate basis set to model the light inside each slit as a function of wavelength. While the signal to noise in each column may be too low to measure the robust spatial distribution of light in each column, especially for the faintest objects in our survey, the total object flux contained within the slit is sufficient to measure the width of the light distribution. Thus, after fitting each column, the total flux contained in the Gaussian model is summed along the spectral direction in each trace. We fit a single Gaussian to the total flux to determine the best spatial offset and width of the flux distribution.

The second stage of spectral extraction is similar to the first except proceeds with the knowledge of the spatial extent of each object derived in the first step. This phase of the extraction also removes the requirement that the sky contribution to the sky+object trace be identically the sky measured in the sky-only trace. Instead the value of the sky is fit simultaneously with the object model. This change in the sky fitting allows the edges of the traces, were there may be contribution from the wings of two nearby traces, to be handled properly. Figure 6.7 (panels (e) and (f)) show the results of second pass extraction. Panel (e) shows the best-fitting two-dimensional sky model and panel (f) shows the science frame after this sky model has been subtracted. The third stage of spectral extraction uses the model for the spatial distribution of light measured in the first pass of extraction to perform an optimal extraction (Robertson, 1986) of the object light.

The PRIMUS data-model keeps the extracted spectra from slit A and slit B sep-

arate (as they are subject to different bad pixel masks and are observed through different physical slits. As discussed in §6.5, the observations from slit A and slit B are kept separate throughout the redshift fitting process as well. While our analysis doesn't use a coadded spectrum between slit A and slit B, a coadded spectrum can be helpful for quality assurance tests and thus we perform a simple coaddition of slit A and slit B for each exposure. To perform this coaddition, we simply shift the spectrum from slit A by the integer number of pixels the telescope is nodded in the spectral direction between the slit A and slit B. The coadded spectrum is then calculated by taking the pixel-masked average of the two apertures.

6.4 Calibration

6.4.1 Wavelength Calibration

Wavelength calibration is not a trivial practice for PRIMUS low-resolution spectra. Normal methods involving arc lamp spectra are complicated since any lamp with many nearby lines will result in heavily blended spectra at PRIMUS resolution making line identification difficult. Moderate resolution spectroscopy often can use the locations of night sky lines to determine the wavelength solution, but, as shown in Figure 6.6, the sky observed at PRIMUS resolution only has three strong lines present. Furthermore, the three strong lines present in PRIMUS sky spectra are all located at $\lambda \approx 6000\text{Å}$ and do not span enough wavelength range to even determine an approximate dispersion.

Each PRIMUS mask was observed with a helium lamp in order to obtain a reference for wavelength calibration. Helium has a relatively simple spectrum in the optical and the lines are well separated in wavelength such that the PRIMUS resolution does not result in heavily blended features. After helium spectra are

extracted for each object slit, we first stretch each helium arc spectrum to match the dispersion expected from a model helium arc spectrum derived from empirical measurements of the He line strengths in the IMACS helium lamps. This stretching corrects for varying dispersion of the PRIMUS prism as a function of location on the IMACS focal plane. After each spectrum has been stretched the composite spectrum is fitted as a linear combination of Gaussians at the known locations of helium emission lines and a polynomial background to model contamination from continuum light, both from ambient light in the dome and any continuum produced in the lamp itself. This final stage of fitting measures the global dispersion of the prism. Figure 6.10 shows the composite helium spectrum for a PRIMUS mask; the black line shows the observed spectrum (plotting in the native pixels rather than wavelength). The vertical red lines show the positions of known helium lines; after fitting, the locations of observed spectral lines match the expected locations quite well. Generally, we find our fits to the arc spectra are quite good. There are caveats to using this method directly, however. As the helium arc images are often taken in the afternoon, the thermal properties of the instrument are quite different during these observations than the science observations taken during the night. Furthermore, the helium lamps illuminate a screen on the sky; while this approach is preferred over internal lamps which do not follow the same light path as objects observed in the dome, the dome screen is still not a perfect flat screen and the light from the screen may have systematic wavelength differences compared to objects observed from infinity.

Initial wavelength calibration using the helium arc method described above showed that the measured dispersion as a function of focal plane position matched that predicted based on the optical model of the IMACS instrument and measured properties of the PRIMUS prism. While arc images are taken for every
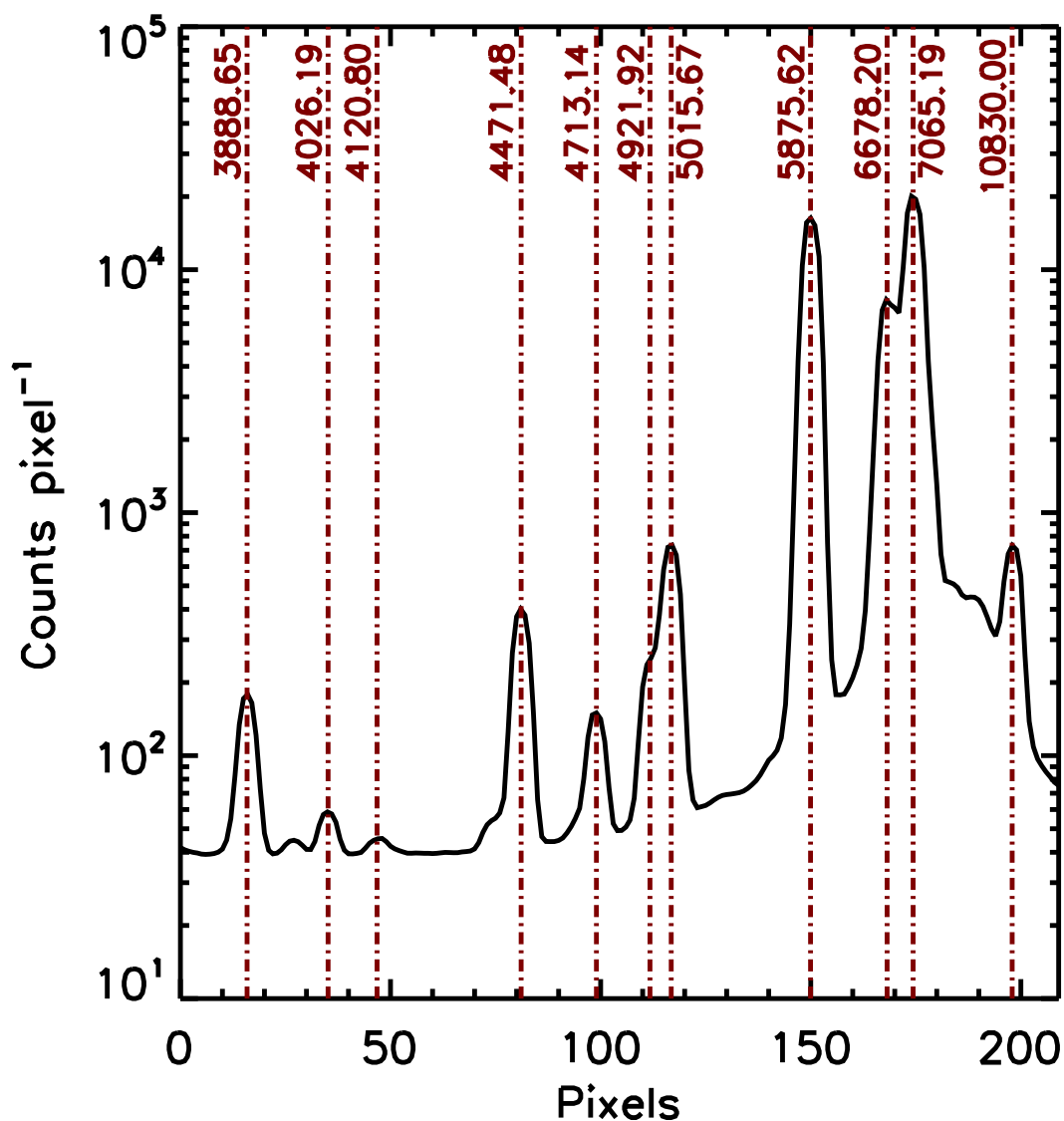
Figure 6.10 Composite helium arc spectrum for a PRIMUS mask. The black line shows the average spectrum of helium arc lines after the differential stretching between each aperture due to the prism dispersion function varying spatially over the IMACS focal plane has been removed. This composite is fit with a linear combination of Gaussian emission lines and a polynomial background term to account for ambient light in the dome or continuum emission from the lamp itself. determine the global dispersion of the instrument. The vertical lines mark the location and label the wavelengths of strong helium emission lines. Combining the global term from the composite spectrum and the stretching term applied to each slit provides a wavelength solution for each object.

mask and used as a check of the instrumental wavelength model, PRIMUS wavelengths are currently based fully on the optical model of IMACS and PRIMUS prism. In this approach, each spectrum is assigned a wavelength solution based on its position on the IMACS focal plane. The wavelength solution is tweaked by fitting a model sky spectrum to the measured sky brightness in each slit allowing the position of the object to vary around its nominal position on the focal plane. While the unblended sky lines in PRIMUS spectra at $\lambda \sim 6000\text{Å}$ do not cover a wide wavelength baseline, the strong lines provide a robust signal to search for small offsets in the object positions on the focal plane. Once each object on a IMACS CCD is modeled, we fit a two-dimensional sixth order Legendre polynomial to the inferred offsets measured from individual objects. This global fit is then used to create a final wavelength solution of each object. We use the global fit rather than the fits from individual objects to guard against catastrophic fitting failures on individual objects. Some positions in which the sky spectrum was measured may have been contaminated by an object or may have had a bad column which affects the strong sky lines resulting in poor sky fits; using the entire image to constrain the wavelengths rather than basing it on single objects allows these object to be well calibrated.

6.4.2 Alignment Errors

The method used to wavelength calibrate PRIMUS spectra described in §6.4.1 ties the wavelength of the object spectra to the zero-point determined from comparisons with the sky spectra. In detail, however, the sky spectrum uniformly fills the PRIMUS slits whereas the object spectrum may not completely fill the slit and is often not perfectly centered on the slit. Thus, objects may have slightly different wavelength zero-points than the sky, especially if the objects are not centered in the slit. We correct for systematic object alignment errors in a two step process.
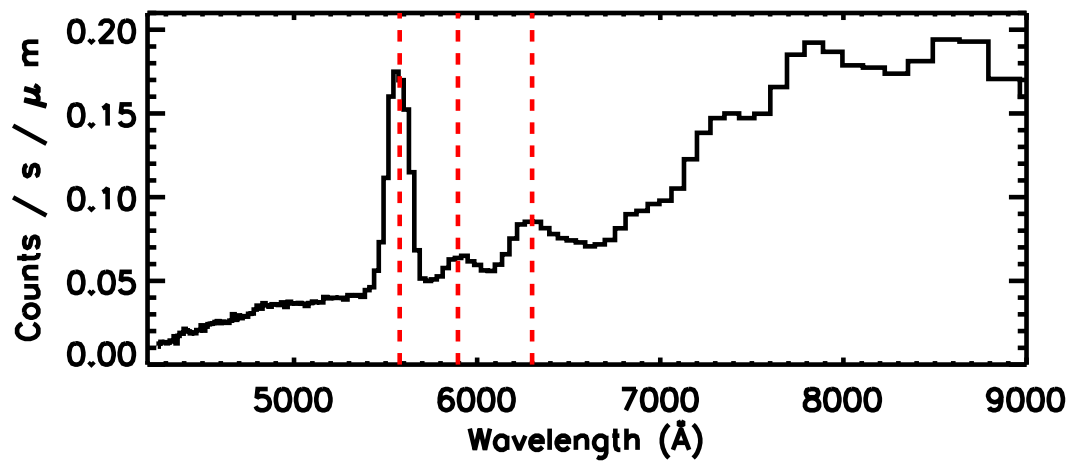
Figure 6.11 Example PRIMUS sky spectrum after wavelength calibration. The positions of three strong sky lines are marked for comparison. The sky spectrum is used to determine the best offset between the nominal location of the object on the IMACS focal plane; offsets on the focal plane correspond to changes in the wavelength solution of the sky. After fitting for the offsets for each object on a CCD, we fit a global polynomial to the ensemble and use this best-fitting model to derive wavelength solutions for each slit. Using the sky spectrum as a normalization for the wavelength solution works well for objects which fill the slits or which are well-centered; objects that have systematic misalignments will have systematic wavelength errors, as well.

During the two-dimensional extractions, we fit for the best centroid of the object light in the slit. Thus, we have a two-dimensional map of each object's offset in the spatial direction (but no information about an object's offset in the dispersion direction). In general, an alignment error may be a result of an offset in the x or y directions or an offset in rotation. The spatial offset of objects in the slits lets us solve for the offset in the spatial direction and the net offset in angle between the slits and the objects. After fitting for these offsets, we recalculate the wavelengths for each object based on their new inferred locations on the focal plane.

In order to measure any offset in the spectral direction, we need to look at the spectra themselves. Once the two offsets described above are removed, the remaining error is a global shift in the spectral direction, so we can solve for one bulk shift based on as many slits as possible. To make this correction, we consider each of the F star candidates we targeted as calibration stars. We compare the broadband photometry for each star to the predicted colors of F stars from a grid of Kurucz (1993) models in temperature, metallicity, and surface gravity. The best fitting template is then convolved to the PRIMUS resolution and the PRIMUS throughput correction (described in §6.4.3), including an approximation to telluric absorption expected at the airmass at which the mask was observed. We fit the spectrum in the wavelength range $6000\text{Å} < \lambda < 8500\text{Å}$ at 20 values for the offset between the nominal wavelengths and the object wavelengths ranging between -3 and 3 pixels. This wavelength region was chosen as it contains strong atmospheric water absorption lines with known wavelengths and which provide a strong signal to match between the data and model. The shift which minimizes the χ^2 between data and model is chosen to be the best shift for a given star and we take the $\Delta\chi^2 = 1$ range as the 1σ error on the shift. As this fit is dominated by matching the expected and observed wavelengths of the strong telluric features,

template choice errors do not significantly bias the best fit shift. We use the telluric features in our alignment correction as the key absorption features of F stars are located blueward of 4000 Å where the IMACS quantum efficiency is quite low and thus the signal to noise in our spectroscopy is quite poor. The telluric features are also appealing as they are located in a portion of the spectrum where many key spectral features are observed in the galaxies of interest and do not require large extrapolations from the pixels at $\lambda < 4500$Å which are not used when fitting galaxy spectra. After each of the 15-30 F stars have been fit on a mask, we remove objects in which the best fitting F star template has $\chi^2 > 3000$ over the full 150 PRIMUS pixels. The global shift is then taken to be the error-weighted mean of the remaining F stars. The wavelengths for every object on the mask is shifted by the amount determined from the entire mask to create the final wavelength vector.

6.4.3 Throughput

Flux calibration in PRIMUS is done quite differently than traditional spectroscopic surveys. Rather than apply a fluxing calibration to all of our spectra, we instead track the appropriate fluxing vector for each slit and use this as a inverse fluxing vector when modeling PRIMUS data. The throughput correction used in PRIMUS is built on many individual corrections that, when applied in ensemble, convert physical flux units to counts. First, the atmospheric extinction as a function of wavelength are corrected. Our baseline atmospheric correction uses the optical extinction measured at Palomar. Early comparisons between this extinction model and our data from Las Campanas showed that the strengths of the water and OH bands at 6900, 7300, 7600, 8300, 9500 Å were too strong in the original model and were manually tuned to more closely match the absorption seen in PRIMUS spectra.

During each PRIMUS observing run, we observe a DA white dwarf with previously measured spectrophotometry (e.g, Hamuy et al., 1992, 1994). We observe these stars without a slit mask, removing the effects of slit losses. The star is placed on each IMACS CCD in turn and on each CCD the star is observed twice with 10″ offsets between the two images. This offset allows for robust local sky subtraction on each exposure simply by subtracting the two dithered images. DA white dwarfs are chosen as these stars have deep Balmer absorption lines which are strong enough to be easily detected in our PRIMUS spectra; these absorption lines allow us to wavelength self-calibrate the spectra. Extracted spectra from each CCD are compared to spectrophotometry in the literature to determine the instrumental throughout for each of the eight IMACS CCDs. Figure 6.12 shows the throughput of the IMACS optical, CCDs, and prism for two standard stars measured over 5 different nights. The black line shows the average throughput curve. While this curve provides the overall throughput correction of the system, it is also important to consider finer scale throughput variations.

In addition to the overall CCD and instrumental throughput, we utilize the sky spectra to determine a mean CCD-to-CCD variation. We find that each of the eight IMACS CCDs has different quantum efficiency; ignoring this difference would lead to significant long wavelength fluxing errors. Figure 6.13 shows the average inter-CCD variation compared to CCD 5. These average curves were generated by constructing the average sky on each CCD for approximately 80 masks observed over the full PRIMUS survey and measuring the mean ratio between the master sky on each CCD compared to CCD 5. We find that these inter-CCD variations are quite consistent from mask to mask, with variations on the order of 5%. On each mask, we further use the sky spectra to determine a a slit-to-slit correction to account for chromatic variations as a function of position on
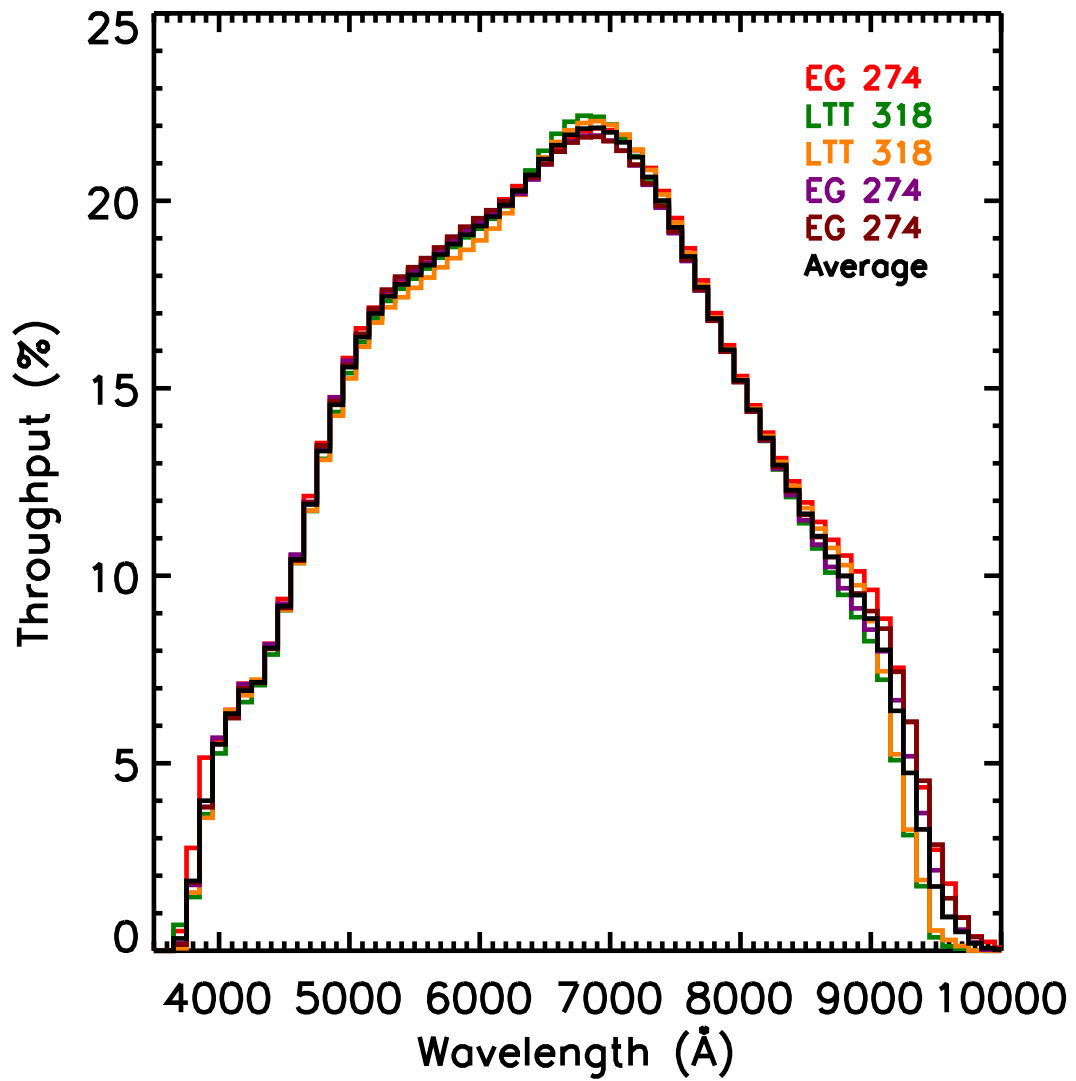
Figure 6.12 Throughput derived based on slitless observations of two DA white dwarfs over 5 different nights in 2006. Each colored line shows the derived throughput while the black line shows the mean fluxing vector for the IMACS optics, prism, and CCD quantum efficiency.

the IMACS focal plane. For each slit, we compare the observed sky spectrum to the mean sky spectrum for the entire CCD; we calculate a quadratic correction to bring the observed sky spectrum to the mean.

As a final correction, we utilize the F stars targeted on each of the PRIMUS masks. The photometry of each F star is compared to a grid of Kurucz (1993) models to determine the best-fit temperature, gravity, and metallicity. We then compare the data to the best fitting template which has been multiplied by each of the throughput corrections described above. The mean ratio between the data and the modified template across all of the SDSS and SWIRE masks, on which we have robust F star selection, is used as a final throughput correction to bring the PRIMUS counts per second to physical energy units.

6.5   Redshift Fitting

Once the PRIMUS spectra are extract and calibration as described in §6.3 and §6.4 the key goal of the PRIMUS project is to measure redshifts for each object. At this time, the specifics of the spectral fitting strategy have not been completely finalized; this section will serve as an introduction to the the current technique used and an outline for possible changes currently being explored.

6.5.1   Current Technique

Our current redshift fitting technique strives to reproduce the observed spectrum for each object by finding the best linear combination of ten spectral templates. Our templates consist of five continuum templates which were trained to span the full range of galaxy spectral energy distributions measured in the Sloan Digital Sky Survey (Blanton et al., 2003c) and four emission line templates. At the resolution of PRIMUS spectroscopy, weak emission lines will not make significant contribution to the observed spectrum and thus our emission line templates
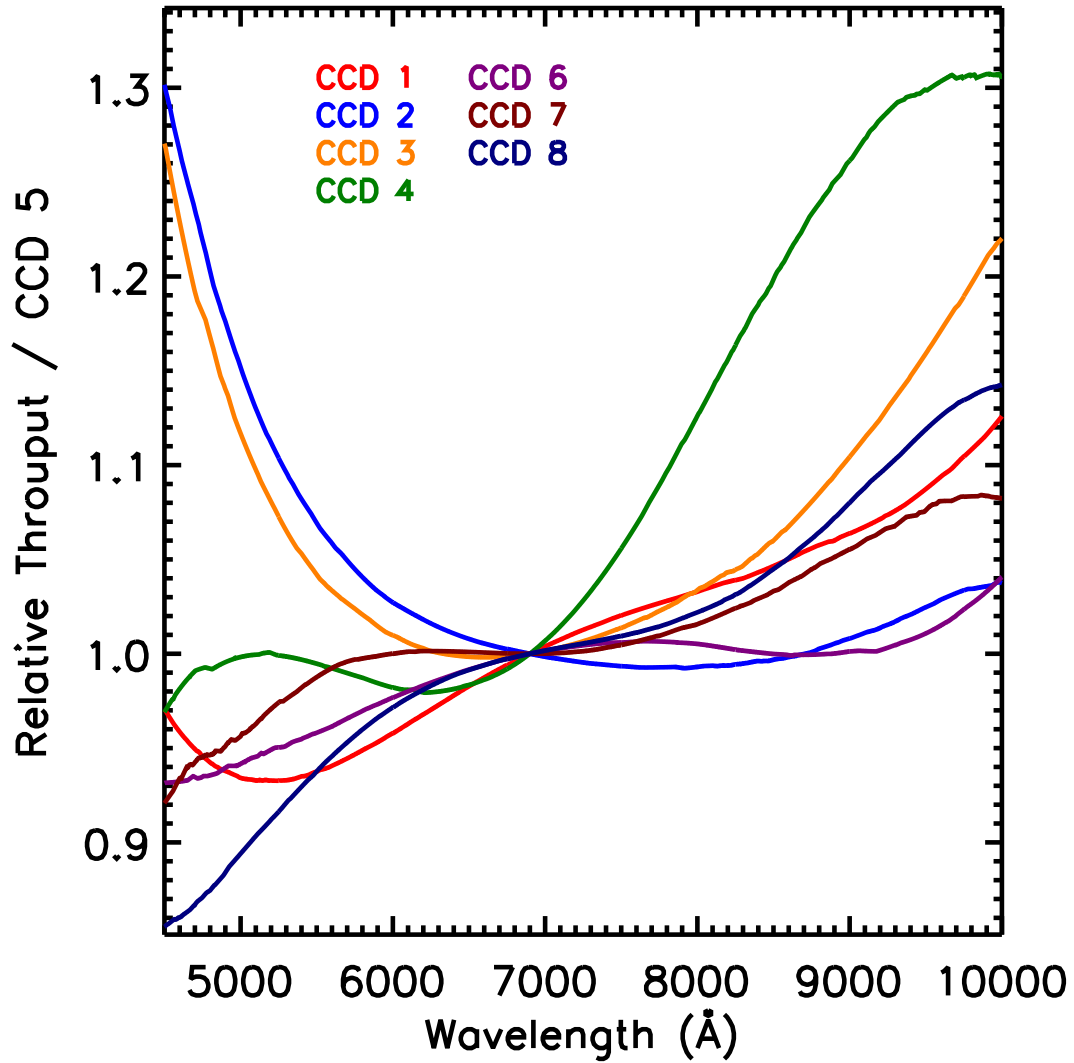
Figure 6.13 Variations in quantum efficiency between IMACS CCDs. Each of the seven curves shows the relative throughput of the IMACS CCDs compared to CCD 5. We use the measured sky spectrum for each object to create a master sky spectrum on each CCD; the curves shown are the average inter-CCD variations over approximately 80 PRIMUS masks.

only include the strongest lines: [O$\textsc{ii}$]$\lambda 3727$, [O$\textsc{iii}$]$\lambda 5007$, Hα, and a template with both Hβ and Hα in a ratio of (1:2.7). We allow Hα to vary independently from the Hβ and Hα pair in order to allow for redding in the emission lines to mimic the contribution of [N$\textsc{ii}$] to the Hα flux. The continuum templates used in our spectral fitting are shown in Figure 6.14. The templates shown in panels (b) and (c) were modified by hand to include a strong [O$\textsc{ii}$]$\lambda 3727$ emission line to the continuum model to guard against unphysical fits which required very blue stellar continua without the presence of emission lines.

At a given test redshift, a PRIMUS spectrum is fit by determining the best non-negative linear combination of our nine spectra templates. When doing this fit, we jointly fit the spectrum measured in slit A and slit B rather than fitting the mean spectrum which may depend on the method used to coadd the two apertures. We then compare this best fit template to the data and determine a second-order fluxing correction to apply to improve the fit. We then repeat the fitting with this flux-tweak applied. This flux-tweaking is iterated until we converge to a final best fit model the redshift being tested. Each object is fitted on a grid of redshift from $z = 0$ to $z = 1.2$ with spacing of $\Delta z = 0.01$. We then locate minima in the χ^2 as a function of redshift via quadratic interpolation. The data are refit at the deepest five minima in the χ^2 surface; the best-fit galaxy redshift is the redshift which results in the minimum final χ^2. Figure 6.15 shows one example of our redshift fitting. The top panel shows PRIMUS observations for an $i = 20.7$ galaxy with a known redshift of 0.650 from the VVDS survey. The red and blue points show the spectral extractions from slit A and slit B separately. The solid black line is the best fitting galaxy model at a redshift of 0.655. The lower panel shows the distribution of χ^2 as a function of redshift. The best fitting PRIMUS redshift is marked by a dot-dashed bar whereas the known high-resolution red-
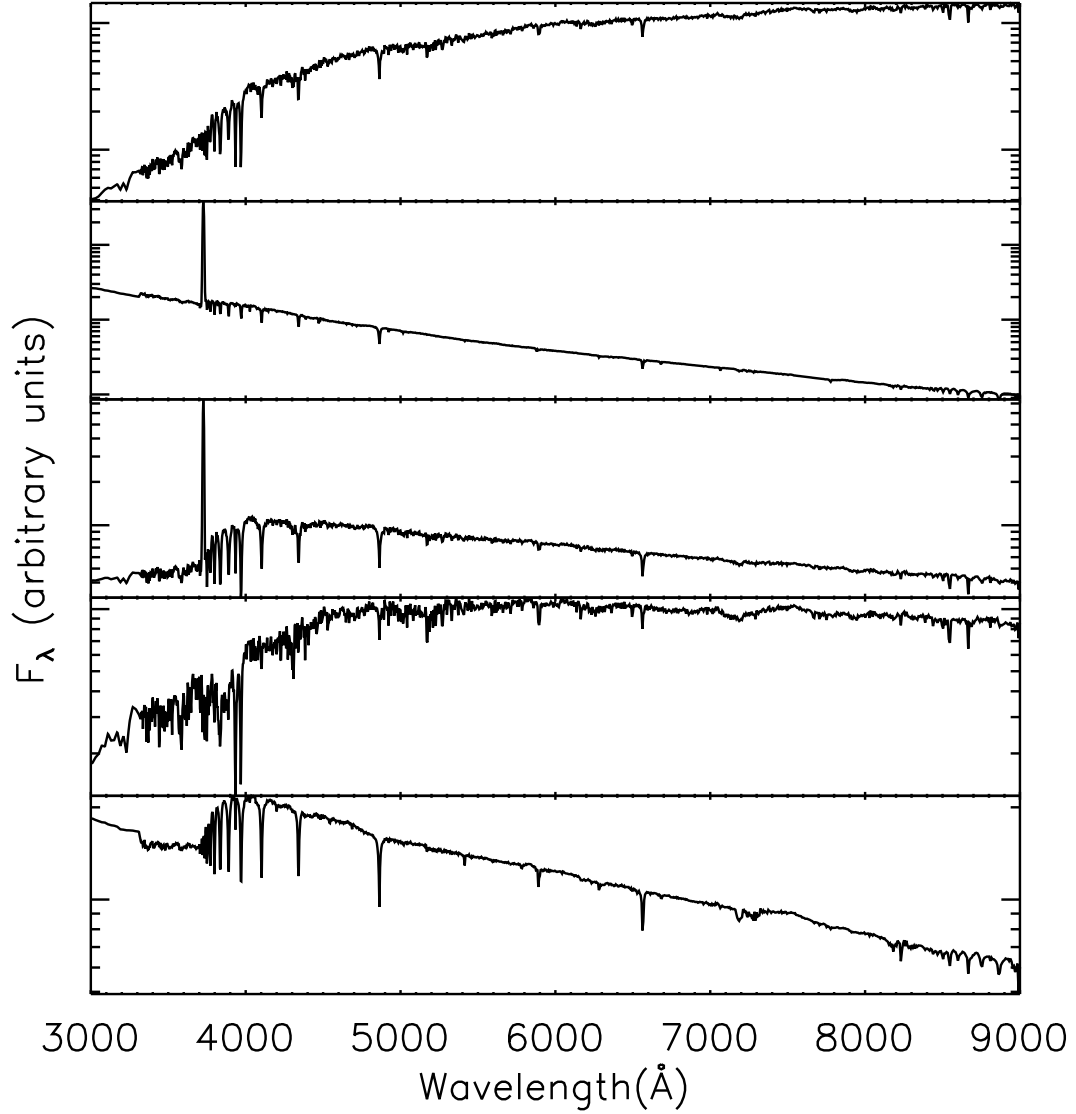
Figure 6.14 Five continuum templates used to fit PRIMUS spectra. At a fixed red-shift, a PRIMUS spectrum is fit as the best non-negative combination of these five continuum spectra and four emission line templates as well as allowing for large scale fluxing errors as described in the text. These five templates were chosen to span the full range of galaxy photometry observed by SDSS. The $[\text{O\,\textsc{ii}}]\lambda3727$ emission lines in the second and third templates were included to help resolve degeneracies between 4000 Å breaks and Balmer breaks in our low-resolution spectroscopy.
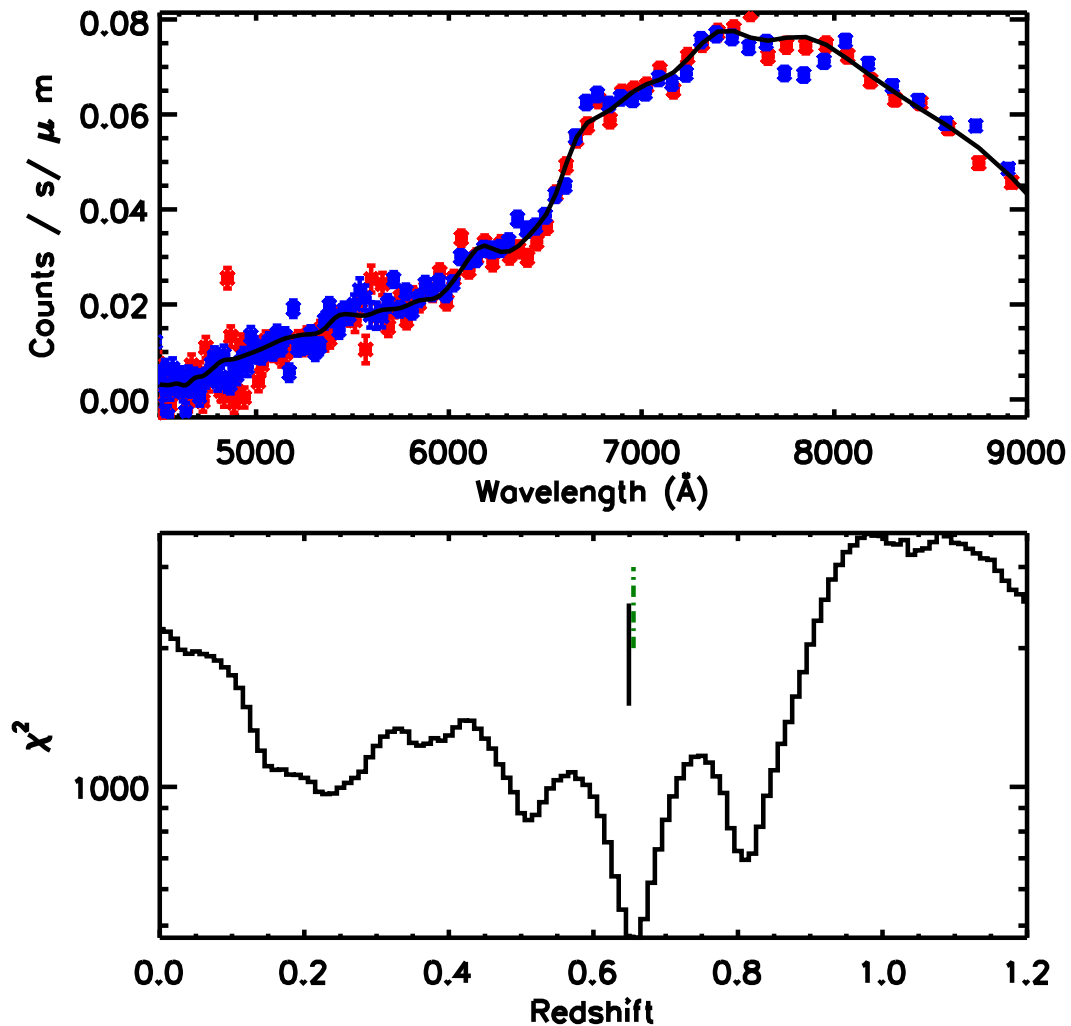
Figure 6.15 The top panel shows the extracted PRIMUS spectrum of a $i = 20.7$ galaxy. The red and blue points show the flux measurements (and 1σ errorbars) as recorded in the A and B slit respectively. The strong 4000 Å break characteristic of old stellar populations is clear at the redshift of $z = 0.650$ as measured by the VVDS survey. The solid black line shows our best fitting model for the observed flux. The bottom panel shows the run of χ^2 as a function of redshift derived when fitting this galaxy. The dot-dashed line shows the redshift measured by PRIMUS, $z_{\mathrm{PRIMUS}} = 0.655$, and the solid black bar shows the value obtained from high-resolution spectroscopy.

shift is marked with the solid bar.

In much the same way we fit galaxies, we also fit each object with an AGN template (Vanden Berk et al., 2001) with an additional power-law component to find the best-fitting AGN redshift. Finally, we also fit a grid of stellar models and a grid of powerlaws of varying spectral index to each object. Any object that is significantly better fit by a powerlaw, AGN or stellar template, compared to the galaxy template, is flagged. For our discussion, here, we only consider those object not flagged as possible stars, AGNs, or powerlaws. While these objects are interesting in their own right, more work is needed to understand the redshift success for non-galaxy sources. We further flag any galaxies which have a second χ^2 minimum within $\Delta\chi^2 = 1$ of the best fitting redshift.

In order to test our redshift fitting and extraction, PRIMUS observed ~ 2100 galaxies with known redshifts from the VVDS or DEEP2 surveys. Figure 6.16 shows the raw comparison between the known high-resolution redshifts and PRIMUS best-fit redshifts for these calibration sources. Here, we only plot objects with signal-to-noise ratio of 12 or larger and which were unflagged during all stages of spectral extraction; we find that below this signal-to-noise threshold, the data quality becomes too poor to recover redshifts for a large fraction of our objects. While we clearly recover the base one-to-one relationship expected, this plot has a large number of significant outliers - far more than acceptable for our scientific goals. There are several causes for the outliers seen in the figure. For example, the plume of objects with $\Delta z \sim 0.1$ at $z_{\mathrm{highres}} \sim 0.7 - 0.9$ arise due to a confusion between the 4000 Å break of an old stellar population with a Balmer break characteristic of stars younger than 1 Gyr. A key problem with this confusion is that the redshift fitter has too much freedom; a galaxy that, in reality, is a blue galaxy with a Balmer break is being fit with an old stellar population. In

order to reproduce the blue UV continuum, the fitter adds a large contribution of very young stars leading to a galaxy with a 4000 Å break and blue continuum. In other words, the non-negative linear combination allows for non-physical configurations such as a galaxy with a large population of old stars and a large population of young stars with no intermediate age populations. The large population of outliers with PRIMUS redshifts less than $z = 0.2$ seem to be due to how we have modified our young continuum templates with an [OII]$\lambda3727$ emission line but no others. A blue galaxy which has no emission lines is well fit by a blue galaxy at a broad range of redshifts; templates with $z > 0.2$, however, are ruled out as the strong [OII]$\lambda3727$ emission line in our blue templates would enter into the PRIMUS data.

6.5.2 Future Directions

Several modifications of the redshift fitter have been planned. Firstly, the current redshift fitting technique includes no information about the broadband photometry of any source. As the majority of our fluxing errors in PRIMUS are likely long-baseline errors, the photometry of a galaxy can constrain the galaxy spectra on long wavelength baselines while the spectroscopy uses the higher resolution information to get the most precise redshift possible. In order to explore how much including the photometry may help our current technique, we performed a simple test. For each galaxy, we compared the broadband photometry to the photometry predicted from a grid of Bruzual & Charlot (2003) SSPs. The comparison between the photometry and SSPs yields a probability distribution function (PDF) based on the photometry alone; we multiply this PDF by the PDF obtained from fitting the spectroscopy using the method described in §6.5.1. If the best-fitting redshift from this product was inconsistent at more than 3σ from the redshift determined from spectroscopy alone, we flag the galaxy. In this way, we
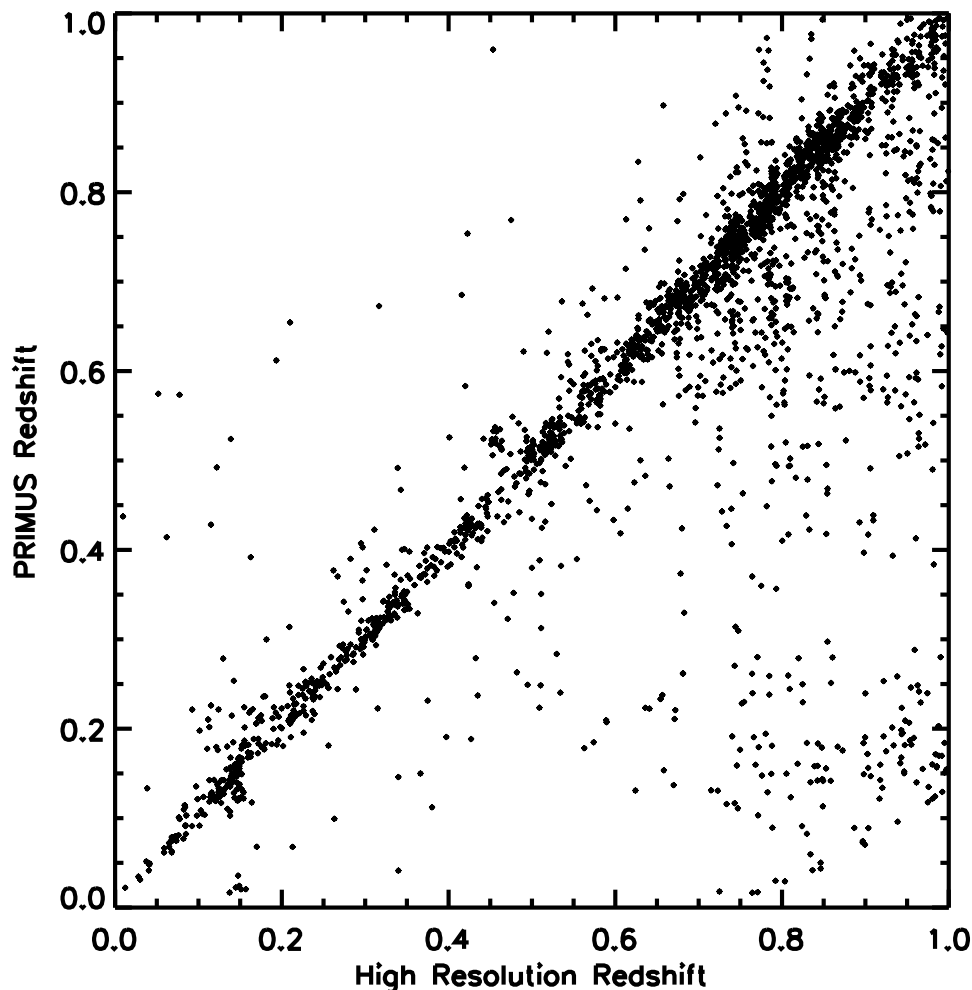
Figure 6.16 PRIMUS redshift measurements are plotted against redshifts mea-
sured from high-resolution spectroscopy from the VVDS or DEEP2 surveys. The
PRIMUS redshifts here are derived by fitting the PRIMUS spectroscopy alone; no
photometric information from the broad-band photometry is included in our fits.
Many of the outliers from the one-to-one relation are due to errors in the tem-
plate construction based on the non-negative least squares combination of five
continuum templates and four emission line templates. This model basis allows
galaxies to be fit with unphysical templates such as an old stellar population with
a large contribution of young stars without any contribution of intermediate age
stars. Furthermore, the lack of emission lines redward of 4000Å in any of our
continuum templates, even those representing very young stellar populations,
allows for a wide variety of blue galaxies to be fit by young models at $z < 0.2$
where the wavelength range observed by PRIMUS would have no contribution
from [OII]$\lambda 3727$ which is included in our continuum templates. As described in
§6.5.2, including photometry when performing fits will help break some of the
degeneracies between templates which result in poor redshifts. Future work on
new redshift fitting techniques will likely further decrease our rate of redshift
failures.

discriminate between galaxies with good PRIMUS fits and those with problematic fits. Figure 6.17 shows the correlation between the high-resolution redshift and PRIMUS redshift after this cut has been applied. The flagging used in this method provides a clean sample of galaxies with good PRIMUS fits; we find an rms scatter of $\sigma_z/(1 + z) \approx 1.5\%$. Clearly the photometry for a large fraction of the outlier sources would heavily disfavor the best-fit PRIMUS redshift and if the photometry were used in the template fitting, it would likely influence which template is chosen. The next step beyond using photometry as a check after the spectroscopy has been fit is to include the photometry in the fitting directly. This has the added benefit in that template choices which are heavily disfavored by the photometry but which may be accepted in the presence of the spectroscopy alone will be down weighted.

A second alteration underway is to move away from choosing the best linear combination of five continuum templates to a scheme in which we have many (perhaps 50-100) templates that we have chosen to span the full range of galaxy properties as a set of individuals (i.e. without considering the linear combination). In this scenario, we would fit each galaxy as a linear combination of a single continuum template and emission lines and then ask which of our templates best fits as a function of redshift. This technique is advantageous as one can choose the training set from which to base the final template set to be an actual spectroscopic dataset; if the templates are representative of all the galaxies in a high-resolution dataset, they will likely also be sufficient in describing PRIMUS spectra. We plan on using the AGES dataset to train the templates used with this method. The strength of this method compared to the current technique is that one cannot choose non-physical galaxies in this approach. Each template is a real example of a galaxy that exists in nature and non-physical combinations, which
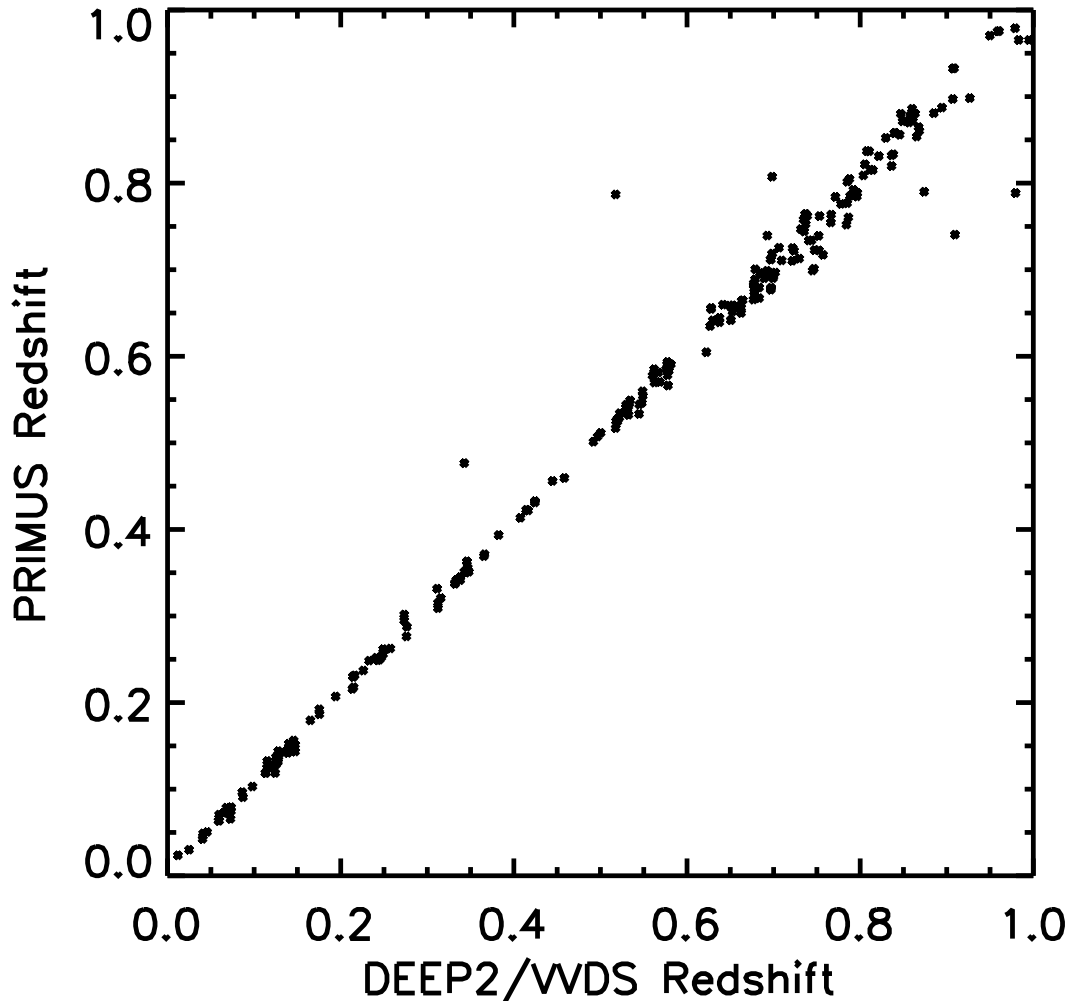
Figure 6.17 The same as Figure 6.16 except we also fit the broadband photometry of each object with a grid of Bruzual & Charlot (2003) SSP models. We recalculate the redshift of each object based on the product of the photometric and spectroscopic probability distribution functions; if the new redshift is larger than 3σ from the redshift derived from spectroscopy alone, we flag that galaxy. The galaxies plotted here only include objects whose redshifts are consistent with both their observed photometry and spectroscopy. While this method is not ideal as a large fraction of the sample is rejected, it indicates that including photometric information when fitting for redshifts may help improve the accuracy of PRIMUS redshifts. Incorporating photometry into our redshift fitting is one chief path of current work in the project.

lead to errors in the current implementation, are eliminated by construction

6.6   Current *PRIMUS* Status

PRIMUS observations completed in January 2008. All data have been extracted using the pipeline described in §6.3 and §6.4. As described in §6.5.2, several advancements are currently being coded for the redshift fitting, so the full dataset have not been fully fit at this point, but all calibration objects with known redshifts have been fully fit and are actively being used to optimize our technique.

Table 6.4 lists the targeting and signal-to-noise statistics for each of the PRIMUS fields. For each field, we list its area and statistics concerning the primary sample galaxies, only bright ($i < 22.5$) galaxies, and full collection of slits. For both the primary and bright samples, we list the total number of available targets in the area we surveyed, the total number of objects that received slits, and the fraction of galaxies which resulted in a spectrum with high enough signal-to-noise ratio to recover a redshift. The threshold to determine a redshift is set arbitrarily at S/N>12; we expect to recover many redshifts at lower-S/N, but the completeness below this S/N will likely be a strong function of galaxy type. In general, we assign slits to $\sim 95\%$ of our primary galaxy sample and obtain redshifts for 70% of the primary galaxies with spectra extracted from PRIMUS images. Finally, we list the total number of slits that were cut for each survey. It's important to note that the total number of slits reports each slit that was cut regardless of the type of object. Thus, objects observed on multiple masks are counted more than once and the total number includes observations of blank sky. In the primary survey area suitable for statistical studies of galaxy evolution, PRIMUS collected more than 350,000 spectra, $\sim 160,000$ of which were of our primary galaxy sample. If we consider the full sample of available $i < 22.5$ galaxies in our survey

footprint, we target 77% of the galaxies meeting our flux limit and 80% of these objects have spectra of quality sufficient to measure a redshift. Thus, we expect to obtain redshifts for 62% of the galaxies to $i < 22.5$ in our fields Figures 6.18 - 6.23 show the sky coverage of each of the primary fields. In each figure, the points show the spatial distribution of targets in the input photometry catalog and the grey area show the footprint of the primary PRIMUS survey area. Blue regions mark areas which are excluded from the primary PRIMUS survey area due to target selection inhomogeneities or areas where only one mask of the designed pair was observed. While these areas provide additional redshifts, they are not considered for statistical studies to ensure they do not bias results.

The PRIMUS dataset holds a wealth of information about the evolution of galaxies over the second half of cosmic history. PRIMUS is the largest existing sample of redshifts for galaxies with *Spitzer* photometry and X-ray fluxes and thus is uniquely suited to probe the evolution of the star formation rate, stellar masses, and nuclear activity of galaxies since $z = 1$. In §7, we discuss several of the scientific investigations planned using this dataset; these investigations will not only allow us to use our superb dataset to do science but will also result in a number of derived quantities associated with our galaxy sample.

While many of the details of our data reduction are in flux, we intend to converge on an initial full reduction of our data by July 2008. During the summer of fall of 2008, we intend to produce a limited data release of early PRIMUS spectroscopy to the public. While the scope of this data release is still being discussed, it will likely constrain spectra and redshift for the brightest galaxies observed during the spring of 2006.Even once we have a robust catalog of redshifts for each object in our survey, our work is far from over. In order to do science, we will need to understand the details of the PRIMUS window functions and se-
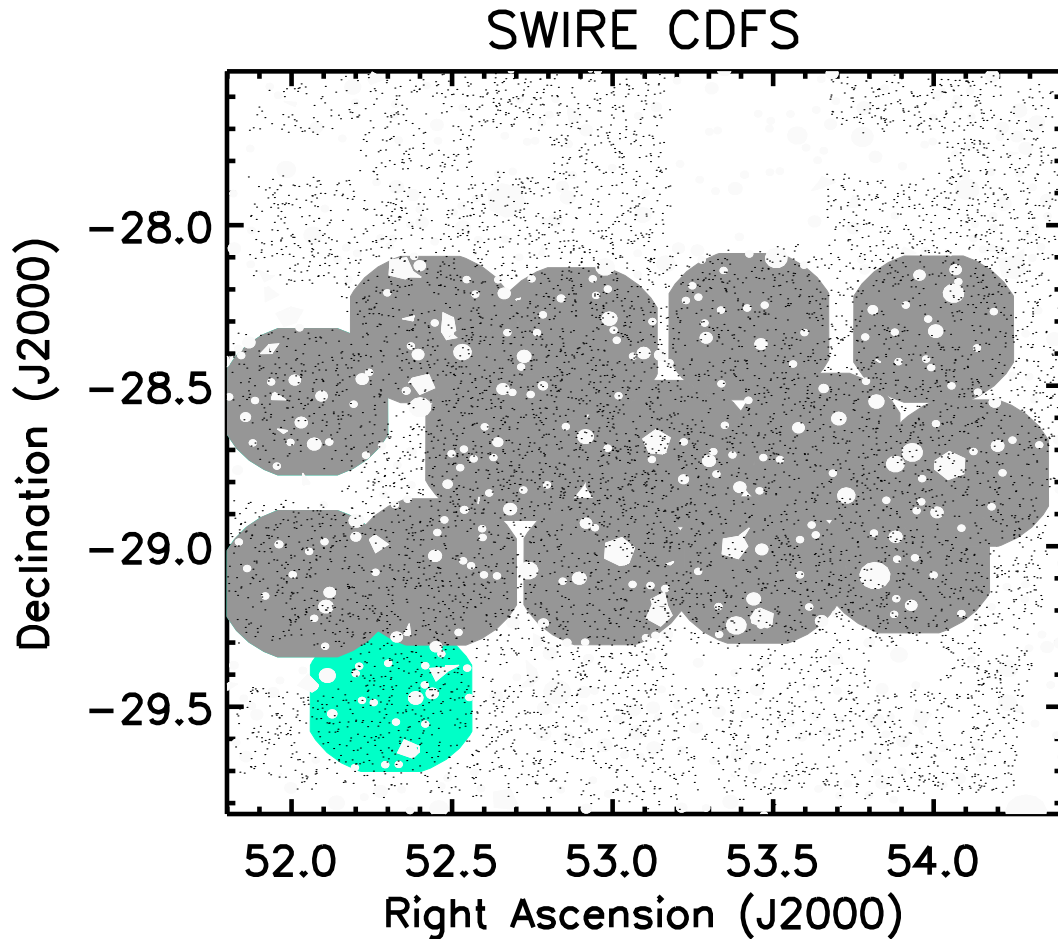
Figure 6.18 PRIMUS coverage of the Chandra Deep Field South. The black points show a random subset of the input catalog to outline the available optical imaging. The shaded grey regions show the PRIMUS footprint; white holes in the grey regions denote areas excluded due to the presence of a bright star. The blue area marks a portion of the survey that has either partial observations (one mask of a pair was observed) or have different selection functions from the majority of the survey due to mask design problems. Blue regions are excluded from the primary PRIMUS area are not included in any statistical investigations or in the numbers presented in Table 6.4.
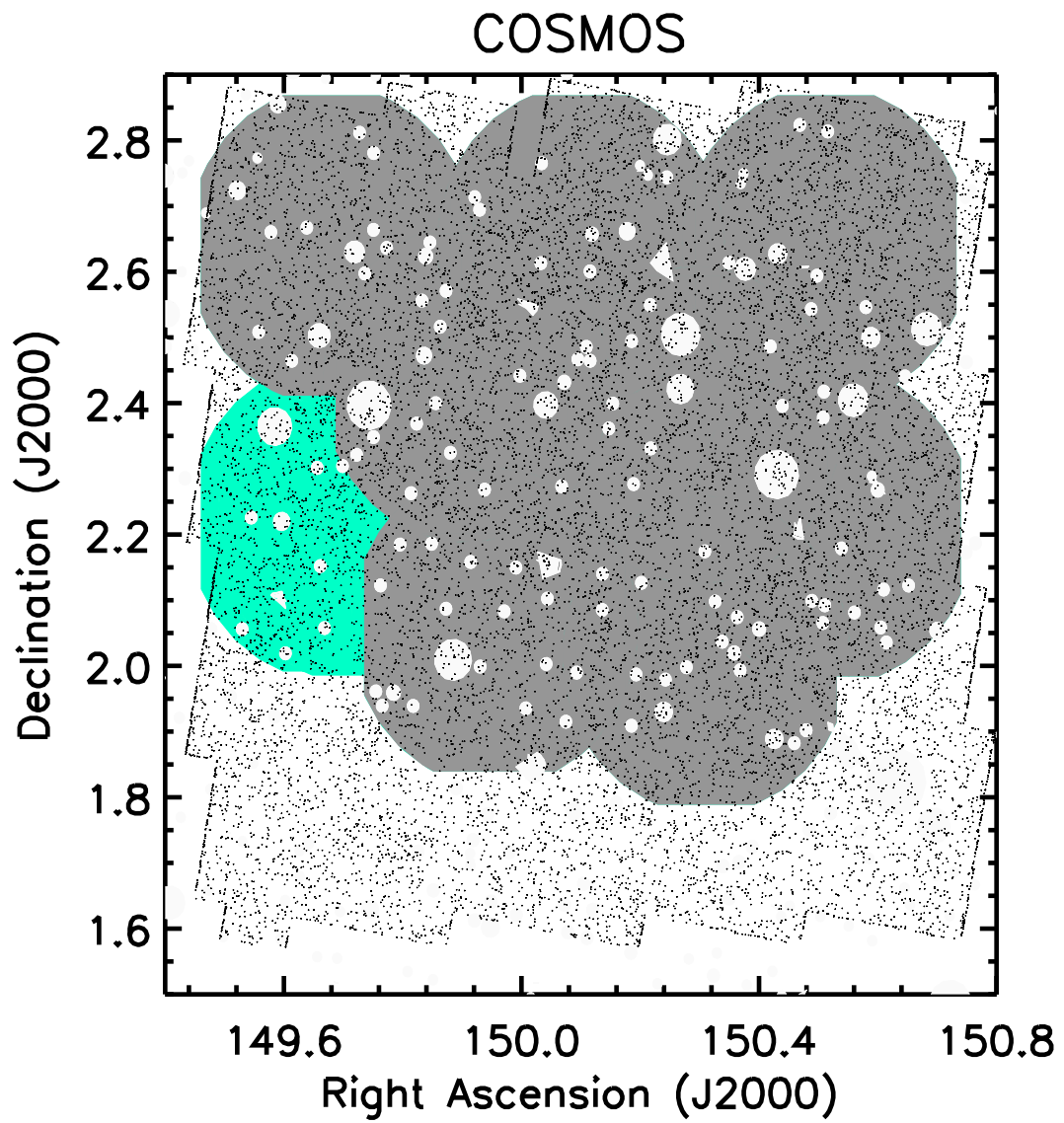
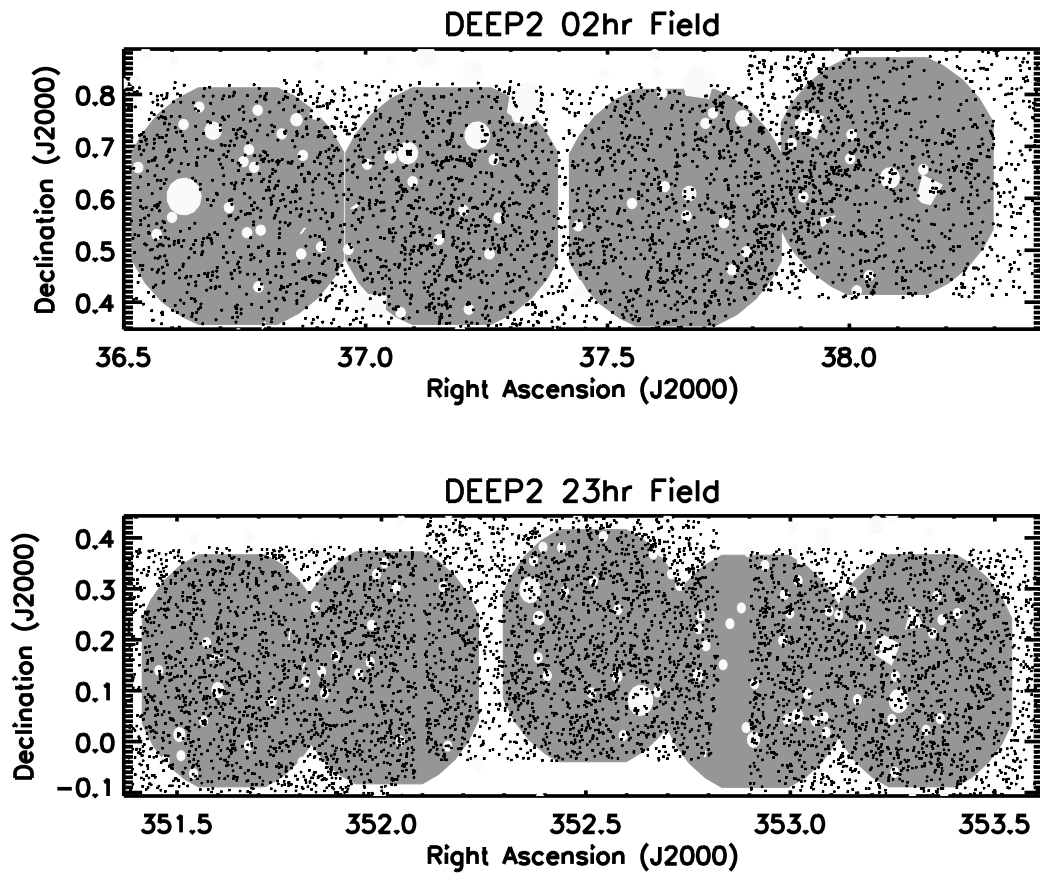Figure 6.19 Same as Figure 6.18 but illustrating the coverage of the COSMOS field.

Figure 6.20 Same as Figure 6.18 but illustrating the coverage of two DEEP2 fields with PRIMUS spectroscopy.
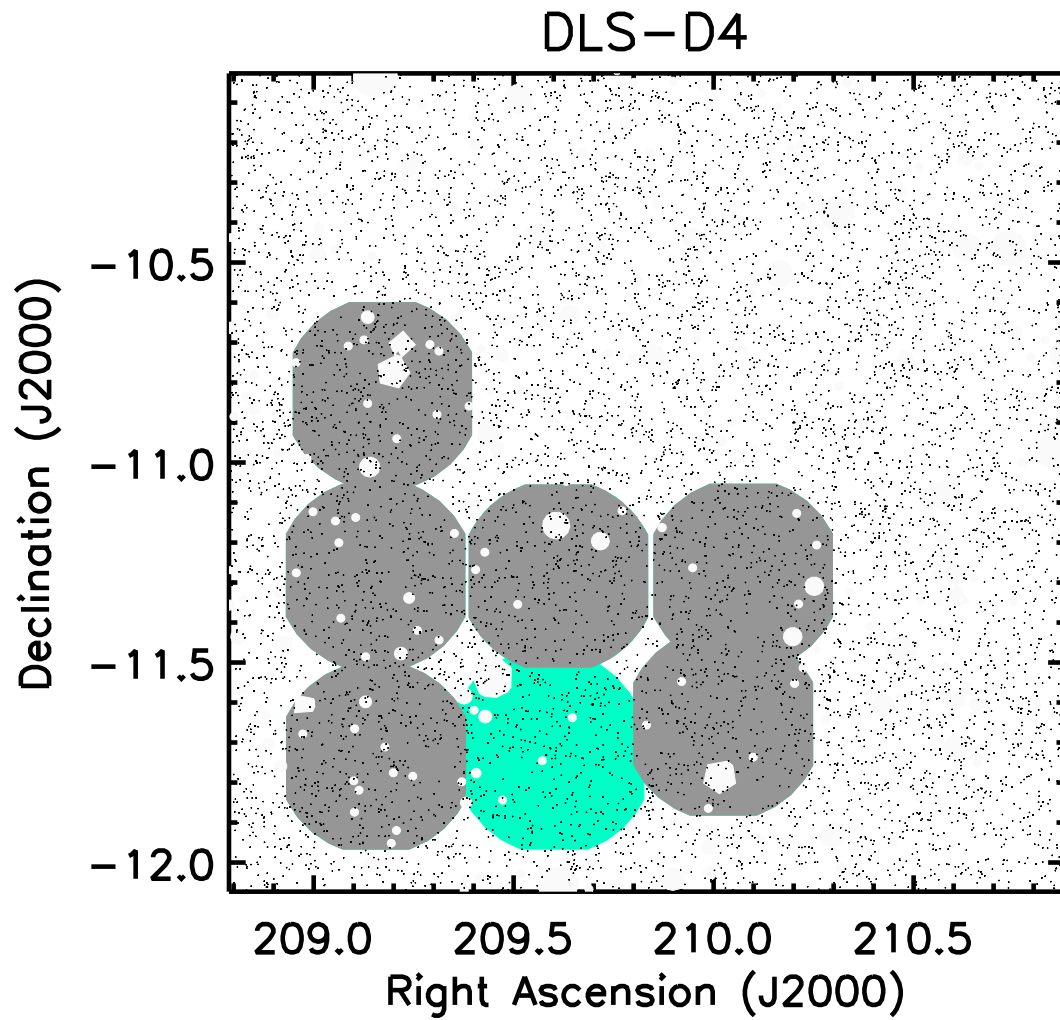
Figure 6.21 Same as Figure 6.18 but illustrating the coverage of the DLS-D4 field.

Table 6.4.   PRIMUS Field Statistics Including Only *Primary* Survey Area

| Survey	Area (deg^2)	$N_{prim,phot}$	$N_{prim,obs}$	$f_{prim,success}$	$N_{bright,phot}$	$N_{bright,obs}$	$f_{bright,success}$	$N_{observed}$	$f_{success}$
(1)	(2)	(3)	(4)	(5)	(6)	(7)	(8)	(9)	(10)
CDFS	2.29	33958	32839	80.0	34410	29669	91.0	64713	64.9
COSMOS	1.08	18814	17620	67.0	28318	23539	73.0	52491	59.2
DEEP2-02hr	0.70	9578	9108	78.0	7782	5866	94.0	22507	67.9
DEEP2-23hr	0.84	10801	10519	76.0	10482	9026	85.0	18967	59.7
DLS-D4	1.03	21884	20838	59.0	26542	21941	66.0	43569	55.3
ELAIS-S1	1.03	15734	15022	79.0	15517	13116	90.0	52491	63.9
XMM-SWIRE	3.08	61692	57086	64.0	76798	51422	78.0	112987	49.1
Total	10.05	172461	163032	70.2	199849	154579	80.0	367725	57.9
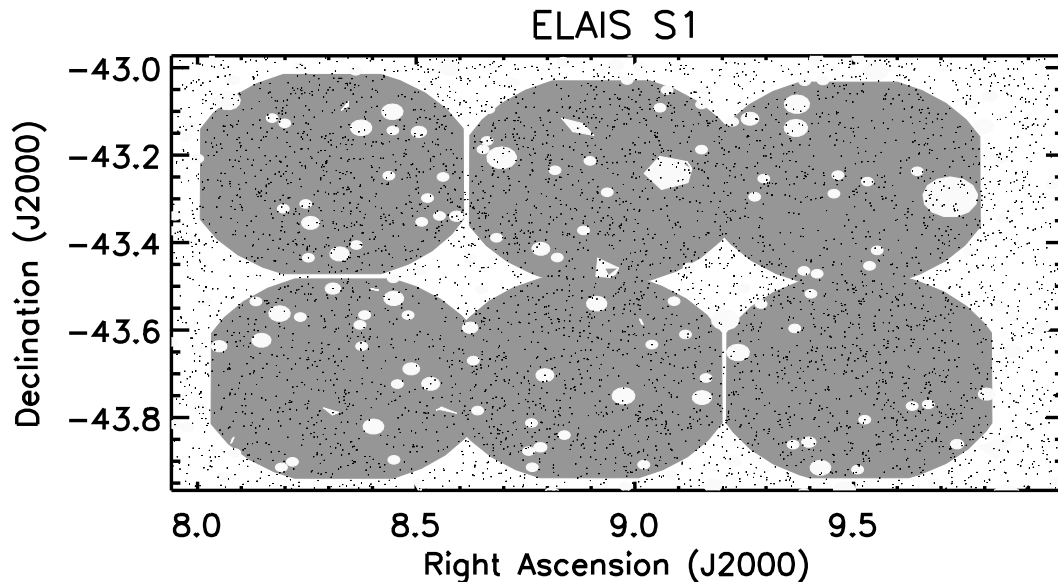
Figure 6.22 Same as Figure 6.18 but illustrating the coverage of the ELAIS S1 field.

lection functions, especially when comparing objects targeted based on different imaging datasets. We will produce catalogs of galaxy properties such as stellar masses, star formation rates, luminosities, and rest-frame colors. Furthermore, we will produce k-corrections which transform the very inhomogeneous photometry used to target sample galaxies to a standard rest-frame scale allowing for comparisons based on galaxies targeted from different input photometry. We may also need to re-photometer the existing optical images used to select galaxies to ensure we have aperture matched fluxes in each band for robust colors and to ensure fluxes measured from all imaging datasets are self-consistent.

The key goal of the PRIMUS project is to maximize the legacy value of existing deep, wide-area imaging datasets, especially those with existing multiwavelength data. Thus, it is a key goal of the project to release a user-friendly catalog of all PRIMUS data, including derived raw frames, extracted spectra, redshift catalog, window function, selection function, and derived galaxy properties to the public. Our current plan is to produce this full data release the summer of 2010.
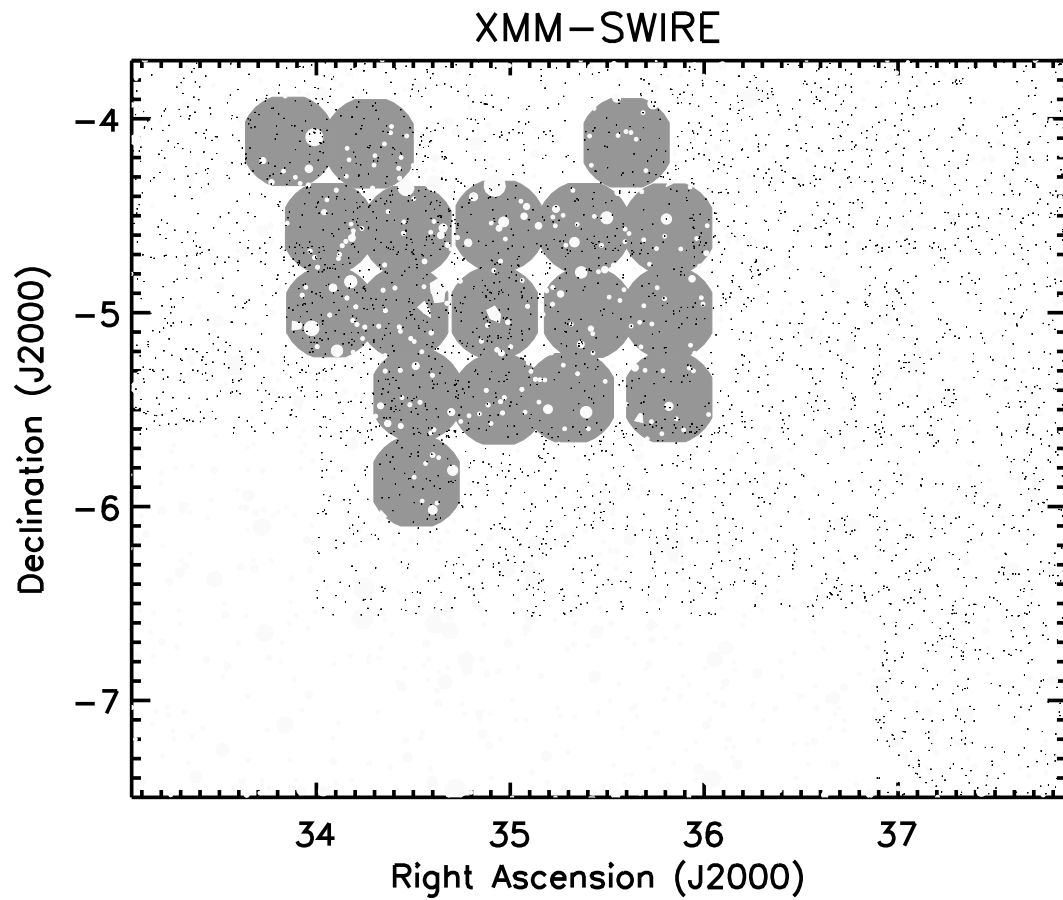
Figure 6.23 Same as Figure 6.18 but illustrating the coverage of the XMM-SWIRE field. In this figure, we include targets selected as part of CFHTLS imaging of the field as well as targets selected based on optical imaging from Subaru.

CHAPTER 7

FUTURE DIRECTION

Throughout this disseration, we have focused on understanding the evolution of the most massive galaxies. These galaxies, as the endpoints of the cosmological history, provide an observational constraint on the details of the efficiency and frequency of merging and star formation over the last half of cosmic history. The massive galaxies considered throughout this work grow by less than $\sim 10\%$ by mass through the formation of stars since $z = 1$. Thus, any growth in the total stellar mass in these systems must be fueled by the galaxies must be powered by mergers between galaxies which result in little or no new star formation. Furthermore, we find that total growth in the massive red galaxy population is quite small with a growth of 50% in the total stellar mass in massive red galaxies over the last half of cosmic history.

All of the results presented in this disseration have relied on high-resolution spectra to measure redshifts, derive spectral line strengths, and to classify objects. In Chapter 6, we introduced PRIMUS, a new redshift survey aiming to map the universe to $z \sim 1$ using low-resolution spectrsocopy to very quickly observe several thousand galaxies simultaneously. This new sample will allow us to perform countless investigations of the evolution of galaxy properties both as a function of cosmic time and as a function on environment. This chapter serves as an introduction to several of the scientific projects which will be made possible with the new PRIMUS dataset.

As described in Chapter 6, the PRIsm MUlti-object Survey (PRIMUS) is a new redshift survey which has obtained 300,000 galaxy spectra over 10 square degrees with copious multiwavelength observations from *Spitzer*, *Chandra*, *HST*, *GALEX*,

and *XMM-Newton*. My research in the coming years will capitalize on the wealth of data we have in hand from PRIMUS as well as other deep, wide-field redshift surveys, in order to measure the growth and evolution of galaxies over half of cosmic history and to quantify the importance of AGN on these processes. Our quantifications of galaxy growth since redshift of unity will be directly compared to theoretical models to more physically constrain the phenomenological models currently used to predict galaxy properties in simulations.

7.1   A Unique Redshift Survey

With the recent advent of wide-field imagers on large telescopes as well as deep, wide-field, surveys with space observatories such as *Spitzer*, *Chandra*, and *HST* the volume probed by photometry far overshadows the volume with complementary spectroscopy. While photometric redshifts are often sufficient to study the gross properties of populations, redshifts with accuracies of $\Delta z/(1 + z) \approx 3 - 5\%$ are not sufficient to accurately divide galaxy samples into all but the coarsest environmental subdivisions Cooper et al. (2005). Higher accuracies can be reached when enough photometric bandpasses are utilized, but the observational cost of obtaining many filters of deep, wide-field imaging in many bands hinders all but pencil-beam applications.

As described in the previous chapter, PRIsm MUlti-object Survey (PRIMUS) fills the need for deep, wide-field spectroscopy to maximize the scientific potential of existing multiwavelength photometry. The fields observed as part of PRIMUS were chosen to maximize the long-term impact of PRIMUS spectroscopy and to increase the legacy value of existing panchromatic imaging. Specifically, we targeted fields with deep *Spitzer*, *Chandra*, *HST*, *GALEX*, or *XMM-Newton* observations but little existing spectroscopy. These panchromatic observations

will allow for measurements of the stellar masses, morphologies, star formation rates, and AGN activity, as well as the evolution of these properties as a function of redshift, local galaxy environment, and galaxy type over more than half of cosmic history. Many attempts to measure the evolution of galaxy properties have utilized high-redshift surveys combined with a single low-reshift data point from SDSS as an evolutionary baseline. By observing the full redshift range $0.2 < z < 1.0$ in PRIMUS, we remove the need for external calibration samples and the associated systematic effects; evolution will be measured fully within the PRIMUS dataset. When completed, PRIMUS will include 300,000 galaxy spectra to $z = 1$ over 10 square degrees and will probe comparable volumes and numbers of galaxies as low-redshift benchmark surveys such as 2dF and SDSS. PRIMUS is be the largest intermediate-redshift galaxy survey and the largest collection of redshifts for galaxies with *Spitzer* and X-ray imaging observed to date. With its unique size, PRIMUS will revolutionize investigations of AGN and galaxy evolution at intermediate-redshifts and be the standard bearer for years to come. A great deal of scientific investigations will be possible with PRIMUS and much of my research in the next several years will draw upon this rich dataset.

7.2   The Assembly History of Galaxies Since z=1.0:

The popular ΛCDM cosmological world model predicts the late assembly of progressively more massive dark matter halos through mergers of smaller systems (Kauffmann, 1995). Coupled with the mergers of dark matter halos is the merging of luminous matter and thus it is expected that galaxies have grown significantly through mergers since $z = 1$ (De Lucia et al., 2006). The relative importance of mass growth through in-situ star formation versus the assembly of stars through mergers is poorly observationally constrained, however. In Chapters 4 and 5 we

showed that star formation plays a small role in the build up of massive galaxies since $z \sim 1$. This new investigation will constrain how much star formation versus star formation-less mergers contribute to the growth of galaxies of different types and living in different environment over the same epoch.

Being the largest spectroscopic sample of intermediate-redshift galaxies with superb panchromatic photometry, PRIMUS is an ideal dataset to measure the evolution of galaxy properties as a function of redshift, environment, and galaxy type. In order to understand the interplay between the stellar mass growth and star formation rate in galaxies, we will use PRIMUS redshifts and mid-infrared photometry from *Spitzer* to measure the evolution of the star formation rate and stellar masses of galaxies as a function of galaxy color and local galaxy environment as well as the joint evolution of the star formation rate and stellar mass distributions. The stellar mass growth in galaxies is directly controlled by the assembly history of the galaxy plus the formation of new stars. Measurements of the star formation rates determine the latter value, and thus careful measurements of the joint evolution of the star formation rate and stellar mass growth will allow us to measure the relative importance of mass assembly through mergers and the creation of new stars in-situ in all types of galaxies over the latter half of cosmic history, a key test of any model of galaxy evolution.

How stellar mass growth occurs is a fundamental question in galaxy astrophysics. The universal stellar mass has increased consistently over the last eight billion years, even as the global star-formation rate has declined (Brinchmann & Ellis 2000; Rudnick et al. 2003; Fontana et al. 2004; Drory et al. 2005). More specifically, recent work has indicated that L^* galaxies on the red sequence have been built up by about 30% in stellar mass through mergers since $z \sim 1$ (Bell et al. 2005; Faber et al. 2007; Blanton 2006; Brown et al. 2007), perhaps mostly with smaller

red galaxies (Masjedi et al. 2007). Meanwhile, the blue galaxy sequence has appeared to build up steadily (Blanton 2006), perhaps experiencing a significant loss due to mergers and/or quenching (Bell et al. 2007).

Stellar mass growth of galaxies occurs through two basic routes: through star-formation and through accretion of smaller galaxies. Star-formation rates out to $z = 1$ tell us how much stellar mass has formed during that period (e.g. Hopkins 2004). By comparing this growth to the build-up in stellar mass, we can determine the relative contribution due to the merging of galaxies. While galaxy merging can also be detected directly (van Dokkum et al. 1999; Lin et al. 2004; Masjedi et al. 2007; De Propris et al. 2007), it is notoriously difficult to convert observations of close pair counts or interacting systems into estimates of galaxy growth.

To distinguish these contributions to stellar mass growth, we must consider jointly the red sequence of galaxies, and the blue sequence of galaxies. The former may grow primarily due to mergers, while the latter grow primarily due to star-formation. Indeed, one of the roles of mergers may be to induce the consumption of all remaining gas in blue galaxies, quenching their star-formation and turning them into red galaxies (e.g., Robertson et al. 2006). Tracing this evolutionary path requires measuring the relative build-up of stellar mass on each sequence independently.

The growth of stellar mass as a function of time is clearly affected by the surrounding environment of each galaxy, as local observations have made abundantly clear (e.g. Blanton et al. 2005b). In some galaxies, it is clear that the environment actually plays the dominant role: either by ending star-formation in disks (for example, spirals that fall into clusters and turn into S0s) or by growing due to mergers with smaller galaxies (for example, cD galaxies in cluster centers).

A careful, complete, and high signal-to-noise census of stellar mass growth can track the effects of these processes.

7.3 Understanding the Quenching of Star Formation in All Galaxies Since $z \sim 1$:

Numerous theoretical models have been proposed to remove the cold gas reservoir from massive galaxies in order to quench star formation in these systems and allow them to fade into the population of red and dead galaxies observed today (Scannapieco et al., 2005; Hopkins et al., 2005; Croton et al., 2006; De Lucia et al., 2006). While, phenomenologically, these models reproduce the observed distribution of galaxy colors and masses, the observational support for a direct connection between AGN and the quenching of star formation is weak. Studies of the properties and evolution of AGN hosts can help place constraints on this problem, but it is notoriously difficult to select a complete sample of AGN without extensive multiwavelength observations. Furthermore, as the properties of galaxies are highly correlated, it is vital that any investigation of AGN hosts can quantify evolutionary effects as a function of stellar mass, local galaxy environment, and galaxy color. In likely the best attempt to quantify the connection between AGN and star formation quenching to date, the superb multiwavelength observations of the 0.5 deg^2 AEGIS field (Davis et al., 2007) were used to measure the effect of AGN feedback on the star formation in galaxies at $z < 1.4$. Based on 240 AGN in the field, only weak evidence that AGNs are the *direct* cause for the quenching of star formation at $z < 1.4$ was found (Bundy et al., 2007).

In order to maximize the volume probed by deep multiwavelength imaging and spectroscopy, we will utilize a combination of the AGN and Galaxy Evolution Survey (AGES) and PRIMUS to investigate the impact of AGN on the truncation of star formation in galaxies at $0.1 < z < 1.0$. The superset of these two

surveys will contain nearly 20 deg^2 of spectroscopy with archival IRAC and MIPS imaging, 7 square degrees of *GALEX* imaging, and nearly 15 deg^2 of X-ray imaging from *Chandra* and *XMM-Newton*. Thus, the combined area is a factor of 40 larger than previous attempts to statistically measure the importance of AGN feedback on star formation quenching. The unprecedented area available with multiwavelength imaging and spectroscopy available from the combination of AGES and PRIMUS will dramatically decrease cosmic variance errors, making this the best dataset available for this study in the near future.

Several studies have concluded that green galaxies have a higher fraction of AGNs than their red and blue counterparts. This overabundance of AGNs associated with galaxies between the blue cloud of star forming galaxies and the red-sequence of passive evolution may support the scenario wherein AGNs trigger the quenching of star formation in their hosts (Yan et al., 2006; Salim et al., 2007; Silverman et al., 2008). Using star formation rates traced by UV and far-infrared photometry, we will measure the stellar mass at which star formation is truncated in normal galaxies as a function of redshift. This quenching mass has been well measured at $z \sim 1$, but our study will be the largest such investigation at intermediate redshifts providing the first constraints on the evolution of the quenching mass below $z = 0.7$ with massive statistics. If AGNs are, in fact, the cause for the quenching of star formation, we would expect the evolution of the characteristic mass of AGN hosts to evolve in a similar manner as the observed evolution in the quenching mass; we will test this directly by comparing the evolution of the stellar mass function of AGN hosts to that of normal galaxies at $z < 1$.

Clearly, the presence of an AGN in a galaxy is of much concern when measuring stellar masses, even when based on photometry extending from the X-ray

to far-infrared. Great care will be taken to quantify this contamination to our stellar masses to ensure our conclusions are not strongly biased. Previous authors have claimed the stellar masses they estimate are robust to the presence of AGN contamination using an X-ray selected AGN sample (Bundy et al., 2007). We will utilize several AGN samples, each selected independently based on optical, X-ray, and mid-infrared selection techniques to quantify the effects of AGN selection on our conclusions. Additionally, we will utilize deep HST imaging of the COSMOS field and ancillary mid-infrared and X-ray imaging to quantify the fraction of galaxy light confined to a central point source based upon various AGN selection methods as a secondary estimate of our contamination.

The uniquely large sample available from the combination of AGES and PRIMUS will allow us to investigate the relative importance of AGN activity and the local environment on shaping the star formation histories of galaxies. One may expect the truncation of star formation to occur more strongly in overdense environments where effects such as ram pressure stripping, galaxy harassment, and strangulation heat and remove cold gas from galaxies in addition to any processes at work in the field. Studies with DEEP2 at $z \sim 1$ found that quenching is accelerated in extremely dense environments compared to very underdense systems, but found only small differences between galaxies in less extreme environments (Bundy et al., 2006). Our sample will survey over an order of magnitude larger area at $0.1 < z < 1.0$ with a factor of 35 more spectra allowing us to quantify the effect of more subtle environmental changes on the downsizing of galaxy populations. By measuring the strength of star-formation quenching as a function of local environment, we will directly measure the role of the ensemble of environmental processes on the truncation of star formation in groups and clusters.

7.4   AGN Formation and Feedback Models

Different models of AGN formation and evolution make measurably different predictions for the local environments and clustering properties of AGNs. Kauffmann & Haehnelt (2002) use a semi-analytic model in which AGNs are fueled by galaxy mergers, where the peak AGN luminosity depends on the mass of gas accreted by the black hole, and the AGN luminosity declines exponentially after the merger event. This leads to a natural prediction that brighter AGNs reside in more massive galaxies, such that the AGN clustering amplitude should be strongly luminosity-dependent.

More recently, Hopkins et al. (2005) present an alternative model in which bright and faint AGNs are in similar physical systems but are in different stages of their life cycles. This work is inspired by numerical simulations of galaxy mergers which incorporate black hole growth and feedback. This model predicts that faint and bright AGNs reside in similar–mass dark matter halos and that quasar clustering should depend only weakly on luminosity. The model also predicts that AGNs are initially obscured in the post-merger phase, and that feedback from the central engine blows away much of surrounding gas and dust, revealing an optically bright quasar. Eventually an elliptical galaxy is created, which may host a lower-luminosity AGN.

In contrast, the semi-analytic model of Croton et al. (2006) combines a prescription of merger-driven black hole growth with an independent mode for cold gas accretion in large halos. This model assumes that some fraction of cold gas must be present to trigger a bright AGN phase during a galaxy merger; thus gas-free galaxies are not expected to shine as bright AGNs and only those mergers which occur outside of group environments at $z < 1$ will contain the requisite cold gas to fuel a strong AGN. This model predicts that bright AGNs should clus-

ter similarly to star-forming galaxies at the same redshift, less than the clustering predicted by other models.

The key to discriminating between different AGNs formation models is to measure the clustering of AGN as a function of luminosity and redshift and put the results in context by comparing to the clustering of galaxies over the same epoch. Model predictions are currently poorly constrained, due to the small existing samples of AGNs with spectroscopic redshifts beyond $z = 0.1$. The correlation function of bright optically-selected quasars has been measured to $z = 3$ using 20,000 objects in the 2dF QSO Redshift Survey (Croom et al., 2005) though the error bars are large ($\sim$30%) due to the low number density of QSOs. The clustering amplitude of lower-luminosity AGNs has been measured well only at $z = 0.1$ using the large SDSS dataset (Wake et al., 2004).

We can discriminate between AGN formation models by measuring the clustering and environments of quasars and lower-luminosity AGNs at $0.2 < z < 1.0$. We will select AGNs in fields that have both *Spitzer* and *Chandra* imaging as well as spectroscopy from the PRIMUS redshift survey. Using 200,000 PRIMUS redshifts over 10 deg^2 with existing or proposed *Spitzer* photometry, we will measure the local environment of each AGN using the overdensity of nearby galaxies relative to the mean density. We will also measure the clustering amplitude of the AGNs as a function of scale, on both small and large scales, covering $0.1 - 20h^{-1}$ Mpc. To measure the clustering amplitude of AGNs we do not have to use the auto-correlation function of the AGNs, which is very sensitive to spatially-varying selection functions and would be noisy due to the relatively small AGN sample size. Instead, we will measure the clustering of galaxies *around* the AGN through the cross-correlation function and then divide by the correlation function of the galaxies themselves to determine the AGN clustering strength. This allows

a relatively high S/N measurement of the clustering of rare AGN as long as there are large samples of galaxies to compare with (e.g, Coil et al., 2007).

APPENDIX A

THE LUMINOSITY FUNCTION

The luminosity function is a key tool for many branches of astrophysics. Quite simply, the luminosity function measures the probability distribution of objects as a function of their luminosity. In galaxy studies, the luminosity has a history beginning only shortly after Hubble discovered that M33 and M31 were too distant to be within in the Milky Ways itself. A full history of the galaxy luminosity function is beyond the scope here, but the interested reader can find a historical summary of the galaxy luminosity function and several examples of its utility in Binggeli et al. (1988). By convention, the luminosity function, $\phi(M)$, is defined to be the number of galaxies per luminosity (or magnitude) interval per volume element and often has units of $\mathrm{Mpc}^{-3}\,\mathrm{Mag}^{-1}$.

Numerous computational methods have been utilized when calculating luminosity functions. The Vmax method (Schmidt, 1968), a simple method used in this dissertation, groups objects into bins of luminosity. In this method, the luminosity function is calculated simply as

$$\phi(M_i) = \sum_j W_j V\mathrm{max}_j \tag{A.1}$$

where $V_{\mathrm{max},j}$ is the maximum volume object j could have occupied and been included in the sample. Here, W_j is defined as

$$W_j = \begin{cases} s_j & \mathrm{if} M_i - \Delta M/2 < M_j < M_i + \Delta M/2; \\ 0 & \mathrm{else.} \end{cases} \tag{A.2}$$

and s_j is the selection probability, included targeting rate, and spectroscopic and photometric incompleteness, for object j. The Vmax method, while assuming no parametric form for the shape of the luminosity function and simple to calculate

for a flux-limited survey, can become difficult to determine when a sample has complex incompleteness as a function of galaxy properties.

When fitting a luminosity function, parametric forms are often adopted to characterize the evolution in the population. The exact form used depends strongly on the population considered, but power-laws and Schecter functions (Schechter, 1976) are commonly used throughout the literature. The Schecter function is defined such that

$$\phi(L)dL - \phi^* \left(\frac{L}{L^*} \right)^\alpha \exp \left(-\frac{L}{L^*} \right) \frac{dL}{L^*} \tag{A.3}$$

In this parameterization, the luminosity function is a power-law with slope α at low luminosities and exponentially declines at the bright end. As much of optical astronomy has been developed in the magnitude system, it is often practical, though less elegant, to express the Schecter function in magnitudes such that

$$\phi(M)dM = \frac{2}{5}\phi^*(\ln 10) \left[10^{\frac{2}{5}(M^*-M)} \right]^{\alpha+1} \exp \left[-10^{\frac{2}{5}(M^*-M)} \right] dM. \tag{A.4}$$

In these parameterizations, L^* (or M^*) represents the characteristic luminosity where the luminosity function transitions between an exponential tail and a power law and the characteristic number density of the population is characterized by ϕ^*.

REFERENCES

Abazajian, K., et al.2003, AJ, 126, 2081

Abazajian, K., et al. 2004, AJ, 128, 502

Abazajian, K., et al. 2005, AJ, 129, 1755

Adelman-McCarthy, J. K., et al. 2007, ArXiv e-prints, 707, arXiv:0707.3413

Adelman-McCarthy, J. K., et al. 2007, ApJS, 172, 634

Adelman-McCarthy, J. K., et al. 2006, ApJS, 162, 38

Andreon, S. 2003, A&A, 409, 37

Arimoto, N. & Yoshii, Y. 1987, A&A, 173, 23

Bahcall, N. A., et al. 2003, ApJS, 148, 243

Baldry, I. K., Glazebrook, K., Brinkmann, J., Ivezić, Ž., Lupton, R. H., Nichol, R. C., & Szalay, A. S. 2004, ApJ, 600, 681

Baldry, I. K., Balogh, M. L., Bower, R. G., Glazebrook, K., Nichol, R. C., Bamford, S. P., & Budavari, T. 2006, MNRAS, 373, 469

Ball, N. M., Loveday, J., Brunner, R. J., Baldry, I. K., & Brinkmann, J. 2006, MN-RAS, 373, 845

Balogh, M. L., Miller, C., Nichol, R., Zabludoff, A., & Goto, T. 2005, MNRAS, 360, 587

Barger, A. J., Cowie,L. L., Brandt, W. N., Capak, P., Garmire, G. P., Horn-schemeier,A. E., Steffen, A. T., & Wehner, E. H. 2002, AJ, 124, 1839

Barger, A. J., Cowie, L. L., Capak, P., Alexander, D. M., Bauer, F. E., Brandt, W. N., Garmire, G. P., & Hornschemeier, A. E. 2003, ApJL, 584, L61

Barger, A. J., Cowie,L. L., Mushotzky, R. F., Yang, Y., Wang, W.-H., Steffen, A. T., & Capak, P. 2005, AJ, 129, 578

Bauer, A. E., Drory, N., Hill, G. J., & Feulner, G. 2005, ApJL, 621, L89

Becker, R. H., White, R. L., & Helfand, D. J. 1995, ApJ, 450, 559

Bell, E. F., & de Jong, R. S. 2000, MNRAS, 312, 497

Bell, E. F., et al. 2004, ApJ, 608, 752

Bell, E. F., et al. 2005, ApJ, 625, 23

Bell, E. F., Phleps, S.,Somerville, R. S., Wolf, C., Borch, A., & Meisenheimer, K. 2006, ApJ, 652, 270

Bell, E. F., et al. 2006, ApJ, 640, 241

Bell, E. F., Zheng, X. Z., Papovich, C., Borch, A., Wolf, C., & Meisenheimer, K. 2007, ApJ, 663, 834

Belokurov, V., et al. 2006, ApJL, 642, L137

Belokurov, V., et al. 2007, ApJ, 658, 337

Bennett, C. L., et al. 1996, ApJL, 464, L1

Bennett, C. L., et al. 2003, ApJ, 583, 1

Benson, A. J., Bower, R. G., Frenk, C. S., Lacey, C. G., Baugh, C. M., & Cole, S. 2003, ApJ, 599, 38

Bernardi, M., Renzini, A., da Costa, L. N., Wegner, G., Alonso, M. V., Pellegrini, P. S., Rité, C., & Willmer, C. N. A. 1998, ApJL, 508, L143

Bernardi, M., et al. 2003, AJ, 125, 1882

Bernardi, M., et al. 2003a, AJ, 125, 1817

Bernardi, M., et al. 2003b, AJ, 125, 1849

Bernardi, M., et al. 2003c, AJ, 125, 1866

Bernardi, M., et al. 2003d, AJ, 125, 1882

Bernardi, M., Sheth,R. K., Nichol, R. C., Schneider,D. P., & Brinkmann, J. 2005, AJ, 129,61

Bernardi, M., Nichol, R. C., Sheth, R. K., Miller, C. J., & Brinkmann, J. 2006, AJ, 131, 1288

Bertin, E., &Arnouts, S. 1996, A&AS, 117, 393

Binggeli, B., Sandage, A., & Tammann, G. A. 1988, ARA&A, 26, 509

Blake, C., & Bridle, S. 2005, MNRAS, 363, 1329

Blakeslee, J. P., et al. 2003, ApJL, 596, L143

Blanton, M. R., et al. 2001, AJ, 121, 2358

Blanton, M. R., et al. 2003, ApJ, 592, 819

Blanton, M. R., et al. 2003, ApJ, 594, 186

Blanton, M. R., Lin, H., Lupton, R. H., Maley, F. M., Young, N., Zehavi, I., & Loveday, J. 2003, AJ, 125, 2276

Blanton, M. R., et al. 2003,AJ, 125, 2348

Blanton, M. R., et al. 2005, AJ, 129, 2562

Blanton, M. R., Eisenstein, D., Hogg, D. W., Schlegel, D. J., & Brinkmann, J. 2005, ApJ, 629, 143

Blanton, M. R. 2006, ApJ,648, 268

Bower, R. G., Lucey, J. R., & Ellis, R. S. 1992, MNRAS, 254, 589

Bower, R. G., Benson, A. J., Malbon, R., Helly, J. C., Frenk, C. S., Baugh, C. M., Cole, S., & Lacey, C. G. 2006, MNRAS, 370, 645

Boyle, B. J., Shanks, T., Croom, S. M., Smith, R. J., Miller, L., Loaring, N., & Heymans, C. 2000, MNRAS, 317, 1014

Brand, K., et al. 2005, ApJ, 626, 723

Brand, K., et al. 2006, ApJ, 644, 143

Brand, K., et al. 2006, ApJ, 641, 140

Bressan, A., Chiosi, C., & Tantalo, R. 1996, A&A, 311, 425

Brinchmann, J., & Ellis, R. S. 2000, ApJL, 536, L77

Bromley, B. C., Press, W. H., Lin, H., & Kirshner, R. P. 1998, ApJ, 505, 25

Brough, S., Collins, C. A., Burke, D. J., Mann, R. G., & Lynam, P. D. 2002, MNRAS, 329, L53

Brown, M. J. I., Dey, A., Jannuzi, B. T., Lauer, T. R., Tiede, G. P., & Mikles, V. J. 2003, ApJ, 597, 225

Brown, M. J. I., Jannuzi,B. T., Dey, A., & Tiede, G. P. 2005, ApJ, 621, 41

Brown, M. J. I., et al. 2006, ApJ, 638, 88

Brown, M. J. I., Dey, A., Jannuzi, B. T., Brand, K., Benson, A. J., Brodwin, M., Croton, D. J., & Eisenhardt, P. R. 2007, ApJ, 654, 858

Bruzual, G., & Charlot, S. 2003, MNRAS, 344, 1000

Budavári, T., et al. 2003, ApJ, 595, 59

Bundy, K., et al. 2006, ApJ, 651, 120

Bundy, K., et al. 2007, ArXiv e-prints, 710, arXiv:0710.2105

Butcher, H., & Oemler, A., Jr. 1978, ApJ, 226, 559

Butcher, H., & Oemler, A., Jr. 1984, ApJ, 285, 426

Caldwell, N., Rose, J. A., & Concannon, K. D. 2003, AJ, 125, 2891

Carlberg, R. G., Cowie, L. L., Songaila, A., & Hu, E. M. 1997, ApJ, 484, 538

Cattaneo, A., Dekel, A., Devriendt, J., Guiderdoni, B., & Blaizot, J. 2006, MNRAS, 370, 1651

Chabrier, G. 2003, PASP,115, 763

Chen, H.-W., et al. 2003,ApJ, 586, 745

Chiu, K., et al. 2005, AJ, 130, 13

Cimatti, A., et al. 2004, Nature, 430, 184

Cimatti, A., Daddi, E., & Renzini, A. 2006, A&A, 453, L29

Clemens, M. S., Bressan, A., Nikolic, B., Alexander, P., Annibali, F., & Rampazzo, R. 2006, MNRAS, 370, 702

Cohen, J. G., Hogg, D. W., Pahre, M. A., Blandford, R., Shopbell, P. L., & Richberg, K. 1999, ApJS, 120, 171

Coil, A. L., Hennawi, J. F., Newman, J. A., Cooper, M. C., & Davis, M. 2007, ApJ, 654, 115

Coil, A. L., et al. 2008,ApJ, 672, 153

Colless, M., et al. 2003, ArXiv Astrophysics e-prints, arXiv:astro-ph/0306581

Conroy, C., Ho, S., & White, M. 2007, MNRAS, 379, 1491

Conroy, C., Wechsler,R. H., & Kravtsov, A. V. 2007, ArXiv Astrophysics e-prints,arXiv:astro-ph/0703374

Cooper, M. C., Newman, J. A., Madgwick, D. S., Gerke, B. F., Yan, R., & Davis, M. 2005, ApJ, 634, 833

Cooper, M. C., et al. 2008, MNRAS, 383, 1058

Cowie, L. L., Songaila, A., Hu, E. M., & Cohen, J. G. 1996, AJ, 112, 839

Cowie, L. L., Songaila, A., & Barger, A. J. 1999, AJ, 118, 603

Cristiani, S., et al. 2004, ApJL, 600, L119

Croom, S. M., Smith, R. J., Boyle, B. J., Shanks, T., Miller, L., Outram, P. J., & Loaring, N. S. 2004, MNRAS, 349, 1397

Croom, S. M., et al. 2005, MNRAS, 356, 415

Croton, D. J., et al. 2006, MNRAS, 365, 11

Davis, M., & Huchra, J. 1982, ApJ, 254, 437

Davis, M., Huchra, J., Latham, D. W., & Tonry, J. 1982, ApJ, 253, 423

Davis, M., et al. 2003,Proc. SPIE, 4834, 161

Davis, M., et al. 2007, ApJL, 660, L1

Davé, R. 2007, ArXiv e-prints, 710, arXiv:0710.0381

Dawson, S., et al. 2004, ApJ, 617, 707

De Lucia, G., Springel, V., White, S. D. M., Croton, D., & Kauffmann, G. 2005, ArXiv Astrophysics e-prints, arXiv:astro-ph/0509725

De Lucia, G., Springel, V., White, S. D. M., Croton, D., & Kauffmann, G. 2006, MNRAS,366,499

De Lucia, G., et al. 2007, MNRAS, 374, 809

Dekel, A., & Birnboim, Y. 2006, MNRAS, 368, 2

Dekel, A., & Birnboim, Y. 2008, MNRAS, 383, 119

de Propris, R., Stanford, S. A., Eisenhardt, P. R., Dickinson, M., & Elston, R. 1999, AJ, 118, 719

De Propris, R., Conselice, C. J., Liske, J., Driver, S. P., Patton, D. R., Graham, A. W., & Allen, P. D. 2007, ApJ, 666, 212

de Vaucouleurs, G. 1948, Annales d'Astrophysique, 11, 247

de Vaucouleurs, G. 1961, ApJS, 5, 233

de Vries, W. H., Morganti, R., Röttgering, H. J. A., Vermeulen, R., van Breugel, W., Rengelink, R., & Jarvis, M. J. 2002, AJ, 123, 1784

Desai, V., et al. 2006, ApJ, 641, 133

Dey, A., et al. 2005, ApJ, 629, 654

Di Matteo, T., Springel, V., & Hernquist, L. 2005, Nature, 433, 604

Dickinson, M., Papovich, C., Ferguson, H. C., & Budavári, T. 2003, ApJ, 587, 25

Dinescu, D. I., et al. 2002, ApJL, 575, L67

Djorgovski, S. G., Stern, D., Mahabal, A. A., & Brunner, R. 2003, ApJ, 596, 67

Dressler, A., & Gunn, J. E. 1983, ApJ, 270, 7

Dressler, A. 1980, ApJ, 236, 351

Drory, N., Salvato, M., Gabasch, A., Bender, R., Hopp, U., Feulner, G., & Pannella, M. 2005, ApJL, 619, L131

Duffau, S., Zinn, R., Vivas, A. K., Carraro, G., Méndez, R. A., Winnick, R., & Gallart, C. 2006, ApJL, 636, L97

Efstathiou, G., Bernstein, G., Tyson, J. A., Katz, N., & Guhathakurta, P. 1991, ApJL, 380, L47

Eggen, O. J., Lynden-Bell, D., & Sandage, A. R. 1962, ApJ, 136, 748

Einstein, A. 1915, Sitzungsberichte der Königlich Preußischen Akademie der Wissenschaften (Berlin), Seite 844-847., 844

Einstein, A. 1916, Annalen der Physik, 354, 769

Eisenhardt, P. R., et al. 2004, ApJS, 154, 48

Eisenstein, D. J., et al. 2001, AJ, 122, 2267

Eisenstein, D. J., et al. 2003, ApJ, 585, 694

Eisenstein, D. J., Blanton, M., Zehavi, I., Bahcall, N., Brinkmann, J., Loveday, J., Meiksin, A., & Schneider, D. 2005, ApJ, 619, 178

Eisenstein, D. J., et al. 2006, ApJS, 167, 40

Eisenstein, D. J., et al. 2006, AJ, 132, 676

Ellis, R. S., Smail, I., Dressler, A., Couch, W. J., Oemler, A. J., Butcher, H., & Sharples, R. M. 1997, ApJ, 483, 582

Ellis, S. C., Driver, S. P., Allen, P. D., Liske, J., Bland-Hawthorn, J., & De Propris, R. 2005, MNRAS, 363, 1257

Elston, R. J., et al. 2005, in press, arXiv:astro-ph/0511249

Elvis, M., Risaliti, G., & Zamorani, G. 2002, ApJL, 565, L75

Faber, S. M. 1972, A&A, 20, 361

Faber, S. M. 1973, ApJ, 179, 731

Faber, S. M., et al. 2003, Proc. SPIE, 4841, 1657

Faber, S. M., et al. 2007, ApJ, 665, 265

Fabricant, D. G., Hertz, E. N., Szentgyorgyi, A. H., Fata, R. G., Roll, J. B., & Zajac, J. M. 1998, Proc. SPIE, 3355, 285

Fabricant, D., et al. 2005, PASP, 117, 1411

Fan, X., et al. 2000, AJ,120, 1167

Fan, X., et al. 2001a, AJ, 121, 31

Fan, X., et al. 2001b, AJ,121, 54

Fan, X., et al. 2001c, AJ, 122, 2833

Fan, X., et al. 2003, AJ, 125, 1649

Fan, X., et al. 2004, AJ,128, 515

Fan, X., et al. 2005, in press, arXiv:astro-ph/0512080

Fazio, G. G., et al. 2004, ApJS, 154, 10

Ferrarese, L., & Merritt, D. 2000, ApJL, 539, L9

Ferreras, I., Charlot, S., & Silk, J. 1999, ApJ, 521, 81

Figer, D. F., Kim, S. S.,Morris, M., Serabyn, E., Rich, R. M., & McLean, I. S. 1999,
ApJ, 525,750

Fioc, M., & Rocca-Volmerange , B. 1999, ArXiv Astrophysics e-prints, arXiv:astro-ph/9912179

Flores, H., et al. 1999, ApJ, 517, 148

Fontana, A., et al. 2004, A&A, 424, 23

Fontana, A., et al. 2006, A&A, 459, 745

Fukugita, M., Ichikawa, T., Gunn, J. E., Doi, M., Shimasaku, K., & Schneider, D. P.
1996, AJ, 111, 1748

Fukugita, M., Nakamura, O., Turner, E. L., Helmboldt, J., & Nichol, R. C. 2004, ApJL, 601, L127

Gebhardt, K., et al. 2000, ApJL, 539, L13

Gladders, M. D., Lopez-Cruz, O., Yee, H. K. C., & Kodama, T. 1998, ApJ, 501, 571

Gladders, M. D., & Yee, H. K. C. 2005, ApJS, 157, 1

Glazebrook, K., & Bland-Hawthorn, J. 2001, PASP, 113, 197

Glazebrook, K., et al. 2004, Nature, 430, 181

Goto, T., Yamauchi, C., Fujita, Y., Okamura, S., Sekiguchi, M., Smail, I., Bernardi, M., & Gomez, P. L. 2003, MNRAS, 346, 601

Goto, T., et al. 2003, PASJ, 55, 771

Graham, A. W., Driver, S. P., Petrosian, V., Conselice, C. J., Bershady, M. A., Crawford, S. M., & Goto, T. 2005, AJ, 130, 1535

Groth, E. J., & Peebles, P. J. E. 1977, ApJ, 217, 385

Gunn, J. E., et al. 1998, AJ, 116, 3040

Gunn, J. E., et al. 2006, AJ, 131, 2332

Guzzo, L., et al. 2007, ApJS, 172, 254

Haarsma, D. B., Partridge, R. B., Windhorst, R. A., & Richards, E. A. 2000, ApJ, 544, 641

Hammer, F., et al. 1997, ApJ, 481, 49

Hamuy, M., Walker, A. R., Suntzeff, N. B., Gigoux, P., Heathcote, S. R., & Phillips, M. M. 1992, PASP, 104, 533

Hamuy, M., Suntzeff, N. B., Heathcote, S. R., Walker, A. R., Gigoux, P., & Phillips, M. M. 1994, PASP, 106, 566

Harrison, E. R. 1970, Phys. Rev. D, 1, 2726

Hashimoto, Y., Oemler, A. J., Lin, H., & Tucker, D. L. 1998, ApJ, 499, 589

Heavens, A., Panter,B., Jimenez, R., & Dunlop, J. 2004, Nature, 428, 625

Helmi, A., White, S. D. M., de Zeeuw, P. T., & Zhao, H. 1999, Nature, 402, 53

Higdon, J. L., et al.2005, ApJ, 626, 58

Ho, L. C., Filippenko, A. V., & Sargent, W. L. W. 1997, ApJ, 487, 568

Ho, S., Lin, Y.-T., Spergel, D., & Hirata, C. M. 2007, ArXiv e-prints, 706, arXiv:0706.0727

Hogg, D. W., Cohen, J. G.,Blandford, R., & Pahre, M. A. 1998, ApJ, 504, 622

Hogg, D. W., et al. 2003, ApJL, 585, L5

Hogg, D. W., et al. 2004, ApJL, 601, L29 25,000-5,337

Hogg, D. W., Finkbeiner, D. P., Schlegel, D. J., & Gunn, J. E. 2001, AJ, 122, 2129

Holden, B. P., Stanford, S. A., Eisenhardt, P., & Dickinson, M. 2004, AJ, 127, 2484

Holden, B. P., et al. 2005, ApJ, 626, 809

Hopkins, A. M. 2004, ApJ, 615, 209

Hopkins, P. F. Hernquist, L., Martini, P., Cox, T. J., Robertson, B., Di Matteo, T., & Springel, V. 2005, ApJL, 625, L71

Hopkins, A. M., & Beacom, J. F. 2006, ApJ, 651, 142

Hopkins, P. F., Hernquist, L., Cox, T. J., Di Matteo, T., Robertson, B., & Springel, V. 2006, ApJS, 163, 1

Hopkins, P. F., Hernquist, L., Cox, T. J., Robertson, B., & Springel, V. 2006, ApJS, 163, 50

Hopkins, P. F., Cox, T. J., Keres, D., & Hernquist, L. 2007, ArXiv e-prints, 706, arXiv:0706.1246

Hopkins, P. F., Hernquist, L., Cox, T. J., & Keres, D. 2007, ArXiv e-prints, 706, arXiv:0706.1243

Houck, J. R., et al. 2005, ApJL, 622, L105

Hu, W., & Dodelson, S. 2002, ARA&A, 40, 171

Hubble, E. P. 1925, The Observatory, 48, 139

Hubble, E. 1929, Proceedings of the National Academy of Science, 15, 168

Hubble, E. P. 1936, Yale University Press,

Huchra, J., Davis, M., Latham, D., & Tonry, J. 1983, ApJS, 52, 89

Ivezić, Ž., et al. 2004, Astronomische Nachrichten, 325, 583

Jannuzi, B. T., & Dey, A. 1999, ASP Conf. Ser. 191: Photometric Redshifts and the Detection of High Redshift Galaxies, 191, 111

Jiang, L., et al. 2006, AJ, 131, 2788

Jimenez, R., Bernardi, M., Haiman, Z., Panter, B., & Heavens, A. F. 2006, ArXiv Astrophysics e-prints, arXiv:astro-ph/0610724

Juneau, S., et al. 2005, ApJL, 619, L135

Kang, X., Jing, Y. P., Mo, H. J., Boumlrner, G. 2005, ApJ, 631, 21

Katz, N., & Gunn, J. E. 1991, ApJ, 377, 365

Kauffmann, G. & Charlot, S. 1998, MNRAS, 294, 705

Kauffmann, G. 1995, MNRAS, 274, 161

Kauffmann, G., Charlot, S., & White, S. D. M. 1996, MNRAS, 283, L117

Kauffmann, G., & Haehnelt, M. 2000, MNRAS, 311, 576

Kauffmann, G., & Haehnelt, M. G. 2002, MNRAS, 332, 529

Kauffmann, G., et al. 2003, MNRAS, 346, 1055

Kenter, A., et al. 2005, ApJS, 161, 9

Khan, S. A., et al. 2005,ApJL, 631, L9

Kodama, T. 1997, Ph.D. thesis, Univ. Tokyo

Kodama, T. & Arimoto, N. 1997, A&A, 320, 41

Kodama, T., Arimoto, N., Barger, A. J., & Arag'on-Salamanca, A. 1998, A&A, 334, 99

Kodama, T., Bower, R. G., & Bell, E. F. 1999, MNRAS, 306, 561

Kollmeier, J. A., et al. 2005, ArXiv Astrophysics e-prints, arXiv:astro-ph/0508657

Komatsu, E., et al. 2008, ArXiv e-prints, 803, arXiv:0803.0547

Kormendy, J. 2004, Coevolution of Black Holes and Galaxies, 1

Kormendy, J., & Richstone, D. 1995, ARA&A, 33, 581

Kron, R. G. 1980, ApJS, 43, 305

Kroupa, P. 2001, MNRAS, 322,231

Kurucz, R. 1993, ATLAS9 Stellar Atmosphere Programs and 2 km/s grid. Kurucz CD-ROM No. 13. Cambridge, Mass.: Smithsonian Astrophysical Observatory, 1993, 13

Larson, R. B. 1974, MNRAS, 166, 585

Larson, R. B. 1998, MNRAS, 301, 569

Larson,R. B., Tinsley, B. M., & Caldwell, C. N. 1980, ApJ, 237, 692

Lauer, T. R., et al. 2007,ApJ, 662, 808

Lauer, T. R. 1988, ApJ, 325, 49

Leavitt, H. S. 1908, Annals of Harvard College Observatory, 60, 87

Le Borgne, D., et al. 2006, ApJ, 642, 48

Le Fèvre, O.,et al. 2000, MNRAS, 311, 565

Le Fèvre, O., et al. 2004, A&A, 428, 1043

Lilly, S. J., Le Fevre, O., Crampton, D., Hammer, F., & Tresse, L. 1995, ApJ, 455, 50

Lilly, S. J., Le Fevre, O., Hammer, F., & Crampton, D. 1996, ApJL, 460, L1

Lin, H., Kirshner, R. P., Shectman, S. A., Landy, S. D., Oemler, A., Tucker, D. L., & Schechter, P. L. 1996, ApJ, 464, 60

Lin, H., Yee, H. K. C., Carlberg,R. G., Morris, S. L., Sawicki, M., Patton, D. R., Wirth, G., & Shepherd, C. W. 1999, ApJ, 518

Lin, L., et al. 2004, ApJL, 617, L9

Lonsdale, C. J., et al. 2003, PASP, 115, 897

Lotz, J. M., et al. 2008, ApJ, 672, 177

Lugger, P. M. 1984, ApJ, 278, 51

López-Cruz, O., Barkhouse, W. A., & Yee, H. K. C. 2004, ApJ, 614, 679

Lupton, R. H., Gunn, J. E., & Szalay, A. S. 1999, AJ, 118, 1406

Lupton, R. H., Gunn, J. E., Ivezić, Z., Knapp, G. R., Kent, S., & Yasuda, N. 2001, ASP Conf. Ser. 238:Astronomical Data Analysis Software and Systems X, 10, 269

Lynden-Bell, D. 1969, Nature, 223, 690

Madau, P., Ferguson, H. C., Dickinson, M. E., Giavalisco, M., Steidel, C. C., & Fruchter, A. 1996, MNRAS, 283, 1388

Mahabal, A., Stern, D., Bogosavljević, M., Djorgovski, S. G., & Thompson, D. 2005, ApJL, 634, L9

Majewski, S. R., Munn, J. A., & Hawley, S. L. 1994, ApJL, 427, L37

Majewski, S. R., Skrutskie, M. F., Weinberg, M. D., & Ostheimer, J. C. 2003, ApJ, 599, 1082

Maness, H., et al. 2007, ArXiv e-prints, 707, arXiv:0707.2382

Maraston, C. 2005, MNRAS,362, 799

Masjedi, M., et al. 2006, ApJ, 644, 54

Masjedi, M., Hogg, D. W., & Blanton, M. R. 2007, ArXiv e-prints, 708, arXiv:0708.3240

Matteucci, F. & Tornambe, A. 1987, A&A, 185, 51

McCarthy, P. J., al. 2004, ApJL, 614, L9

McCrady, N.,Gilbert,A. M., & Graham, J. R. 2003, ApJ, 596, 240

McIntosh, D. H., Zabludoff, A. I., Rix, H.-W., & Caldwell, N. 2005, ApJ, 619, 193

McIntosh, D. H., Guo, Y., Hertzberg, J., Katz, N., Mo, H. J., van den Bosch, F. C., & Yang, X. 2007, ArXiv e-prints, 710, arXiv:0710.2157

Mei, S., et al. 2006, ApJ, 639, 81

Menci, N., Fontana, A., Giallongo, E., & Salimbeni, S. 2005, ApJ, 632, 49

Menci, N., Fontana, A., Giallongo, E., Grazian, A., & Salimbeni, S. 2006, ApJ, 647, 753

Miralda-Escudé, J., & Kollmeier, J. A. 2005, ApJ, 619, 30

Mobasher, B., et al. 2004, ApJL, 600, L167

Moore, B., Ghigna, S., Governato, F., Lake, G., Quinn, T., Stadel, J., & Tozzi, P. 1999, ApJL, 524, L19

Murray, S. S., et al. 2005, ApJS, 161, 1

Navarro, J. F., & White, S. D. M. 1994, MNRAS, 267, 401

Nelan, J. E., Smith, R. J., Hudson, M. J., Wegner, G. A., Lucey, J. R., Moore, S. A. W., Quinney, S. J., & Suntzeff, N. B. 2005, ApJ, 632, 137

Newberg, H. J., et al. 2002, ApJ, 569, 245

Newberg, H. J., Yanny, B., Cole, N., Beers, T. C., Re Fiorentin, P., Schneider, D. P., & Wilhelm, R. 2007, ApJ, 668, 221

O'Connell, R. W. 1980, ApJ, 236, 430

O'Donnell, J. E. 1994, ApJ, 422, 158

Oke, J. B. 1974, ApJS, 27, 21

Oke, J. B., & Gunn, J. E. 1983, ApJ, 266, 713

Padmanabhan, N., et al. 2005, MNRAS, 359, 237

Papovich, C., Dickinson, M., Giavalisco, M., Conselice, C. J., & Ferguson, H. C. 2005, ApJ, 631, 101

Peebles, P. J. E., & Yu, J. T. 1970, ApJ, 162, 815

Penzias, A. A., & Wilson, R. W. 1965, ApJ, 142, 419

Perez, M. J., Tissera, P. B., Scannapieco, C., Lambas, D. G., & de Rossi, M. E. 2006, A&A, 459, 361

Pier, J. R., Munn, J. A., Hindsley, R. B., Hennessy, G. S., Kent, S. M., Lupton, R. H., & Ivezić, Ž. 2003, AJ, 125, 1559

Pimbblet, K. A., Smail, I., Edge, A. C., O'Hely, E., Couch, W. J., & Zabludoff, A. I. 2006, MNRAS, 366, 645

Poggianti, B. M., et al. 2001, ApJ, 563, 118

Postman, M., & Geller, M. J. 1984, ApJ, 281, 95

Press, W. H. 2002, Numerical recipes in C++ : the art of scientific computing by William H. Press. xxviii, 1,002 p. : ill. ; ISBN : 0521750334,

Pérez-González, P. G., et al. 2005, ApJ, 630, 82

Pérez-González, P. G., et al. 2008, ApJ, 675, 234

Quintero, A. D., et al. 2004, ApJ, 602, 190

Rhoads, J. E., Malhotra, S., Dey, A., Stern, D., Spinrad, H., & Jannuzi, B. T. 2000, ApJL, 545, L85

Rhoads, J. E., et al. 2003, AJ, 125, 1006

Rhoads, J. E., et al. 2004, ApJ, 611, 59

Richards, G. T.,et al. 2002, AJ, 123, 2945

Richards, G. T.,et al. 2005, MNRAS, 360, 839

Richards, G. T., et al. 2006, ArXiv Astrophysics e-prints, arXiv:astro-ph/0601434

Richards, G. T., et al. 2006b, ArXiv Astrophysics e-prints, arXiv:astro-ph/0601558

Rieke, G. H., Loken, K.,Rieke, M. J., & Tamblyn, P. 1993, ApJ, 412, 99

Rieke, G. H., et al. 2004, ApJS, 154, 25

Rines, K., Finn, R., & Vikhlinin, A. 2007, ApJL, 665, L9

Robertson, J. G. 1986, PASP, 98, 1220

Robertson, B., Hernquist, L., Cox, T. J., Di Matteo, T., Hopkins, P. F., Martini, P., & Springel, V. 2006, ApJ, 641, 90

Roll, J. B., Fabricant, D. G ., & McLeod, B. A. 1998, Proc. SPIE, 3355, 324

Rose, J. A. 1985, AJ, 90, 1927

Rudnick, G., et al. 2003, ApJ, 599, 847

Sako, M., et al. 2008, AJ, 135, 348

Salim, S., et al. 2007, ApJS, 173, 267

Salpeter, E. E. 1955, ApJ, 121, 161

Salpeter, E. E. 1964, ApJ, 140, 796

Sandage, A. & Visvanathan, N. 1978, ApJ, 225, 742

Scannapieco, E., Silk, J., & Bouwens, R. 2005, ApJL, 635, L13

Schechter, P. 1976, ApJ, 203, 297

Schectman, S., Landy, S., Oemler, A., Tucker, D., Kirshner, R., Lin, H., & Schechter, P. 1995, Wide Field Spectroscopy and the Distant Universe, 98

Schlegel, D. J., Finkbeiner, D. P., & Davis, M. 1998, ApJ, 500, 525

Schmidt, M., & Green, R. F. 1983, ApJ, 269, 352

Schmidt, M. 1968, ApJ, 151, 393

Schneider, D. P., et al. 2005, AJ, 130, 367

Scoville, N., et al. 2007, ApJS, 172, 1

Searle, L., & Zinn, R. 1978, ApJ, 225, 357

Seo, H.-J., Eisenstein, D. J., & Zehavi, I. 2007, ArXiv e-prints, 712, arXiv:0712.1643

Sharp, R. G., Crampton, D., Hook, I. M., & McMahon, R. G. 2004, MNRAS, 350, 449

Shectman, S. A., Landy, S. D., Oemler, A., Tucker, D. L., Lin, H., Kirshner, R. P., & Schechter, P. L. 1996, ApJ, 470, 172

Silk, J., & Rees, M. J. 1998, A&A, 331, L1

Silverman, J. D., et al. 2008, ApJ, 675, 1025

Small, T. A., Sargent, W. L. W., & Hamilton, D. 1997, ApJS, 111, 1

Smith, J. A., et al. 2002, AJ, 123, 2121

Smoot, G. F., et al. 1992, ApJL, 396, L1

Songaila, A., & Cowie, L. L. 2002, AJ, 123, 2183

Spergel, D. N., et al. 2007, ApJS, 170, 377

Springel, V., et al. 2005, Nature, 435, 629

Springel, V., Di Matteo, T., & Hernquist, L. 2005, ApJL, 620, L79

Springel, V., Frenk, C. S., & White, S. D. M. 2006, Nature, 440, 1137

Stanford, S. A., et al. 2005, ApJL, 634, L129

Steinmetz, M., & Mueller, E. 1994, A&A, 281, L97

Stern, D., Spinrad, H., Eisenhardt, P., Bunker, A. J., Dawson, S., Stanford, S. A., & Elston, R. 2000, ApJL, 533, L75

Stern, D., et al. 2005, ApJ, 631, 163

Stern, D., et al. 2006, ArXiv Astrophysics e-prints, arXiv:astro-ph/0608603

Stolte, A., Brandner, W., Grebel, E. K., Lenzen, R., & Lagrange, A.-M. 2005, ApJL, 628, L113

Stoughton, C., et al. 2002, AJ, 123, 485

Stoughton, C., et al. 2002, Proc. SPIE, 4836, 339

Strateva, I., et al. 2001, AJ, 122, 1861

Strauss, M. A., et al. 2002, AJ, 124, 1810

Sunyaev, R. A. 1978, The large scale structure of the universe, p. 393 - 404, 393

Terlevich, A. I., Kuntschner, H., Bower, R. G., Caldwell, N., & Sharples, R. M. 1999, MNRAS, 310, 445

Terlevich, A. I., Caldwell, N., & Bower, R. G. 2001, MNRAS, 326, 1547

Thomas, D., Maraston, C., Bender, R., & Mendes de Oliveira, C. 2005, ApJ, 621, 673

Thoul, A. A., & Weinberg, D. H. 1995, ApJ, 442, 480

Toomre, A. 1974, The Formation and Dynamics of Galaxies, 58, 347

Trager, S. C., Faber, S. M., Worthey, G., & González, J. J. 2000, AJ, 120, 165

Trager, S. C., Faber,S. M., Worthey, G., & González, J. J. 2000, AJ, 119, 1645

Tran, K.-V. H., van Dokkum, P., Franx, M., Illingworth, G. D., Kelson, D. D., & Schreiber, N. M. F. 2005, ApJL, 627, L25

Tremaine, S., et al. 2002, ApJ, 574, 740

Tremonti, C. A., et al. 2004, ApJ, 613, 898

Tresse, L., et al. 2007, A&A, 472, 403

Trump, J. R., et al. 2006, ApJS, 165, 1

Tucker, D. L., et al. 2006, Astronomische Nachrichten, 327, 821

Vanden Berk, D. E., et al. 2001, AJ, 122, 549

van Dokkum, P. G.,Franx, M., Kelson, D. D., Illingworth, G. D., Fisher, D., & Fabricant, D. 1998, ApJ,500, 714

van Dokkum, P. G., Franx, M., Fabricant, D., Kelson, D. D., & Illingworth, G. D. 1999, ApJL, 520, L95

van Dokkum, P. G., Franx, M., Fabricant, D., Illingworth, G. D., & Kelson, D. D. 2000, ApJ, 541, 95

van Dokkum, P. G., Stanford, S. A., Holden, B. P., Eisenhardt, P. R., Dickinson, M., & Elston, R. 2001,ApJL, 552, L101

van Dokkum, P. G. 2005, AJ, 130, 2647

van Dokkum, P. 2007, ArXiv e-prints, 710, arXiv:0710.0875

Visvanathan, N., & Sandage, A. 1977, ApJ, 216, 214

Wake, D. A., et al. 2004, ApJL, 610, L85

Wake, D. A., Collins, C. A., Nichol, R. C., Jones, L. R., & Burke, D. J. 2005, ApJ, 627, 186

Wake, D. A., et al. 2006, MNRAS, 372, 537

Wang, J. X., et al. 2004, ApJL, 608, L21

Wake, D. A., et al. 2008, ArXiv e-prints, 802, arXiv:0802.4288

Warren, S., & Hewett, P. 2002, ASP Conf. Ser. 283: A New Era in Cosmology, 283, 369

Weedman, D. W., et al. 2006, ArXiv Astrophysics e-prints, arXiv:astro-ph/0606740

White, M., Zheng, Z., Brown, M. J. I., Dey, A., & Jannuzi, B. T. 2007, ApJL, 655, L69

Whitmore, B. C., & Gilmore, D. M. 1991, ApJ, 367, 64

Williams, G. G., Olszewski, E., Lesser, M. P., & Burge, J. H. 2004, Proc. SPIE, 5492, 787

Willmer, C. N. A., et al. 2006, ApJ, 647, 853

Willott, C. J., elfosse, X., Forveille, T., Delorme, P., & Gwyn, S. D. J. 2005, ApJ, 633, 630

Wilson, G., Cowie, L. L., Barger, A. J., & Burke, D. J. 2002, AJ, 124, 1258

Wolf, C., Meisenheimer, K., Rix, H.-W., Borch, A., Dye, S., & Kleinheinrich, M. 2003, A&A, 401, 73

Wolf, C., Wisotzki, L., Borch,A., Dye, S., Kleinheinrich, M., & Meisenheimer, K. 2003, A&A, 408, 499

Worthey, G., Trager, S. C., & Faber, S. M. 1995, ASP Conf. Ser. 86: Fresh Views of Elliptical Galaxies, 86, 203

Wyithe, J. S. B., & Loeb, A. 2002, ApJ, 581, 886

Yan, R., Newman, J. A., Faber, S. M., Konidaris, N., Koo, D., & Davis, M. 2006, ApJ, 648, 281

York, D. G., et al. 2000, AJ, 120, 1579

Zabludoff, A. I., Zaritsky, D., Lin, H., Tucker, D., Hashimoto, Y., Shectman, S. A., Oemler, A., & Kirshner, R. P. 1996, ApJ, 466, 104

Zehavi, I., et al. 2004, ApJ, 608, 16

Zehavi, I., et al. 2005, ApJ, 630, 1

Zehavi, I., et al. 2005, ApJ, 621, 22

Zeldovich, Y. B. 1972, MNRAS, 160, 1P

Zepf, S. E., Whitmore, B. C., & Levison, H. F. 1991, ApJ, 383, 524

Zheng, W., et al. 2000, AJ, 120, 1607

Zheng, Z., et al. 2005, ApJ, 633, 791